

**Synthesis, Structure, Characterization, and Functional Properties of  
New Mixed Metal Polar Oxides**

---

A Dissertation

Presented to

the Faculty of the Department of Chemistry

University of Houston

---

In Partial Fulfillment

of the Requirements for the Degree of

Doctor of Philosophy

---

By

Sau Doan Nguyen

December, 2012

# **Synthesis, Structure, Characterization, and Functional Properties of New Mixed Metal Polar Oxides**

---

Sau Doan Nguyen

Approved by:

---

Dr. P. Shiv Halasyamani, Chairman

---

Dr. Angela Moeller

---

Dr. T. Randall Lee

---

Dr. Arnold M. Guloy

---

Dr. James K. Meen

---

Dean, College of Natural Sciences and Mathematics

## **Acknowledgments**

I would like to thank my advisor, Prof. P. Shiv Halasyamani, for having and supporting me during the time I did my PhD study in his lab. With his supervision I can see my remarkable progress in research, my big improvement in working skills, and importantly this successful work. Thank you for helping me from the very first time of my graduate study, sharing me your invaluable lessons, providing your precious time and endless patience in guiding me through my four years of doing my PhD research at University of Houston. I deeply thank you and wish you the best.

I would like to thank Dr. Sang-Hwan Kim for helping me in doing electronic structure calculation, Dr. Hong-Young Chang for guiding me to do the single crystal X-ray diffraction, and Dr. Jeongho Yeon for many research discussions and his friendship. I also thank other group members, Dr. Weiguo Zhang, Dr. Elise Pachoud, Sunwoo Kim, Tran Thi Thanh Thao, and Hana Lee for their support.

I wish to thank the journal referees for their reviews on my research papers. I also want to thank the committee members, Prof. Angela Moeller, Prof. Arnold Guloy, Prof. T. Randall Lee, and Prof. James K. Meen for their valuable time in reading and reviewing my dissertation.

I would like to thank my wife for her endless support. I thank you for taking care of me, understanding me, and looking after our child when I was doing my PhD research. A special thank is also for my little son who bring me joy, love, and energy for my PhD trip.

**Synthesis, Structure, Characterization, and Functional Properties of  
New Mixed Metal Polar Oxides**

---

An Abstract of a Dissertation

Presented to

the Faculty of the Department of Chemistry

University of Houston

---

In Partial Fulfillment

of the Requirements for the Degree of

Doctor of Philosophy

---

By

Sau Doan Nguyen

December, 2012



## Abstract

Functional polar oxide materials occupy a very crucial position in modern technology. The polar oxide materials exhibit many technologically important properties like second-harmonic generation, piezoelectricity, pyroelectricity, and possibly ferroelectricity caused by their polar crystal structure. Though the structure-property relationship in polar oxide materials is well studied, the understanding of how the structural building units are joined to form a new polar crystal structure has been less sufficient. A synthetic approach using cations susceptible to second-order Jahn Teller (SOJT) distortion like octahedrally coordinated  $d^0$  cations ( $\text{Ti}^{4+}$ ,  $\text{V}^{5+}$ ,  $\text{Mo}^{6+}$ ) and lone-pair cations ( $\text{Sn}^{2+}$ ,  $\text{Sb}^{3+}$ ,  $\text{Te}^{4+}$ ) is successful in preparing new polar oxide materials. We were successful in preparing several new polar oxide materials,  $\text{Zn}_2(\text{MoO}_4)(\text{AO}_3)$  ( $\text{A} = \text{Se}^{4+}$ ,  $\text{Te}^{4+}$ ) ( $P2_1$ ),  $\text{BiO}(\text{IO}_3)$  ( $Pca2_1$ ),  $\text{Li}_6(\text{Mo}_2\text{O}_5)_3(\text{SeO}_3)_6$  ( $Pmn2_1$ ),  $\text{Na}_2(\text{WO}_3)_3(\text{SeO}_3) \cdot 2\text{H}_2\text{O}$  ( $P3_1c$ ), and  $\text{Na}_6(\text{W}_6\text{O}_{19})(\text{SeO}_3)_2$  ( $C2$ ) and other centrosymmetric materials,  $\text{Li}_2(\text{MO}_4)(\text{TeO}_3)_2$  ( $\text{M} = \text{Mo}^{6+}$ ,  $\text{W}^{6+}$ ) ( $P2_1/n$ ). In this dissertation, we report the syntheses, crystal structures, physical properties, functional properties, and understanding of the structure-property relationship of the reported oxide materials.

The dissertation consists of six chapters.

Chapter 1 describes the second-order Jahn Teller effects on the polyhedral distortions of octahedrally coordinated  $d^0$  and lone-pair cations and functional properties of noncentrosymmetric and polar materials.

In Chapter 2, two new isostructural oxide materials,  $\text{Zn}_2(\text{MoO}_4)(\text{TeO}_3)$  and  $\text{Zn}_2(\text{MoO}_4)(\text{SeO}_3)$  are described with respect to their synthesis, structural and physical characterization, and electronic structure.

In Chapter 3, a new polar iodate consisting of two lone-pair cations,  $\text{BiO}(\text{IO}_3)$  with very large SHG efficiency is structurally and physically characterized.

In Chapter 4, the synthesis and characterization of two new isostructural centrosymmetric oxides,  $\text{Li}_2(\text{MO}_4)(\text{TeO}_3)$  ( $\text{M} = \text{Mo}^{6+}$  and  $\text{W}^{6+}$ ) and a new polar oxide material,  $\text{Li}_6(\text{Mo}_2\text{O}_5)_3(\text{SeO}_3)_6$  are reported.

In Chapter 5, two new polar oxide materials,  $\text{Na}_2(\text{WO}_3)_3(\text{SeO}_3) \cdot 2\text{H}_2\text{O}$  and  $\text{Na}_6(\text{W}_6\text{O}_{19})(\text{SeO}_3)_2$  are introduced with respect to the synthetic procedures and structural characterization.

Chapter 6 gives a summary of my work and suggestions of future work for the reported oxides.

## Table of Contents

Acknowledgment	iii
Abstract	v
Table of Contents	vii
List of Figures	x
List of Tables	xvi
List of Abbreviations	xix
CHAPTER 1.	<b>Polyhedral Distortion of Octahedrally Coordinated <math>d^0</math> Cations and Lone-Pair Cations and Functional Properties of Noncentrosymmetric and Polar Materials</b>
1.1	Second-order Jahn Teller (SOJT) electronic distortions on octahedrally coordinated $d^0$ cations and lone-pair cations 1
1.1.1	SOJT distortions of octahedrally coordinated $d^0$ cations 1
1.1.2	SOJT distortions of lone-pair cations 4
1.2	Functional properties of noncentrosymmetric polar materials 7
1.2.1	Second-harmonic generation 8
1.2.2	Piezoelectricity 9
1.2.3	Polarization measurements: pyroelectricity and ferroelectricity 10
1.3	References 13
CHAPTER 2.	<b>Synthesis, Characterization, and Structure–Property Relationships in Two New Polar Oxides: <math>\text{Zn}_2(\text{MoO}_4)(\text{SeO}_3)</math> and <math>\text{Zn}_2(\text{MoO}_4)(\text{TeO}_3)</math></b>
2.1	Abstract 16
2.2	Introduction 17
2.3	Experimental details 18
2.3.1	Synthesis 18
2.3.2	Characterization 20

2.4	Results and discussion	28
2.5	Conclusion	45
2.6	References	46

**CHAPTER 3. BiO(IO<sub>3</sub>): A New Polar Iodate that Exhibits an Aurivillius-type (Bi<sub>2</sub>O<sub>2</sub>)<sup>2+</sup> Layer and a Large SHG Response**

3.1	Abstract	53
3.2	Introduction	53
3.3	Experimental details	55
3.3.1	Synthesis	55
3.3.2	Characterization	56
3.4	Results and discussion	62
3.5	Conclusion	73
3.6	References	74

**CHAPTER 4. Synthesis, Structure, and Characterization of New Li<sup>+</sup> – d<sup>0</sup> – Lone-pair – Oxides: Noncentrosymmetric Polar Li<sub>6</sub>(Mo<sub>2</sub>O<sub>5</sub>)<sub>3</sub>(SeO<sub>3</sub>)<sub>6</sub> and Centrosymmetric Li<sub>2</sub>(MO<sub>3</sub>)(TeO<sub>3</sub>) (M = Mo<sup>6+</sup> or W<sup>6+</sup>)**

4.1	Abstract	82
4.2	Introduction	83
4.3	Experimental details	85
4.3.1	Synthesis	85
4.3.2	Characterization	86
4.4	Results and discussion	97
4.5	Conclusion	116
4.6	References	117

**CHAPTER 5.      Synthesis, Structure, and Characterization of Two New Polar  
Sodium Tungsten Selenites:  $\text{Na}_2(\text{WO}_3)_3(\text{SeO}_3)\cdot 2\text{H}_2\text{O}$  and  
 $\text{Na}_6(\text{W}_6\text{O}_{19})(\text{SeO}_3)_2$**

5.1	Abstract	125
5.2	Introduction	126
5.3	Experimental details	128
5.3.1	Synthesis	128
5.3.2	Characterization	130
5.4	Results and discussion	140
5.5	Conclusion	162
5.6	References	163

**CHAPTER 6.      Conclusions and Future Work**

6.1	General conclusions	174
6.2	$\text{Zn}_2(\text{MoO}_4)(\text{AO}_3)$ ( $\text{A} = \text{Se}^{4+}$ or $\text{Te}^{4+}$ ) system	175
6.3	Bi-I-O system	175
6.4	Li - M - A oxide system ( $\text{M} = \text{Mo}^{6+}$ or $\text{W}^{6+}$ ; $\text{A} = \text{Se}^{4+}$ or $\text{Te}^{4+}$ )	176
6.5	Na-W-Se oxide system	176
6.6	References	178

## List of Figures

<b>Figure 1.1</b>	Distorted polyhedra of octahedrally coordinated $d^0$ and lone-pair cations.	2
<b>Figure 1.2</b>	Molecular orbital diagram for the $MO_6$ octahedron of $d^0$ cations and second-order Jahn Teller distortion band diagram for $MO_6$ octahedra in the extended structure.	3
<b>Figure 1.3</b>	Molecular orbital diagram for the $AO_3$ polyhedra of lone-pair cations in the trigonal planar geometry (top) and in the trigonal pyramid (bottom).	6
<b>Figure 1.4</b>	The Venn diagram shows functional properties of materials with respect to their crystal symmetry.	7
<b>Figure 1.5</b>	Examples of Type 1 SHG phase-matching $BiO(IO_3)$ and nonphase-matching $Na_2(WO_3)_3(SeO_3) \cdot 2H_2O$ materials. The curves are drawn to guide the eye and are not fits to the data.	9
<b>Figure 1.6</b>	The measured piezoelectric curve for $BiO(IO_3)$ .	10
<b>Figure 1.7</b>	The temperature-dependent polarization loop, and the plots of maximum polarization and pyroelectric coefficient versus temperature for $Zn_2(MoO_4)(TeO_3)$ .	11
<b>Figure 1.8</b>	A typical hysteresis loop for ferroelectric $BaTiO_3$ .	12
<b>Figure 2.1</b>	Ball-and-stick and polyhedral representations of $Zn_2(MoO_4)(SeO_3)$ in the bc-plane. The arrows indicate the approximate directions of the dipole moment on the $SeO_3$ polyhedron. Electron localization function (ELF) with $\eta = 0.9$ is shown, indicating that the lone-pair on the $Se^{4+}$ is stereoactive.	29
<b>Figure 2.2</b>	Ball-and-stick (top) and polyhedral (bottom) diagrams of $Zn_2(MoO_4)(SeO_3)$ in the ab-plane. Note that the polyhedra share edges and corners resulting in the three-dimensional crystal structure.	30
<b>Figure 2.3</b>	IR data and assignments for $Zn_2(MoO_4)(SeO_3)$ and	31

	$\text{Zn}_2(\text{MoO}_4)(\text{TeO}_3)$ .	
<b>Figure 2.4</b>	UV-vis diffuse reflectance spectroscopy data for $\text{Zn}_2(\text{MoO}_4)(\text{SeO}_3)$ and $\text{Zn}_2(\text{MoO}_4)(\text{TeO}_3)$ .	32
<b>Figure 2.5</b>	Thermogravimetric and differential thermal analysis data for $\text{Zn}_2(\text{MoO}_4)(\text{SeO}_3)$ and $\text{Zn}_2(\text{MoO}_4)(\text{TeO}_3)$ .	33
<b>Figure 2.6</b>	Particle size vs. SHG intensity data for $\text{Zn}_2(\text{MoO}_4)(\text{SeO}_3)$ and $\text{Zn}_2(\text{MoO}_4)(\text{TeO}_3)$ . The curves are drawn to guide the eye and are not fits to the data.	34
<b>Figure 2.7</b>	Displacement vs. electric field plots for $\text{Zn}_2(\text{MoO}_4)(\text{SeO}_3)$ and $\text{Zn}_2(\text{MoO}_4)(\text{TeO}_3)$ .	35
<b>Figure 2.8</b>	Frequency-dependent hysteresis loops (top) and pyroelectric coefficient vs. temperature plot (bottom) for $\text{Zn}_2(\text{MoO}_4)(\text{SeO}_3)$ and $\text{Zn}_2(\text{MoO}_4)(\text{TeO}_3)$ . The curves do not indicate ferroelectric hysteresis, that is, polarization reversal, rather dielectric loss.	37
<b>Figure 2.9</b>	Total and projected density of states plots for (a) $\text{Zn}_2(\text{MoO}_4)(\text{SeO}_3)$ and (b) $\text{Zn}_2(\text{MoO}_4)(\text{TeO}_3)$ . The dotted vertical line at 0 eV indicates $E_F$ .	39
<b>Figure 2.10</b>	The detailed PDOS plots for $\text{Se}^{4+}$ and $\text{Te}^{4+}$ cations. The dotted vertical line at 0 eV indicates $E_F$ .	40
<b>Figure 2.11</b>	-COHP plots for A-O, A-ns-O-2sp, A-np-O-2sp orbital interactions for $\text{Zn}_2(\text{MoO}_4)(\text{AO}_3)$ ( $A = \text{Se}^{4+}$ or $\text{Te}^{4+}$ ). The dotted vertical line at 0 eV indicates $E_F$ .	40
<b>Figure 2.12</b>	Density of states (top) and projected density of states (middle) plots for $\text{Zn}_2(\text{MoO}_4)(\text{SO}_3)$ and a crystal orbital Hamilton population (bottom) plot for S-O bonds.	41
<b>Figure 3.1</b>	Ball-and-stick representation of $\text{BiO}(\text{IO}_3)$ (a) and polyhedral representation of the Aurivillius phase ( $m = 2$ ) (b). Note the similar $(\text{Bi}_2\text{O}_2)^{2+}$ cationic layer in each material.	63
<b>Figure 3.2</b>	Ball-and-stick representation of $\text{BiO}(\text{IO}_3)$ in the bc-plane. The partially parallel and anti-parallel alignments of the polarization	64

attributable to the  $\text{IO}_3$  and  $\text{BiO}_6$  polyhedra respectively are shown. A net macroscopic polarization directed toward the c-axis is represented by the large black arrow. Note that the violet lobe-like isosurfaces ( $\eta = 0.9$ ) obtained from electron localization function calculation using Quantum Espresso were used to visualize stereoactive lone-pairs on the  $\text{Bi}^{3+}$  and  $\text{I}^{5+}$  cations

<b>Figure 3.3</b>	IR data and assignments for $\text{BiO}(\text{IO}_3)$ .	65
<b>Figure 3.4</b>	UV-vis diffuse reflectance spectroscopy data for $\text{BiO}(\text{IO}_3)$ .	66
<b>Figure 3.5</b>	Thermogravimetric and differential thermal analysis data for $\text{BiO}(\text{IO}_3)$ .	66
<b>Figure 3.6</b>	Particle size vs. SHG intensity data for $\text{BiO}(\text{IO}_3)$ . The curve is drawn to guide the eye and is not a fit to the data.	67
<b>Figure 3.7</b>	Displacement vs. electric field plots for $\text{BiO}(\text{IO}_3)$ .	68
<b>Figure 3.8</b>	Frequency-dependent polarization loops (top), polarization vs. electric field loops (middle), and maximum polarization and pyroelectric coefficient versus temperature plot for $\text{BiO}(\text{IO}_3)$	70
<b>Figure 3.9</b>	Total and projected density of states plots for $\text{BiO}(\text{IO}_3)$ . The dotted vertical line at 0 eV indicates $E_F$ .	72
<b>Figure 3.10</b>	The detailed PDOS plots for $\text{BiO}(\text{IO}_3)$ . The dotted vertical line at 0 eV indicates $E_F$ .	72
<b>Figure 3.11</b>	-COHP plots for I-O, Bi-O orbital interactions for $\text{BiO}(\text{IO}_3)$ . The dotted vertical line at 0 eV indicates $E_F$ .	73
<b>Figure 4.1</b>	The polyhedra representation of $\text{Li}_6(\text{Mo}_2\text{O}_5)_3(\text{SeO}_3)_6$ in the bc-plane. Spheres in the diagram are $\text{Li}^+$ cations (yellow), $\text{Mo}^{6+}$ cations (blue), $\text{Se}^{4+}$ cations (green), and $\text{O}^{2-}$ anions (red).	98
<b>Figure 4.2</b>	Ball-and-stick representations of $[\text{6}(\text{MoO}_{2/1}\text{O}_{3/2}\text{O}_{1/3})^{-5/3}\text{3}(\text{SeO}_{2/2}\text{O}_{1/3})^{+4/3}\text{3}(\text{SeO}_{1/1}\text{O}_{2/2})^0]^{6-}$ zig-zag layers in the ab-plane (top) and connectivity between $\text{Mo}_2\text{O}_{10}$ dimers and $\text{SeO}_3$ polyhedra in the layer section (bottom). Spheres in the diagram are $\text{Mo}^{6+}$ cations (blue), $\text{Se}^{4+}$ cations (green), and $\text{O}^{2-}$ anions (red).	99



	The Li <sup>+</sup> cations have been removed for clarity.	
<b>Figure 4.3</b>	The polyhedra representation of Li <sub>2</sub> (MoO <sub>3</sub> )(TeO <sub>3</sub> ) in the bc- plane. Spheres in the diagram are Li <sup>+</sup> cations (yellow), Mo <sup>6+</sup> cations (blue), Te <sup>4+</sup> cations (green), and O <sup>2-</sup> anions (red).	100
<b>Figure 4.4</b>	Ball-and-stick representations of [(MoO <sub>3</sub> O <sub>3/2</sub> ) <sup>-3</sup> (TeO <sub>3/2</sub> ) <sup>+1</sup> ] <sup>2-</sup> zig-zag layers in the ab-plane (top) and connectivity between MoO <sub>6</sub> and TeO <sub>3</sub> polyhedra in the layer (bottom). Spheres in the diagram are Mo <sup>6+</sup> cations (blue), Te <sup>4+</sup> cations (green), and O <sup>2-</sup> anions (red). The Li <sup>+</sup> cations have been removed for clarity.	101
<b>Figure 4.5</b>	Ball-and-stick representations of (a) Li <sub>6</sub> (Mo <sub>2</sub> O <sub>5</sub> ) <sub>3</sub> (SeO <sub>3</sub> ) <sub>6</sub> in bc-plane and (b) Li <sub>2</sub> (MO <sub>3</sub> )(TeO <sub>3</sub> ) (M = Mo <sup>6+</sup> or W <sup>6+</sup> ) in ab-plane. The arrows indicate the approximate directions of the dipole moments of the MoO <sub>6</sub> (blue) and AO <sub>3</sub> (A = Se <sup>4+</sup> or Te <sup>4+</sup> ) (green) polyhedra in the unit cell. Electron localization function (ELF) plots with η = 0.9 is also shown. The lobe-like isosurfaces near top of AO <sub>3</sub> polyhedra are consistent with a stereoactive lone-pair on the A cations. The Li <sup>+</sup> cations have been removed for clarity.	106
<b>Figure 4.6</b>	IR data and assignments for Li <sub>6</sub> (Mo <sub>2</sub> O <sub>5</sub> ) <sub>3</sub> (SeO <sub>3</sub> ) <sub>6</sub> and Li <sub>2</sub> (MO <sub>3</sub> )(TeO <sub>3</sub> ) (M = Mo <sup>6+</sup> or W <sup>6+</sup> ).	107
<b>Figure 4.7</b>	UV-vis diffuse reflectance spectroscopy data for Li <sub>6</sub> (Mo <sub>2</sub> O <sub>5</sub> ) <sub>3</sub> (SeO <sub>3</sub> ) <sub>6</sub> and Li <sub>2</sub> (MO <sub>3</sub> )(TeO <sub>3</sub> ) (M = Mo <sup>6+</sup> or W <sup>6+</sup> ).	109
<b>Figure 4.8</b>	Thermogravimetric and differential thermal analysis data for Li <sub>6</sub> (Mo <sub>2</sub> O <sub>5</sub> ) <sub>3</sub> (SeO <sub>3</sub> ) <sub>6</sub> and Li <sub>2</sub> (MO <sub>3</sub> )(TeO <sub>3</sub> ) (M = Mo <sup>6+</sup> or W <sup>6+</sup> ).	111
<b>Figure 4.9</b>	Particle-size vs. SHG intensity data for Li <sub>6</sub> (Mo <sub>2</sub> O <sub>5</sub> ) <sub>3</sub> (SeO <sub>3</sub> ) <sub>6</sub> . The curve is drawn to guide the eye and is not a fit to the data.	112
<b>Figure 4.10</b>	The displacement vs. electric field plot for Li <sub>6</sub> (Mo <sub>2</sub> O <sub>5</sub> ) <sub>3</sub> (SeO <sub>3</sub> ) <sub>6</sub> .	113
<b>Figure 4.11</b>	Field-dependent (left) and frequency-dependent (right) polarization-electric field loops and a pyroelectric coefficient vs. temperature plot (bottom) for Li <sub>6</sub> (Mo <sub>2</sub> O <sub>5</sub> ) <sub>3</sub> (SeO <sub>3</sub> ) <sub>6</sub> .	115
<b>Figure 5.1</b>	Thermogravimetric and differential thermal analysis (TG and	129

- DTA) data and X-ray powder diffraction (XRD) for  $\text{Na}_6(\text{W}_6\text{O}_{19})(\text{SeO}_3)_2$  synthesis.
- Figure 5.2** Ball-and-stick (top) and polyhedra (bottom) representations of  $\text{Na}_2(\text{WO}_3)_3(\text{SeO}_3) \cdot 2\text{H}_2\text{O}$  in the (110) plane. Spheres in the diagram are  $\text{Na}^+$  cations (yellow),  $\text{W}^{6+}$  cations (blue),  $\text{Se}^{4+}$  cations (green), and  $\text{O}^{2-}$  anions (red). Isolated red spheres are  $\text{H}_2\text{O}$  molecules. 142
- Figure 5.3** Ball-and-stick (top) and polyhedra (bottom) representations of  $\text{Na}_2(\text{WO}_3)_3(\text{SeO}_3) \cdot 2\text{H}_2\text{O}$  in the ab-plane. Spheres in the diagram are  $\text{Na}^+$  cations (yellow),  $\text{W}^{6+}$  cations (blue),  $\text{Se}^{4+}$  cations (green), and  $\text{O}^{2-}$  anions (red). Isolated red spheres are  $\text{H}_2\text{O}$  molecules. 143
- Figure 5.4** Ball-and-stick (left) and polyhedra (right) representations of  $\text{Na}_6(\text{W}_6\text{O}_{19})(\text{SeO}_3)_2$  in the ac-plane. Spheres in the diagram are  $\text{Na}^+$  cations (yellow),  $\text{W}^{6+}$  cations (blue),  $\text{Se}^{4+}$  cations (green), and  $\text{O}^{2-}$  anions (red). 145
- Figure 5.5** Ball-and-stick (left) and polyhedra (right) representations of  $\text{Na}_6(\text{W}_6\text{O}_{19})(\text{SeO}_3)_2$  in the ab-plane. Spheres in the diagram are  $\text{Na}^+$  cations (yellow),  $\text{W}^{6+}$  cations (blue),  $\text{Se}^{4+}$  cations (green), and  $\text{O}^{2-}$  anions (red). 146
- Figure 5.6** Plots of hexagonal tungsten oxide (HTO) layer distances and cell parameter of the polar HTO layered materials versus alkali cation radius. 148
- Figure 5.7** Ball-and-stick representations of (a)  $\text{Na}_2(\text{WO}_3)_3(\text{SeO}_3) \cdot 2\text{H}_2\text{O}$  in (110) plane and (b)  $\text{Na}_6(\text{W}_6\text{O}_{19})(\text{SeO}_3)_2$  in ab-plane. Electron localization function (ELF) plots with  $\eta = 0.9$  is also shown. The lobe-like isosurfaces near top of  $\text{SeO}_3$  polyhedra are consistent with stereoactive lone-pairs on the  $\text{Se}^{4+}$  cations. The  $\text{H}_2\text{O}$  molecules in  $\text{Na}_2(\text{WO}_3)_3(\text{SeO}_3) \cdot 2\text{H}_2\text{O}$  and  $\text{Na}^+$  cations have been removed for clarity. 152
- Figure 5.8** IR data and assignments for  $\text{Na}_2(\text{WO}_3)_3(\text{SeO}_3) \cdot 2\text{H}_2\text{O}$  and 154

	$\text{Na}_6(\text{W}_6\text{O}_{19})(\text{SeO}_3)_2$ .	
<b>Figure 5.9</b>	UV-vis diffuse reflectance spectroscopy data	153
	$\text{Na}_2(\text{WO}_3)_3(\text{SeO}_3) \cdot 2\text{H}_2\text{O}$ and $\text{Na}_6(\text{W}_6\text{O}_{19})(\text{SeO}_3)_2$ .	
<b>Figure 5.10</b>	Thermogravimetric and differential thermal analysis data, and powder X-ray diffraction patterns of $\text{Na}_2(\text{WO}_3)_3(\text{SeO}_3) \cdot 2\text{H}_2\text{O}$ and $\text{Na}_6(\text{W}_6\text{O}_{19})(\text{SeO}_3)_2$ residuals after thermal analyses.	157
<b>Figure 5.11</b>	Particle-size vs. SHG intensity data for $\text{Na}_2(\text{WO}_3)_3(\text{SeO}_3) \cdot 2\text{H}_2\text{O}$ and $\text{Na}_6(\text{W}_6\text{O}_{19})(\text{SeO}_3)_2$ . The curves are drawn to guide the eye and are not fits to the data.	158
<b>Figure 5.12</b>	The displacement vs. electric field plot for $\text{Na}_2(\text{WO}_3)_3(\text{SeO}_3) \cdot 2\text{H}_2\text{O}$ and $\text{Na}_6(\text{W}_6\text{O}_{19})(\text{SeO}_3)_2$ .	159
<b>Figure 5.13</b>	Frequency-dependent (left) polarization-electric field loops and a pyroelectric coefficient vs. temperature plot (right) for $\text{Na}_2(\text{WO}_3)_3(\text{SeO}_3) \cdot 2\text{H}_2\text{O}$ and $\text{Na}_6(\text{W}_6\text{O}_{19})(\text{SeO}_3)_2$ .	161

## List of Tables

<b>Table 2.1</b>	Crystallographic data for $\text{Zn}_2(\text{MoO}_4)(\text{AO}_3)$ ( $\text{A} = \text{Se}^{4+}$ or $\text{Te}^{4+}$ ).	21
<b>Table 2.2</b>	Atomic coordinates and equivalent isotropic displacement parameters ( $\text{\AA}^2$ ) for $\text{Zn}_2(\text{MoO}_4)(\text{AO}_3)$ ( $\text{A} = \text{Se}^{4+}$ or $\text{Te}^{4+}$ ).	22
<b>Table 2.3</b>	Selected bond distances ( $\text{\AA}$ ) for $\text{Zn}_2(\text{MoO}_4)(\text{AO}_3)$ ( $\text{A} = \text{Se}^{4+}$ or $\text{Te}^{4+}$ ).	23
<b>Table 2.4</b>	Bond valence sum (BVS), bond strain index (BSI), global instability index (GII), and unit cell dipole moment ( $\mu$ ) for $\text{Zn}_2(\text{MoO}_4)(\text{AO}_3)$ ( $\text{A} = \text{Se}^{4+}$ or $\text{Te}^{4+}$ ).	28
<b>Table 2.5.</b>	IR peak assignments for $\text{Zn}_2(\text{MoO}_4)(\text{SeO}_3)$ and $\text{Zn}_2(\text{MoO}_4)(\text{TeO}_3)$ .	31
<b>Table 2.6</b>	SHG efficiencies ( $\times \alpha\text{-SiO}_2$ ), piezoelectric responses, ( $d_{33}$ ), pyroelectric coefficients ( $P_T$ ), and maximum polarization ( $P_m$ ) for $\text{Zn}_2(\text{MoO}_4)(\text{AO}_3)$ ( $\text{A} = \text{Se}^{4+}$ or $\text{Te}^{4+}$ ).	36
<b>Table 2.7</b>	Bond length ( $\text{\AA}$ ) of S-O bonds of hypothetical $\text{Zn}_2(\text{MoO}_4)(\text{SO}_3)$ , compared to those of Se-O bonds of $\text{Zn}_2(\text{MoO}_4)(\text{SeO}_3)$ .	42
<b>Table 2.8</b>	Bond angles for the asymmetric $\text{AO}_3$ trigonal pyramids in $\text{Zn}_2(\text{MoO}_4)(\text{AO}_3)$ ( $\text{A} = \text{S}^{4+}$ , $\text{Se}^{4+}$ , and $\text{Te}^{4+}$ ). Note that the structure of $\text{Zn}_2(\text{MoO}_4)(\text{SO}_3)$ is hypothetical.	42
<b>Table 3.1</b>	Crystallographic data for $\text{BiO}(\text{IO}_3)$ .	57
<b>Table 3.2</b>	Atomic coordinates and equivalent isotropic displacement parameters ( $\text{\AA}^2$ ) for $\text{BiO}(\text{IO}_3)$ .	57
<b>Table 3.3</b>	Selected bond distances ( $\text{\AA}$ ) for $\text{BiO}(\text{IO}_3)$ .	58
<b>Table 3.4</b>	Bond valence sum (BVS), bond strain index (BSI), global instability index (GII), unit cell dipole moment ( $\mu$ ), SHG efficiencies ( $\times \alpha\text{-SiO}_2$ ), piezoelectric responses, ( $d_{33}$ ), pyroelectric coefficients ( $P_T$ ), and maximum polarization ( $P_m$ ) for $\text{BiO}(\text{IO}_3)$ .	63
<b>Table 3.5</b>	IR peak assignments for $\text{BiO}(\text{IO}_3)$ .	65
<b>Table 4.1</b>	Crystallographic data for $\text{Li}_6(\text{Mo}_2\text{O}_5)_3(\text{SeO}_3)_6$ , $\text{Li}_2(\text{MoO}_3)(\text{TeO}_3)$ ,	88

	and $\text{Li}_2(\text{WO}_3)(\text{TeO}_3)$ .	
<b>Table 4.2</b>	Atomic coordinates and equivalent isotropic displacement parameters ( $\text{\AA}^2$ ) for $\text{Li}_6(\text{Mo}_2\text{O}_5)_3(\text{SeO}_3)_6$ .	89
<b>Table 4.3</b>	Atomic coordinates and equivalent isotropic displacement parameters ( $\text{\AA}^2$ ) for $\text{Li}_2(\text{MoO}_3)(\text{TeO}_3)$ and $\text{Li}_2(\text{WO}_3)(\text{TeO}_3)$	92
<b>Table 4.4</b>	Selected bond distances ( $\text{\AA}$ ) for $\text{Li}_6(\text{Mo}_2\text{O}_5)_3(\text{SeO}_3)_6$	93
<b>Table 4.5</b>	Selected bond distances ( $\text{\AA}$ ) for $\text{Li}_2(\text{MoO}_3)(\text{TeO}_3)$ and $\text{Li}_2(\text{WO}_3)(\text{TeO}_3)$ .	94
<b>Table 4.6</b>	Bond valence sum (BVS), bond strain index (BSI), global instability index (GII), and unit cell dipole moment ( $\mu$ ) of $\text{Li}_6(\text{Mo}_2\text{O}_5)_3(\text{SeO}_3)_6$ and $\text{Li}_2(\text{MO}_3)(\text{TeO}_3)$ ( $\text{M} = \text{Mo}^{6+}$ or $\text{W}^{6+}$ ).	104
<b>Table 4.7</b>	Distortion magnitudes of $\text{MO}_6$ octahedra and dipole moments of $\text{MO}_6$ ( $\text{M} = \text{Mo}^{6+}$ or $\text{W}^{6+}$ ) and $\text{AO}_3$ ( $\text{A} = \text{Se}^{4+}$ or $\text{Te}^{4+}$ ) polyhedra in $\text{Li}_6(\text{Mo}_2\text{O}_5)_3(\text{SeO}_3)_6$ and $\text{Li}_2(\text{MO}_3)(\text{TeO}_3)$ .	105
<b>Table 4.8</b>	IR peak assignments for $\text{Li}_6(\text{Mo}_2\text{O}_5)_3(\text{SeO}_3)_6$ and $\text{Li}_2(\text{MO}_3)(\text{TeO}_3)$ ( $\text{M} = \text{Mo}^{6+}$ or $\text{W}^{6+}$ ).	108
<b>Table 4.9</b>	SHG efficiency ( $\times \alpha\text{-SiO}_2$ ), piezoelectric response, $d_{33}$ (pm/V), pyroelectric coefficient, $P_T$ ( $\mu\text{C}/\text{m}^2\text{K}$ ), and maximum polarization, $P_m$ ( $\mu\text{C}/\text{m}^2$ ) for $\text{Li}_6(\text{Mo}_2\text{O}_5)_3(\text{SeO}_3)_6$ .	116
<b>Table 5.1</b>	Crystallographic data for $\text{Na}_2(\text{WO}_3)_3(\text{SeO}_3)\cdot 2\text{H}_2\text{O}$ and $\text{Na}_6(\text{W}_6\text{O}_{19})(\text{SeO}_3)_2$ .	132
<b>Table 5.2</b>	Atomic coordinates and equivalent isotropic displacement parameters ( $\text{\AA}^2$ ) for $\text{Na}_2(\text{WO}_3)_3(\text{SeO}_3)\cdot 2\text{H}_2\text{O}$	133
<b>Table 5.3</b>	Atomic coordinates and equivalent isotropic displacement parameters ( $\text{\AA}^2$ ) for $\text{Na}_6(\text{W}_6\text{O}_{19})(\text{SeO}_3)_2$	134
<b>Table 5.4</b>	Selected bond distances ( $\text{\AA}$ ) for $\text{Na}_2(\text{WO}_3)_3(\text{SeO}_3)\cdot 2\text{H}_2\text{O}$ and $\text{Na}_6(\text{W}_6\text{O}_{19})(\text{SeO}_3)_2$ .	136
<b>Table 5.5</b>	Bond valence sums, BSI and GII index values for $\text{Na}_2(\text{WO}_3)_3(\text{SeO}_3)\cdot 2\text{H}_2\text{O}$ and $\text{Na}_6(\text{W}_6\text{O}_{19})(\text{SeO}_3)_2$ .	146
<b>Table 5.6</b>	Alkali cation radius, hexagonal tungsten oxide (HTO) layer	147

distances, and space groups of the polar HTO layered materials.

<b>Table 5.7</b>	Distortion magnitudes of $\text{WO}_6$ octahedra and dipole moments of $\text{WO}_6$ and $\text{SeO}_3$ polyhedra in $\text{Na}_2(\text{WO}_3)_3(\text{SeO}_3) \cdot 2\text{H}_2\text{O}$ and $\text{Na}_6(\text{W}_6\text{O}_{19})(\text{SeO}_3)_2$ .	150
<b>Table 5.8</b>	IR peak assignments for $\text{Na}_2(\text{WO}_3)_3(\text{SeO}_3) \cdot 2\text{H}_2\text{O}$ and $\text{Na}_6(\text{W}_6\text{O}_{19})(\text{SeO}_3)_2$ .	154
<b>Table 5.9</b>	SHG efficiency ( $\times \alpha\text{-SiO}_2$ ), piezoelectric responses, $d_{33}$ (pm/V), pyroelectric coefficients at 60 °C, $P_T$ ( $\mu\text{C}/\text{m}^2\text{K}$ ), and maximum polarization, $P_m$ ( $\mu\text{C}/\text{m}^2$ ) for $\text{Na}_2(\text{WO}_3)_3(\text{SeO}_3) \cdot 2\text{H}_2\text{O}$ and $\text{Na}_6(\text{W}_6\text{O}_{19})(\text{SeO}_3)_2$ .	160

## **List of Abbreviations**

BSI	Bond Strain Index
BVS	Bond Valence Sum
COHP	Crystal Orbital Hamilton Population
CS	Centrosymmetric
DFT	Density Functional Theory
DTA	Differential Thermal Analysis
ELF	Electron Localization Function
GGA	Generalized Gradient Approximation
GII	Global Instability Index
HOMO	Highest Occupied Molecular Orbital
HTO	Hexagonal Tungsten Oxide
IR	Infrared
LUMO	Lowest Unoccupied Molecular Orbital
MP	Monkhorst-Pack
MT	Martins-Troullier
NAO	Numerical Atomic Orbital
NCS	Noncentrosymmetric
NLO	Nonlinear Optical
PDOS	Projected Density Of States
PP	Pseudopotential
PTFE	Polytetrafluoroethylene
PW	Plane Wave
PXRD	Powder X-Ray Diffraction
SHG	Second Harmonic Generation
SOJT	Second-Order Jahn Teller
TDOS	Total Density Of States
TGA	Thermogravimetric Analysis
UV-vis	Ultraviolet-Visible

The following chapters are modified versions of papers published or submitted:

**CHAPTER 2.** Nguyen, S. D.; Kim, S.-H.; Halasyamani, P. S. “Synthesis, Characterization and Structure–Property Relationships in Two New Polar Oxides:  $\text{Zn}_2(\text{MoO}_4)(\text{SeO}_3)$  and  $\text{Zn}_2(\text{MoO}_4)(\text{TeO}_3)$ ”, *Inorg. Chem.* **2011**, *50*, 5215.

**CHAPTER 3.** Nguyen, S. D.; Yeon, J.; Kim, S.-H.; Halasyamani, P. S. “ $\text{BiO}(\text{IO}_3)$ : A New Polar Iodate that Exhibits an Aurivillius-type  $(\text{Bi}_2\text{O}_2)^{2+}$  Layer and a Large SHG Response”, *J. Am. Chem. Soc.* **2011**, *133*, 12422.

**CHAPTER 4.** Nguyen, S. D.; Halasyamani, P. S. “Synthesis, Structure and Characterization of New  $\text{Li}^+ - d^0 - \text{Lone-pair} - \text{Oxides}$ : Noncentrosymmetric Polar  $\text{Li}_6(\text{Mo}_2\text{O}_5)_3(\text{SeO}_3)_6$  and Centrosymmetric  $\text{Li}_2(\text{MO}_3)(\text{TeO}_3)$  ( $\text{M} = \text{Mo}^{6+}$  or  $\text{W}^{6+}$ )”, *Inorg. Chem.* **2012**, *51*, 9529.

**CHAPTER 5.** Nguyen, S. D.; Halasyamani, P. S. “Synthesis, Structure, and Characterization of Two New Polar Sodium Tungsten Selenites:  $\text{Na}_2(\text{WO}_3)_3(\text{SeO}_3) \cdot 2\text{H}_2\text{O}$  and  $\text{Na}_6(\text{W}_6\text{O}_{19})(\text{SeO}_3)_2$ ”, *Inorg. Chem.* Submitted.



## **CHAPTER 1. Polyhedral Distortion of Octahedrally Coordinated $d^0$ Cations and Lone-Pair Cations and Functional Properties of Noncentrosymmetric and Polar Materials**

### **1.1 Second-order Jahn Teller electronic distortions on octahedrally coordinated $d^0$ cations and lone-pair cations**

Octahedrally coordinated  $d^0$  cations ( $M = \text{Ti}^{4+}, \text{Zr}^{4+}, \text{Hf}^{4+}, \text{V}^{5+}, \text{Nb}^{5+}, \text{Ta}^{5+}, \text{Mo}^{6+}$ , and  $\text{W}^{6+}$ ) and lone-pair cations ( $A = \text{Sn}^{2+}, \text{Sb}^{3+}, \text{S}^{4+}, \text{Se}^{4+}, \text{Te}^{4+}$ , and  $\text{I}^{5+}$ ) are main ingredients in preparing noncentrosymmetric or polar oxide materials. The asymmetric oxide coordination environments of those cations are basic structural building units in noncentrosymmetric crystal structures and primary responding units for piezoelectric, pyroelectric, ferroelectric, dielectric, and nonlinear optical phenomena (see Figure 1.1). In the following sections, we will describe the second-order Jahn Teller (SOJT) distortion effects on octahedrally coordinated  $d^0$  cations,  $M$ , and lone-pair cations,  $A$ .

#### **1.1.1 SOJT distortions of octahedrally coordinated $d^0$ cations**

The general orbital interaction diagram for an  $\text{MO}_6$  molecular group is provided in Figure 1.2. The highest occupied molecular orbitals (HOMO) are mainly composed of nonbonding filled O 2p orbitals and the lowest unoccupied molecular orbitals (LUMO) are mainly composed of empty d metal orbitals. In an extended structure, a mixing of nonbonding filled O 2p orbitals with empty d metal orbitals results in a host of degenerate states which can be removed by a spontaneous displacement of the cation

from the center of the octahedron. The HOMO-LUMO mixing degree tends to increase as the increasing ratio of charge/size on the cations lowers the energy of the empty d orbitals. This electronic effect is usually referred as the second-order Jahn Teller (SOJT) distortion.<sup>1-7</sup> The SOJT distortion is the primary cause for octahedral distortions of the  $d^0$  cations observed oxide materials. Under SOJT distortion,  $MO_6$  octahedra are experimentally observed in three different distorted ways: (i)  $C_4$ -type distortion with one ‘short’, four ‘normal’, and one ‘long’ M-O bond distances; (ii)  $C_2$ -type distortion with two ‘short’, two ‘normal’, and two ‘long’ M-O bond distances; (iii)  $C_3$ -type distortion with three ‘short’ and three ‘long’ M-O bond distances.<sup>8,9</sup> Usually the short M-O bond distances are associated with terminal oxide ligands.

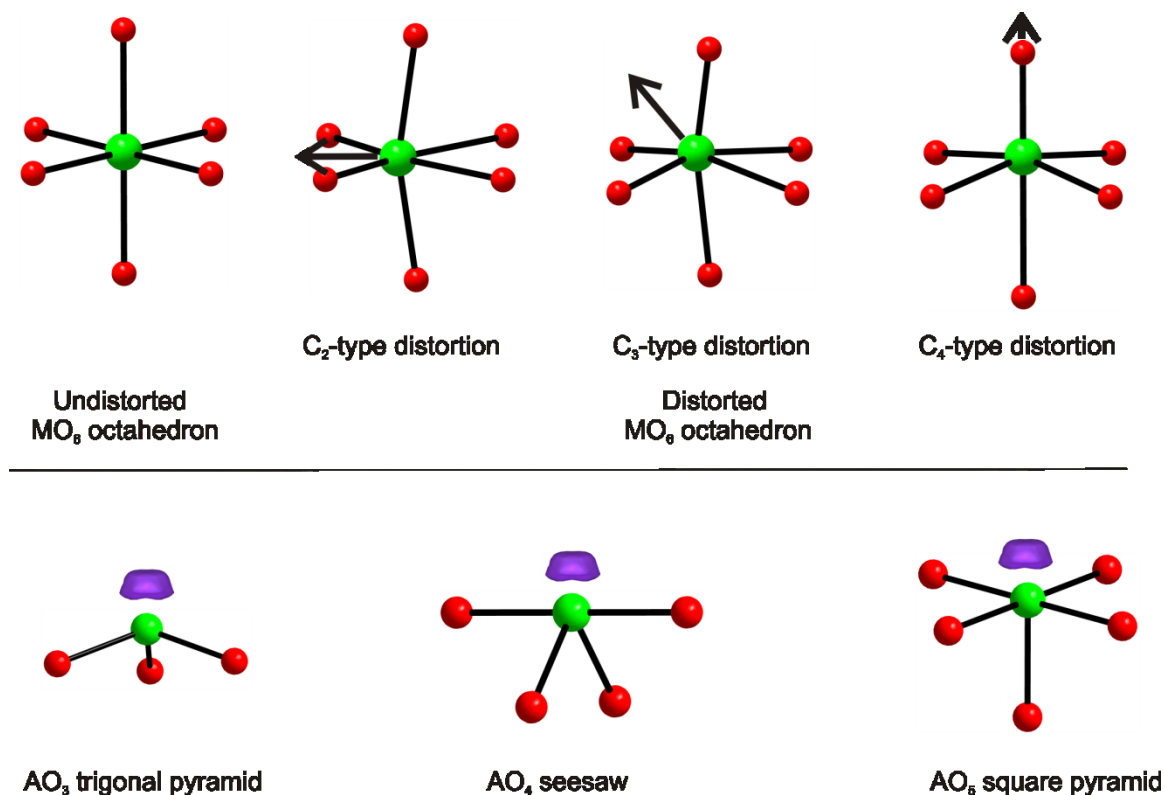


**Figure 1.1** Distorted polyhedra of octahedrally coordinated  $d^0$  and lone-pair cations.

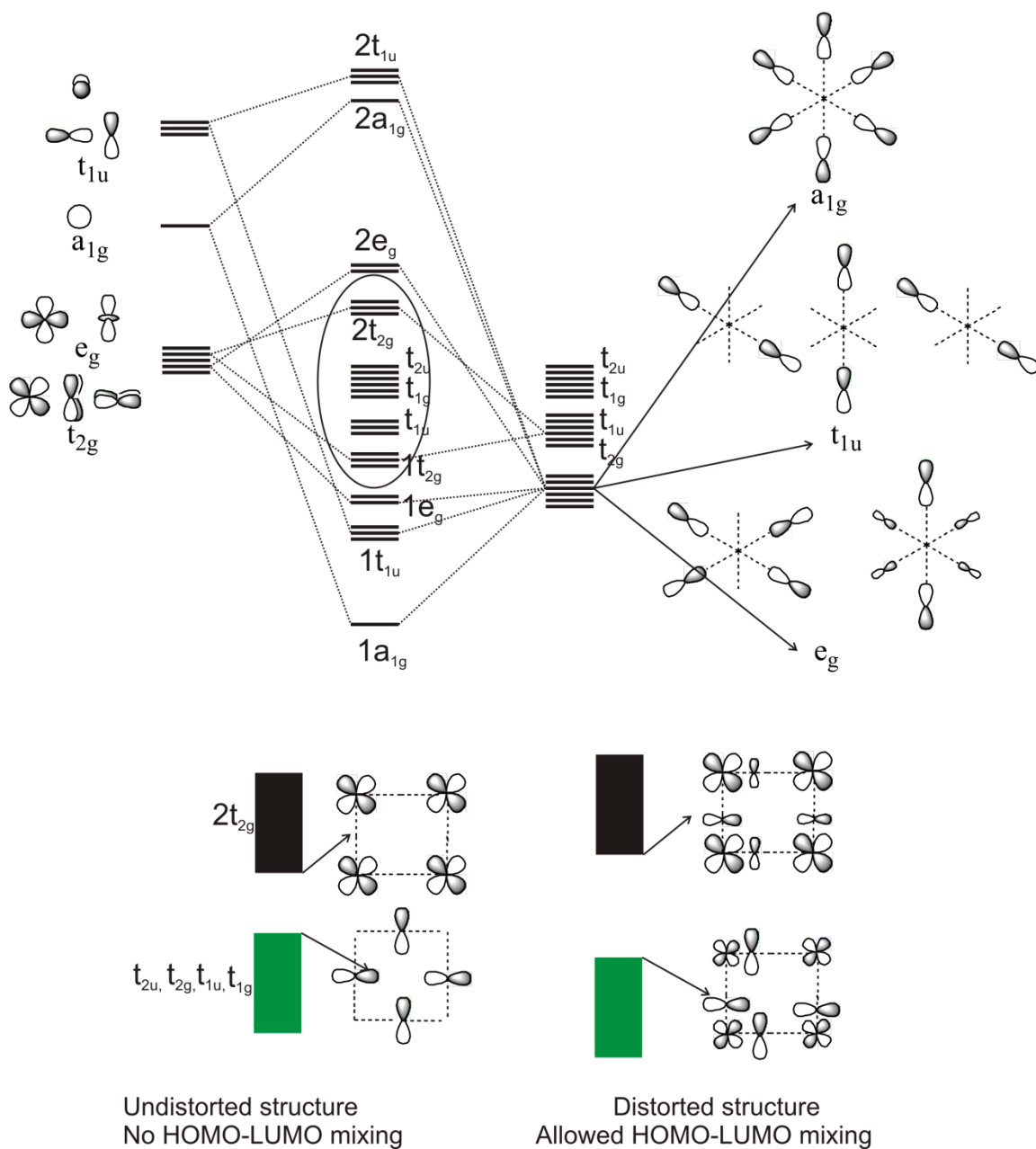


**Figure 1.2** Molecular orbital diagram for the  $MO_6$  octahedron of  $d^0$  cations and second-order Jahn Teller distortion band diagram for  $MO_6$  octahedra in the extended structure.

### 1.1.2 Polyhedral distortion of lone-pair cations

The asymmetric oxide polyhedra of lone-pair cations are attributable to their stereoactive lone-pairs.<sup>10,11</sup> The stereoactive lone-pairs are assumed to occupy a vertex of ideal polyhedra with the same occupation space as oxide ligands. The distances from stereoactive lone-pairs to the cations are calculated using the above assumption by Galy.<sup>12</sup> However, not all lone-pair cations always exhibit the stereoactive lone-pairs. Lone-pair cations like  $\text{Sn}^{2+}$ ,  $\text{Sb}^{3+}$ ,  $\text{Se}^{4+}$ , and  $\text{I}^{5+}$  always exhibit the stereoactive lone-pairs in their oxide coordinated environments. Some heavier lone-pair cations like  $\text{Tl}^+$ ,  $\text{Pb}^{2+}$ , and  $\text{Bi}^{3+}$  show the stereoactive lone-pairs under some circumstances. It has been argued that the formation of the stereoactive lone-pairs in these heavier cations is strongly associated with the covalent strength of A-O bonds.<sup>13</sup> For example, a  $\text{Tl}^+$  cation shows inactive lone-pairs when its bond valence sum to oxygen is less than 0.33 vu. However in  $\text{Tl}_3\text{BO}_4$   $\text{Tl}^+$  cations are connected to three oxide ligands of borate anions in a trigonal pyramidal geometry with Tl-O bond valence sum of 0.33 vu, exhibiting the stereoactive lone-pairs.<sup>13</sup> Orgel was the first to explain the stereoactive lone-pair formation on the cations using metal s-p orbital mixing arguments.<sup>14</sup> However, recent theoretical and experimental studies showed that this argument is not complete.<sup>15-18</sup> Based on density functional theory (DFT) calculations of the electronic structure of PbO in litharge and rock salt structures, Watson argued that the stereoactive lone-pair on lead cations cannot come from Pb 6s orbitals as their energies are well below the Fermi level (-7 eV).<sup>17,18</sup> Using X-ray spectroscopic methods, Payne<sup>19</sup> pointed out that there is a portion of O 2p orbitals in Pb 6s orbitals, indicating a mixing between O 2p orbitals and Pb 6 s orbitals,

resulting in filled Pb 6s – O 2p bonding orbitals at -7 eV and filled Pb 6s – O 2p antibonding HOMO orbitals right below the Fermi level. A further mixing between the empty antibonding Pb 6p LUMO orbitals and filled Pb 6s – O 2p antibonding HOMO orbitals stabilizes the HOMO orbitals, resulting in stereoactive lone-pairs on the Pb<sup>2+</sup> cations. Based on these arguments, the authors said that the energy separation between metal s orbitals and O 2p orbitals is a key factor in formation of the stereoactive lone-pair on the cations and proposed the stereochemical activity of the nonbonding lone-pairs for the cations in the order: Sn<sup>2+</sup> > Pb<sup>2+</sup> > Sb<sup>3+</sup> > Bi<sup>3+</sup> > Te<sup>4+</sup> > Po<sup>4+</sup>.<sup>20</sup>

From the viewpoint of chemical bond theories, an equivalent explanation for stereoactive lone-pair formation on these cations comes from the molecular orbital (MO) interaction of AO<sub>x</sub> group (x is the coordination number). Figure 1.3 show the MO diagram for a trigonal planar AO<sub>3</sub> group and its distorted version, that is, the trigonal pyramidal AO<sub>3</sub> group. The HOMO is clearly the filled antibonding orbitals from a mixing of metal s orbitals and O 2p<sub>z</sub> orbitals while the LUMO is empty metal p<sub>z</sub> orbitals. The HOMO-LUMO mixing is not symmetry allowed in trigonal planar AO<sub>3</sub> system. However, the HOMO-LUMO mixing is allowed in trigonal pyramidal AO<sub>3</sub> system, resulting in stabilization of HOMO orbitals and forming the stereoactive lone-pairs on the cations. This electronic distortion is also referred to as the second-order Jahn Teller distortion.<sup>1-7</sup> However, these approaches in explaining the stereoactive lone-pair formation are not able to give a full account for the change in bond angles of AO<sub>x</sub> group, that is why SO<sub>3</sub> groups have bond angles close to trigonal pyramidal angles (109.47°), whereas SnO<sub>3</sub> groups have the bond angles close to right angles (90°).

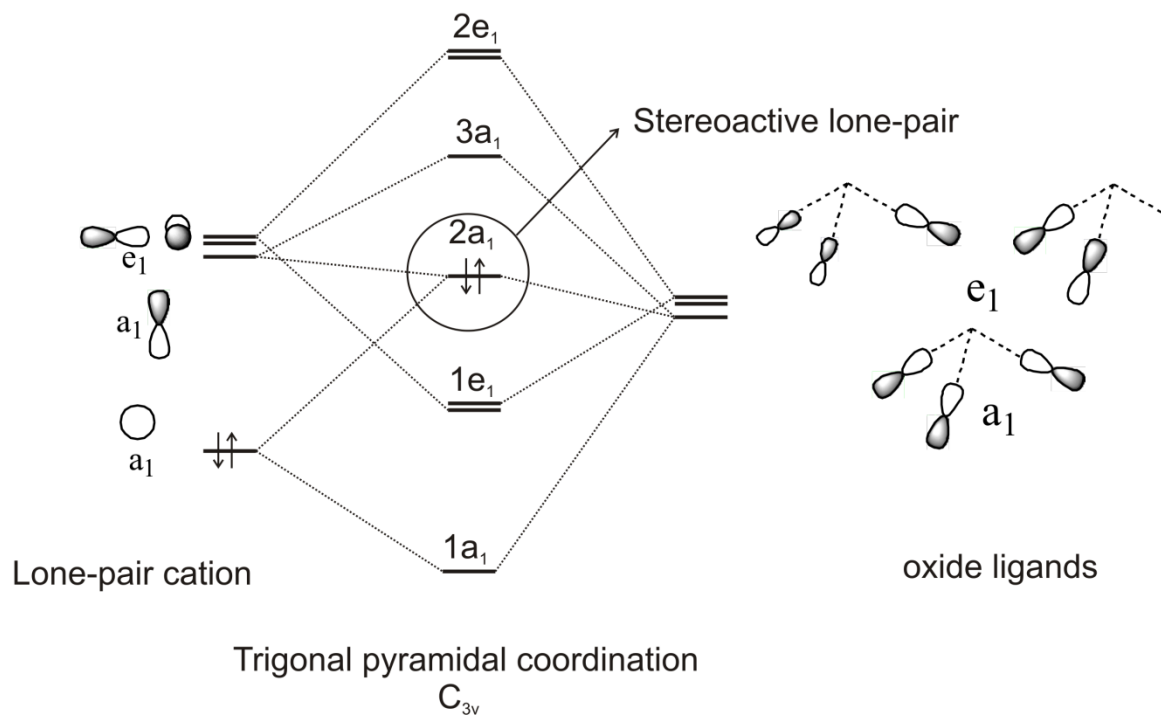
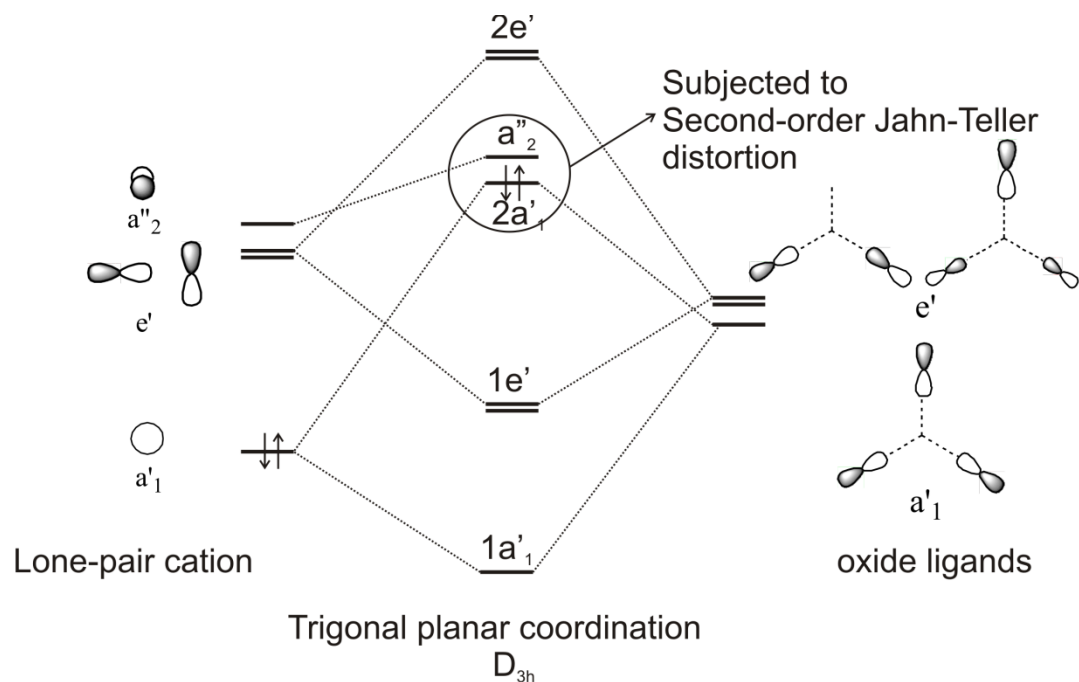


**Figure 1.3** Molecular orbital diagrams for the  $AO_3$  polyhedra of lone-pair cations in the trigonal planar geometry (top) and in the trigonal pyramid (bottom).

## 1.2 Functional properties of noncentrosymmetric polar materials

Materials crystallizing in noncentrosymmetric crystal classes have functional properties such as piezoelectric, second-harmonic generation attributable to their lack of the inversion center in the crystal structure. For noncentrosymmetric materials that crystallize in one of ten polar crystal classes (1, 2, 3, 4, 6, m, mm2, 3m, 4mm, and 6mm), the materials also possess a net polarization along the polar axis and exhibit a pyroelectricity.<sup>21</sup> If the polarization can be reversed, the materials are said to exhibit ferroelectricity. The Venn diagram below describes the functional properties with respect to the symmetry of the materials (see Figure 1.4).<sup>22</sup>

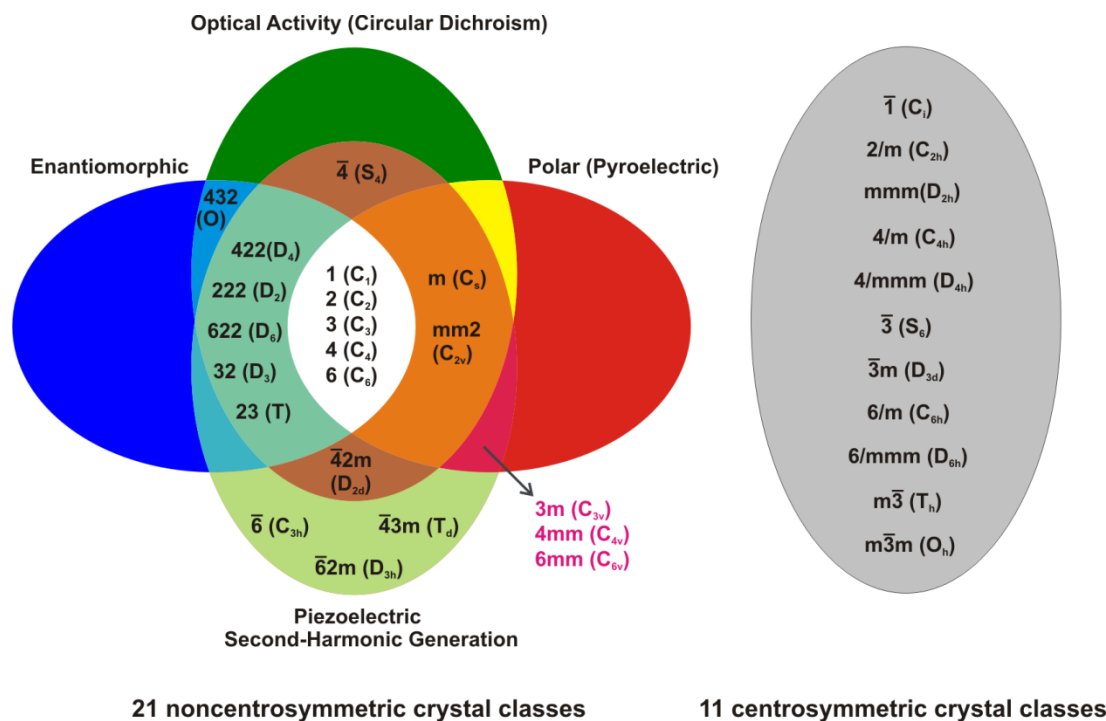


**Figure 1.4** The Venn diagram shows functional properties of materials with respect to their crystal symmetry.

### 1.2.1 Second-harmonic generation

Second-harmonic generation (SHG) was first demonstrated by Peter Franken, A. E. Hill, C. W. Peters, and G. Weinreich by focusing a laser radiation with a wavelength of 694 nm into a quartz sample.<sup>23</sup> Output radiation was produced with a wavelength of 347 nm. SHG is a nonlinear optical process that converts an input radiation with a wavelength,  $\lambda_1$ , to an output radiation with a wavelength,  $\lambda_2 = \lambda_1/2$ . SHG effects are related to the second term of the Taylor series expansion of electric polarization  $P_k$  ( $k = x, y, z$ ) which is only non-zero for a noncentrosymmetric structure.

$$P_k = \chi_{ik}^{(1)} E_i + \chi_{ijk}^{(2)} E_i E_j + \chi_{ijkl}^{(3)} E_i E_j E_l + \dots \quad (1.1)$$

SHG effects were first studied on single crystals. A powder technique to evaluate the SHG behavior of materials was proposed by Kurtz in 1968.<sup>24</sup> Phase-matching occurs when the phase velocities of the input radiation and output radiation are equal. With the powder SHG technique, when phase-matching occurs the SHG efficiency will increase with the particle size and reach to plateau regardless the particle size. The phase-matching is not observed (nonphase-matching) when the SHG efficiency reaches a maximum and then decreases as particle size increases. The particles are sieved into different sizes in the range 20-150 micron for powder SHG measurements. SHG efficiency of new NCS materials is compared either to  $\alpha$ -SiO<sub>2</sub> for the nonphase-matching SHG or to LiNbO<sub>3</sub> for the phase-matching SHG.



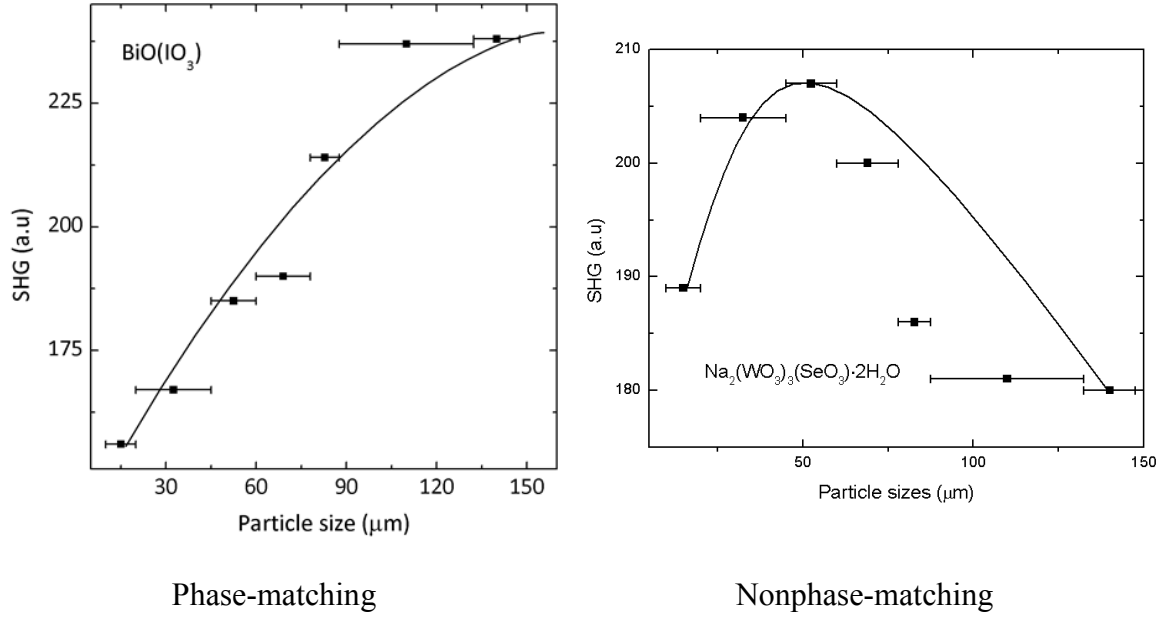


**Figure 1.5** Examples of Type 1 SHG phase-matching  $\text{BiO}(\text{IO}_3)$  and nonphase-matching  $\text{Na}_2(\text{WO}_3)_3(\text{SeO}_3) \cdot 2\text{H}_2\text{O}$  materials. The curves are drawn to guide the eye and are not fits to the data.

The values of  $\langle d_{\text{eff}} \rangle$  for the phase-matching and nonphase-matching SHG materials are calculated using one of two following equations:

$$\langle d_{\text{eff}} \rangle_{PM} = \left\{ \frac{I^{2\omega}(A)}{I^{2\omega}(\text{LiNbO}_3)} * 7.98 \times 10^2 \right\}^{1/2} \quad (1.2)$$

$$\langle d_{\text{eff}} \rangle_{NPM} = \left\{ \frac{I^{2\omega}(A)}{I^{2\omega}(\text{SiO}_2)} * 0.3048 \right\}^{1/2} \quad (1.3)$$

### 1.2.2 Piezoelectricity

The piezoelectric effect is the linear electromechanical coupling between the mechanical and the electrical states in materials with no inversion symmetry. The first direct piezoelectricity was discovered in 1880 by French physicist Pierre Currie.<sup>25</sup> The converse piezoelectricity was mathematically described by Lippmann in 1881 and later

confirmed by the Curies.<sup>26</sup> When an external mechanical stress is applied, an internal electrical field is generated in the crystal. On the other hand, when an external electrical field is applied, a mechanical strain results. With both effects, the piezoelectric coefficients,  $d_{33}$ , are calculated and used to represent the linear electromechanical coupling of the materials.

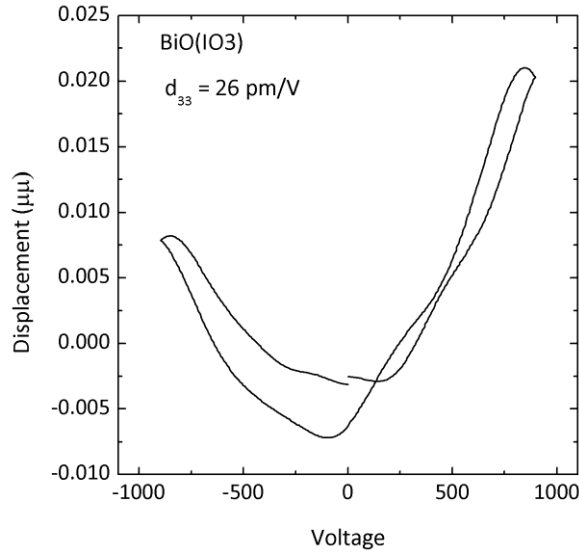


**Figure 1.6** The measured piezoelectric curve for  $\text{BiO}(\text{IO}_3)$ .

### 1.2.3 Polarization measurements: pyroelectricity and ferroelectricity

Polar materials exhibit a spontaneous polarization which is temperature-dependent. The change in the polarization of the polar materials as the temperature varies generates a voltage across the crystal. That effect is called pyroelectricity. If the polarization can be “switched” under the application of an external electrical field, the material is said to be ferroelectric. The pyroelectric coefficient,  $p$ , is used to measure the change in the spontaneous polarization vector with temperature<sup>27</sup>

$$p = \frac{dP_r}{dT} \quad (1.4)$$

Here  $P_r$  is the remnant polarization. The pyroelectric effect is accompanied by thermal stress, that is, the expansion or contraction because of the change in crystal temperature, resulting in an internal mechanical strain in the crystal. During the pyroelectric effect the piezoelectric effect will occur and contribute to the net polarization. To exclude the piezoelectric effect, it is necessary to keep the crystal under constant strain during the pyroelectric measurement, which is technically very difficult. For polar materials reported in this dissertation, the pyroelectric measurement is carried out under the unclamped condition, i.e., including the polarization contributed from the accompanying piezoelectric effect.

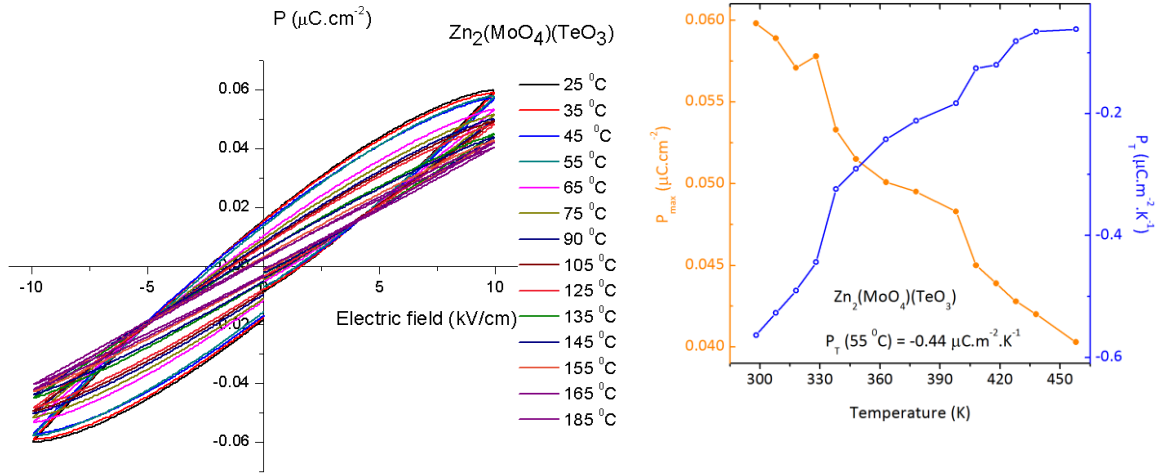


**Figure 1.7** The temperature-dependent polarization loop and plots of the maximum polarization and pyroelectric coefficient versus temperature for  $\text{Zn}_2(\text{MoO}_4)(\text{TeO}_3)$ .

Ferroelectricity is typically represented by a P-E hysteresis loop describing the reversibility of the polarization with the direction of the applied electric field. The typical hysteresis loop is showed in the Figure 1.8. The loop is characterized by the maximum

polarization,  $P_s$ , the remnant polarization,  $P_r$ , and the coercive field,  $E_c$ . Each ferroelectric material possesses a Curie temperature at which the phase transition occurs between centrosymmetric and noncentrosymmetric structures.

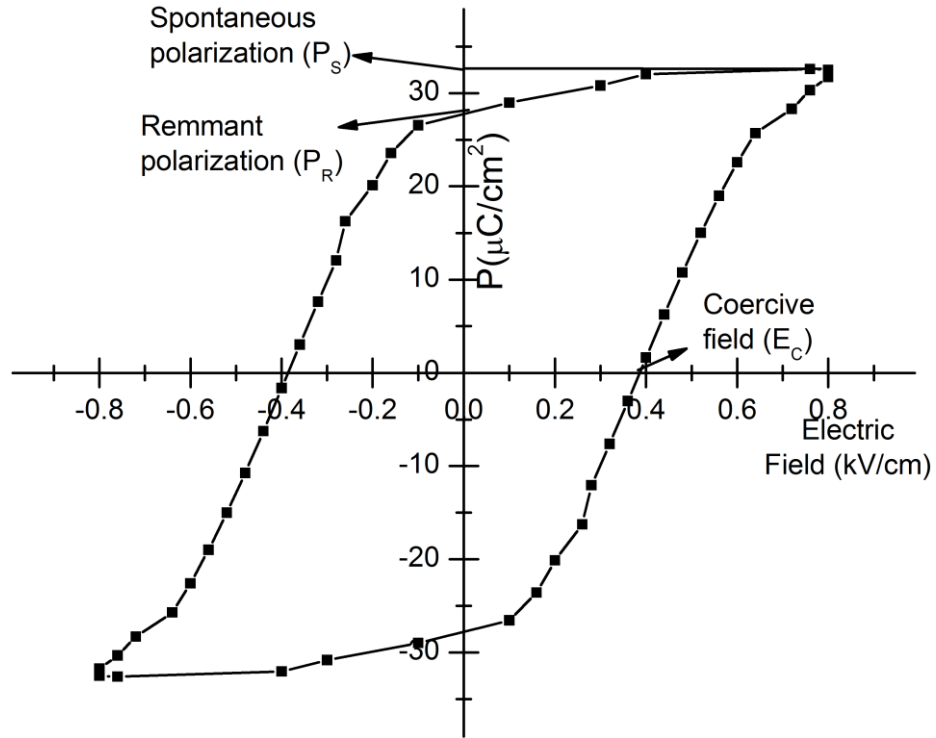


**Figure 1.8** A typical hysteresis loop of ferroelectric BaTiO<sub>3</sub>.

### 1.3 References

1. Bader, R. F. W. *Mol. Phys.* **1960**, 3, 137.
2. Bader, R. F. W. *Can. J. Chem.* **1962**, 40, 1164.
3. Goodenough, J. B. *Annu. Rev. Mater. Sci.* **1998**, 28, 1.
4. Opik, U.; Pryce, M. H. L. *Proc. R. Soc. London, Ser. A* **1957**, 238, 425.
5. Pearson, R. G. *J. Am. Chem. Soc.* **1969**, 91, 4947.
6. Pearson, R. G. *J. Mol. Struct.:THEOCHEM* **1983**, 103, 25.
7. Wheeler, R. A.; Whangbo, M. H.; Hughbanks, T.; Hoffmann, R.; Burdett, J. K.; Albright, T. A. *J. Am. Chem. Soc.* **1986**, 108, 2222.
8. Halasyamani, P. S. *Chem. Mater.* **2004**, 16, 3586.
9. Ok, K. M.; Halasyamani, P. S.; Casanova, D.; Llunell, M.; Alemany, P.; Alvarez, S. *Chem. Mater.* **2006**, 18, 3176.
10. Sidgwick, N. V.; Powell, H. M. *Proc. R. Soc. London, Ser. A* **1940**, 176.
11. Gillespie, R. J.; Nyholm, R. S. *Q. Rev., Chem. Soc.* **1957**, 11, 339.
12. Galy, J.; Meunier, G.; Andersson, S.; Åström, A. *J. Solid State Chem.* **1975**, 13, 142.
13. Brown, I. D. *Chem. Rev.* **2009**, 109, 6858.
14. Orgel, L. E. *J. Chem. Soc.* **1959**, 3815.

15. Lefebvre, I.; Szymanski, M. A.; Olivier-Fourcade, J.; Jumas, J. C. *Phys. Rev. B* **1998**, *58*, 1896.
16. Seshadri, R.; Hill, N. A. *Chem. Mater.* **2001**, *13*, 2892.
17. Watson, G. W.; Parker, S. C. *J. Phys. Chem. B* **1999**, *103*, 1258.
18. Watson, G. W.; Parker, S. C.; Kresse, G. *Phys. Rev. B* **1999**, *59*, 8481.
19. Payne, D. J.; Egdel, R. G.; Walsh, A.; Watson, G. W.; Guo, J.; Glans, P. A.; Learmonth, T.; Smith, K. E. *Phys. Rev. Lett.* **2006**, *96*, 157403.
20. Walsh, A.; Payne, D. J.; Egdel, R. G.; Watson, G. W. *Chem. Soc. Rev.* **2011**, *40*, 4455.
21. *International Tables for Crystallography, Vol. A, Space Group Symmetry*; Hahn, T., Ed.; Kluwer Academic: Dordrecht, Holland, 2006; Vol. A.
22. Halasyamani, P. S.; Poeppelmeier, K. R. *Chem. Mater.* **1998**, *10*, 2753.
23. Franken, P. A.; Hill, A. E.; Peters, C. W.; Weinreich, G. *Phys. Rev. Lett.* **1961**, *7*, 118.
24. Kurtz, S. K.; Perry, T. T. *J. Appl. Phys.* **1968**, *39*, 3798.
25. Curie, P.; Curie, J. *Bulletin de la Société Minéralogique de France* **1880**, *3*.
26. Lippman, G. *Annales de Chimie et de Physique* **1881**, *24*.

27. Lang, S. B.; Das-Gupta, D. K. *Pyroelectricity: Fundamentals and Applications*; Academic Press, 2001; Vol. 4.

## CHAPTER 2. Synthesis, Characterization, and Structure–Property Relationships in Two New Polar Oxides: $\text{Zn}_2(\text{MoO}_4)(\text{SeO}_3)$ and $\text{Zn}_2(\text{MoO}_4)(\text{TeO}_3)$

### 2.1 Abstract

Two new noncentrosymmetric (NCS) polar oxide materials,  $\text{Zn}_2(\text{MoO}_4)(\text{AO}_3)$  ( $\text{A} = \text{Se}^{4+}$  or  $\text{Te}^{4+}$ ), have been synthesized by hydrothermal and solid-state techniques. Their crystal structures have been determined, and characterization of their functional properties (second-harmonic generation, piezoelectricity, and pyroelectricity) has been performed. The isostructural materials exhibit a three-dimensional network consisting of  $\text{ZnO}_4$ ,  $\text{ZnO}_6$ ,  $\text{MoO}_4$ , and  $\text{AO}_3$  polyhedra that share edges and corners. Powder second-harmonic generation (SHG) measurements using the 1064 nm radiation indicate the materials exhibit moderate SHG efficiencies of  $100 \times$  and  $80 \times \alpha\text{-SiO}_2$  for  $\text{Zn}_2(\text{MoO}_4)(\text{SeO}_3)$  and  $\text{Zn}_2(\text{MoO}_4)(\text{TeO}_3)$ , respectively. Particle size vs. SHG efficiency measurements indicate the materials are type 1 nonphase-matchable. Converse piezoelectric measurements resulted in  $d_{33}$  values of  $\sim 14$  and  $\sim 30$  pm/V for  $\text{Zn}_2(\text{MoO}_4)(\text{SeO}_3)$  and  $\text{Zn}_2(\text{MoO}_4)(\text{TeO}_3)$ , respectively, whereas pyroelectric measurements revealed coefficients of  $-0.31$  and  $-0.64 \mu\text{C}/\text{m}^2\text{K}$  at  $55^\circ\text{C}$  for  $\text{Zn}_2(\text{MoO}_4)(\text{SeO}_3)$  and  $\text{Zn}_2(\text{MoO}_4)(\text{TeO}_3)$ , respectively. Frequency-dependent polarization measurements confirmed that the materials are non-ferroelectric, that is, the macroscopic polarization is not reversible, or ‘switchable’. Infrared, UV-vis, thermogravimetric, and differential thermal analysis measurements were also performed.



First-principles density functional theory (DFT) electronic structure calculations were also done. Crystal data:  $\text{Zn}_2(\text{MoO}_4)(\text{SeO}_3)$ , monoclinic, space group  $P2_1$  (No. 4),  $a = 5.1809(4) \text{ \AA}$ ,  $b = 8.3238(7) \text{ \AA}$ ,  $c = 7.1541(6) \text{ \AA}$ ,  $\beta = 99.413(1)^\circ$ ,  $V = 305.2(1) \text{ \AA}^3$ ,  $Z = 2$ ;  $\text{Zn}_2(\text{MoO}_4)(\text{TeO}_3)$ , monoclinic, space group  $P2_1$  (No. 4),  $a = 5.178(4) \text{ \AA}$ ,  $b = 8.409(6) \text{ \AA}$ ,  $c = 7.241(5) \text{ \AA}$ ,  $\beta = 99.351(8)^\circ$ ,  $V = 311.1(4) \text{ \AA}^3$ ,  $Z = 2$ .

## 2.2 Introduction

Noncentrosymmetric (NCS) materials are of topical and technological interests attributable to their functional properties, for example second-harmonic generation (SHG), ferroelectricity, and piezoelectricity.<sup>1-4</sup> A subset of NCS materials is compounds that are polar, that is, materials that exhibit a macroscopic dipole moment. A material is considered polar if it crystallizes in one of 10 polar crystal classes (1, 2, 3, 4, 6, m, mm2, 3m, 4mm, or 6mm).<sup>5</sup> NCS materials may exhibit SHG and piezoelectricity, but *only* polar NCS compounds exhibit pyroelectric and may be additionally ferroelectric. With ferroelectricity, the observed macroscopic polarization is reversible, or switchable, in the presence of an external electric field,<sup>6</sup> whereas with pyroelectricity the polarization is not reversible, but the magnitude of the polarization varies as a function of temperature.<sup>1</sup> Thus, ferroelectricity is a subset of pyroelectricity. In other words, all ferroelectrics are pyroelectrics, but the converse is not true. With respect to new materials, a number of strategies have been published towards the design and synthesis of new polar materials.<sup>7-23</sup> Our strategy has been to synthesize new polar oxide materials that contain cations susceptible to second-order Jahn Teller distortions.<sup>24-32</sup> These cations are octahedrally coordinated  $d^0$  transition metals cations ( $\text{Ti}^{4+}$ ,  $\text{Nb}^{5+}$ ,  $\text{W}^{6+}$ , etc.) and cations that exhibit a

stereoactive lone-pair ( $\text{Se}^{4+}$ ,  $\text{Te}^{4+}$ ,  $\text{I}^{5+}$ , etc.). In both of these families of the cations, the local metal coordination is NCS *and* polar. If the individual polar polyhedra align, macroscopic polarity is observed, and the aforementioned functional properties may be observed. This design strategy has also been exploited successfully in oxyfluoride materials.<sup>12,15,33</sup> We have successfully synthesized and characterized a variety of new polar oxide materials.<sup>34-46</sup> The magnitudes of these functional phenomena are critically dependent on the individual polar polyhedra, as well as the extent of their alignment in the crystal structure.

In this chapter, we report on the synthesis, structure, and functional properties of two new polar oxide materials,  $\text{Zn}_2(\text{MoO}_4)(\text{SeO}_3)$  and  $\text{Zn}_2(\text{MoO}_4)(\text{TeO}_3)$ . The polar materials contain a cation with a stereoactive lone-pair,  $\text{Se}^{4+}$  or  $\text{Te}^{4+}$ , and a  $d^0$  transition metal cation,  $\text{Mo}^{6+}$ . A second-order Jahn Teller (SOJT) distortion is, however, only observed in the former cations, as the  $\text{Mo}^{6+}$  cations are in tetrahedral coordination environments. In addition, although both materials are polar, we demonstrate that the polarity is not reversible – the materials are not ferroelectric. Finally, structure-property relationships and theoretical calculations are discussed and presented.

## 2.3 Experimental details

### 2.3.1 Synthesis

$\text{ZnO}$  (Alfa Aesar, 99.9%),  $\text{SeO}_2$  (Alfa Aesar, 99.4%),  $\text{TeO}_2$  (GFS, 99.6%),  $\text{MoO}_3$  (Alfa Aesar, 99.9%) were used as received. Bulk polycrystalline and crystals of  $\text{Zn}_2(\text{MoO}_4)(\text{SeO}_3)$  were prepared by combining 0.163 g ( $2.00 \times 10^{-3}$  mol) of  $\text{ZnO}$ , 0.110 g ( $1.00 \times 10^{-3}$  mol) of  $\text{SeO}_2$ , and 0.144 g ( $1.00 \times 10^{-3}$  mol) of  $\text{MoO}_3$ . The mixture was

thoroughly ground and pressed into a pellet, and placed in a fused silica tube that was evacuated and flame-sealed. The sealed ampule was heated to 380 °C for 24 h, to 500 °C for 24 h, and finally to 550 °C for 48 h before being cooled to room temperature at 6 °C per hour. The product consisted of colorless rod-shaped crystals (~10% yield based on ZnO) and white powder. Powder X-ray diffraction (PXRD) data indicated that the crystals and the powder were the same phase.

Crystals of  $\text{Zn}_2(\text{MoO}_4)(\text{TeO}_3)$  were grown using hydrothermal techniques. 0.163 g ( $2.00 \times 10^{-3}$  mol) of ZnO, 0.160 g ( $1.00 \times 10^{-3}$  mol) of  $\text{TeO}_2$ , 0.144 g ( $1.00 \times 10^{-3}$  mol) of  $\text{MoO}_3$ , and 3 mL of  $\text{NH}_4\text{Cl}/\text{NH}_3$  1M buffer solution were placed in a 23 mL Teflon-lined autoclave that was subsequently closed. The autoclave was heated to 230 °C for 2 days and then cooled slowly to room temperature at a rate of 6 °C h<sup>-1</sup>. The product consisted of colorless rod-shaped crystals (~30% yield based on ZnO) and white polycrystalline powder. As with the  $\text{Zn}_2(\text{MoO}_4)(\text{SeO}_3)$  synthesis, the crystals and white powder were shown to be the same phase by PXRD. Polycrystalline  $\text{Zn}_2(\text{MoO}_4)(\text{TeO}_3)$  was prepared by combining 0.163 g ( $2.00 \times 10^{-3}$  mol) of ZnO, 0.160 g ( $1.00 \times 10^{-3}$  mol) of  $\text{TeO}_2$ , and 0.144 g ( $1.00 \times 10^{-3}$  mol) of  $\text{MoO}_3$ . This mixture was ground and pressed into a pellet. The pellet was heated to 550 °C in air for 2 days and cooled to room temperature at 3 °C per min. The product was then reground and the above process was repeated three times in order to get a single phase. The reaction and purity of the resultant sample were monitored by PXRD until its PXRD pattern was consistent with the PXRD pattern generated from its single crystal structure data.

### 2.3.2 Characterization

#### Single Crystal X-ray Diffraction

For  $\text{Zn}_2(\text{MoO}_4)(\text{SeO}_3)$ , a colorless rod-shaped crystal ( $0.04 \times 0.02 \times 0.02 \text{ mm}^3$ ), and for  $\text{Zn}_2(\text{MoO}_4)(\text{TeO}_3)$ , a colorless rod-shaped crystal ( $0.06 \times 0.01 \times 0.01 \text{ mm}^3$ ), were used for single-crystal X-ray data collection. Data were collected using a Siemens SMART APEX diffractometer equipped with a 1K CCD area detector using graphite-monochromated Mo  $K\alpha$  radiation. A hemisphere of data was collected using a narrow-frame method with scan widths of  $0.30^\circ$  in  $\omega$  and an exposure time of 40 s per frame. The first 50 frames were remeasured at the end of the data collection to monitor instrument and crystal stability. The data were integrated using the Siemens SAINT program,<sup>47</sup> with the intensities corrected for Lorentz polarization, air absorption, and absorption attributable to the variation in the path length through the detector face plate. Psi-scans were used for the absorption correction on the hemisphere of data.<sup>48</sup> The data were solved and refined using SHELXS-97 and SHELXL-97, respectively.<sup>49,50</sup> All of the atoms were refined with anisotropic thermal parameters, and the refinement converged for  $I > 2\sigma(I)$ . All calculations were performed using the WinGX-98 crystallographic software package.<sup>51</sup> The structure was checked for missing symmetry elements using PLATON.<sup>52</sup> The Flack parameters<sup>53</sup> were refined to 0.00(3) and 0.00(2) for  $\text{Zn}_2(\text{MoO}_4)(\text{SeO}_3)$  and  $\text{Zn}_2(\text{MoO}_4)(\text{TeO}_3)$ , respectively. Table 2.1, 2.2, and 2.3 show the crystallographic data, atomic coordination, and bond distances for  $\text{Zn}_2(\text{MoO}_4)(\text{SeO}_3)$  and  $\text{Zn}_2(\text{MoO}_4)(\text{TeO}_3)$ , respectively.

**Table 2.1** Crystallographic data for  $\text{Zn}_2(\text{MoO}_4)(\text{AO}_3)$  ( $\text{A} = \text{Se}^{4+}$  or  $\text{Te}^{4+}$ ).

formula	$\text{Zn}_2(\text{MoO}_4)(\text{SeO}_3)$	$\text{Zn}_2(\text{MoO}_4)(\text{TeO}_3)$
fw (g/mol)	417.64	466.28
T(K)	296.0(2)	296.0(2)
$\lambda$ (Å)	0.71073	0.71073
Crystal system	Monoclinic	Monoclinic
Space group	$P2_1$ (No.4)	$P2_1$ (No.4)
$a$ (Å)	5.1809(4)	5.178(4)
$b$ (Å)	8.3238(7)	8.409(6)
$c$ (Å)	7.1541(6)	7.241(5)
$\beta$	98.413(1)	99.351 (8)
$V$ (Å <sup>3</sup> )	305.2 (1)	311.1(4)
$Z$	2	2
$\rho_{\text{calcd}}$ (g/cm <sup>3</sup> )	4.545	4.978
$\mu$ (mm <sup>-1</sup> )	15.765	14.212
$2 \theta_{\text{max}}$ (deg)	57.8	57.6
$R$ (int)	0.0265	0.0228
Reflections collected/unique	1944/1269	1940/976
Parameter refined	102	102
GOF ( $F^2$ )	1.075	1.099
$R(F)^{\text{a}}$	0.0182	0.0212
$R_w(F_o^2)^{\text{b}}$	0.0437	0.0542
Flack param.	0.00(3)	0.00(2)

---

$$^{\text{a}}R(F) = \Sigma||F_o| - |F_c||/\Sigma|F_o|. \quad ^{\text{b}}R_w(F_o^2) = [\Sigma w(F_o^2 - F_c^2)^2/\Sigma w(F_o^2)^2]^{1/2}$$

**Table 2.2** Atomic coordinates and equivalent isotropic displacement parameters ( $\text{\AA}^2$ ) for  $\text{Zn}_2(\text{MoO}_4)(\text{AO}_3)$  ( $\text{A} = \text{Se}^{4+}$  or  $\text{Te}^{4+}$ ).

$\text{Zn}_2(\text{MoO}_4)(\text{SeO}_3)$				
Atoms	x	y	z	U(eq)
Se(1)	0.5429(1)	0.2425(1)	0.3822(1)	0.013(1)
Mo(1)	0.0741(1)	0.5314(1)	0.0151(1)	0.014(1)
Zn(1)	0.9387(1)	0.5441(1)	0.4939(1)	0.015(1)
Zn(2)	0.5326(1)	0.3633(1)	0.7727(1)	0.015(1)
O(1)	0.7018(6)	0.0620(4)	0.3757(5)	0.018(1)
O(2)	0.7667(6)	0.3364(4)	0.5444(5)	0.017(1)
O(3)	0.8040(6)	0.5505(4)	0.8297(5)	0.021(1)
O(4)	0.3378(6)	0.2079(4)	0.5468(5)	0.017(1)
O(5)	0.2793(7)	0.3778(5)	0.9553(5)	0.023(1)
O(6)	0.2493(6)	0.7108(5)	0.0449(5)	0.022(1)
O(7)	0.9753(7)	0.4806(6)	0.2305(5)	0.027(1)
$\text{Zn}_2(\text{MoO}_4)(\text{TeO}_3)$				
Atoms	x	y	z	U(eq)
Te(1)	0.5161(1)	0.2505(1)	0.3550(1)	0.010(1)
Mo(1)	0.0778(1)	0.5314(1)	0.0158(1)	0.010(1)
Zn(1)	0.9488(1)	0.5392(1)	0.4894(1)	0.012(1)
Zn(2)	0.5220(1)	0.3596(1)	0.7605(1)	0.012(1)
O(1)	0.7038(9)	0.0582(6)	0.3655(7)	0.014(1)
O(2)	0.7551(9)	0.3479(7)	0.5461(7)	0.012(1)
O(3)	0.7916(9)	0.5559(7)	0.8427(7)	0.016(1)
O(4)	0.3115(9)	0.2093(6)	0.5433(7)	0.014(1)
O(5)	0.2767(9)	0.3781(7)	0.9590(7)	0.017(1)
O(6)	0.2561(10)	0.7076(7)	0.0501(7)	0.020(1)
O(7)	0.9039(10)	0.4721(9)	0.2319(7)	0.023(1)

U(eq) is defined as one third of the trace of the orthogonalized  $U_{ij}$  tensor.

**Table 2.3** Selected bond distances (Å) for Zn<sub>2</sub>(MoO<sub>4</sub>)(AO<sub>3</sub>) (A = Se<sup>4+</sup> or Te<sup>4+</sup>).

Zn <sub>2</sub> (MoO <sub>4</sub> )(SeO <sub>3</sub> )		Zn <sub>2</sub> (MoO <sub>4</sub> )(TeO <sub>3</sub> )	
Bonds	Distances	Bonds	Distances
Zn(1)–O(1)	1.963(3)	Zn(1)–O(1)	1.937(5)
Zn(1)–O(2)	2.002(3)	Zn(1)–O(2)	1.973(5)
Zn(1)–O(4)	1.968(3)	Zn(1)–O(4)	1.953(5)
Zn(1)–O(7)	1.990(3)	Zn(1)–O(7)	1.998(6)
Zn(2)–O(1)	2.227(3)	Zn(2)–O(1)	2.155(5)
Zn(2)–O(2)	2.184(3)	Zn(2)–O(2)	2.118(5)
Zn(2)–O(3)	2.099(3)	Zn(2)–O(3)	2.181(5)
Zn(2)–O(4)	2.197(3)	Zn(2)–O(4)	2.168(5)
Zn(2)–O(5)	1.986(3)	Zn(2)–O(5)	2.016(5)
Zn(2)–O(6)	2.040(3)	Zn(2)–O(6)	2.079(5)
Se–O(1)	1.717(3)	Te–O(1)	1.882(5)
Se–O(2)	1.705(3)	Te–O(2)	1.887(5)
Se–O(4)	1.721(3)	Te–O(4)	1.890(5)
Mo–O(3)	1.789(3)	Mo–O(3)	1.790(5)
Mo–O(5)	1.755(4)	Mo–O(5)	1.766(6)
Mo–O(6)	1.744(4)	Mo–O(6)	1.743(5)
Mo–O(7)	1.749(3)	Mo–O(7)	1.763(5)

### Powder X-ray Diffraction

The X-ray powder diffraction data were collected using a PANalytical X'PertPRO diffractometer at room temperature (Cu  $K\alpha$  radiation, flat plate geometry) equipped with

X'Celerator detector. Data were collected in the  $2\theta$  range of  $5 - 70^\circ$  with a step size of  $0.008^\circ$  and a step time of 0.3s.

### **Infrared Spectroscopy**

Infrared (IR) spectra were recorded on a Matteson FTIR 5000 spectrometer in the spectral range of  $400 - 4000\text{ cm}^{-1}$  at room temperature. The sample (5 mg) was finely ground with dry KBr (100 mg). This powder mixture was then transferred to a stainless steel IR holder and pressed to a semi-transparent pellet ( $\sim 0.2\text{ mm}$  thick).

### **UV–vis Diffuse Reflectance Spectroscopy**

UV–vis diffuse reflectance spectra were collected with a Varian Cary 500 scan UV–vis–NIR spectrophotometer over the spectral range of  $200\text{--}2000\text{ nm}$  at room temperature. Polytetrafluoroethylene (PTFE) was used as a standard material for baseline correction. The sample was thoroughly mixed with PTFE, and this mixture was used for UV–vis measurements. Reflectance spectra were converted to absorbance based on the Kubelka–Munk equation.<sup>54,55</sup>

### **Thermal Analysis**

Thermogravimetric and differential thermal analyses were simultaneously carried out on an EXSTAR6000 TG/DTA 6300 Thermogravimetric/Differential Thermal Analysis system (SII NanoTechnology Inc.). The sample ( $\sim 20\text{ mg}$ ) was placed in a platinum crucible that was heated (cooled) at a rate of  $10\text{ }^\circ\text{C}/\text{min}$  in the range of  $25\text{--}700\text{ }^\circ\text{C}$  for  $\text{Zn}_2(\text{MoO}_4)(\text{SeO}_3)$  and  $25\text{--}850\text{ }^\circ\text{C}$  for  $\text{Zn}_2(\text{MoO}_4)(\text{TeO}_3)$  under flowing nitrogen gas. A



platinum crucible containing 20 mg of  $\text{Al}_2\text{O}_3$  was used as the reference during the measurements.

### **Second-harmonic Generation**

Powder SHG measurements were performed at room temperature on a modified Kurtz-NLO system,<sup>56</sup> using a pulsed Nd:YAG laser with a wavelength of 1064 nm. The methodology and instrumentation details have been published.<sup>3</sup> The SHG efficiency has been shown to be particle size dependent.<sup>56</sup> Thus, the polycrystalline samples were ground and sieved into distinct particle size ranges (20–45, 45–63, 63–75, 75–90, and 90–120  $\mu\text{m}$ ). In order to evaluate relative SHG efficiencies of the measured samples with known SHG materials and to calculate their average nonlinear optical (NLO) susceptibilities,  $\langle d_{\text{eff}} \rangle_{\text{exp}}$ , crystalline  $\alpha\text{-SiO}_2$  was also ground and sieved into the same particle size ranges. No index matching fluid was used in the experiment.

### **Piezoelectric Measurements**

Converse piezoelectric measurements were performed at room temperature using a Radiant Technologies RT66A piezoelectric test system with a TREK (609E-6) high voltage amplifier, Precision Materials Analyzer, Precision High Voltage Interface, and MTI 2000 Fotonic Sensor.  $\text{Zn}_2(\text{MoO}_4)(\text{SeO}_3)$  and  $\text{Zn}_2(\text{MoO}_4)(\text{TeO}_3)$  samples were pressed in pellets (~10 mm diameter and ~1 mm thick).  $\text{Zn}_2(\text{MoO}_4)(\text{SeO}_3)$  pellet was placed in the fused silica tube that was evacuated and flame-sealed. Both pellets were sintered at 550 °C for 1 day. Silver paste was applied to both sides of the sintered pellets as electrodes, and the pellets were cured at 300 °C for 72 h in air. These pellets were also used in polarization measurements.

## Polarization Measurements

The polarization measurements were done on a Radiant Technologies Model RT66A ferroelectric test system with a TREK high-voltage amplifier in the temperature range of 25–185 °C in a Delta Model 9023 environmental test chamber. The unclamped pyroelectric coefficient, defined as  $dP/dT$ , was determined by measuring the polarization as a function of temperature. The methodology and instrumentation details have been published.<sup>3</sup> To measure the potential ferroelectric behavior, frequency-dependent polarization measurements were done at room temperature under static electric field of 10–15 kV/cm between 50–1000 Hz. For the pyroelectric measurements, the polarization was measured statically from room temperature to 185 °C in various increments with an electric field of 12 kV/cm and at 100 Hz. The temperature was allowed to stabilize before the polarization was measured.

## Computational Details

First-principles density functional theory (DFT)<sup>57,58</sup> electronic structure calculations for  $\text{Zn}_2(\text{MoO}_4)(\text{SeO}_3)$  and  $\text{Zn}_2(\text{MoO}_4)(\text{TeO}_3)$  were carried out using numerical atomic orbitals (NAO)<sup>59</sup> and plane wave (PW) pseudopotential(PP) methods as implemented in SIESTA<sup>59,60</sup> (3.0-rc2 version)<sup>61</sup> and Quantum ESPRESSO (4.1.2 version)<sup>62</sup> packages, respectively. For the NAOPP calculations in SIESTA, norm-conserving Martins-Troullier (MT) pseudopotentials<sup>63</sup> for all the elements were used with the generalized gradient approximation (GGA)<sup>64</sup> for exchange-correlation corrections. A split-valence double- $\zeta$  basis set was used for all atoms where polarization orbitals were included as obtained with an energy shift of 0.1 eV. The energy cutoff of the real space integration mesh was

300 Rydberg (Ry). A  $6 \times 4 \times 4$  Monkhorst–Pack (MP)<sup>65</sup> k-mesh was used for sampling the Brillouin zone. A self-consistency was achieved within the total energy change less than  $10^{-4}$  eV. The experimental crystal structures were adapted for all calculations. Crystal orbital Hamilton population (COHP)<sup>66</sup> calculations were also performed using the NAOPP method after the total energy was self-consistently achieved.

Electron localization function (ELF)<sup>67,68</sup> calculations were performed using the PWPP method. Norm-conserving MT pseudopotentials for all the elements were used with the GGA for exchange-correlation corrections. The pseudopotentials generated from the Fritz Haber Institute (FHI) code were converted for the calculations.<sup>69</sup> A plane wave energy cutoff was set to 37 Ry. The Brillouin zone was sampled using a  $6 \times 4 \times 4$  MP k-mesh. A total energy convergence threshold was set to  $10^{-6}$  Ry indicated self-consistency. The experimental crystal structures were employed for all calculations.

A hypothetical structure,  $\text{Zn}_2(\text{MoO}_4)(\text{SO}_3)$ , was obtained using the PWPP method in order to systematically study the electronic structures of  $\text{Zn}_2(\text{MoO}_4)(\text{AO}_3)$  ( $\text{A} = \text{S}^{4+}$ ,  $\text{Se}^{4+}$ , and  $\text{Te}^{4+}$ ). Initially, the structure of  $\text{Zn}_2(\text{MoO}_4)(\text{SO}_3)$  was adapted to the structure of  $\text{Zn}_2(\text{MoO}_4)(\text{SeO}_3)$  where Se is replaced by S. Structural optimization was employed with the GGA for the exchange-correlation corrections. The experimental symmetry of  $\text{Zn}_2(\text{MoO}_4)(\text{SeO}_3)$  was retained during the relaxation. The Hellmann–Feynman force and the total energy changes were set to  $10^{-3}$  Ry per atomic unit (a.u.) and  $10^{-4}$  Ry, respectively, between two consecutive self-consistent field steps. A planewave energy cutoff was set to 37 Ry. For all of the structural figures and electronic structure results, the program VESTA was used.<sup>70</sup>

## 2.4 Results and discussion

### Structures

$\text{Zn}_2(\text{MoO}_4)(\text{AO}_3)$  ( $\text{A} = \text{Se}^{4+}$  or  $\text{Te}^{4+}$ ) represent two new polar oxides ( $P2_1$ ). The isostructural compounds exhibit three-dimensional crystal structures that contain  $\text{ZnO}_4$ ,  $\text{ZnO}_6$ ,  $\text{MoO}_4$ , and  $\text{AO}_3$  polyhedra (see Figure 2.1). There are two crystallographically unique zinc sites, hereafter Zn(1) and Zn(2), that have tetrahedral and octahedral coordination environments respectively. The  $\text{ZnO}_4$  tetrahedra share edges with an  $\text{AO}_3$  polyhedron and a  $\text{ZnO}_6$  octahedron, and share corners with an additional  $\text{AO}_3$  polyhedron,  $\text{ZnO}_6$  octahedron, and  $\text{MoO}_4$  tetrahedron. This complex connectivity results in the three-dimensional crystal network (see Figure 2.2). In connectivity terms, the structure may be written as  $[(\text{ZnO}_{1/2}\text{O}_{3/3})^{1-} (\text{ZnO}_{3/3}\text{O}_{3/2})^{3-} (\text{MoO}_{4/2})^{2+} (\text{AO}_{3/3})^{2+}]^0$ . For  $\text{Zn}_2(\text{MoO}_4)(\text{SeO}_3)$  ( $\text{Zn}_2(\text{MoO}_4)(\text{TeO}_3)$ ), the Zn(1)–O, Zn(2)–O, Mo–O and Se–O(Te–O) bond distances are in the range of 1.963(5)–2.002(3)(1.937(5)–1.998(5)) Å, 1.986(3)–2.227(3)(2.016(5)–2.181(5)) Å, 1.744(4)–1.789(3)(1.743(5)–1.790(5)) Å and 1.705(3)–1.721(3)(1.882(5)–1.890(5)) Å, respectively. The bond valence calculations for  $\text{Zn}^{2+}$ ,  $\text{Mo}^{6+}$ , and  $\text{Se}^{4+}(\text{Te}^{4+})$  resulted in values 1.89–1.99, 5.87–5.97, and 3.89(3.83), respectively (see Table 2.4).

**Table 2.4** Bond valence sum (BVS), bond strain index (BSI), global instability index (GII), and unit cell dipole moment ( $\mu$ , Debye) for  $\text{Zn}_2(\text{MoO}_4)(\text{AO}_3)$  ( $\text{A} = \text{Se}^{4+}$  or  $\text{Te}^{4+}$ ).

Compound	BVS (vu)				BSI	GII	$\mu$
	Zn(1) <sup>2+</sup>	Zn(2) <sup>2+</sup>	A <sup>4+</sup>	Mo <sup>6+</sup>			
$\text{Zn}_2(\text{MoO}_4)(\text{SeO}_3)$	1.89	1.99	3.89	5.97	0.110	0.077	16.5
$\text{Zn}_2(\text{MoO}_4)(\text{TeO}_3)$	1.98	1.98	3.83	5.87	0.096	0.101	14.2

As stated earlier  $\text{Zn}_2(\text{MoO}_4)(\text{AO}_3)$  ( $\text{A} = \text{Se}^{4+}$  or  $\text{Te}^{4+}$ ) are found in a polar space group  $P2_1$  (No. 4). Thus it is relevant to discuss the structural origin of the polarity. Only the  $\text{Mo}^{6+}$  and  $\text{A}^{4+}$  cations are amenable to SOJT distortions; however, a SOJT distortion is not observed in  $\text{Mo}^{6+}$  attributable to its tetrahedral coordination. Thus, only the  $\text{A}^{4+}$  cations undergo the SOJT distortion. This distortion results in the formation of a stereoactive lone-pair that creates a locally asymmetric and polar  $\text{AO}_3$  coordination environment (see Figure 2.1). The arrows in Figure 2.1 indicate the approximate direction of the local dipole moment on the  $\text{AO}_3$  polyhedron. As seen, there is some ‘constructive addition’ resulting in a net moment directed approximately toward the -b-axis direction. We will be discussing the stereoactive lone-pair and its relevance to the observed functional properties, that is, second-harmonic generation, pyroelectricity, and piezoelectricity, later in the chapter.

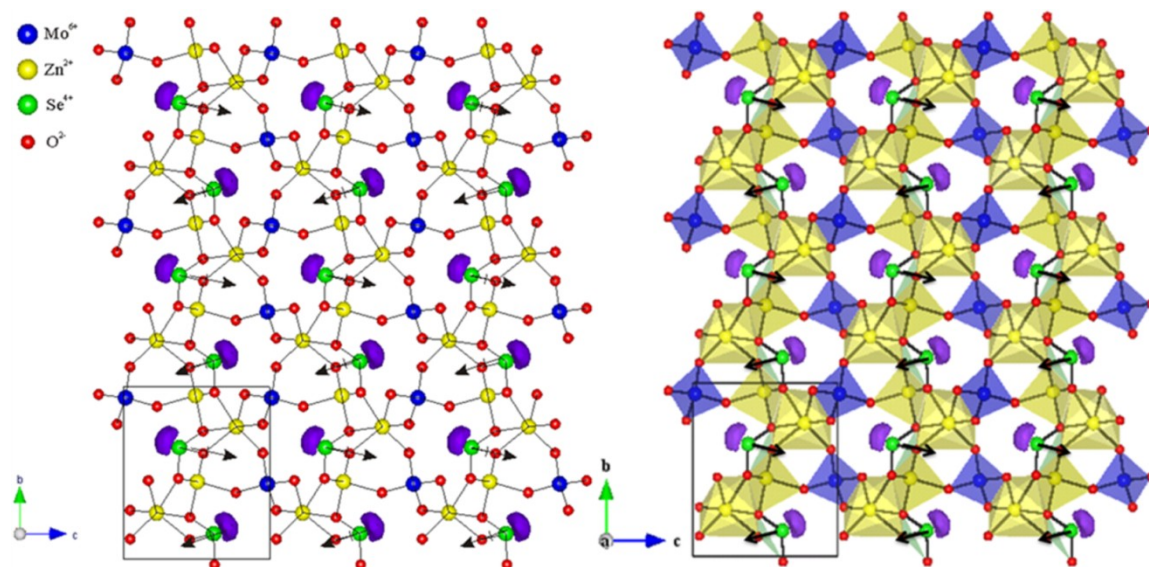


**Figure 2.1** Ball-and-stick and polyhedral representations of  $\text{Zn}_2(\text{MoO}_4)(\text{SeO}_3)$  in the bc-plane. The arrows indicate the approximate directions of the dipole moment on the  $\text{SeO}_3$

polyhedron. Electron localization function (ELF) with  $\eta = 0.9$  is shown, indicating that the lone-pair on the  $\text{Se}^{4+}$  is stereoactive.

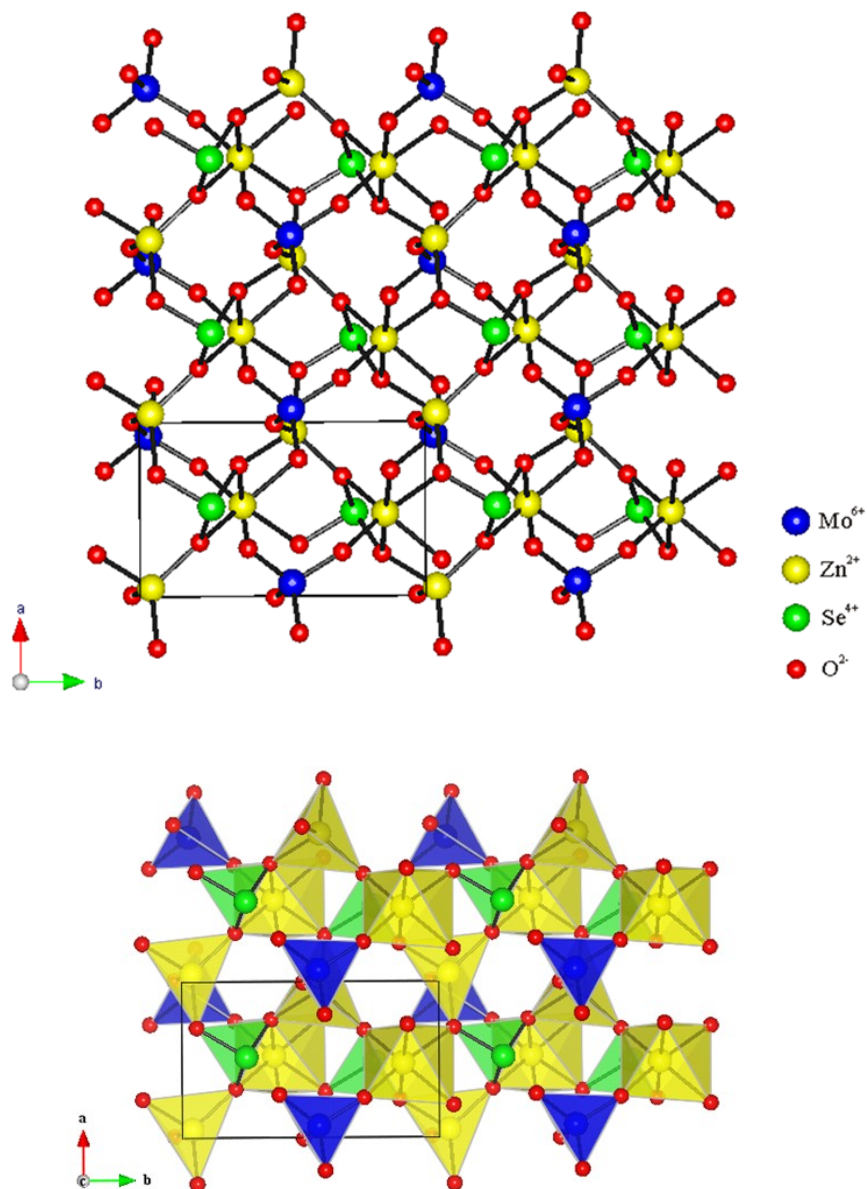


**Figure 2.2** Ball-and-stick (top) and polyhedral (bottom) diagrams of  $\text{Zn}_2(\text{MoO}_4)(\text{SeO}_3)$  in the  $ab$ -plane. Note that the polyhedra share edges and corners resulting in the three-dimensional crystal structure.

## Infrared Spectroscopy

The infrared (IR) spectra for  $\text{Zn}_2(\text{MoO}_4)(\text{AO}_3)$  ( $\text{A} = \text{Se}^{4+}$  or  $\text{Te}^{4+}$ ) revealed absorption bands of Mo–O, Se(Te)–O vibrations in the 400–1000  $\text{cm}^{-1}$  range. The Mo–O stretching vibrations were observed around 811–940  $\text{cm}^{-1}$ , whereas Se(Te)–O stretching vibrations were seen around 673–750  $\text{cm}^{-1}$ . The absorption band occurring below 650  $\text{cm}^{-1}$  can be assigned to Mo–O–Se(Te) bending vibrations. These assignments are in good agreement with the literature.<sup>71-73</sup>

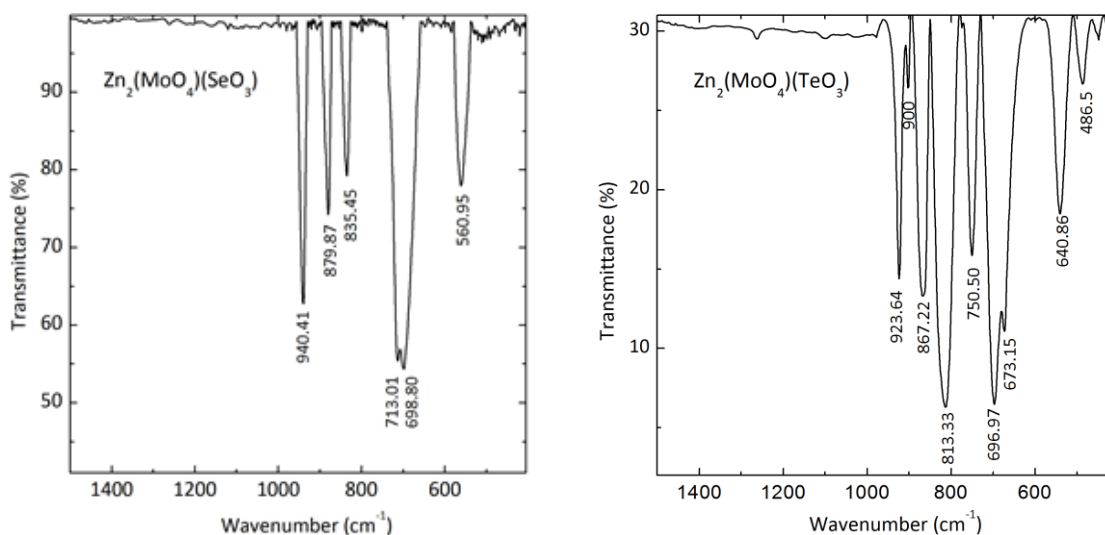


**Figure 2.3** IR data and assignments for  $\text{Zn}_2(\text{MoO}_4)(\text{SeO}_3)$  and  $\text{Zn}_2(\text{MoO}_4)(\text{TeO}_3)$ .

**Table 2.5** IR peak assignments for  $\text{Zn}_2(\text{MoO}_4)(\text{SeO}_3)$  and  $\text{Zn}_2(\text{MoO}_4)(\text{TeO}_3)$ .

$\text{Zn}_2(\text{MoO}_4)(\text{SeO}_3)$ ( $\text{cm}^{-1}$ )			$\text{Zn}_2(\text{MoO}_4)(\text{TeO}_3)$ ( $\text{cm}^{-1}$ )		
$\nu(\text{Se} - \text{O})$	$\nu(\text{Mo} - \text{O})$	$\nu(\text{Mo} - \text{O} - \text{Se})$	$\nu(\text{Te} - \text{O})$	$\nu(\text{Mo} - \text{O})$	$\nu(\text{Mo} - \text{O} - \text{Te})$
713	940	590	750	923	640
698	879		69	867	586
	835		673	811	

## UV–vis Diffuse Reflectance Spectroscopy

Reflectance spectra of  $\text{Zn}_2(\text{MoO}_4)(\text{AO}_3)$  ( $\text{A} = \text{Se}^{4+}$  or  $\text{Te}^{4+}$ ) were converted to absorbance using the Kubelka–Munk function:<sup>54,55</sup>

$$F(R) = \frac{K}{S} = \frac{(1 - R)^2}{2R} \quad (2.1)$$

where  $R$ ,  $K$ , and  $S$  represent the reflectance, the absorption, and the scattering, respectively. In a  $F(R)$  versus  $E$  (eV) plot, extrapolating the linear part of the rising curve to zero provides onset absorption of 4.2 and 4.1 eV for  $\text{Zn}_2(\text{MoO}_4)(\text{SeO}_3)$  and  $\text{Zn}_2(\text{MoO}_4)(\text{TeO}_3)$ , respectively (see Figure 2.4). These values are in good agreement with the energy gap obtained from their calculated electronic band structures. For these materials, the top of the valence band mainly consists of O-2sp orbitals, whereas the bottom of the conduction band is mainly composed of contribution from Mo-4d. Thus, energy gap is mainly attributable to ligand-to-metal, O-2sp to Mo-4d, charge transfer.<sup>74,75</sup>

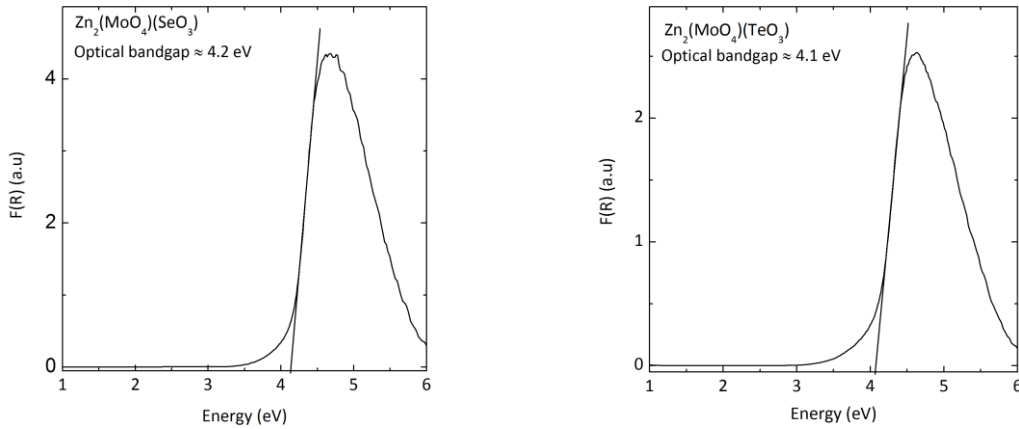


**Figure 2.4** UV–vis diffuse reflectance spectroscopy data for  $\text{Zn}_2(\text{MoO}_4)(\text{SeO}_3)$  and  $\text{Zn}_2(\text{MoO}_4)(\text{TeO}_3)$ .



## Thermal Analysis

The thermal stability of  $\text{Zn}_2(\text{MoO}_4)(\text{AO}_3)$  ( $\text{A} = \text{Se}^{4+}$  or  $\text{Te}^{4+}$ ) were investigated through thermogravimetric and differential thermal analyses (TGA and DTA) (see Figure 2.5). The TGA and DTA data of  $\text{Zn}_2(\text{MoO}_4)(\text{SeO}_3)$  indicated that the oxide releases  $\text{SeO}_2$  at  $\sim 500^\circ\text{C}$  and subsequently decomposes to  $\text{ZnO}$ ,  $\text{ZnMoO}_4$  and  $\text{Zn}_3\text{Mo}_2\text{O}_9$ . The TGA and DTA data of  $\text{Zn}_2(\text{MoO}_4)(\text{TeO}_3)$  revealed that the oxide melts at approximately  $831^\circ\text{C}$ . As seen in the TGA data, no weight loss was observed in the range of  $25\text{--}850^\circ\text{C}$ , but the DTA data revealed an endothermic (exothermic) peak around  $831^\circ\text{C}$  ( $817^\circ\text{C}$ ) in the heating (cooling) cycle. Also, the PXRD pattern of the melted  $\text{Zn}_2(\text{MoO}_4)(\text{TeO}_3)$  sample is consistent with the as-synthesized  $\text{Zn}_2(\text{MoO}_4)(\text{TeO}_3)$ .

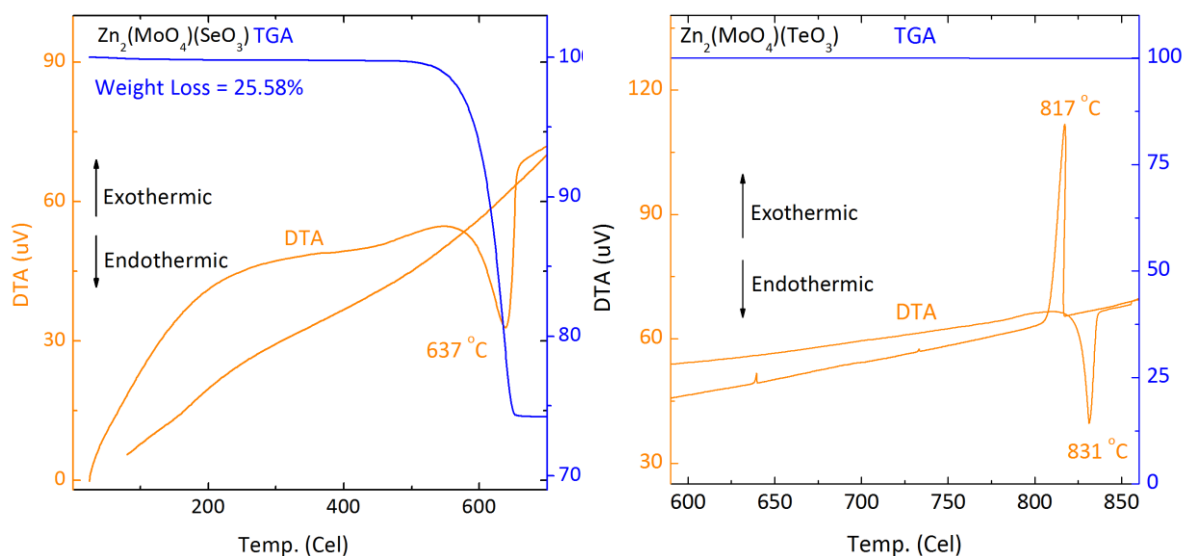


**Figure 2.5** Thermogravimetric and differential thermal analysis data for  $\text{Zn}_2(\text{MoO}_4)(\text{SeO}_3)$  and  $\text{Zn}_2(\text{MoO}_4)(\text{TeO}_3)$ .

## Second-harmonic Generation

Powder SHG measurements in the particle size range of 25–120  $\mu\text{m}$  indicated that  $\text{Zn}_2(\text{MoO}_4)(\text{AO}_3)$  ( $\text{A} = \text{Se}^{4+}$  or  $\text{Te}^{4+}$ ) are non-phase matching with comparable efficiencies (see Figure 2.6). Their powder SHG efficiencies were  $\sim 100 \times$  and  $\sim 80 \times \alpha\text{-SiO}_2$  in the particle size range of 45–63  $\mu\text{m}$  for  $\text{Zn}_2(\text{MoO}_4)(\text{SeO}_3)$  and  $\text{Zn}_2(\text{MoO}_4)(\text{TeO}_3)$ , respectively. These indicate  $\text{Zn}_2(\text{MoO}_4)(\text{SeO}_3)$  and  $\text{Zn}_2(\text{MoO}_4)(\text{TeO}_3)$  fall into the class C of SHG materials as defined by Kurtz and Perry.<sup>56</sup> The average NLO susceptibilities,  $\langle d_{\text{eff}} \rangle_{\text{exp}}$ , can be estimated to be  $\sim 5.79$  pm/V and  $\sim 4.78$  pm/V, respectively.<sup>3</sup> The moderate SHG efficiencies are attributable to the partial alignment of the  $\text{AO}_3$  polyhedra. As seen in Figure 2.1, the moments associated with the  $\text{AO}_3$  polyhedra are not parallel. In fact, the moments are only partially aligned. This partial ‘constructive addition’ results in the observed moderate SHG efficiencies of  $\sim 100 \times$  and  $\sim 80 \times \alpha\text{-SiO}_2$  for  $\text{Zn}_2(\text{MoO}_4)(\text{SeO}_3)$  and  $\text{Zn}_2(\text{MoO}_4)(\text{TeO}_3)$  respectively.

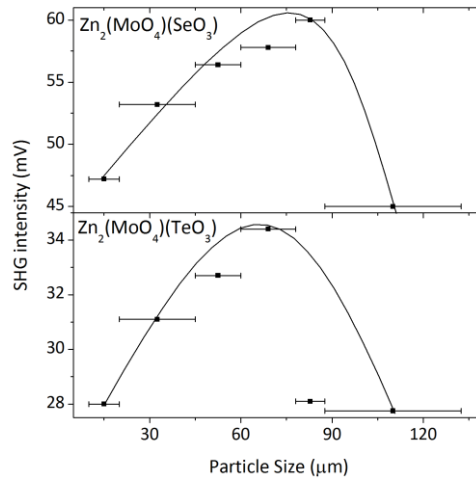


**Figure 2.6** Particle size vs. SHG intensity data for  $\text{Zn}_2(\text{MoO}_4)(\text{SeO}_3)$  and  $\text{Zn}_2(\text{MoO}_4)(\text{TeO}_3)$ . The curves are drawn to guide the eye and are not fits to the data.

## Piezoelectric Measurements

Converse piezoelectric measurements were performed on  $\text{Zn}_2(\text{MoO}_4)(\text{AO}_3)$  ( $\text{A} = \text{Se}^{4+}$  or  $\text{Te}^{4+}$ ) at room temperature. With each sample, a voltage of 2000 V at 50 Hz was applied. The  $d_{33}$  piezoelectric charge constants, which is defined as the ratio between the strain produced and the electrical voltage applied, for  $\text{Zn}_2(\text{MoO}_4)(\text{SeO}_3)$  and  $\text{Zn}_2(\text{MoO}_4)(\text{TeO}_3)$  were estimated to be 14.1 and 30.0 pm/V, respectively (see Figure 2.7).

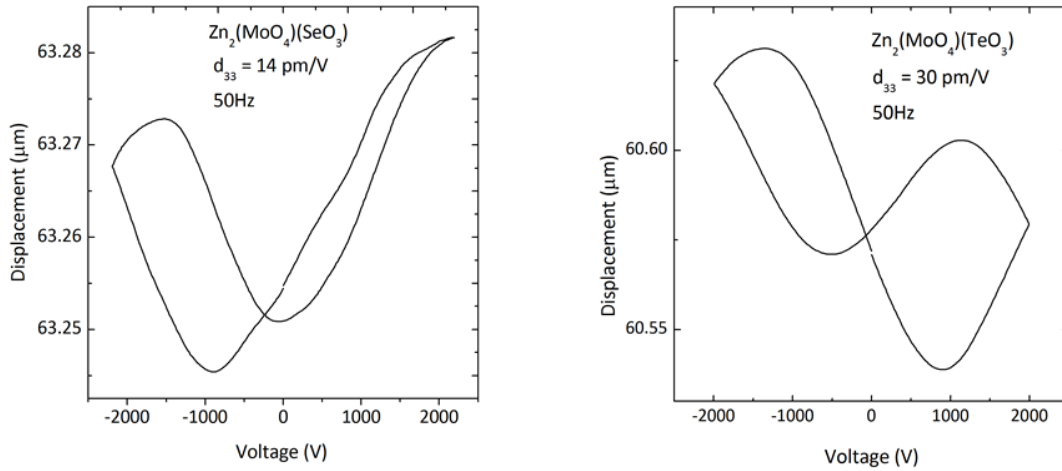


**Figure 2.7** Displacement vs. electric field plots for  $\text{Zn}_2(\text{MoO}_4)(\text{SeO}_3)$  and  $\text{Zn}_2(\text{MoO}_4)(\text{TeO}_3)$ .

## Polarization Measurements

The reported materials are not only NCS, but also are polar – a macroscopic dipole moment is observed. The macroscopic polarity suggests the possibility for ferroelectric behavior. Ferroelectric hysteresis measurements were performed on pressed pellets, and polarization loops were observed. In addition, these loops did appear to exhibit frequency dependence (see Figure 2.8). However, these loops are not attributable to ferroelectric

hysteresis, that is, the reported materials are not ferroelectric – the macroscopic polarization cannot be reversed in the presence of an external electric field. It has been demonstrated that these types of loops have been erroneously attributed to ferroelectric behavior.<sup>76</sup> With the reported materials, it is important to understand why the materials, although polar, are not ferroelectric. As stated earlier, for ferroelectric behavior to occur the macroscopic polarization must be switchable in the presence of an external electric field. This implies that the local moments must also be reversed. In  $\text{Zn}_2(\text{MoO}_4)(\text{AO}_3)$  ( $\text{A} = \text{Se}^{4+}$  or  $\text{Te}^{4+}$ ), only the  $\text{SeO}_3$  and  $\text{TeO}_3$  polyhedra exhibit a local dipole moment. Thus it is these dipole moments that must be reversed for ferroelectric behavior to occur. We have already shown that the energy barrier to inversion of a  $\text{SeO}_3$  polyhedron is  $\sim 5.3$  eV,<sup>45</sup> which is substantially larger than what is observed in ferroelectric  $\text{BaTiO}_3$  ( $1.8 \times 10^{-2}$  eV) and  $\text{PbTiO}_3$  ( $2.0 \times 10^{-1}$  eV).<sup>77</sup> Preliminary calculations suggest that the barrier to inversion of a  $\text{TeO}_3$  polyhedron is nearly 7 eV. Thus polarization reversal in  $\text{Zn}_2(\text{MoO}_4)(\text{AO}_3)$  ( $\text{A} = \text{Se}^{4+}$  or  $\text{Te}^{4+}$ ) is energetically very unfavorable, rendering the materials non-ferroelectric. The materials are, however, pyroelectric.

**Table 2.6** SHG efficiencies ( $\times \alpha\text{-SiO}_2$ ), piezoelectric responses, ( $d_{33}$ ), pyroelectric coefficients ( $P_T$ ), and maximum polarization ( $P_m$ ) for  $\text{Zn}_2(\text{MoO}_4)(\text{AO}_3)$  ( $\text{A} = \text{Se}^{4+}$  or  $\text{Te}^{4+}$ ).

Compound	Functional properties			
	SHG	$d_{33}^c$	$P_T^d$	$P_m^f$
$\text{Zn}_2(\text{MoO}_4)(\text{SeO}_3)$	100	14	-0.31	0.034
$\text{Zn}_2(\text{MoO}_4)(\text{TeO}_3)$	80	30	-0.64	0.060
$^c \text{pm/V}$ , $^d \text{at } 55^\circ\text{C}$ ( $\mu\text{C/m}^2\text{K}$ ), $^f \text{at } 100 \text{ Hz}$ ( $\mu\text{C/cm}^2$ )				

Pyroelectric measurements were performed by measuring the spontaneous polarization ( $P_s$ ) as a function of temperature. The values of the pyroelectric coefficient, which is defined as  $dP/dT$ , for  $\text{Zn}_2(\text{MoO}_4)(\text{SeO}_3)$  and  $\text{Zn}_2(\text{MoO}_4)(\text{TeO}_3)$  at 55 °C are -0.31 and -0.64  $\mu\text{C}/\text{m}^2\text{K}$ , respectively (see Table 2.6).

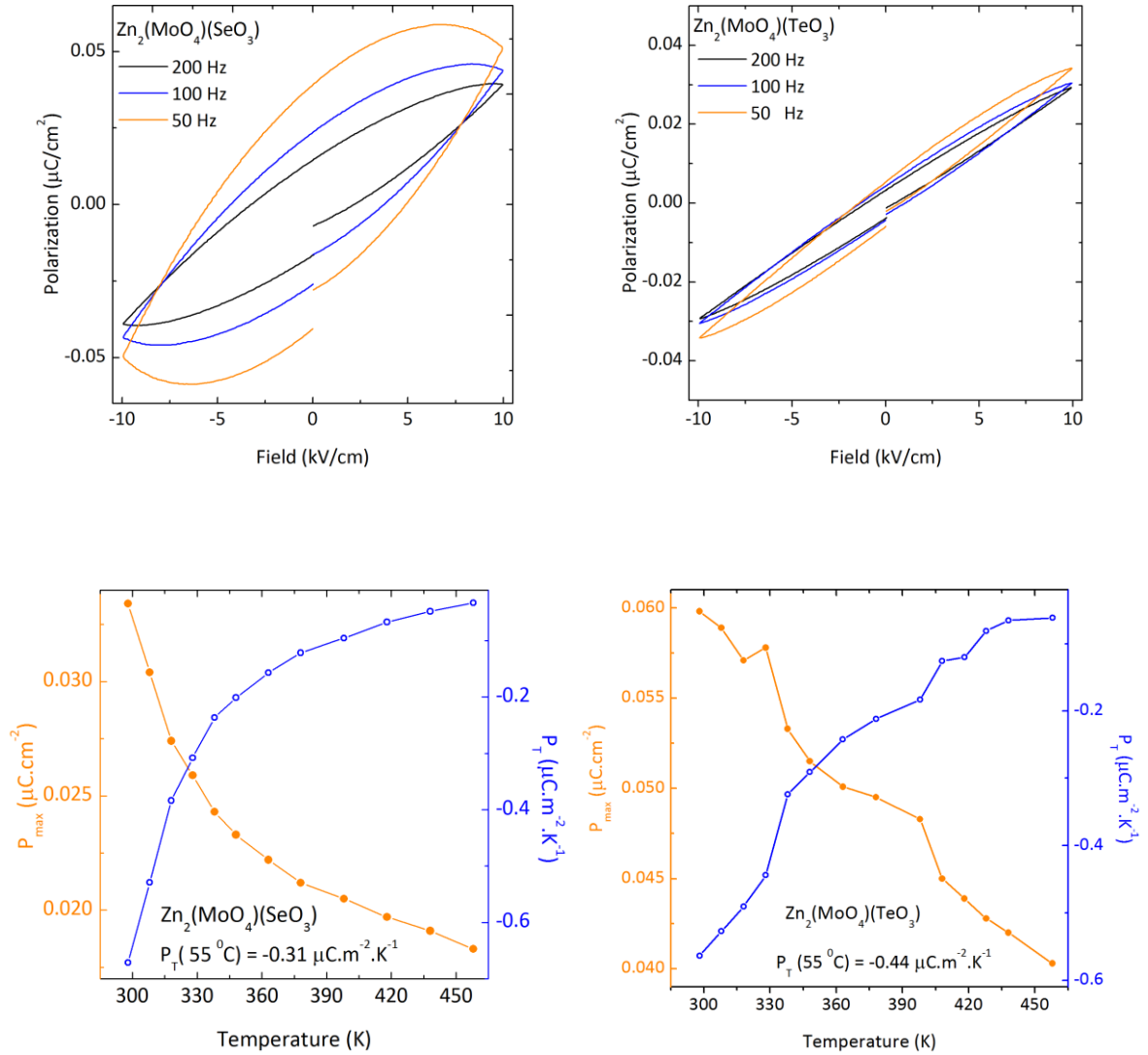


**Figure 2.8** Frequency-dependent hysteresis loops (top) and pyroelectric coefficient vs. temperature plots (bottom) for  $\text{Zn}_2(\text{MoO}_4)(\text{AO}_3)$  ( $A = \text{Se}^{4+}$  or  $\text{Te}^{4+}$ ). The curves do not indicate ferroelectric hysteresis, that is, polarization reversal, rather dielectric loss.

## Electronic Band Structures

The electronic band structures of  $\text{Zn}_2(\text{MoO}_4)(\text{AO}_3)$  ( $\text{A} = \text{Se}^{4+}$  or  $\text{Te}^{4+}$ ) were performed using the NAOPP method. The total density of states (TDOS) and projected density of states (PDOSs) of both materials are shown in Figure 2.9 where an energy gap of 3.3 eV and 3.1 eV reveals at the Fermi level ( $E_F$ ) for  $\text{Zn}_2(\text{MoO}_4)(\text{SeO}_3)$  and  $\text{Zn}_2(\text{MoO}_4)(\text{TeO}_3)$ , respectively. The energy gaps indicate their insulating nature that is consistent with the observed energy gaps of 4.2 eV and 4.1 eV observed in the UV-Vis diffuse reflectance spectra of  $\text{Zn}_2(\text{MoO}_4)(\text{SeO}_3)$  and  $\text{Zn}_2(\text{MoO}_4)(\text{TeO}_3)$ , respectively.<sup>78-80</sup> Overall, their electronic structures are similar because the materials are isostructural. As seen in Figure 2.9, narrow and broad valence bands that are separated by approximately 3 eV, are shown near -10 eV and -7 eV relative to  $E_F$ . The PDOSs indicate that the narrow band consists of almost equal amount of O-2s and Se-4s(Te-5s) contributions. The broad band has contributions from O-2sp, Zn-3d, Mo-4d, and Se-4sp(Te-5sp). As seen in PDOSs, the bottom part of the band ( $\sim -7$  eV to  $\sim -6$  eV) is mostly contributed by O-2sp and Se-4p(Te-5p), and the middle part of the band ( $\sim -6$  eV to  $\sim -2.5$  eV) is composed of mainly Zn-3d and O-2sp, and the top part of the band ( $\sim -2.5$  eV to  $E_F$ ) consists of mostly O-2sp. In fact, the bottom part of the band indicates Se(Te)-O interactions where three DOS peaks and one peak shown in each DOSs of  $\text{Zn}_2(\text{MoO}_4)(\text{SeO}_3)$  and  $\text{Zn}_2(\text{MoO}_4)(\text{TeO}_3)$  are mainly attributable to the differences in the Se-O and Te-O bond lengths. The middle part of the band indicates a weak interaction between O-2sp and Zn-3d, consistent with the ionic character of the  $\text{Zn}^{2+}(3d^{10})$  cations. The top part of the band is indicative of the nonbonding character of O-2sp. However, a relatively small contribution of Se-4sp or Te-

5sp is observed directly below the  $E_F$  in both electronic structures as seen in Figure 2.10 that is associated with their lone-pair formation on  $\text{Se}^{4+}$  or  $\text{Te}^{4+}$  cations, respectively.

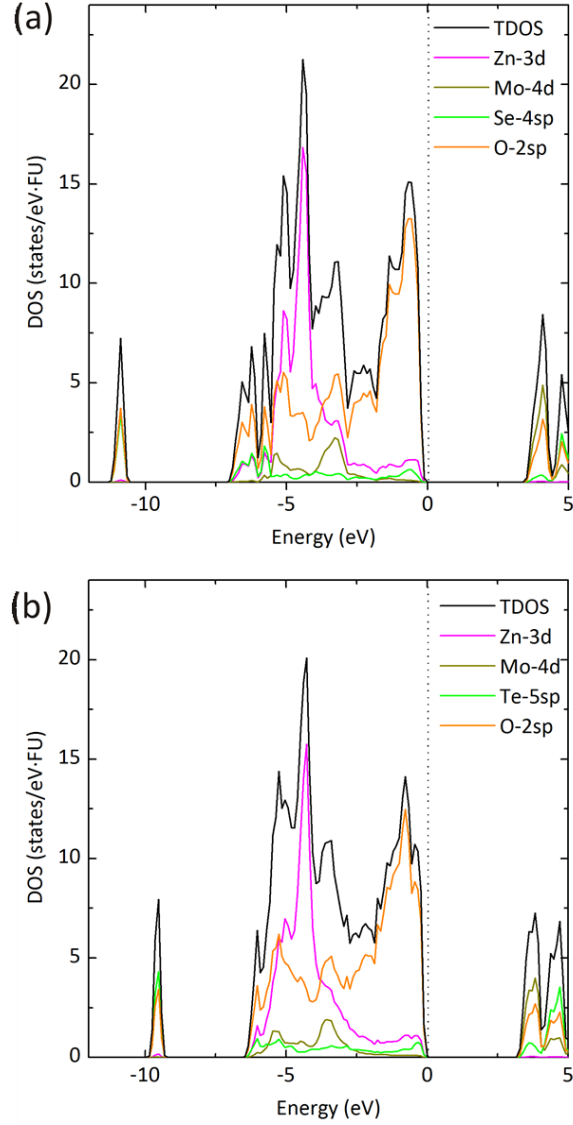


**Figure 2.9** Total and projected density of states plots for (a)  $\text{Zn}_2(\text{MoO}_4)(\text{SeO}_3)$  and (b)  $\text{Zn}_2(\text{MoO}_4)(\text{TeO}_3)$ . The dotted vertical line at 0 eV indicates  $E_F$ .

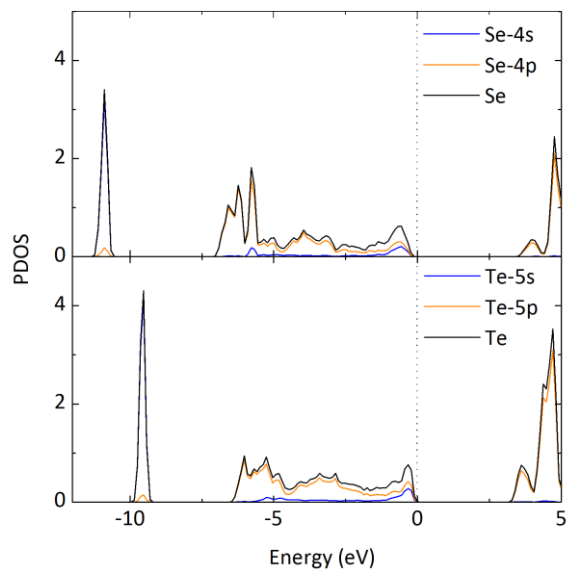


**Figure 2.10** The detailed PDOS plots for  $\text{Se}^{4+}$  and  $\text{Te}^{4+}$ . The dotted vertical line at 0 eV indicates  $E_F$ .

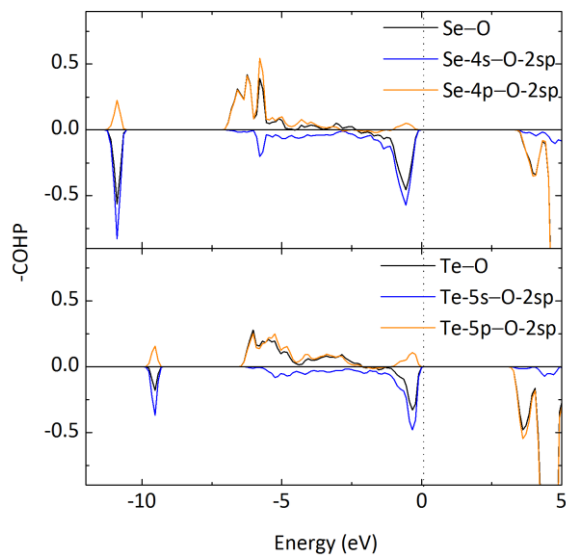


**Figure 2.11** -COHP plots for A-O, A-ns-O-2sp, A-np-O-2sp orbital interaction for  $\text{Zn}_2(\text{MoO}_4)(\text{AO}_3)$  ( $A = \text{Se}^{4+}$  or  $\text{Te}^{4+}$ ). The dotted vertical line at 0 eV indicates  $E_F$ .



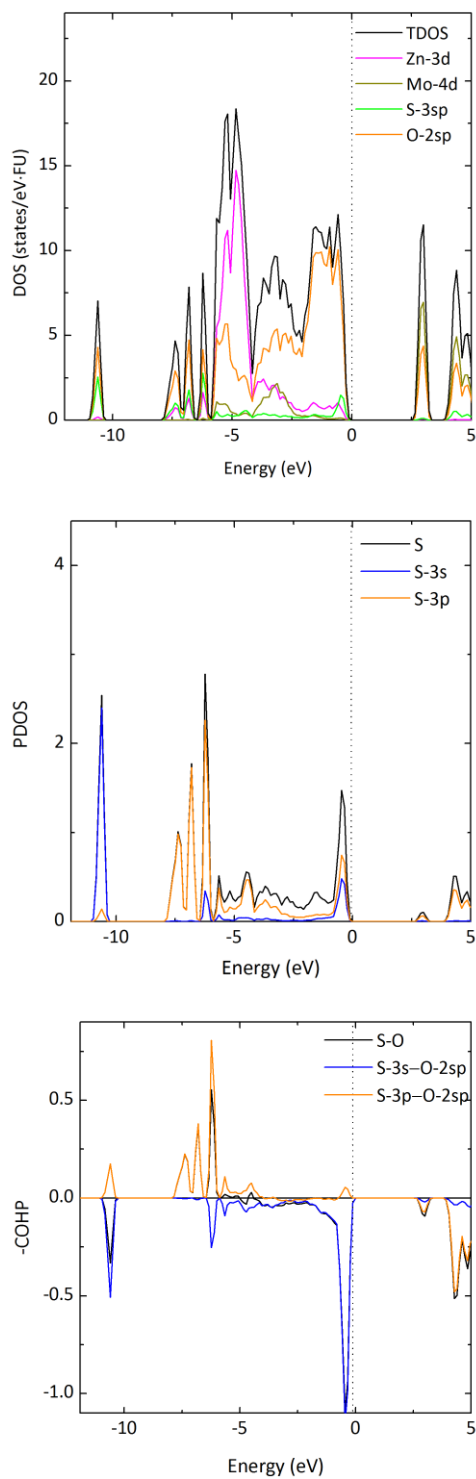


**Figure 2.12** Density of states (top) and projected density of states (middle) plots for  $\text{Zn}_2(\text{MoO}_4)(\text{SO}_3)$  and a crystal orbital Hamilton population (bottom) plot for S-O bonds.

**Table 2.7** Bond lengths (Å) of S-O bonds of hypothetical  $\text{Zn}_2(\text{MoO}_4)(\text{SO}_3)$ , compared to those of Se-O bonds of  $\text{Zn}_2(\text{MoO}_4)(\text{SeO}_3)$ .

$\text{Zn}_2(\text{MoO}_4)(\text{SO}_3)$		$\text{Zn}_2(\text{MoO}_4)(\text{SeO}_3)$	
Bond	Distance	Bond	Distance
S–O(1)	1.572	Se–O(1)	1.717(3)
S–O(2)	1.605	Se–O(2)	1.705(3)
S–O(4)	1.588	Se–O(4)	1.721(3)

**Table 2.8** Bond angles for the asymmetric  $\text{AO}_3$  trigonal pyramids in  $\text{Zn}_2(\text{MoO}_4)(\text{AO}_3)$  ( $\text{A} = \text{S}^{4+}$ ,  $\text{Se}^{4+}$ , and  $\text{Te}^{4+}$ ). Note that the structure of  $\text{Zn}_2(\text{MoO}_4)(\text{SO}_3)$  is hypothetical.

Compound	Bond Angle ( $^\circ$ )	
$\text{Zn}_2(\text{MoO}_4)(\text{SO}_3)$	$\angle \text{O}(1)\text{--S--O}(2)$	103.5
	$\angle \text{O}(2)\text{--S--O}(4)$	94.2
	$\angle \text{O}(1)\text{--S--O}(4)$	106.5
	<b>Average</b>	<b>101.4(6.4)</b>
$\text{Zn}_2(\text{MoO}_4)(\text{SeO}_3)$	$\angle \text{O}(1)\text{--Se--O}(2)$	98.0(2)
	$\angle \text{O}(2)\text{--Se--O}(4)$	92.2(2)
	$\angle \text{O}(1)\text{--Se--O}(4)$	102.9(2)
	<b>Average</b>	<b>97.6(5.3)</b>
$\text{Zn}_2(\text{MoO}_4)(\text{TeO}_3)$	$\angle \text{O}(1)\text{--Te--O}(2)$	94.1(2)
	$\angle \text{O}(2)\text{--Te--O}(4)$	85.9(2)
	$\angle \text{O}(1)\text{--Te--O}(4)$	99.2(2)
	<b>Average</b>	<b>93.1(6.5)</b>

In order to gain insight how their lone-pair electrons are formed, the crystal orbital Hamilton population (–COHPs) were calculated for Se(Te–O) interactions utilizing the NAOPP method. In Figure 2.11, the –COHP curves for Se–O and Te–O interactions are similar overall, and reveal the anti-bonding character near the  $E_F$ . There is, however, a major difference. If the narrow band states in the –COHP and PDOS are examined more closely, that is, the bands near -10eV relative to  $E_F$ , we observe that for –COHP(narrow band) / PDOS(narrow band) the Te–O interactions are much weaker compared with the Se–O interactions. Their similar DOSs and –COHPs, specifically the anti-bonding character of Se(Te)–O near the  $E_F$  for both materials raises a relevant question, “Are the driving forces similar or different for the stereoactive lone-pair formation on  $\text{Se}^{4+}$  and  $\text{Te}^{4+}$  cations?” In other words, which mechanism - sp-mixing on the cations alone or sp-mixing on the cations with the oxygen orbitals, is favorable for stereoactive lone-pair formation with each cation? In order to address these issues, we thought it would be relevant to examine structural and electronic aspects of  $\text{SO}_3$ ,  $\text{SeO}_3$ , and  $\text{TeO}_3$  trigonal pyramids. The S–O bond distances of the hypothetical  $\text{Zn}_2(\text{MoO}_4)(\text{SO}_3)$  and the O–A–O bond angles for  $(\text{MoO}_4)(\text{SO}_3)$ ,  $\text{Zn}_2(\text{MoO}_4)(\text{SeO}_3)$ , and  $\text{Zn}_2(\text{MoO}_4)(\text{TeO}_3)$  are provided in the table 2.7 and 2.8. Thus, a hypothetical electronic band structure for  $\text{Zn}_2(\text{MoO}_4)(\text{SO}_3)$  was obtained with its optimized structure (see Computational Details and Figure 2.12). As anticipated, the TDOS and PDOSs for  $\text{Zn}_2(\text{MoO}_4)(\text{SO}_3)$  are very similar to  $\text{Zn}_2(\text{MoO}_4)(\text{SeO}_3)$  and  $\text{Zn}_2(\text{MoO}_4)(\text{TeO}_3)$ . In spite of the similarity, there are differences in the electronic and structural aspects - the relative contribution of S-3s, Se-4s, and Te-5s in the PDOSs, the relative strength of S–O, Se–O and Te–O interactions in the narrow band in the –COHPs analyses, and a change in the O–A–O angle of the  $\text{AO}_3$  trigonal

pyramids, respectively. As seen in the PDOSs, the contributions of the s-orbital of the A cations *increase* from S to Se to Te, whereas the relative strengths of the A–O interactions *decrease* from S to Se to Te. These electronic differences indicate the s-orbital becomes localized going from S to Se to Te. This is consistent with earlier observations.<sup>78-82</sup> In fact, with the overall electronic aspects,  $\text{Zn}_2(\text{MoO}_4)(\text{SeO}_3)$  is much more similar to  $\text{Zn}_2(\text{MoO}_4)(\text{SO}_3)$  compared with  $\text{Zn}_2(\text{MoO}_4)(\text{TeO}_3)$ . Thus, sp-mixing of the A cations decrease from S and Se to Te. With the structural aspects, the O-A-O angles decrease from  $101.4^\circ$  to  $97.6(2)^\circ$  to  $93.1(2)^\circ$  for  $\text{A} = \text{S}^{4+}$ ,  $\text{Se}^{4+}$ , and  $\text{Te}^{4+}$ , respectively. This reduction in O-A-O angle indicates greater localization of the A-s orbital and strength of the A-O interaction. Consequently, both electronic and structural aspects indicate that the formation of the stereoactive lone-pair is similar for the  $\text{S}^{4+}$  and  $\text{Se}^{4+}$  cations, but different compared with the  $\text{Te}^{4+}$  cation. The lone-pair formation on the  $\text{S}^{4+}$  and  $\text{Se}^{4+}$  cations are mainly attributable to the sp-mixing on the cations alone, whereas, for the  $\text{Te}^{4+}$  cation, the stereoactive lone-pair is attributable to cation sp-mixing through Te-O interactions.<sup>82</sup> Despite the different origins for the lone-pair formation, the antibonding character of A–O bonds appears near the  $E_F$ , as a result of the relatively lower energy levels of Se-4s(Te-5s) than that of O-2p with the valence state of  $\text{Se}(4s^2 4p^0)(\text{Te}(5s^2 5p^0))$ .

To better examine and understand the lone-pair characteristics on the  $\text{Se}^{4+}$  and  $\text{Te}^{4+}$  cations, electron localization function (ELF) calculations were performed using the PWPP method. Figure 2.1 shows the ELF isosurface for  $\eta = 0.9$  where, as anticipated, a lobe-like isosurface is observed near the  $\text{A}^{4+}$  cation. This isosurface may be considered as a stereoactive lone-pair.

## 2.5 Conclusion

Two new isostructural polar oxide materials,  $\text{Zn}_2(\text{MoO}_4)(\text{SeO}_3)$  and  $\text{Zn}_2(\text{MoO}_4)(\text{TeO}_3)$ , have been synthesized and characterized. The materials exhibit three-dimensional crystal structures consisting of  $\text{ZnO}_4$ ,  $\text{ZnO}_6$ ,  $\text{MoO}_4$ , and  $\text{AO}_3$  ( $\text{A} = \text{Se}^{4+}$  or  $\text{Te}^{4+}$ ) polyhedra. The polarity of the materials may be structurally derived from the partial alignment of the NCS and polar  $\text{AO}_3$  polyhedra. Attributable to this partial alignment, Moderate SHG efficiencies of  $100 \times$  and  $80 \times \alpha\text{-SiO}_2$  for  $\text{Zn}_2(\text{MoO}_4)(\text{SeO}_3)$  and  $\text{Zn}_2(\text{MoO}_4)(\text{TeO}_3)$  respectively are observed. Although the materials exhibit macroscopic polarization, the materials are not ferroelectric as the polarization is not reversible.

## 2.6 References

1. Lang, S. B.; Das-Gupta, D. K. *Pyroelectricity: Fundamentals and Applications*; Academic Press: 2001; Vol. 4.
2. Lang, S. B. *Phys. Today* **2005**, 58, 31.
3. Ok, K. M.; Chi, E. O.; Halasyamani, P. S. *Chem. Soc. Rev.* **2006**, 35, 710.
4. Khomskii, D. I. *Physics* **2009**, 2, 20.
5. *International Tables for Crystallography, Vol. A, Space Group Symmetry*; Hahn, T., Ed.; Kluwer Academic: Dordrecht, Holland, 2006; Vol. A.
6. Lines, M. E.; Glass, A. M. *Principles and Applications of Ferroelectrics and Related Materials*; Oxford University Press: Oxford, 1991.
7. Heier, K. R.; Norquist, A. J.; Halasyamani, P. S.; Duarte, A.; Stern, C. L.; Poeppelmeier, K. R. *Inorg. Chem.* **1999**, 38, 762.
8. Welk, M. E.; Norquist, A. J.; Stern, C. L.; Poeppelmeier, K. R. *Inorg. Chem.* **2000**, 39, 3946.
9. Welk, M. E.; Norquist, A. J.; Stern, C. L.; Poeppelmeier, K. R. *Inorg. Chem.* **2001**, 40, 5479.
10. Welk, M. E.; Norquist, A. J.; Arnold, F. P.; Stern, C. L.; Poeppelmeier, K. R. *Inorg. Chem.* **2002**, 41, 5119.
11. Do, J.; Kanatzidis, M. G. *J. Alloys Compd.* **2004**, 381, 41.

12. Izumi, H. K.; Kirsch, J. E.; Stern, C. L.; Poeppelmeier, K. R. *Inorg. Chem.* **2005**, *44*, 884.
13. Kong, F.; Huang, S.-P.; Sun, Z.-M.; Mao, J.-G.; Cheng, W.-D. *J. Am. Chem. Soc.* **2006**, *128*, 7750.
14. Jiang, H.-L.; Xie, Z.; Mao, J.-G. *Inorg. Chem.* **2007**, *46*, 6495.
15. Marvel, M. R.; Lesage, J.; Baek, J.; Halasyamani, P. S.; Stern, C. L.; Poeppelmeier, K. R. *J. Am. Chem. Soc.* **2007**, *129*, 13963.
16. Banerjee, S.; Malliakas, C. D.; Jang, J. I.; Ketterson, J. B.; Kanatzidis, M. G. *J. Am. Chem. Soc.* **2008**, *130*, 12270.
17. Jiang, H.-L.; Huang, S.-P.; Fan, Y.; Mao, J.-G.; Cheng, W.-D. *Chem. Eur. J.* **2008**, *14*, 1972.
18. Chung, I.; Song, J.-H.; Jang, J. I.; Freeman, A. J.; Ketterson, J. B.; Kanatzidis, M. G. *J. Am. Chem. Soc.* **2009**, *131*, 2647.
19. Hu, T.; Qin, L.; Kong, F.; Zhou, Y.; Mao, J.-G. *Inorg. Chem.* **2009**, *48*, 2193.
20. Sun, C.-F.; Hu, C.-L.; Xu, X.; Ling, J.-B.; Hu, T.; Kong, F.; Long, X.-F.; Mao, J.-G. *J. Am. Chem. Soc.* **2009**, *131*, 9486.
21. Zhang, S.-Y.; Jiang, H.-L.; Sun, C.-F.; Mao, J.-G. *Inorg. Chem.* **2009**, *48*, 11809.
22. Bera, T. K.; Jang, J. I.; Song, J.-H.; Malliakas, C. D.; Freeman, A. J.; Ketterson, J. B.; Kanatzidis, M. G. *J. Am. Chem. Soc.* **2010**, *132*, 3484.

23. Chung, I.; Jang, J.-I.; Malliakas, C. D.; Ketterson, J. B.; Kanatzidis, M. G. *J. Am. Chem. Soc.* **2010**, *132*, 384.
24. Opik, U.; Pryce, M. H. L. *Proc. R. Soc. London, Ser. A* **1957**, 238, 425.
25. Bader, R. F. W. *Mol. Phys.* **1960**, *3*, 137.
26. Bader, R. F. W. *Can. J. Chem.* **1962**, *40*, 1164.
27. Pearson, R. G. *J. Am. Chem. Soc.* **1969**, *91*, 4947.
28. Pearson, R. G. *J. Mol. Struct.:THEOCHEM* **1983**, *103*, 25.
29. Wheeler, R. A.; Whangbo, M. H.; Hughbanks, T.; Hoffmann, R.; Burdett, J. K.; Albright, T. A. *J. Am. Chem. Soc.* **1986**, *108*, 2222.
30. Kunz, M.; Brown, I. D. *J. Solid State Chem.* **1995**, *115*, 395.
31. Goodenough, J. B. *Annu. Rev. Mater. Sci.* **1998**, *28*, 1.
32. Halasyamani, P. S.; Poeppelmeier, K. R. *Chem. Mater.* **1998**, *10*, 2753.
33. Marvel, M. R.; Pinlac, R. A. F.; Lesage, J.; Stern, C. L.; Poeppelmeier, K. R. *Z. Anorg. Allg. Chem.* **2009**, *635*, 869.
34. Goodey, J.; Broussard, J.; Halasyamani, P. S. *Chem. Mater.* **2002**, *14*, 3174.
35. Ra, H.-S.; Ok, K. M.; Halasyamani, P. S. *J. Am. Chem. Soc.* **2003**, *125*, 7764.
36. Ok, K. M.; Halasyamani, P. S. *Angew. Chem., Int. Ed.* **2004**, *43*, 5489.
37. Chi, E. O.; Ok, K. M.; Porter, Y.; Halasyamani, P. S. *Chem. Mater.* **2006**, *18*, 2070.



38. Sivakumar, T.; Ok, K. M.; Halasyamani, P. S. *Inorg. Chem.* **2006**, *45*, 3602.
39. Kim, J.-H.; Baek, J.; Halasyamani, P. S. *Chem. Mater.* **2007**, *19*, 5637.
40. Chang, H. Y.; Sivakumar, T.; Ok, K. M.; Halasyamani, P. S. *Inorg. Chem.* **2008**, *47*, 8511.
41. Kim, Y.; Seo, I.-s.; Martin, S. W.; Baek, J.; Halasyamani, P. S.; Arumugam, N.; Steinfink, H. *Chem. Mater.* **2008**, *20*, 6048.
42. Chang, H. Y.; Kim, S.-H.; Ok, K. M.; Halasyamani, P. S. *Chem. Mater.* **2009**, *21*, 1654.
43. Chang, H.-Y.; Kim, S.-H.; Halasyamani, P. S.; Ok, K. M. *J. Am. Chem. Soc.* **2009**, *131*, 2426.
44. Chang, H.-Y.; Kim, S.-H.; Ok, K. M.; Halasyamani, P. S. *J. Am. Chem. Soc.* **2009**, *131*, 6865.
45. Kim, S.-H.; Yeon, J.; Halasyamani, P. S. *Chem. Mater.* **2009**, *21*, 5335.
46. Chang, H. Y.; Kim, S. W.; Halasyamani, P. S. *Chem. Mater.* **2010**, *22*, 3241.
47. *SAINT, Program for Area Detector Absorption Correction, version 4.05*; Siemens Analytical X-ray Systems, Inc.: Madison, WI, 1995.
48. North, A. C. T.; Phillips, D. C.; Mathews, F. S. *Acta Crystallogr.* **1968**, *24*, 351.
49. Sheldrick, G. M. *SHELXL-97 - A Program for Crystal Structure Refinement.*; University of Goettingen: Goettingen, 1997.

50. Sheldrick, G. M. *SHELXS-97 - A Program for Automatic Solution of Crystal Structures.*; University of Goettingen: Goettingen, Germany, 1997.
51. Farrugia, L. J. *J. Appl. Crystallogr.* **1999**, *32*, 837.
52. Spek, A. L. *PLATON*; Utrecht University: Utrecht, The Netherlands, 2001.
53. Flack, H. *Acta Crystallogr.* **1983**, *39*, 876.
54. Kubelka, P.; Munk, F. Z. *Tech. Phys.* **1931**, *12*, 593.
55. Tauc, J. *Mater. Res. Bull.* **1970**, *5*, 721.
56. Kurtz, S. K.; Perry, T. T. *J. Appl. Phys.* **1968**, *39*, 3798.
57. Hohenberg, P.; Kohn, W. *Phys. Rev.* **1964**, *136*, B864.
58. Kohn, W.; Sham, L. J. *Phys. Rev.* **1965**, *140*, A1133.
59. Junquera, J.; Paz, O.; Sanchez-Portal, D.; Artacho, E. *Phys. Rev. B: Condens. Matter* **2001**, *64*, 235111/1.
60. Ordejon, P.; Artachio, E.; Soler, J. M. *Phys. Rev. B: Condens. Matter* **1996**, *53*, R10441.
61. Torres, J. A.; Artacho, E.; Cela, J. M.; Gale, J.; García, A.; Junquera, J.; Martin, R. M.; Ordejón, P.; Sánchez, D.; Soler, J. M. *SIESTA-3.0-rc2*; [www.icmab.es/siesta/](http://www.icmab.es/siesta/):2010.
62. Giannozzi, P. *J. Phys: Condens. Matter* **2009**, *21*, 395502.
63. Troullier, N.; Martins, J. L. *Phys. Rev. B: Condens. Matter* **1991**, *43*, 1993.

64. Perdew, J. P.; Burke, K.; Ernzerhof, M. *Phys. Rev. Lett.* **1996**, *77*, 3865.
65. Monkhorst, H. J.; Pack, J. D. *Phys. Rev. B* **1976**, *13*, 5188.
66. Dronskowski, R.; Bloechl, P. E. *J. Phys. Chem.* **1993**, *97*, 8617.
67. Becke, A. D.; Edgecombe, K. E. *J. Chem. Phys.* **1990**, *92*, 5397.
68. Silvi, B.; Savin, A. *Nature* **1994**, *371*, 683.
69. <http://www.fhi-berlin.mpg.de/th/fhi98md/fhi98PP/>: 2004.
70. Momma, K.; Izumi, F. *J. Appl. Crystallogr.* **2008**, *41*, 653.
71. Ok, K. M.; Halasyamani, P. S. *Chem. Mater.* **2001**, *13*, 4278.
72. Shen, Y.-L.; Jiang, H.-L.; Xu, J.; Mao, J.-G.; Cheah, K. W. *Inorg. Chem.* **2005**, *44*, 9314.
73. Kong, F.; Xu, X.; Mao, J.-G. *Inorg. Chem.* **2010**, *49*, 11573.
74. Cotton, F. A.; Wilkinson, G.; Murillo, C.; Bochmann, M. *Advanced Inorganic Chemistry*; 6th ed. John Wiley & Sons, Inc: New York, 1999.
75. Yeon, J.; Kim, S.-H.; Halasyamani, P. S. *Inorg. Chem.* **2010**, *49*, 6986.
76. Scott, J. F. *J. Phys.: Condens. Matter* **2008**, *20*, 021001.
77. Cohen, R. E. *Nature* **1992**, *358*, 136.
78. Eng, H. W.; Barnes, P. W.; Auer, B. M.; Woodward, P. M. *J. Solid State Chem.* **2003**, *175*, 94.

79. Mizoguchi, H.; Eng, H. W.; Woodward, P. M. *Inorg. Chem.* **2004**, *43*, 1667.
80. Mizoguchi, H.; Woodward, P. M. *Chem. Mater.* **2004**, *16*, 5233.
81. Payne, D. J.; Egde, R. G.; Walsh, A.; Watson, G. W.; Guo, J.; Glans, P. A.; Learmonth, T.; Smith, K. E. *Phys. Rev. Lett.* **2006**, *96*, 157403.
82. Kim, M. K.; Kim, S.-H.; Chang, H.-Y.; Halasyamani, P. S.; Ok, K. M. *Inorg. Chem.* **2010**, *49*, 7028.

## CHAPTER 3. BiO(IO<sub>3</sub>): A New Polar Iodate that Exhibits an Aurivillius-type (Bi<sub>2</sub>O<sub>2</sub>)<sup>2+</sup> Layer and a Large SHG Response

### 3.1 Abstract

A new noncentrosymmetric (NCS) and polar material containing two lone-pair cations, Bi<sup>3+</sup> and I<sup>5+</sup>, and exhibiting an Aurivillius-type (Bi<sub>2</sub>O<sub>2</sub>)<sup>2+</sup> layer has been synthesized and structurally characterized. The material, BiO(IO<sub>3</sub>), exhibits strong second-harmonic generation (SHG), ~ 12.5 x KDP (or ~ 500 x α-SiO<sub>2</sub>), using 1064 nm radiation, and is found in the NCS polar orthorhombic space group *Pca2<sub>1</sub>* (No. 29). The structure consists of (Bi<sub>2</sub>O<sub>2</sub>)<sup>2+</sup> cationic layers that are connected to (IO<sub>3</sub>)<sup>-</sup> anions. The macroscopic polarity, observed along the c-axis direction, may be attributed to the alignment of the IO<sub>3</sub> polyhedra. In addition to the crystal structure and SHG measurements, polarization and piezoelectric measurements were performed, as well as the electronic structure analysis.

### 3.2 Introduction

The synthesis and characterization of new functional materials, e.g., nonlinear optical materials, piezoelectric/pyroelectric materials, multiferroics, are of topical and technological interest.<sup>1-3</sup> This is clearly the situation with polar compounds, i.e., materials that exhibit a macroscopic dipole moment. Functional properties such as pyroelectricity, ferroelectricity, and multiferroic behavior are restricted to polar materials. Although the crystallographic symmetry requirements for polarity have been extensively discussed,<sup>4</sup> it remains an ongoing challenge to synthesize new polar compounds. A variety of strategies

have been suggested towards the design and synthesis of new polar oxide materials.<sup>5-22</sup> We have focused on synthesizing new oxide materials<sup>23-36</sup> that contain cations susceptible to second-order Jahn-Teller (SOJT) distortions,<sup>37-44</sup> i.e., octahedrally coordinated  $d^0$  cations ( $\text{Ti}^{4+}$ ,  $\text{Nb}^{5+}$ ,  $\text{W}^{6+}$ , etc.) and cations with a non-bonded electron pair ( $\text{Se}^{4+}$ ,  $\text{Te}^{4+}$ ,  $\text{I}^{5+}$ , etc.). With both families, the cation is in a locally polar coordination environment. When the local polar environments are aligned in the crystal structure, a macroscopically polar material is observed.

A class of materials that has not been explored extensively is oxides that contain two lone-pair cations. Relatively few of these types of materials are known, and many of these such as  $\text{TeSeO}_4$ ,<sup>45,46</sup>  $\text{Pb}_3\text{SeO}_5$ ,<sup>33</sup>  $\text{Ln}_3\text{Pb}_3(\text{IO}_3)_{13}$  ( $\mu^3\text{-O}$ ) ( $\text{Ln} = \text{La} - \text{Nd}$ ),<sup>47</sup>  $\text{Bi}_2\text{SeO}_5$ ,<sup>48,49</sup>  $\text{Bi}(\text{SeO}_3)\text{Cl}$ ,<sup>50</sup> and  $\text{Bi}_2\text{TeO}_5$ <sup>51</sup> are noncentrosymmetric. Interestingly, all of the aforementioned NCS materials are also polar. A lone-pair cation that has received considerable interest is  $\text{I}^{5+}$ . A variety of asymmetric coordination environments are found with  $\text{I}^{5+}$ , such as  $\text{IO}_3$ ,  $\text{IO}_4$ , and  $\text{IO}_5$ .<sup>25,52-58</sup> Of these, the first is the most common. With respect to bismuth(III) iodates, two materials have been reported,  $\text{Bi}(\text{IO}_3)_3$  (space group  $P-1$ ) and  $\text{Bi}(\text{IO}_3)_3 \cdot 2\text{H}_2\text{O}$  (space group  $P2_1/n$ ).<sup>59,60</sup> As seen from the respective space groups, both compounds are centrosymmetric.  $\text{Bi}^{3+}$  cations are also found in Aurivillius phases,<sup>61-63</sup> many of which are polar. The Aurivillius structure is built up from alternate layers of  $(\text{Bi}_2\text{O}_2)^{2+}$  cations and perovskite-like  $(\text{A}_{m-1}\text{B}_m\text{O}_{3m+1})^{2-}$  anionic blocks, with  $m$  being an integer corresponding to the number of corner-shared octahedra forming the perovskite blocks. The macroscopic polarity observed in some Aurivillius phases is attributable structurally to the  $(\text{Bi}_2\text{O}_2)^{2+}$  layer, as well as the perovskite block. In this chapter, we report on a new polar material,  $\text{BiO}(\text{IO}_3)$ , that not only contains two lone-pair

cations,  $\text{Bi}^{3+}$  and  $\text{I}^{5+}$ , but also exhibits an Aurivillius type  $(\text{Bi}_2\text{O}_2)^{2+}$  layer. Instead of a perovskite-like block between the  $(\text{Bi}_2\text{O}_2)^{2+}$  layer, polar  $\text{IO}_3$  polyhedra are observed.

### 3.3 Experimental details

#### 3.3.1 Synthesis

$\text{Bi}(\text{NO}_3)_3 \cdot 5\text{H}_2\text{O}$  (Mallinckrodt, Analytical reagent),  $\text{HNO}_3$  (Mallinckrodt, ~68%), and  $\text{HIO}_3$  (Alfa Aesar, 99.5%) were used as received. A 1M  $\text{HNO}_3$  solution was obtained by diluting 10 mL of  $\text{HNO}_3$  (~68%) in 100 mL of water. Crystals and polycrystalline powder of  $\text{BiO}(\text{IO}_3)$  were synthesized by hydrothermal methods. 0.485 g (1.00 mmol) of  $\text{Bi}(\text{NO}_3)_3 \cdot 5\text{H}_2\text{O}$ , 0.176 g (1.00 mmol) of  $\text{HIO}_3$ , and 3 mL of 1M  $\text{HNO}_3$  were placed in a 23-mL Teflon-lined autoclave. The autoclave was closed, heated to 200 °C, held for 1 week, and cooled slowly to room temperature at a rate 6 °C  $\text{h}^{-1}$ . The product was recovered by filtration and washed with distilled water. The product, yellow thin plate-shaped crystals and white polycrystalline powder, were recovered in near quantitative yield based on  $\text{Bi}(\text{NO}_3)_3 \cdot 5\text{H}_2\text{O}$ . The powder X-ray diffraction patterns of the crystals and the white powder were identical to the calculated powder X-ray diffraction pattern which is generated from the single crystal X-ray diffraction data of  $\text{BiO}(\text{IO}_3)$ , indicating they were the same phase.

### 3.3.2 Characterization

#### Single Crystal X-ray Diffraction

A yellow thin plate-shaped crystal ( $0.06 \times 0.05 \times 0.01 \text{ mm}^3$ ) was used for single-crystal X-ray diffraction data collection. Data were collected using a Siemens SMART APEX diffractometer equipped with a 1K CCD area detector using graphite-monochromated Mo K $\alpha$  radiation. A hemisphere of data was collected using a narrow-frame method with scan widths of  $0.30^\circ$  in  $\omega$  and an exposure time of 35 s per frame. The first 50 frames were remeasured at the end of the data collection to monitor instrument and crystal stability. The data were integrated using the Siemens SAINT program,<sup>64</sup> with the intensities corrected for Lorentz, polarization, air absorption, and absorption attributable to the variation in the path length through the detector face plate. Psi-scans were used for the absorption correction on the hemisphere of data.<sup>65</sup> The data were solved and refined using SHELXS-97 and SHELXL-97, respectively.<sup>66,67</sup> All of the atoms were refined with anisotropic thermal parameters, and the refinement converged for  $I > 2\sigma(I)$ . All calculations were performed using the WinGX-98 crystallographic software package.<sup>68</sup> The structure was checked for missing symmetry elements using PLATON.<sup>69</sup> The Flack parameter<sup>70</sup> was refined to 0.002(5). Tables 3.1, 3.2, and 3.3 show the crystallographic data, atomic coordination, and bond distances for BiO(IO<sub>3</sub>), respectively.



**Table 3.1** Crystallographic data for BiO(IO<sub>3</sub>).

BiO(IO <sub>3</sub> )			
fw (g/mol)	399.88	$\rho_{\text{calcd}}$ (g/cm <sup>3</sup> )	7.399
T(K)	296.0(2)	$\mu$ (mm <sup>-1</sup> )	57.560
$\lambda$ (Å)	0.71073	$2\theta_{\text{max}}$ (deg)	57.60
Crystal system	Orthorhombic	$R$ (int)	0.0404
Space group	$Pca2_1$ (No.29)	Reflections collected/unique	1956/859
$a$ (Å)	5.6584(4)	Parameters	56
$b$ (Å)	11.0386(8)	GOF ( $F^2$ )	1.110
$c$ (Å)	5.7476(4)	$R$ ( $F$ ) <sup>a</sup>	0.0193
$V$ (Å <sup>3</sup> )	359.00 (4)	$R_w(F_o^2)$ <sup>b</sup>	0.0483
$Z$	4	Flack param.	0.002(5)

$$^a R(F) = \Sigma ||F_o| - |F_c|| / \Sigma |F_o|. \quad ^b R_w(F_o^2) = [\Sigma w(F_o^2 - F_c^2)^2 / \Sigma w(F_o^2)^2]^{1/2}$$

**Table 3.2** Atomic coordinates and equivalent isotropic displacement parameters (Å<sup>2</sup>) for BiO(IO<sub>3</sub>).

Atoms	x	y	z	U(eq)
Bi(1)	0.0209(1)	0.1104(1)	0.6971(1)	0.013(1)
I(1)	0.4977(1)	0.3671(1)	0.6726(2)	0.011(1)
O(1)	0.2664(11)	0.0032(3)	0.9250(8)	0.012(1)
O(2)	0.3794(8)	0.2196(4)	0.5772(7)	0.016(1)
O(3)	0.6520(8)	0.2979(4)	0.9150(7)	0.021(1)
O(4)	0.2474(8)	0.4328(4)	0.8247(7)	0.018(1)

U(eq) is defined as one third of the trace of the orthogonalized U<sub>ij</sub> tensor

**Table 3.3** Selected bond distances (Å) for BiO(IO<sub>3</sub>).

Bonds	Distances	Bonds	Distances
Bi–O(1)	2.246(6)	I–O(2)	1.844(4)
Bi–O(1)#1	2.301(5)	I–O(3)	1.813(4)
Bi–O(1)#2	2.316(5)	I–O(4)	1.816(4)
Bi–O(1)#4	2.581(5)		
Bi–O(2)	2.458(4)		
Bi–O(2)#3	2.558(4)		

Symmetry transformations used to generate equivalent atoms:

#1 -x+1/2,y,z-1/2 #2 x-1/2,-y,z #3 -x+1/2,y,z+1/2 #4 -x,-y,z-1/2

### **Powder X-ray Diffraction**

The PXRD data were collected using a PANalytical X’PertPRO diffractometer at room temperature (Cu  $K\alpha$  radiation, flat plate) equipped with X’Celerator detector. Data were collected in the  $2\theta$  range of 5 – 70° with a step size of 0.008° and a step time of 0.3s.

### **Infrared Spectroscopy**

Infrared (IR) spectra were recorded on a Matteson FTIR 5000 spectrometer in the spectral range of 400 – 4000 cm<sup>-1</sup> at room temperature. The sample (2 mg) was finely ground with dry KBr (100 mg). This powder mixture was then transferred to a stainless steel IR holder and pressed to a semi-transparent pellet (~0.2 mm thick).

### **UV–vis Diffuse Reflectance Spectroscopy**

UV–vis diffuse reflectance spectra were collected with a Varian Cary 500 scan UV–vis–NIR spectrophotometer over the spectral range of 200–2000 nm at room

temperature. Polytetrafluoroethylene (PTFE) was used as a standard material for baseline correction. The sample was thoroughly mixed with PTFE and this mixture was used for UV–vis measurements. Reflectance spectra were converted to absorbance based on the Kubelka–Munk equation.<sup>71,72</sup>

### **Thermal Analysis**

Thermogravimetric and differential thermal analyses were simultaneously carried out on an EXSTAR6000 TG/DTA 6300 Thermogravimetric/Differential Thermal Analysis system (SII NanoTechnology Inc.). The sample (~20 mg) was placed in a platinum crucible that was heated (cooled) at a rate of 10 °C/min in the range of 25–700 °C for BiO(IO<sub>3</sub>) under flowing nitrogen gas. A platinum crucible containing 20 mg of Al<sub>2</sub>O<sub>3</sub> was used as the reference during the measurements.

### **Second-harmonic Generation**

Powder SHG measurements were performed at room temperature on a modified Kurtz-NLO system,<sup>73</sup> using a pulsed Nd:YAG laser with a wavelength of 1064 nm. The methodology and instrumentation details have been published.<sup>2</sup> The SHG efficiency has been shown to be particle size dependent.<sup>73</sup> Thus, the polycrystalline samples were ground and sieved into distinct particle size ranges (20–45, 45–63, 63–75, 75–90, and 90–120 μm). In order to evaluate relative SHG efficiencies of the measured samples with known SHG materials and calculate their average non-linear optical (NLO) susceptibilities,  $\langle d_{eff} \rangle_{exp}$ , and crystalline  $\alpha$ -SiO<sub>2</sub> was also ground and sieved into the same particle size ranges. No index matching fluid was used in the experiment.

## **Piezoelectric Measurements**

Converse piezoelectric measurements were performed at room temperature using a Radiant Technologies RT66A piezoelectric test system with a TREK (609E-6) high voltage amplifier, Precision Materials Analyzer, Precision High Voltage Interface, and MTI 2000 Fotonic Sensor.  $\text{BiO}(\text{IO}_3)$  sample was pressed in a pellet (~10 mm diameter and ~0.8 mm thick). The pellet was sintered at 300 °C for 1 week. Silver paste was applied to both sides of the sintered pellet as electrodes, and the pellet was cured at 200 °C for 2 weeks, at 250 °C for 1 day, and finally at 300 °C for 2 hours in air. A voltage of 900 V at 50 Hz was applied and the piezoelectric data were obtained by averaging of 10 measurements. These pellets were also used in polarization measurements.

## **Polarization Measurements**

The polarization measurements were done on a Radiant Technologies Model RT66A ferroelectric test system with a TREK high-voltage amplifier in the temperature range of 25–185 °C in a Delta Model 9023 environmental test chamber. The unclamped pyroelectric coefficient, defined as  $dP/dT$ , was determined by measuring the polarization as a function of temperature. The methodology and instrumentation details have been published.<sup>2</sup> The pellet used for piezoelectric measurements is also used for polarization measurements. To measure the potential ferroelectric behavior, frequency-dependent polarization measurements were done at room temperature under static electric field of 6-11 kV/cm between 50-200 Hz. For the pyroelectric measurements, the polarization was measured statically from room temperature to 190 °C in various increments with an

electric field of 11 kV/cm and at 50 Hz. The temperature was allowed to stabilize before the polarization was measured.

### **Computational Details**

First-principle density functional theory (DFT)<sup>74,75</sup> electronic structure calculations for BiO(IO<sub>3</sub>) were carried out using numerical atomic orbitals (NAO)<sup>76</sup> and plane wave (PW) pseudopotential(PP) methods as implemented in SIESTA (3.0-rc2 version)<sup>77,78</sup> and Quantum ESPRESSO (4.1.2 version) packages,<sup>79</sup> respectively. For the NAOPP calculations in SIESTA, norm-conserving Martins-Troullier (MT)<sup>80</sup> pseudopotentials for all the elements were used with the generalized gradient approximation (GGA)<sup>81</sup> for exchange-correlation corrections. A split-valence double- $\zeta$  basis set was used for all atoms where polarization orbitals were included as obtained with an energy shift of 0.1 eV. The energy cutoff of the real space integration mesh was 300 Rydberg (Ry). A  $10 \times 8 \times 6$  Monkhorst–Pack (MP)<sup>82</sup> k-mesh was used for sampling the Brillouin zone. A self-consistency was achieved within the total energy change less than  $10^{-6}$  Ry. The experimental crystal structures were adapted for all calculations. Crystal orbital Hamilton population (COHP)<sup>83</sup> calculations were also performed using the NAOPP method after the total energy was self-consistently achieved.

Electron localization function (ELF)<sup>84,85</sup> calculations were performed using the PWPP method. Norm-conserving MT pseudopotentials for all the elements were used with the GGA for exchange-correlation corrections. The pseudopotentials generated from the Fritz Haber Institute (FHI) code were converted for the calculations.<sup>86</sup> A plane wave energy cutoff was set to 37 Ry. The Brillouin zone was sampled using a  $10 \times 8 \times 6$  MP k-mesh.

A total energy convergence threshold was set to  $10^{-6}$  Ry indicated self-consistency. The experimental crystal structures were employed for all calculations. For all of the structural figures and electronic structure results, the program VESTA was used.<sup>87</sup>

### 3.4 Results and discussion

#### Structures

BiO(IO<sub>3</sub>) crystallizes in the polar NCS space group  $Pca2_1$  (No. 29), and exhibits a layered structural topology (see Figure 3.1a). The structure may be described as containing layers of (Bi<sub>2</sub>O<sub>2</sub>)<sup>2+</sup> cations that are connected to (IO<sub>3</sub>)<sup>-</sup> anions. The (Bi<sub>2</sub>O<sub>2</sub>)<sup>2+</sup> cationic layer is structurally analogous to those observed in Aurivillius phases (see Figure 3.1b), however, instead of a perovskite-like anion block separating the layers, locally polar iodate anions are observed. The Bi<sup>3+</sup> cations are coordinated to six oxygen atoms with the Bi-O bond distances in the range of 2.246(6) – 2.581(3) Å and the I<sup>5+</sup> cations are coordinated to three oxygen atoms with the I-O bond distances in the range of 1.813(4) – 1.844(4) Å. Bond valence calculations resulted in values of 2.86 and 4.87 vu for Bi<sup>3+</sup> and I<sup>5+</sup>, respectively. In connectivity term, the structure can be written as [(BiO<sub>2/3</sub>O<sub>4/4</sub>)<sup>-1/3</sup>(IO<sub>2/1</sub>O<sub>1/3</sub>)<sup>+1/3</sup>]<sup>0</sup>. Both the Bi<sup>3+</sup> and I<sup>5+</sup> cations are in asymmetric and polar coordination environments attributable to their stereoactive lone-pairs. The occurrence and alignment of the lone-pair profoundly impacts the functional properties of BiO(IO<sub>3</sub>). As seen in Figure 3.2, the polarization attributable to the BiO<sub>6</sub> polyhedra is negligible – the local dipole moments are directed nearly in an anti-parallel manner. With the IO<sub>3</sub> polyhedra, however, the local dipole moment is additive and results in a macroscopic polarization

along the c-axis direction. As we will demonstrate, it is the alignment of the  $I^{5+}$  lone-pair that results in the strong SHG response.

**Table 3.4** Bond valence sum (BVS), bond strain index (BSI), global instability index (GII), unit cell dipole moment ( $\mu$ ), SHG efficiencies ( $\times \alpha\text{-SiO}_2$ ), piezoelectric responses, ( $d_{33}$ ), pyroelectric coefficients ( $P_T$ ), and maximum polarization ( $P_m$ ) for  $\text{BiO}(\text{IO}_3)$ .

Compound	BVS <sup>a</sup>					Functional properties			
	$\text{Bi}^{3+}$	$\text{I}^{5+}$	BSI <sup>a</sup>	GII <sup>a</sup>	$\mu^b$	SHG	$d_{33}^c$	$P_T^d$	$P_m^f$
$\text{BiO}(\text{IO}_3)$	2.86	4.87	0.17	0.19	63.3	500	26	-0.26	0.034

<sup>a</sup>valence unit (vu), <sup>b</sup>Debye, <sup>c</sup>pm/V, <sup>d</sup>at 55 °C ( $\mu\text{C}/\text{m}^2\text{K}$ ), <sup>f</sup>at 100 Hz ( $\mu\text{C}/\text{cm}^2$ )

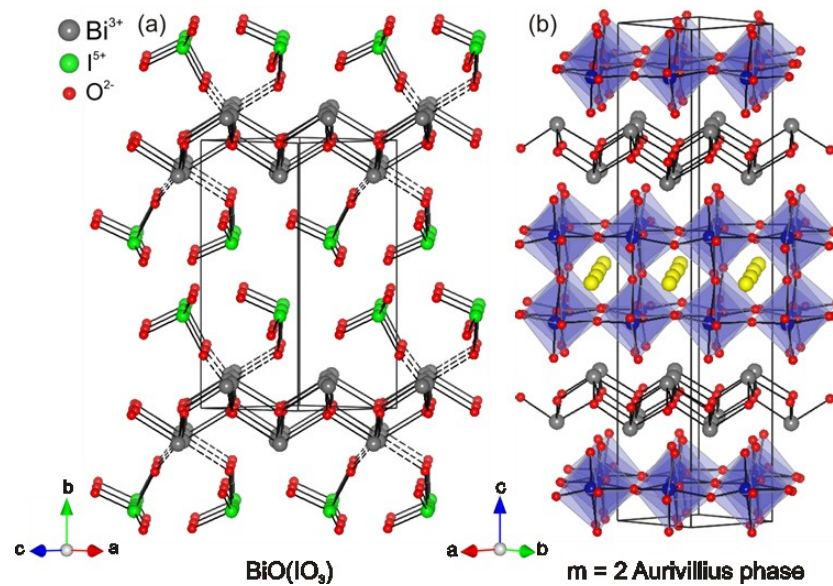


**Figure 3.1** (a) Ball-and-stick representation of  $\text{BiO}(\text{IO}_3)$  and (b) polyhedral representation of the Aurivillius phase ( $m = 2$ ). Note the similar  $(\text{Bi}_2\text{O}_2)^{2+}$  cationic layer in each material.

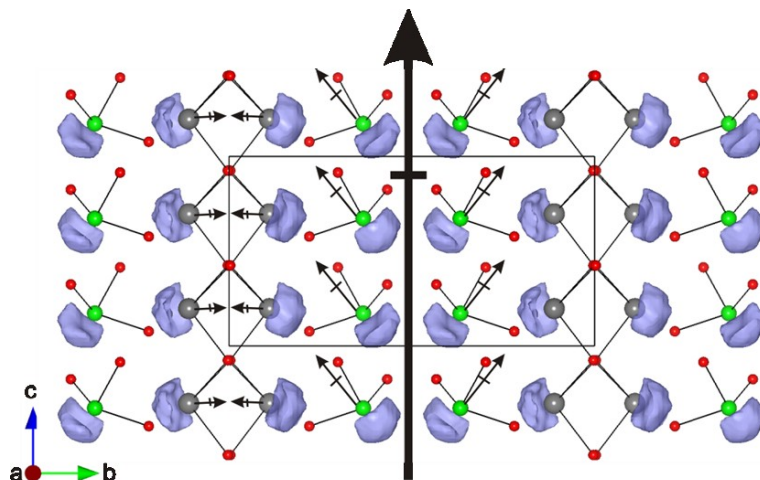


**Figure 3.2** Ball-and-stick representation of BiO(IO<sub>3</sub>) in the bc-plane. The partially parallel and anti-parallel alignments of the polarization attributable to the IO<sub>3</sub> and BiO<sub>6</sub> polyhedra respectively are shown. A net macroscopic polarization directed toward the c-axis is represented by the large black arrow. Note that the violet lobe-like isosurfaces ( $\eta = 0.9$ ) obtained from electron localization function calculation using Quantum Espresso were used to visualize stereo-active lone-pairs on the Bi<sup>3+</sup> and I<sup>5+</sup> cations.

### Infrared Spectroscopy

The infrared (IR) spectra for BiO(IO<sub>3</sub>) revealed absorption bands of I–O, Bi–O vibrations in the 400–1000 cm<sup>−1</sup> range. The I–O stretching vibrations were observed around 700–800 cm<sup>−1</sup>, whereas Bi–O stretching vibrations were seen at 400–550 cm<sup>−1</sup>. These assignments are in good agreement with the literature.<sup>32,88</sup> The IR vibrations and assignments are shown in Figure 3.3.



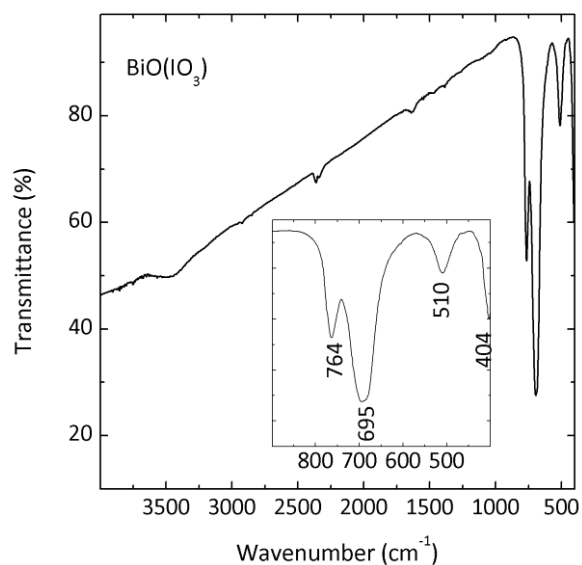


**Figure 3.3** IR data and assignments for BiO(IO<sub>3</sub>).

**Table 3.5** IR peak (cm<sup>-1</sup>) assignments for BiO(IO<sub>3</sub>).

$\nu(\text{I-O})$	$\nu(\text{Bi-O})$
764, 695	510, 404

### UV–vis Diffuse Reflectance Spectroscopy

Reflectance spectra of BiO(IO<sub>3</sub>) were converted to absorbance using the Kubelka–Munk function:<sup>71,72</sup>

$$F(R) = \frac{K}{S} = \frac{(1 - R)^2}{2R} \quad (3.1)$$

where  $R$ ,  $K$ , and  $S$  represent the reflectance, the absorption, and the scattering, respectively. In a  $F(R)$  versus  $E$  (eV) plot, extrapolating the linear part of the rising curve to zero provides the onset absorption of 3.3 eV for BiO(IO<sub>3</sub>).

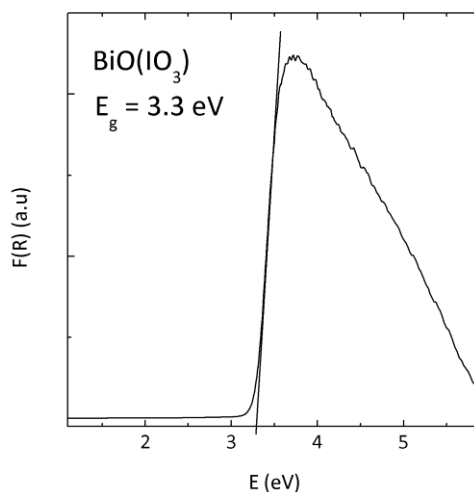


**Figure 3.4** UV–vis diffuse reflectance spectroscopy data for  $\text{BiO}(\text{IO}_3)$ .

### Thermal Analysis

The thermal stability of  $\text{BiO}(\text{IO}_3)$  was investigated through thermogravimetric and differential thermal analyses (TGA and DTA) (see Figure 3.5). As shown in Figure 3.5, the TGA curve showed a weight loss initiated above 400 °C and completed at 600 °C with a total weight loss of 41.0 %. The PXRD pattern of the residuals indicated thermal decomposition of  $\text{BiO}(\text{IO}_3)$  to  $\beta\text{-Bi}_2\text{O}_3$ .

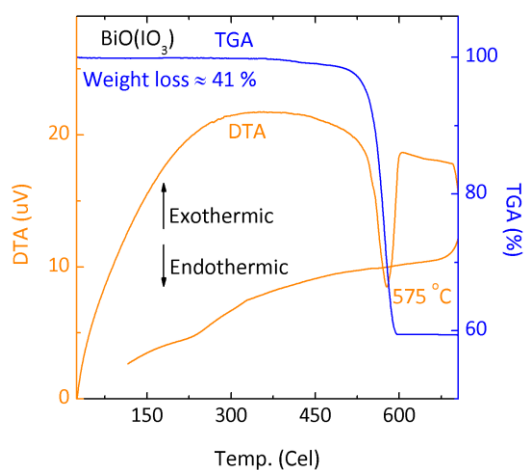


**Figure 3.5** Thermogravimetric and differential thermal analysis data for  $\text{BiO}(\text{IO}_3)$ .

## Second-harmonic Generation

Powder SHG measurements in the particle size range of 25–120  $\mu\text{m}$  indicated that  $\text{BiO}(\text{IO}_3)$  exhibits very large SHG efficiency. Its powder SHG efficiency was  $\sim 12.5 \times$  KDP or  $\sim 500 \times \alpha\text{-SiO}_2$  in the particle size range of 45–63  $\mu\text{m}$ . This efficiency compares well to  $\text{BaTiO}_3$  ( $400 \times \alpha\text{-SiO}_2$ ) and  $\text{LiNbO}_3$  ( $600 \times \alpha\text{-SiO}_2$ ). Particle size vs. SHG efficiency indicate that  $\text{BiO}(\text{IO}_3)$  is type 1 phase-matchable with a calculated  $\langle d_{\text{eff}} \rangle$  of  $\sim 26 \text{ pm/V}$  (see Figure 3.6). As with  $\text{Li}_2\text{Ti}(\text{IO}_3)_6$  and  $\text{Na}_2\text{Ti}(\text{IO}_3)_6$ ,<sup>31,32</sup> the alignment of the iodate lone-pair is, structurally, wholly responsible for the large SHG efficiency. In addition, the SHG efficiency of  $\text{BiO}(\text{IO}_3)$  is similar to  $\text{A}_2\text{Ti}(\text{IO}_3)_6$  ( $\text{A} = \text{Li}^+$  or  $\text{Na}^+$ ), i.e.,  $\langle d_{\text{eff}} \rangle$  of 23 – 26 pm/V.

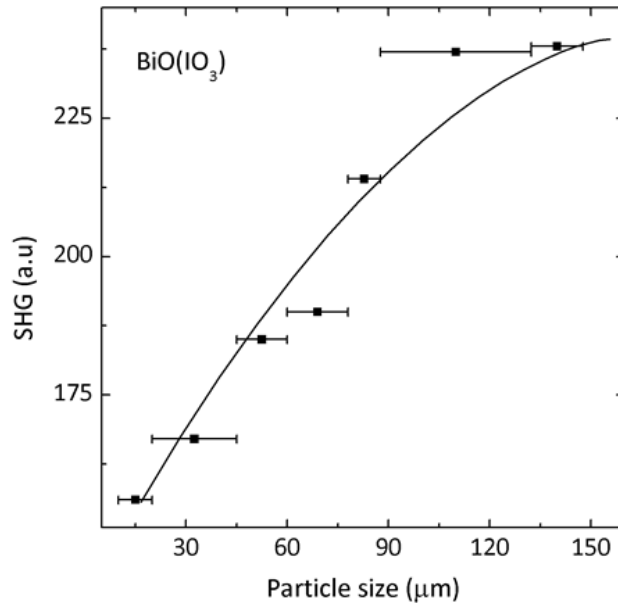


**Figure 3.6** Particle size vs. SHG intensity data for  $\text{BiO}(\text{IO}_3)$ . The curve is drawn to guide the eye and is not a fit to the data.

## Piezoelectric Measurements

Converse piezoelectric measurements were performed on  $\text{BiO}(\text{IO}_3)$  at room temperature. A voltage of 900 V at 50 Hz was applied and the piezoelectric data were obtained by averaging of 10 measurements. The  $d_{33}$  piezoelectric charge constant was estimated to be 26 pm/V (see Figure 3.7). This value compares well with those of other iodates, namely  $\text{LiIO}_3$  ( $d_{33} = 92$  pm/V) and  $\text{KIO}_3$  ( $d_{33} = 39$  pm/V), as well as  $\text{Li}_2\text{Ti}(\text{IO}_3)_6$  ( $d_{33} = 81$  pm/V).<sup>89,90</sup>

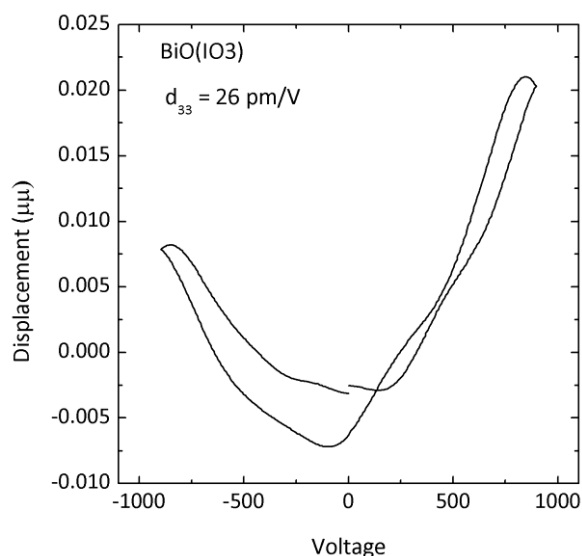


**Figure 3.7** Displacement vs. electric field plots for  $\text{BiO}(\text{IO}_3)$ .

## Polarization Measurements

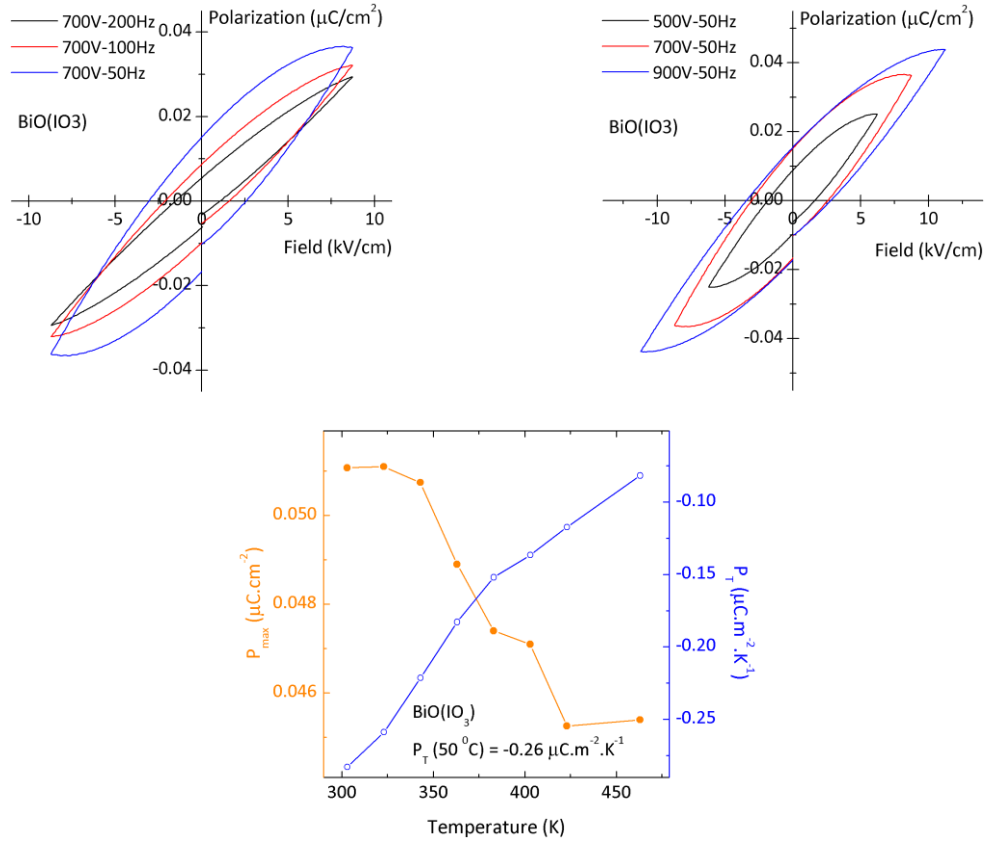
In addition to the SHG phenomenon and piezoelectricity, the polarization properties were also examined. As noted,  $\text{BiO}(\text{IO}_3)$  is polar and exhibits pyroelectric and possibly ferroelectric phenomena. Pyroelectric measurements revealed a pyroelectric coefficient of  $-0.26 \mu\text{C m}^{-2} \text{K}^{-1}$  at  $50^\circ\text{C}$ . Variable frequency ferroelectric measurements were also performed. ‘Hysteresis loops’ were observed, however  $\text{BiO}(\text{IO}_3)$  is not ferroelectric (see

Figure 3.8).<sup>91</sup> Ferroelectricity indicates macroscopic polarization reversal, which in turn implies microscopic (local) polarization reversibility. There are two oxide polyhedra that exhibit local polarity – the asymmetric  $\text{BiO}_6$  and  $\text{IO}_3$  polyhedra. With the  $\text{Bi}^{3+}$  oxide polyhedra, polarization reversal has been observed, for example in  $\text{BiFeO}_3$  as well as the  $m = 2$  Aurivillius phase  $\text{SrBi}_2\text{Ta}_2\text{O}_9$ .<sup>92-94</sup> With the  $\text{IO}_3$  group, we have demonstrated earlier that the energy barrier to inversion is  $\sim 8.5\text{eV}$ .<sup>32</sup> Comparison this value to those of well-known ferroelectrics such as  $\text{BaTiO}_3$  ( $\sim 1.8 \times 10^{-2}\text{eV}$ ) and  $\text{PbTiO}_3$  ( $2.0 \times 10^{-1}\text{eV}$ )<sup>95</sup> clearly demonstrates why  $\text{BiO}(\text{IO}_3)$  is not ferroelectric - polarization reversal for the  $\text{IO}_3$  polyhedra is energetically very unfavorable. It could be argued that the polarization with the  $\text{IO}_3$  remains frozen, whereas the dipole moment associated with the  $\text{BiO}_6$  polyhedra inverses. This is unlikely for two reasons. Firstly, recall that the polarization associated with the  $\text{BiO}_6$  groups is directed in an anti-parallel manner (see Figure 3.2). Any inversion in one polyhedron would be cancelled by its opposite neighbor. This type of ‘reversal’ has been described as an anti-polar ferroelectric.<sup>96</sup> Secondly, invoking an anti-polar ferroelectric mechanism would still require an anti-distortive displacement of the  $\text{Bi}^{3+}$  cations. That displacement coupled with the frozen polarization of the  $\text{IO}_3$  polyhedra would suggest any ferroelectric hysteresis loop would be displaced. As this is not observed, and anti-polar anti-distortive displacements are rather rare, we suggest that the data are consistent with  $\text{BiO}(\text{IO}_3)$  being a non-ferroelectric pyroelectric.

### Electronic Band Structures

The electronic band structures of  $\text{BiO}(\text{IO}_3)$  obtained from both methods are effectively identical. A total and projected density of states (DOS) calculated using the NAOPP

method is seen in Figure 3.9 where there is an energy gap of approximately 2.0 eV between valence and conduction bands. This is in agreement with the insulating nature of BiO(IO<sub>3</sub>). The Fermi level ( $E_F$ ) is set to 0 eV. There are three valence bands revealed in the  $\sim -13 - \sim -10$  eV,  $\sim -10 - \sim -7.5$  eV and  $\sim -7.5$  eV –  $E_F$  termed bottom, middle, and top valence bands, respectively. The projected DOS (PDOS) analysis (see Figure 3.10) reveals that the bottom band is mainly comprised of an almost equal amount of I-5s and O-2sp states and a small amount of Bi-6sp states.



**Figure 3.8** Frequency-dependent polarization loops (top), Polarization vs. electric field loops (middle), and Maximum polarization and pyroelectric coefficient versus temperature plot for BiO(IO<sub>3</sub>)

The middle band consists of mainly Bi-6s states with small amounts of I-5sp and O-2sp. The top band has two regions – lower ( $\sim -7.5$  –  $\sim -5.5$  eV) and upper ( $\sim -5.5$  eV –  $E_F$ ) bands. The lower band contains larger contributions from O-2sp and I-5p states with smaller contributions from Bi-6p states, whereas the upper band has significant contributions from O-2sp states with small contributions from I-5p and Bi-6p states. In particular, the top part of the upper band reveals weak contributions of I-5sp and Bi-6sp which are associated with a stereo-active lone pair formation on  $I^{5+}$  and  $Bi^{3+}$  cations. The bottom of Figure 3.10 exhibits the detailed PDOSs for each oxygen where an almost equal amount of O(2), O(3) and O(4) states are seen in the bottom band, as the  $I^{5+}$  cation is bonded to these oxygen atoms. Likewise, the O(1) state highly contributes to the middle band attributable to the Bi-O(1) bonds. The top band contains larger amounts of the states of all the oxygen atoms whose contribution in the upper band is mostly associated with their non-bonding characters in the electronic structure.

The bonding characters of the bands characterized by performing the crystal orbital Hamilton population (-COHP) calculations are also consistent with the PDOS analysis. The -COHP curves (Figure 3.11) for I-O and Bi-O interactions indicate that the bottom and middle bands contain antibonding and bonding characters of I-O and Bi-O bonds, respectively. Also, the -COHP curves reveal antibonding characters in the upper band which is well recognized in terms of the formation of their lone-pairs on each cation where the cation-anion covalent interactions are involved to mediate 5s-5p orbital mixing for  $I^{5+}$  (or 6s-6p orbital mixing for  $Bi^{3+}$ ), resulting in their lone pair formations.

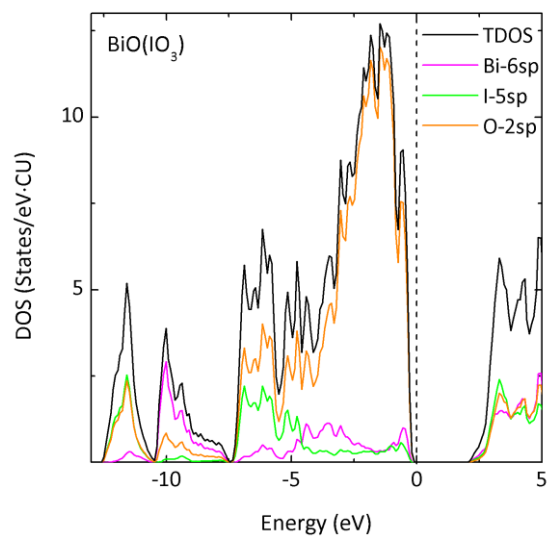


**Figure 3.9** Total and projected density of states plots for  $\text{BiO}(\text{IO}_3)$ . The dotted vertical line at 0 eV indicates  $E_F$ .

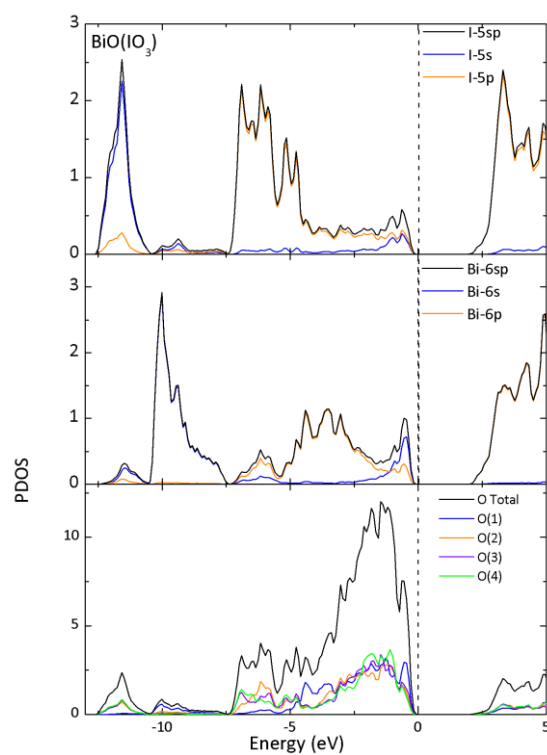


**Figure 3.10** The detailed PDOS plots for  $\text{BiO}(\text{IO}_3)$ . The dotted vertical line at 0 eV indicates  $E_F$ .



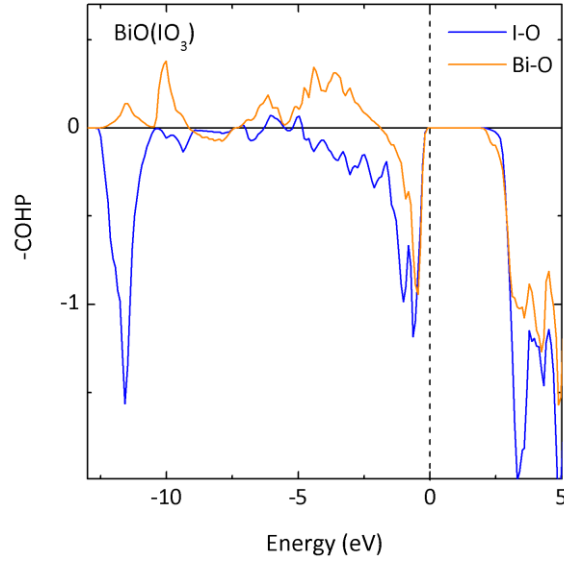


**Figure 3.11** –COHP plots for I–O, Bi–O orbital interaction for BiO(IO<sub>3</sub>). The dotted vertical line at 0 eV indicates  $E_F$ .

### 3.5 Conclusion

In summary, we have synthesized and characterized a new polar material, with a large SHG response  $\sim 12.5 \times$  KDP (or  $\sim 500 \times \alpha$ -SiO<sub>2</sub>), that contains two lone-pair cations and exhibits an Aurivillius type (Bi<sub>2</sub>O<sub>2</sub>)<sup>2+</sup> layer. The observed functional properties are attributable to the stereo-active lone-pair found on both the Bi<sup>3+</sup> and I<sup>5+</sup> cation. We are in the process of synthesizing other polar materials that contain two lone-pair cations and will be reporting on them in the near future.

### 3.6 References

1. Lang, S. B. *Phys. Today* **2005**, 58, 31.
2. Ok, K. M.; Chi, E. O.; Halasyamani, P. S. *Chem. Soc. Rev.* **2006**, 35, 710.
3. Khomskii, D. I. *Physics* **2009**, 2, 20.
4. *International Tables for Crystallography, Vol. A, Space Group Symmetry*; Hahn, T., Ed.; Kluwer Academic: Dordrecht, Holland, 2006; Vol. A.
5. Heier, K. R.; Norquist, A. J.; Halasyamani, P. S.; Duarte, A.; Stern, C. L.; Poeppelmeier, K. R. *Inorg. Chem.* **1999**, 38, 762.
6. Welk, M. E.; Norquist, A. J.; Stern, C. L.; Poeppelmeier, K. R. *Inorg. Chem.* **2000**, 39, 3946.
7. Welk, M. E.; Norquist, A. J.; Stern, C. L.; Poeppelmeier, K. R. *Inorg. Chem.* **2001**, 40, 5479.
8. Welk, M. E.; Norquist, A. J.; Arnold, F. P.; Stern, C. L.; Poeppelmeier, K. R. *Inorg. Chem.* **2002**, 41, 5119.
9. Izumi, H. K.; Kirsch, J. E.; Stern, C. L.; Poeppelmeier, K. R. *Inorg. Chem.* **2005**, 44, 884.
10. Kong, F.; Huang, S.-P.; Sun, Z.-M.; Mao, J.-G.; Cheng, W.-D. *J. Am. Chem. Soc.* **2006**, 128, 7750.

11. Marvel, M. R.; Lesage, J.; Baek, J.; Halasyamani, P. S.; Stern, C. L.; Poeppelmeier, K. R. *J. Am. Chem. Soc.* **2007**, *129*, 13963.
12. Banerjee, S.; Malliakas, C. D.; Jang, J. I.; Ketterson, J. B.; Kanatzidis, M. G. *J. Am. Chem. Soc.* **2008**, *130*, 12270.
13. Jiang, H.-L.; Huang, S.-P.; Fan, Y.; Mao, J.-G.; Cheng, W.-D. *Chem. Eur. J.* **2008**, *14*, 1972.
14. Chung, I.; Song, J.-H.; Jang, J. I.; Freeman, A. J.; Ketterson, J. B.; Kanatzidis, M. G. *J. Am. Chem. Soc.* **2009**, *131*, 2647.
15. Marvel, M. R.; Pinlac, R. A. F.; Lesage, J.; Stern, C. L.; Poeppelmeier, K. R. *Z. Anorg. Allg. Chem.* **2009**, *635*, 869.
16. Sun, C.-F.; Hu, C.-L.; Xu, X.; Ling, J.-B.; Hu, T.; Kong, F.; Long, X.-F.; Mao, J.-G. *J. Am. Chem. Soc.* **2009**, *131*, 9486.
17. Zhang, S.-Y.; Jiang, H.-L.; Sun, C.-F.; Mao, J.-G. *Inorg. Chem.* **2009**, *48*, 11809.
18. Bera, T. K.; Jang, J. I.; Song, J.-H.; Malliakas, C. D.; Freeman, A. J.; Ketterson, J. B.; Kanatzidis, M. G. *J. Am. Chem. Soc.* **2010**, *132*, 3484.
19. Chung, I.; Jang, J.-I.; Malliakas, C. D.; Ketterson, J. B.; Kanatzidis, M. G. *J. Am. Chem. Soc.* **2010**, *132*, 384.
20. Kong, F.; Xu, X.; Mao, J.-G. *Inorg. Chem.* **2010**, *49*, 11573.

21. Yang, B.-P.; Hu, C.-L.; Xu, X.; Sun, C.-F.; Zhang, J.-H.; Mao, J.-G. *Chem. Mater.* **2010**, *22*, 1545.
22. Sun, C.-F.; Hu, C.-L.; Xu, X.; Yang, B.-P.; Mao, J.-G. *J. Am. Chem. Soc.* **2011**, *133*, 5561.
23. Goodey, J.; Broussard, J.; Halasyamani, P. S. *Chem. Mater.* **2002**, *14*, 3174.
24. Ra, H.-S.; Ok, K. M.; Halasyamani, P. S. *J. Am. Chem. Soc.* **2003**, *125*, 7764.
25. Ok, K. M.; Halasyamani, P. S. *Angew. Chem., Int. Ed.* **2004**, *43*, 5489.
26. Chi, E. O.; Ok, K. M.; Porter, Y.; Halasyamani, P. S. *Chem. Mater.* **2006**, *18*, 2070.
27. Sivakumar, T.; Ok, K. M.; Halasyamani, P. S. *Inorg. Chem.* **2006**, *45*, 3602.
28. Kim, J.-H.; Baek, J.; Halasyamani, P. S. *Chem. Mater.* **2007**, *19*, 5637.
29. Chang, H. Y.; Sivakumar, T.; Ok, K. M.; Halasyamani, P. S. *Inorg. Chem.* **2008**, *47*, 8511.
30. Chang, H. Y.; Kim, S.-H.; Ok, K. M.; Halasyamani, P. S. *Chem. Mater.* **2009**, *21*, 1654.
31. Chang, H.-Y.; Kim, S.-H.; Halasyamani, P. S.; Ok, K. M. *J. Am. Chem. Soc.* **2009**, *131*, 2426.
32. Chang, H.-Y.; Kim, S.-H.; Ok, K. M.; Halasyamani, P. S. *J. Am. Chem. Soc.* **2009**, *131*, 6865.

33. Kim, S.-H.; Yeon, J.; Halasyamani, P. S. *Chem. Mater.* **2009**, *21*, 5335.
34. Chang, H. Y.; Kim, S. W.; Halasyamani, P. S. *Chem. Mater.* **2010**, *22*, 3241.
35. Yeon, J.; Kim, S.-H.; Halasyamani, P. S. *Inorg. Chem.* **2010**, *49*, 6986.
36. Zhang, W.; Li, F.; Kim, S.-H.; Halasyamani, P. S. *Cryst. Growth Des.* **2010**, *10*, 4091.
37. Opik, U.; Pryce, M. H. L. *Proc. R. Soc. London, Ser. A* **1957**, *238*, 425.
38. Bader, R. F. W. *Mol. Phys.* **1960**, *3*, 137.
39. Pearson, R. G. *J. Am. Chem. Soc.* **1969**, *91*, 4947.
40. Pearson, R. G. *J. Mol. Struct.:THEOCHEM* **1983**, *103*, 25.
41. Wheeler, R. A.; Whangbo, M. H.; Hughbanks, T.; Hoffmann, R.; Burdett, J. K.; Albright, T. A. *J. Am. Chem. Soc.* **1986**, *108*, 2222.
42. Kunz, M.; Brown, I. D. *J. Solid State Chem.* **1995**, *115*, 395.
43. Goodenough, J. B. *Annu. Rev. Mater. Sci.* **1998**, *28*, 1.
44. Halasyamani, P. S.; Poeppelmeier, K. R. *Chem. Mater.* **1998**, *10*, 2753.
45. Porter, Y.; Bhuvanesh, N. S. P.; Halasyamani, P. S. *Inorg. Chem.* **2001**, *40*, 1172.
46. Porter, Y.; Ok, K. M.; Bhuvanesh, N. S. P.; Halasyamani, P. S. *Chem. Mater.* **2001**, *13*, 1910.
47. Hu, T.; Qin, L.; Kong, F.; Zhou, Y.; Mao, J.-G. *Inorg. Chem.* **2009**, *48*, 2193.

48. Rademacher, O.; Göbel, H.; Ruck, M.; Oppermann, H. Z. *Kristallogr. - New Cryst. Struct.* **2001**, *216*, 29.
49. Dityatyev, O. A.; Smidt, P.; Stefanovich, S. Y.; Lightfoot, P.; Dolgikh, V. A.; Opperman, H. *Solid State Sci.* **2004**, *6*, 915.
50. Berdonosov, P. S.; Stefanovitch, S. Y.; Dolgikh, V. A. *J. Solid State Chem.* **2000**, *149*, 236.
51. Ok, K. M.; Bhuvanesh, N. S. P.; Halasyamani, P. S. *Inorg. Chem.* **2001**, *40*, 1978.
52. Bean, A. C.; Campana, C. F.; Kwon, O.; Albrecht-Schmitt, T. E. *J. Am. Chem. Soc.* **2001**, *123*, 8806.
53. Sykora, R. E.; Wells, D. M.; Albrecht-Schmitt, T. E. *Inorg. Chem.* **2002**, *41*, 2697.
54. Sykora, R. E.; Deakin, L.; Mar, A.; Skanthakumar, S.; Soderholm, L.; Albrecht-Schmitt, T. E. *Chem. Mater.* **2004**, *16*, 1343.
55. Bray, T. H.; Beitz, J. V.; Bean, A. C.; Yu, Y.; Albrecht-Schmitt, T. E. *Inorg. Chem.* **2006**, *45*, 8251.
56. Sullens, T. A.; Almond, P. M.; Byrd, J. A.; Beitz, J. V.; Bray, T. H.; Albrecht-Schmitt, T. E. *J. Solid State Chem.* **2006**, *179*, 1192.
57. Phanon, D.; Gautier-Luneau, I. *Angew. Chem., Int. Ed.* **2007**, *46*, 8488.
58. Chai, W.; Lin, J.; Song, L.; Shu, K.; Qin, L.; Shi, H.; Guo, J. *Solid State Sci.* **2010**, *12*, 2100.

59. Bentría, B.; Benbortal, D.; Bagieu-Beucher, M.; Masse, R.; Mosset, A. *J. Chem. Crystallogr.* **2003**, *33*, 867.
60. Phanon, D.; Gautier-Luneau, I. *Z. Kristallogr.* **2006**, *221*, 243.
61. Aurivillius, B. *Ark. Kemi* **1949**, 463.
62. Aurivillius, B. *Ark. Kemi* **1949**, 499.
63. Aurivillius, B. *Ark. Kemi* **1950**, *2*, 519.
64. *SAINT, Program for Area Detector Absorption Correction, version 4.05*; Siemens Analytical X-ray Systems, Inc.: Madison, WI, 1995.
65. North, A. C. T.; Phillips, D. C.; Mathews, F. S. *Acta Crystallogr.* **1968**, *24*, 351.
66. Sheldrick, G. M. *SHELXL-97 - A Program for Crystal Structure Refinement.*; University of Goettingen: Goettingen, 1997.
67. Sheldrick, G. M. *SHELXS-97 - A Program for Automatic Solution of Crystal Structures.*; University of Goettingen: Goettingen, Germany, 1997.
68. Farrugia, L. J. *J. Appl. Crystallogr.* **1999**, *32*, 837.
69. Spek, A. L. *PLATON*; Utrecht University: Utrecht, The Netherlands, 2001.
70. Flack, H. *Acta Crystallogr.* **1983**, *39*, 876.
71. Kubelka, P.; Munk, F. *Z. Tech. Phys.* **1931**, *12*, 593.
72. Tauc, J. *Mater. Res. Bull.* **1970**, *5*, 721.

73. Kurtz, S. K.; Perry, T. T. *J. Appl. Phys.* **1968**, *39*, 3798.
74. Hohenberg, P.; Kohn, W. *Phys. Rev.* **1964**, *136*, B864.
75. Kohn, W.; Sham, L. J. *Phys. Rev.* **1965**, *140*, A1133.
76. Junquera, J.; Paz, O.; Sanchez-Portal, D.; Artacho, E. *Phys. Rev. B: Condens. Matter* **2001**, *64*, 235111/1.
77. Sánchez-Portal, D.; Ordejón, P.; Canadell, E.; Kaltsoyannis, N., McGrady, J. E., Eds.; Springer Berlin / Heidelberg: 2004; Vol. 113, p 103.
78. Torres, J. A.; Artacho, E.; Cela, J. M.; Gale, J.; García, A.; Junquera, J.; Martin, R. M.; Ordejón, P.; Sánchez, D.; Soler, J. M. *SIESTA-3.0-rc2*; <http://www.icmab.es/siesta/>; 2010.
79. Giannozzi, P. *J. Phys: Condens. Matter.* **2009**, *21*, 395502.
80. Troullier, N.; Martins, J. L. *Phys. Rev. B: Condens. Matter* **1991**, *43*, 1993.
81. Perdew, J. P.; Burke, K.; Ernzerhof, M. *Phys. Rev. Lett.* **1996**, *77*, 3865.
82. Monkhorst, H. J.; Pack, J. D. *Phys. Rev. B* **1976**, *13*, 5188.
83. Dronskowski, R.; Bloechl, P. E. *J. Phys. Chem.* **1993**, *97*, 8617.
84. Becke, A. D.; Edgecombe, K. E. *J. Chem. Phys.* **1990**, *92*, 5397.
85. Silvi, B.; Savin, A. *Nature* **1994**, *371*, 683.
86. <http://www.fhi-berlin.mpg.de/th/fhi98md/fhi98PP/>; 2004.



87. Momma, K.; Izumi, F. *J. Appl. Crystallogr.* **2008**, *41*, 653.
88. Tobon- Zapata, G. E.; Etcheverry, S. B.; Baran, E. J. *J. Mater. Sci. Lett.* **1997**, *16*, 656.
89. Hamid, S. A. *Phys. Status Solidi A* **1977**, *43*, K29.
90. Landolt, H. *Numerical Values and Functions from the Natural Sciences and Technology (New Series), Group 3: Crystal and Solid State Physics*; Springer Verlag: Berlin, 1979; Vol. 11.
91. Scott, J. F. *J. Phys.: Condens. Matter* **2008**, *20*, 021001/1.
92. Shimakawa, Y.; Kubo, Y.; Nakagawa, Y.; Kamiyama, T.; Asano, H.; Izumi, F. *Appl. Phys. Lett.* **1999**, *74*, 1904.
93. Baek, S. H.; Jang, H. W.; Folkman, C. M.; Li, Y. L.; Winchester, B.; Zhang, J. X.; He, Q.; Chu, Y. H.; Nelson, C. T.; Rzechowski, M. S.; Pan, X. Q.; Ramesh, R.; Chen, L. Q.; Eom, C. B. *Nat. Mater.* **2010**, *9*, 309.
94. Hatt, A. J.; Spaldin, N. A.; Ederer, C. *Phys. Rev. B* **2010**, *81*, 054109.
95. Cohen, R. E. *Nature* **1992**, *358*, 136.
96. Lines, M. E.; Glass, A. M. *Principles and Applications of Ferroelectrics and Related Materials*; Oxford University Press: Oxford, 1991.

## CHAPTER 4. Synthesis, Structure, and Characterization of New $\text{Li}^+ - \text{d}^0 - \text{Lone-pair}$ – Oxides: Noncentrosymmetric Polar $\text{Li}_6(\text{Mo}_2\text{O}_5)_3(\text{SeO}_3)_6$ and Centrosymmetric $\text{Li}_2(\text{MO}_3)(\text{TeO}_3)$ ( $\text{M} = \text{Mo}^{6+}$ or $\text{W}^{6+}$ )

### 4.1 Abstract

New lithium –  $\text{d}^0$  cation – lone-pair oxides,  $\text{Li}_6(\text{Mo}_2\text{O}_5)_3(\text{SeO}_3)_6$  ( $Pmn2_1$ ) and  $\text{Li}_2(\text{MO}_3)(\text{TeO}_3)$  ( $P2_1/n$ ) ( $\text{M} = \text{Mo}^{6+}$  or  $\text{W}^{6+}$ ), have been synthesized and characterized. The former is noncentrosymmetric and polar, whereas the latter is centrosymmetric. The crystal structures exhibit zigzag anionic layers composed of distorted  $\text{MO}_6$  and asymmetric  $\text{AO}_3$  ( $\text{A} = \text{Se}^{4+}$  or  $\text{Te}^{4+}$ ) polyhedra. The anionic layers stack along a 2-fold screw axis and are separated by  $\text{Li}^+$  cations. Powder SHG measurements on  $\text{Li}_6(\text{Mo}_2\text{O}_5)_3(\text{SeO}_3)_6$  using 1064 nm radiation reveal a SHG efficiency of approximately  $170 \times \alpha\text{-SiO}_2$ . Particle size vs. SHG efficiency measurements indicate  $\text{Li}_6(\text{Mo}_2\text{O}_5)_3(\text{SeO}_3)_6$  is type 1 nonphase-matchable. Converse piezoelectric measurements result in a  $d_{33}$  value of  $\sim 28$  pm/V and pyroelectric measurements reveal a pyroelectric coefficient of  $-0.43 \mu\text{C}/\text{m}^2\text{K}$  at  $50^\circ\text{C}$  for  $\text{Li}_6(\text{Mo}_2\text{O}_5)_3(\text{SeO}_3)_6$ . Frequency-dependent polarization measurements confirm that  $\text{Li}_6(\text{Mo}_2\text{O}_5)_3(\text{SeO}_3)_6$  is non-ferroelectric, i.e., the macroscopic polarization is not reversible, or ‘switchable’. Infrared, UV-vis, thermogravimetric, differential thermal analysis measurements, and electron localization function calculations were also done for all materials. Crystal data:  $\text{Li}_6(\text{Mo}_2\text{O}_5)_3(\text{SeO}_3)_6$ , space group  $Pmn2_1$  (No. 31),  $a = 8.2687(4) \text{ \AA}$ ,  $b = 16.6546(7) \text{ \AA}$ ,  $c = 19.2321(8) \text{ \AA}$ ,  $V =$

2648.5(2) Å<sup>3</sup>,  $Z = 4$ ; Li<sub>2</sub>(MoO<sub>3</sub>)(TeO<sub>3</sub>), space group  $P2_1/n$  (No. 14),  $a = 5.3830(5)$  Å,  $b = 13.0027(11)$  Å,  $c = 6.9814(6)$  Å,  $\beta = 94.7620(10)^\circ$ ,  $V = 486.97(7)$  Å<sup>3</sup>,  $Z = 4$ .  
 Li<sub>2</sub>(WO<sub>3</sub>)(TeO<sub>3</sub>), space group  $P2_1/n$  (No. 14),  $a = 5.3950(5)$  Å,  $b = 12.9440(12)$  Å,  $c = 7.0149(7)$  Å,  $\beta = 94.2510(10)^\circ$ ,  $V = 488.52(8)$  Å<sup>3</sup>,  $Z = 4$ .

## 4.2 Introduction

Polar materials have many practical applications in electronic and laser technologies owing to their functional properties such as second-harmonic generation (SHG), piezoelectricity, pyroelectricity, and/or ferroelectricity.<sup>1-4</sup> The search for new polar materials continues to be an active and challenging task for material scientists and solid-state chemists. The structure-property relationships of polar materials have been well studied,<sup>4</sup> yet the understanding of how polar structures are created from structural building units is far from complete. The packing and polarization alignment of structural building units are found to depend on cation sizes, hydrogen bonding, and hard and soft cation-anion interactions. Influence of cation sizes on altering structures from centrosymmetric (CS) to noncentrosymmetric (NCS) has been observed and reported for several systems such as MNaNbOF<sub>5</sub> ( $M = K^+$ ,  $Cs^+$ ),<sup>5</sup> A<sub>2</sub>Ti(IO<sub>3</sub>)<sub>6</sub> ( $A = Li^+$ ,  $Na^+$ ,  $K^+$ ,  $Rb^+$ ,  $Cs^+$ , and  $Tl^+$ ),<sup>6</sup> A<sub>2</sub>SeMoO<sub>6</sub> ( $A = Na^+$ ,  $K^+$ ,  $Rb^+$ ),<sup>7</sup> ACuTe<sub>2</sub>O<sub>7</sub>,<sup>8</sup> and A(Mo<sub>2</sub>O<sub>5</sub>)(SeO<sub>3</sub>)<sub>2</sub> ( $A = Sr^{2+}$ ,  $Ba^{2+}$ ,  $Pb^{2+}$ ).<sup>9</sup> Recently, using hydrogen bonding to direct the alignment of polar lambda structural building units, Donakowski et al. have been able to prepare a new polar material, CuVOF<sub>4</sub>(H<sub>2</sub>O)<sub>7</sub>, from CS MVOF<sub>4</sub>(H<sub>2</sub>O)<sub>7</sub> ( $M = Co^{2+}$ ,  $Ni^{2+}$ , and  $Zn^{2+}$ ).<sup>10</sup> In addition, using hard, Na<sup>+</sup>, and soft, Ag<sup>+</sup>, cations, Fry et al. have been able to direct the orientation of polar oxyfluoride groups, thereby altering the undoped NCS polar

$\text{Na}_3\text{WO}_3\text{F}_3$  ( $R\bar{3}$ ) to the doped CS  $\text{Na}_{1.5}\text{Ag}_{1.5}\text{MoO}_3\text{F}_3$  and  $\text{Na}_{1.5}\text{Ag}_{1.5}\text{WO}_3\text{F}_3$  ( $R\bar{3}$ ).<sup>11</sup> Despite these successes, the systematic engineering and design of new polar crystal structures remain an ongoing challenge.

The macroscopic polarity in materials emanates from the local polarity of building blocks of the structure. Chen's group proposed using acentric  $\pi$ -conjugated systems, particularly planar borate rings, to enhance nonlinear optical responses and to direct new noncentrosymmetric (NCS) borate-based materials.<sup>12-15</sup> Recently, Zou et al. have successfully reported a new series of polar alkaline-alkaline earth fluoride carbonates with strong SHG efficiencies based on  $\pi$ -conjugated  $\text{CO}_3^{2-}$  anionic groups.<sup>16</sup> Poeppelmeier et al. have successfully used oxyfluoride groups to create new polar materials,<sup>5,10,17-23</sup> whereas cations that are susceptible to second-order Jahn Teller (SOJT) distortions<sup>24-30</sup> have been successfully employed in preparing many new polar materials in our group as well as others.<sup>6,7,31-55</sup>

With respect to lithium compounds containing SOJT cations, only a few materials have been reported,  $\text{LiVTeO}_5$  ( $P2_12_12_1$ ),<sup>56</sup>  $\text{Li}(\text{VO}_2)_3(\text{TeO}_3)_2$  ( $P-I$ ),<sup>57</sup>  $\text{Li}(\text{MoO}_3)(\text{IO}_3)$  ( $P2_1$ ),<sup>58</sup> and  $\text{Li}_8\text{Bi}_2\text{Mo}_7\text{O}_{28}$  ( $I\bar{4}$ ).<sup>59</sup> Of these only  $\text{Li}(\text{MoO}_3)(\text{IO}_3)$  is polar. No lithium compounds containing  $\text{Mo}^{6+}$  (or  $\text{W}^{6+}$ ) and  $\text{Se}^{4+}$  (or  $\text{Te}^{4+}$ ) have been reported to date even though many polar compounds have been published that contain these SOJT cations and other alkali cations such as  $\text{Na}_2\text{Te}_3\text{Mo}_3\text{O}_{12}$ ,<sup>36</sup>  $\text{R}_2(\text{MO}_3)_3(\text{AO}_3)$  ( $\text{R} = \text{Rb}^+, \text{Cs}^+$ ;  $\text{M} = \text{Mo}^{6+}, \text{W}^{6+}$ ;  $\text{A} = \text{Se}^{4+}, \text{Te}^{4+}$ ).<sup>33,48,60-63</sup> In this chapter, we report on the synthesis and characterization of new lithium –  $d^0$  cation – lone-pair compounds, NCS polar  $\text{Li}_6(\text{Mo}_2\text{O}_5)_3(\text{SeO}_3)_6$  and CS  $\text{Li}_2(\text{MO}_3)(\text{TeO}_3)$  ( $\text{M} = \text{Mo}^{6+}$  or  $\text{W}^{6+}$ ). In addition to the crystal structures, UV-vis and IR

spectroscopy, and thermal analyses for all reported materials, as well as SHG, piezoelectricity, and polarization measurements for  $\text{Li}_6(\text{Mo}_2\text{O}_5)_3(\text{SeO}_3)_6$  are also reported.

### 4.3 Experimental details

#### 4.3.1 Synthesis

$\text{Li}_2\text{MoO}_4$  (Alfa Aesar, 98.5%),  $\text{Li}_2\text{CO}_3$  (Alfa Aesar, 99%),  $\text{SeO}_2$  (Alfa Aesar, 99.4%),  $\text{TeO}_2$  (GFS, 99.6%),  $\text{WO}_3$  (Alfa Aesar, 99.8%) were used as received. Crystals of  $\text{Li}_6(\text{Mo}_2\text{O}_5)_3(\text{SeO}_3)_6$  were prepared by solid state techniques. A mixture of 0.174 g ( $1.00 \times 10^{-3}$  mol) of  $\text{Li}_2\text{MoO}_4$ , and 0.110 g ( $1.00 \times 10^{-3}$  mol) of  $\text{SeO}_2$  was thoroughly ground and pressed into a pellet. The pellet was placed in a Pyrex tube that was evacuated and flame-sealed. The sealed ampule was heated to 300 °C for 12 h and then 450 °C for 24 h, and finally cooled to room temperature at 6 °C h<sup>-1</sup>. The resultant pellet was washed with distilled water, and revealed only colorless rod-shaped crystals. Bulk  $\text{Li}_6(\text{Mo}_2\text{O}_5)_3(\text{SeO}_3)_6$  was prepared by combining 0.174 g ( $1.00 \times 10^{-3}$  mol) of  $\text{Li}_2\text{MoO}_4$ , 0.220 g ( $2.00 \times 10^{-3}$  mol) of  $\text{SeO}_2$ , and 0.144 g ( $1.00 \times 10^{-3}$  mol) of  $\text{MoO}_3$ . The mixture was finely ground and pressed into a pellet. The pellet was placed in a Pyrex tube that was evacuated and flame-sealed. The sealed ampoule was heated to 400 °C for four days with three intermittent regrindings resulting in single phase  $\text{Li}_6(\text{Mo}_2\text{O}_5)_3(\text{SeO}_3)_6$ .

Crystals of  $\text{Li}_2(\text{MoO}_3)(\text{TeO}_3)$  and  $\text{Li}_2(\text{WO}_3)(\text{TeO}_3)$  were grown using hydrothermal techniques. A mixture of 0.110 g ( $1.50 \times 10^{-3}$  mol) of  $\text{Li}_2\text{CO}_3$ , 0.160 g ( $1.00 \times 10^{-3}$  mol) of  $\text{TeO}_2$ , 0.144 g ( $1.00 \times 10^{-3}$  mol) of  $\text{MoO}_3$ , and 3 mL  $\text{H}_2\text{O}$  for  $\text{Li}_2(\text{MoO}_3)(\text{TeO}_3)$ , and a mixture of 0.110 g ( $1.50 \times 10^{-3}$  mol) of  $\text{Li}_2\text{CO}_3$ , 0.160 g ( $1.00 \times 10^{-3}$  mol) of  $\text{TeO}_2$ , 0.232

g ( $1.00 \times 10^{-3}$  mol) of  $\text{WO}_3$ , and 3 mL  $\text{H}_2\text{O}$  for  $\text{Li}_2(\text{WO}_3)(\text{TeO}_3)$  were placed in separate 23mL Teflon-lined autoclaves that were subsequently closed. The autoclaves were heated to 230 °C for 4 days and then cooled slowly to room temperature at a rate of 6 °C  $\text{h}^{-1}$ . The products consisted of only colorless block crystals (~90% yield based on  $\text{MoO}_3$  or  $\text{WO}_3$ ).

Bulk phases of  $\text{Li}_2(\text{MoO}_3)(\text{TeO}_3)$  and  $\text{Li}_2(\text{WO}_3)(\text{TeO}_3)$  were prepared by solid state techniques. A mixture of 0.074 g ( $1.0 \times 10^{-3}$  mol) of  $\text{Li}_2\text{CO}_3$ , 0.160 g ( $1.00 \times 10^{-3}$  mol) of  $\text{TeO}_2$ , and 0.144 g ( $1.00 \times 10^{-3}$  mol) of  $\text{MoO}_3$  for  $\text{Li}_2(\text{MoO}_3)(\text{TeO}_3)$ , and a mixture of 0.074 g ( $1.0 \times 10^{-3}$  mol) of  $\text{Li}_2\text{CO}_3$ , 0.160 g ( $1.00 \times 10^{-3}$  mol) of  $\text{TeO}_2$ , and 0.232 g ( $1.00 \times 10^{-3}$  mol) of  $\text{WO}_3$  for  $\text{Li}_2(\text{WO}_3)(\text{TeO}_3)$  were ground, pressed into pellets, heated in air to 425 °C for  $\text{Li}_2(\text{MoO}_3)(\text{TeO}_3)$  and to 450 °C for  $\text{Li}_2(\text{WO}_3)(\text{TeO}_3)$  for three days with two intermittent regrindings to obtain the pure phases.

#### 4.3.2 Characterization

##### Single Crystal X-ray Diffraction

For  $\text{Li}_6(\text{Mo}_2\text{O}_5)_3(\text{SeO}_3)_6$ , a colorless rod-shaped crystal ( $0.10 \times 0.01 \times 0.01 \text{ mm}^3$ ); for  $\text{Li}_2(\text{MoO}_3)(\text{TeO}_3)$ , a colorless block crystal ( $0.40 \times 0.20 \times 0.20 \text{ mm}^3$ ); for  $\text{Li}_2(\text{WO}_3)(\text{TeO}_3)$ , a colorless block crystal ( $0.04 \times 0.04 \times 0.02 \text{ mm}^3$ ), were used for single-crystal X-ray data collections. Data were collected using a Siemens SMART APEX diffractometer equipped with a 1K CCD area detector using graphite-monochromated Mo  $\text{K}\alpha$  radiation. A hemisphere of data was collected using a narrow-frame method with scan widths of 0.30° in  $\omega$  and an exposure time of 45s per frame. The first 50 frames were re-measured at the end of the data collection to monitor instrument

and crystal stability. The data were integrated using the Siemens SAINT program,<sup>64</sup> with the intensities corrected for Lorentz, polarization, air absorption, and absorption attributable to the variation in the path length through the detector face plate. Psi-scans were used for the absorption correction on the hemisphere of data.<sup>65</sup> The data were solved and refined using SHELXS-97 and SHELXL-97, respectively.<sup>66,67</sup> All of the atoms were refined with anisotropic thermal parameters, and the refinement converged for  $I > 2\sigma(I)$ . All calculations were performed using the WinGX-98 crystallographic software package.<sup>68</sup> The Flack parameter<sup>69</sup> for  $\text{Li}_6(\text{Mo}_2\text{O}_5)_3(\text{SeO}_3)_6$  was refined to 0.000(8). Crystallographic data, atomic coordination, and selected bond distances for  $\text{Li}_6(\text{Mo}_2\text{O}_5)_3(\text{SeO}_3)_6$ ,  $\text{Li}_2(\text{MoO}_3)(\text{TeO}_3)$ , and  $\text{Li}_2(\text{WO}_3)(\text{TeO}_3)$  are given in Tables 5.1-5.5.

### **Powder X-ray Diffraction**

The X-ray powder diffraction data were collected using a PANalytical X'PertPRO diffractometer at room temperature (Cu  $K\alpha$  radiation, flat plate geometry) equipped with X'Celerator detector. Data were collected in the  $2\theta$  range of  $5 - 70^\circ$  with a step size of  $0.008^\circ$  and a step time of 0.3s.

### **Infrared Spectroscopy**

Infrared (IR) spectra were recorded on a Matteson FTIR 5000 spectrometer in the spectral range of  $400 - 4000 \text{ cm}^{-1}$  at room temperature. The sample (5 mg) was finely ground with dry KBr (100 mg). This powder mixture was then transferred to a stainless steel IR holder and pressed to a semi-transparent pellet ( $\sim 0.2 \text{ mm}$  thick).

**Table 4.1** Crystallographic data for  $\text{Li}_6(\text{Mo}_2\text{O}_5)_3(\text{SeO}_3)_6$ ,  $\text{Li}_2(\text{MoO}_3)(\text{TeO}_3)$ , and  $\text{Li}_2(\text{WO}_3)(\text{TeO}_3)$ .

formula	$\text{Li}_6(\text{Mo}_2\text{O}_5)_3(\text{SeO}_3)_6$	$\text{Li}_2(\text{MoO}_3)(\text{TeO}_3)$	$\text{Li}_2(\text{WO}_3)(\text{TeO}_3)$
fw (g/mol)	1619.04	333.42	421.33
T(K)	298.0(2)	298.0(2)	298.0(2)
$\lambda$ (Å)	0.71073	0.71073	0.71073
Crystal system	Orthorhombic	Monoclinic	Monoclinic
Space group	$Pmn2_1$ (No.31)	$P2_1/n$ (No.14)	$P2_1/n$ (No.14)
$a$ (Å)	8.2687(4)	5.3830(5)	5.3950(5)
$b$ (Å)	16.6546(7)	13.0027(11)	12.9440(12)
$c$ (Å)	19.2321(8)	6.9814(6)	7.0149(7)
$\beta$	90	94.7420(10)	94.2510(10)
$V$ (Å <sup>3</sup> )	2648.5(2)	486.97(7)	488.52(8)
$Z$	4	4	4
$\rho_{\text{calcd}}$ (g/cm <sup>3</sup> )	4.060	4.548	5.729
$\mu$ (mm <sup>-1</sup> )	11.138	8.509	29.443
$2\theta_{\text{max}}$ (deg)	53.8	57.8	58.3
$R$ (int)	0.0516	0.0620	0.0441
Reflections collected/unique	15543/4830	3016/1199	3090/1208
Parameters	513	92	92
GOF ( $F^2$ )	0.992	1.169	1.197
$R(F)^a$	0.0282	0.0282	0.0209
$R_w(F_o^2)^b$	0.0633	0.0709	0.0528
Flack param.	0.000(8)	-	-

$$^a R(F) = \Sigma ||F_o| - |F_c|| / \Sigma |F_o|. \quad ^b R_w(F_o^2) = [\Sigma w(F_o^2 - F_c^2)^2 / \Sigma w(F_o^2)^2]^{1/2}$$



**Table 4.2** Atomic coordinates and equivalent isotropic displacement parameters ( $\text{\AA}^2$ ) for  $\text{Li}_6(\text{Mo}_2\text{O}_5)_3(\text{SeO}_3)_6$ .

Atoms	x	y	z	U(eq)
Mo(1)	0.2978(1)	0.6572(1)	0.0529(1)	0.012(1)
Mo(2)	0.2963(1)	0.4976(1)	-0.1632(1)	0.013(1)
Mo(3)	0.2939(1)	0.0104(1)	0.0852(1)	0.013(1)
Mo(4)	0.2042(1)	0.1478(1)	0.3063(1)	0.013(1)
Mo(5)	0.2011(1)	0.3625(1)	0.0624(1)	0.013(1)
Mo(6)	0.2934(1)	0.1492(1)	-0.1960(1)	0.012(1)
Se(1)	0.0000	0.2807(1)	-0.1417(1)	0.014(1)
Se(2)	0.0000	0.7642(1)	0.1276(1)	0.014(1)
Se(3)	0.5000	0.3274(1)	-0.1295(1)	0.012(1)
Se(4)	0.0000	0.0183(1)	-0.0408(1)	0.016(1)
Se(5)	0.5000	0.8416(1)	0.1148(1)	0.014(1)
Se(6)	0.0000	0.5106(1)	-0.2864(1)	0.013(1)
Se(7)	0.5000	0.0345(1)	-0.0825(1)	0.012(1)
Se(8)	0.0000	0.2058(1)	0.1658(1)	0.014(1)
Se(9)	0.0000	0.4834(1)	0.1697(1)	0.014(1)
Se(10)	0.5000	0.7017(1)	-0.0903(1)	0.014(1)
Se(11)	0.5000	0.2634(1)	0.3795(1)	0.015(1)
Se(12)	0.5000	0.2339(1)	0.1058(1)	0.015(1)
O(1)	0.1704(7)	0.5925(3)	0.0138(3)	0.022(1)
O(2)	0.3004(7)	0.6270(4)	0.1377(3)	0.023(1)
O(3)	0.5000	0.6085(4)	0.0217(4)	0.012(2)
O(4)	0.1548(7)	0.7505(3)	0.0671(3)	0.019(1)
O(5)	0.3380(7)	0.7299(3)	-0.0403(3)	0.019(1)

**Table 4.2** Atomic coordinates and equivalent isotropic displacement parameters ( $\text{\AA}^2$ ) for  $\text{Li}_6(\text{Mo}_2\text{O}_5)_3(\text{SeO}_3)_6$  (continued)

Atoms	x	y	z	U(eq)
O(6)	0.5000	0.7456(4)	0.0832(4)	0.014(2)
O(7)	0.3428(7)	0.8840(3)	0.0700(3)	0.015(1)
O(8)	0.5000	0.4922(4)	-0.1123(5)	0.014(2)
O(9)	0.5000	0.7759(5)	-0.1505(4)	0.019(2)
O(10)	0.1570(7)	0.4625(3)	-0.2418(3)	0.016(1)
O(11)	0.0000	0.4177(4)	0.0414(4)	0.015(2)
O(12)	0.5000	0.1874(5)	0.4333(5)	0.022(2)
O(13)	0.0000	0.3003(5)	-0.2252(5)	0.019(2)
O(14)	0.0000	0.6024(5)	-0.2558(5)	0.021(2)
O(15)	0.1613(7)	0.4200(3)	0.1647(3)	0.017(1)
O(16)	0.1567(7)	0.9736(3)	0.0073(3)	0.015(1)
O(17)	0.0000	0.1130(5)	-0.0170(5)	0.023(2)
O(18)	0.3445(7)	0.2428(3)	0.3208(3)	0.019(1)
O(19)	0.1586(6)	0.2119(3)	-0.1311(3)	0.014(1)
O(20)	0.5000	0.0084(4)	0.1346(5)	0.015(2)
O(21)	0.0000	0.6826(5)	0.1744(4)	0.023(2)
O(22)	0.5000	0.2307(4)	-0.1616(5)	0.017(2)
O(23)	0.3396(7)	0.3669(3)	-0.1737(3)	0.014(1)
O(24)	0.1678(8)	0.4822(4)	-0.0958(3)	0.024(2)
O(25)	0.5000	0.0979(4)	-0.2184(4)	0.012(2)
O(26)	0.0000	0.5039(5)	0.2564(5)	0.018(2)
O(27)	0.3454(6)	0.3029(3)	0.1246(3)	0.015(1)
O(28)	0.3410(7)	0.0981(3)	-0.0909(3)	0.015(1)

**Table 4.2** Atomic coordinates and equivalent isotropic displacement parameters ( $\text{\AA}^2$ ) for  $\text{Li}_6(\text{Mo}_2\text{O}_5)_3(\text{SeO}_3)_6$  (continued)

Atoms	x	y	z	U(eq)
O(29)	0.2830(7)	0.5980(3)	-0.1775(3)	0.022(1)
O(30)	0.1561(7)	0.2279(3)	0.2196(3)	0.017(1)
O(31)	0.1720(7)	0.9907(4)	0.1547(3)	0.021(1)
O(32)	0.3286(7)	0.4350(3)	0.0326(3)	0.022(1)
O(33)	0.0000	0.0989(4)	0.2758(4)	0.015(2)
O(34)	0.1712(7)	0.0716(3)	-0.2165(3)	0.022(1)
O(35)	0.5000	0.0199(5)	0.0052(4)	0.017(2)
O(36)	0.3304(7)	0.0901(3)	0.2584(3)	0.023(1)
O(37)	0.0000	0.2878(4)	0.1130(4)	0.016(2)
O(38)	0.2631(7)	0.1111(3)	0.0719(3)	0.022(1)
O(39)	0.2223(7)	0.1094(3)	0.3883(3)	0.021(1)
O(40)	0.2009(7)	0.2931(4)	-0.0033(3)	0.024(1)
O(41)	0.2642(7)	0.2109(4)	-0.2657(3)	0.021(1)
O(42)	0.5000	0.2260(5)	0.0213(5)	0.025(2)
Li(1)	0.0000	0.9953(11)	0.2238(12)	0.020(5)
Li(2)	0.5000	0.0088(13)	0.2397(12)	0.025(5)
Li(3)	0.5000	0.4984(11)	-0.0109(12)	0.023(5)
Li(4)	0.0000	0.5117(14)	-0.0247(12)	0.026(5)
Li(5)	0.2230(20)	0.6666(10)	-0.2666(8)	0.027(4)
Li(6)	0.2160(20)	0.8392(9)	-0.0155(9)	0.031(4)
Li(7)	0.2650(30)	0.6620(11)	0.2339(9)	0.044(5)
Li(8)	0.2340(30)	0.1741(10)	-0.0245(9)	0.040(5)

U(eq) is defined as one third of the trace of the orthogonalized  $U_{ij}$  tensor

**Table 4.3** Atomic coordinates and equivalent isotropic displacement parameters ( $\text{\AA}^2$ ) for  $\text{Li}_2(\text{MoO}_3)(\text{TeO}_3)$  and  $\text{Li}_2(\text{WO}_3)(\text{TeO}_3)$ .

$\text{Li}_2(\text{MoO}_3)(\text{TeO}_3)$				
Atoms	x	y	z	U(eq)
Mo(1)	0.2174(1)	0.0897(1)	0.2472(1)	0.007(1)
Te(1)	-0.2515(1)	0.2078(1)	0.4346(1)	0.007(1)
O(1)	0.3595(6)	-0.0197(2)	0.1633(5)	0.012(1)
O(2)	0.3023(7)	0.0909(3)	0.4921(5)	0.016(1)
O(3)	-0.0999(6)	0.0534(2)	0.2359(5)	0.013(1)
O(4)	-0.4820(6)	0.1919(2)	0.2115(5)	0.010(1)
O(5)	-0.3675(6)	0.3441(2)	0.4671(5)	0.009(1)
O(6)	0.0248(6)	0.2489(2)	0.3084(5)	0.011(1)
Li(1)	0.2994(15)	0.0700(7)	0.7671(12)	0.017(2)
Li(2)	0.2583(16)	-0.1476(7)	0.0164(14)	0.020(2)
$\text{Li}_2(\text{WO}_3)(\text{TeO}_3)$				
Atoms	x	y	z	U(eq)
W(1)	0.2172(1)	0.0929(1)	0.2451(1)	0.009(1)
Te(1)	-0.2507(1)	0.2042(1)	0.4321(1)	0.009(1)
O(1)	0.3550(7)	-0.0201(3)	0.1636(6)	0.014(1)
O(2)	0.3042(8)	0.0929(3)	0.4919(6)	0.017(1)
O(3)	-0.1038(7)	0.0557(3)	0.2396(6)	0.015(1)
O(4)	-0.4847(6)	0.1929(3)	0.2114(5)	0.012(1)
O(5)	-0.3619(6)	0.3426(3)	0.4691(5)	0.010(1)
O(6)	0.0265(7)	0.2482(3)	0.3068(6)	0.013(1)
Li(1)	0.3069(17)	0.0680(8)	0.7639(15)	0.017(2)
Li(2)	0.2562(19)	-0.1460(8)	0.0212(17)	0.021(2)

U(eq) is defined as one third of the trace of the orthogonalized  $U_{ij}$  tensor

**Table 4.4** Selected bond distances (Å) for  $\text{Li}_6(\text{Mo}_2\text{O}_5)_3(\text{SeO}_3)_6$ .

Bonds	Distances	Bonds	Distances	Bonds	Distances
Mo(1)–O(1)	1.684(6)	Mo(4)–O(30)	2.173(6)	Se(3)–O(22)	1.724(7)
Mo(1)–O(2)	1.709(6)	Mo(4)–O(33)	1.964(4)	Se(3)–O(23)	1.707(5)
Mo(1)–O(3)	1.953(4)	Mo(4)–O(36)	1.691(6)	Se(4)–O(16)x2	1.757(5)
Mo(1)–O(4)	1.971(5)	Mo(4)–O(39)	1.709(6)	Se(4)–O(17)	1.642(8)
Mo(1)–O(5)	2.187(6)	Mo(5)–O(11)	1.942(4)	Se(5)–O(6)	1.710(7)
Mo(1)–O(6)	2.303(5)	Mo(5)–O(15)	2.214(6)	Se(5)–O(7)	1.713(5)
Mo(2)–O(8)	1.950(4)	Mo(5)–O(27)	1.960(6)	Se(6)–O(10)x2	1.750(6)
Mo(2)–O(10)	1.989(6)	Mo(5)–O(32)	1.702(6)	Se(6)–O(14)	1.637(8)
Mo(2)–O(23)	2.216(5)	Mo(5)–O(37)	2.294(5)	Se(7)–O(28)x2	1.696(5)
Mo(2)–O(24)	1.697(6)	Mo(5)–O(40)	1.712(6)	Se(7)–O(35)	1.703(9)
Mo(2)–O(26)	2.285(6)	Mo(6)–O(19)	1.974(5)	Se(8)–O(30)	1.694(6)
Mo(2)–O(29)	1.698(5)	Mo(6)–O(22)	2.281(5)	Se(8)–O(37)	1.702(8)
Mo(3)–O(7)	2.164(5)	Mo(6)–O(25)	1.958(4)	Se(9)–O(15)x2	1.704(5)
Mo(3)–O(16)	1.977(6)	Mo(6)–O(28)	2.229(5)	Se(9)–O(26)	1.704(9)
Mo(3)–O(20)	1.951(4)	Mo(6)–O(34)	1.686(6)	Se(10)–O(5)x2	1.714(6)
Mo(3)–O(31)	1.706(6)	Mo(6)–O(41)	1.706(6)	Se(10)–O(9)	1.692(8)
Mo(3)–O(35)	2.301(6)	Se(1)–O(13)	1.639(9)	Se(11)–O(12)	1.635(9)
Mo(3)–O(38)	1.715(6)	Se(1)–O(19)x2	1.753(5)	Se(11)–O(18)x2	1.744(6)
Mo(4)–O(9)	2.272(6)	Se(2)–O(4)x2	1.745(6)	Se(12)–O(27)x2	1.757(5)
Mo(4)–O(18)	1.982(6)	Se(2)–O(21)	1.629(8)	Se(12)–O(42)	1.630(9)

**Table 4.5** Selected bond distances (Å) for  $\text{Li}_2(\text{MoO}_3)(\text{TeO}_3)$  and  $\text{Li}_2(\text{WO}_3)(\text{TeO}_3)$ .

$\text{Li}_2(\text{MoO}_3)(\text{TeO}_3)$		$\text{Li}_2(\text{WO}_3)(\text{TeO}_3)$	
Bonds	Distances	Bonds	Distances
Mo–O(1)	1.733(3)	W–O(1)	1.755(4)
Mo–O(2)	1.740(3)	W–O(2)	1.759(4)
Mo–O(3)	1.768(3)	W–O(3)	1.796(3)
Mo–O(4)	2.124(3)	W–O(4)	2.091(4)
Mo–O(5)	2.151(3)	W–O(5)	2.122(4)
Mo–O(6)	2.369(3)	W–O(6)	2.314(4)
Te–O(4)	1.920(3)	Te–O(4)	1.929(4)
Te–O(5)	1.899(3)	Te–O(5)	1.913(3)
Te–O(6)	1.869(3)	Te–O(6)	1.878(4)

### UV–vis Diffuse Reflectance Spectroscopy

UV–vis diffuse reflectance spectra were collected with a Varian Cary 500 scan UV–vis–NIR spectrophotometer over the spectral range of 200–2000 nm at room temperature. Polytetrafluoroethylene (PTFE) was used as a standard material for the baseline correction. The sample was thoroughly mixed with PTFE and this mixture was used for UV–vis measurements. Reflectance spectra were converted to absorbance using the Kubelka–Munk equation.<sup>70,71</sup>

### Thermal Analysis

Thermogravimetric and differential thermal analyses were simultaneously carried out on an EXSTAR6000 TG/DTA 6300 Thermogravimetric/Differential Thermal Analysis system (SII NanoTechnology Inc.). The sample (~20 mg) was placed in a platinum

crucible that was heated (cooled) at a rate of 10 °C/min in the range of 25–700 °C under flowing nitrogen gas. An empty platinum crucible was used as the reference during the measurements.

### **Second-harmonic Generation**

Powder SHG measurements on  $\text{Li}_6(\text{Mo}_2\text{O}_5)_3(\text{SeO}_3)_6$  were performed at room temperature on a modified Kurtz-NLO system,<sup>72</sup> using a pulsed Nd:YAG laser with a wavelength of 1064 nm. The methodology and instrumentation details have been published.<sup>73</sup> The SHG efficiency has been shown to be particle size dependent.<sup>72</sup> Thus, the polycrystalline samples were ground and sieved into distinct particle size ranges (20–45, 45–63, 63–75, 75–90, and 90–120  $\mu\text{m}$ ). In order to evaluate relative SHG efficiencies of the measured samples with known SHG materials crystalline  $\alpha\text{-SiO}_2$  was also ground and sieved into the same particle size ranges. No index matching fluid was used in the experiments.

### **Piezoelectric Measurements**

Converse piezoelectric measurements were performed at room temperature using a Radiant Technologies RT66A piezoelectric test system with a TREK (model 609E-6) high voltage amplifier, Precision Materials Analyzer, Precision High Voltage Interface, and MTI 2000 Fotonic Sensor.  $\text{Li}_6(\text{Mo}_2\text{O}_5)_3(\text{SeO}_3)_6$  was pressed into a pellet (~8 mm diameter and ~1 mm thick). The pellet was sintered at 300 °C for one week. Silver paste was applied to both sides of the sintered pellet as electrodes, and the pellet was cured at 300 °C for 72 hours in air. This pellet was also used in polarization measurements.

## Polarization Measurements

The polarization measurements were done on a Radiant Technologies Model RT66A ferroelectric test system with a TREK high-voltage amplifier in the temperature range of 25–180 °C in a Delta Model 9023 environmental test chamber. The unclamped pyroelectric coefficient, defined as  $dP/dT$ ,<sup>73</sup> was determined by measuring the polarization as a function of temperature. The methodology and instrumentation details have been published.<sup>73</sup> To measure the potential ferroelectric behavior, frequency-dependent polarization measurements were done at room temperature under static electric field of 5–10 kV/cm between 50–1000 Hz. For the pyroelectric measurements, the polarization was measured statically from room temperature to 180 °C with an electric field of 7.5 kV/cm and at 1000 Hz for  $\text{Li}_6(\text{Mo}_2\text{O}_5)_3(\text{SeO}_3)_6$ . The temperature was allowed to stabilize before the polarization was measured.

## Electron Localization Function (ELF) Calculations

Electron localization function (ELF)<sup>74,75</sup> calculations were performed using the plane-wave pseudo-potential method (PWPP) as implemented in Quantum ESPRESSO (4.1.2 version)<sup>76</sup> package. Norm-conserving MT pseudo-potentials for all the elements were used with the GGA<sup>77</sup> for exchange-correlation corrections. The pseudo-potentials generated from the Fritz Haber Institute (FHI) code<sup>78</sup> were converted for the calculations. The tungsten pseudo-potential was generated using previously reported parameters<sup>79</sup> by the LD1.x program in the Quantum ESPRESSO package.<sup>76</sup> A plane wave energy cutoff was set to 37 Rydberg (Ry). The Brillouin zone was sampled using a  $8 \times 6 \times 7$  Monkhorst–Pack (MP)<sup>80</sup> k-mesh. A total energy convergence threshold of  $10^{-6}$  Ry



indicated self-consistency. The experimental crystal structures were employed for all calculations. The program VESTA was used for all the structural diagrams.<sup>81</sup>

## 4.4 Results and discussion

### Structures

$\text{Li}_6(\text{Mo}_2\text{O}_5)_3(\text{SeO}_3)_6$  crystallizes in the NCS polar orthorhombic space group  $Pmn2_1$ . Polyhedral representations of the material in the  $bc$ -plane are shown in Figure 4.1. The material exhibits zigzag layers that consist of  $\text{MoO}_6$  octahedra and  $\text{SeO}_3$  polyhedra (see Figure 4.2a). Along the  $a$ -axis direction, two  $\text{MoO}_6$  octahedra share an edge to form a  $\text{Mo}_2\text{O}_{10}$  dimer. The  $\text{Mo}_2\text{O}_{10}$  dimers are connected by  $\text{SeO}_3$  polyhedra to form a layer in the  $ab$ -plane. The layers stack along the  $c$ -axis direction, and are separated by the  $\text{Li}^+$  cations (see Figure 4.1). In connectivity terms, the structure may be written as  $[\text{6}(\text{MoO}_{2/1}\text{O}_{3/2}\text{O}_{1/3})^{-5/3} \text{3}(\text{SeO}_{2/2}\text{O}_{1/3})^{+4/3} \text{3}(\text{SeO}_{1/1}\text{O}_{2/2})^0]^{6-}$  with charge balance maintained by six  $\text{Li}^+$  cations. The  $\text{Mo}^{6+}$  cations are octahedrally coordinated to six oxygen atoms with two ‘short’ (1.684(6) - 1.715(6) Å), two ‘normal’ (1.942(4) - 1.989(6) Å), and two ‘long’ (2.173(6) - 2.303(5) Å) Mo-O bonds. The ‘short’ Mo-O bonds are terminal, and as expected the  $\text{Mo}^{6+}$  displaces towards these terminal oxygen atoms, i.e., an edge,  $\text{C}_2$ -type distortion. The  $\text{Se}^{4+}$  cations are in trigonal pyramidal environments, coordinated to three oxygen atoms with Se-O bond distances that range between 1.629(8) - 1.757(5) Å. The  $\text{Li}^+$  cations are observed in four-, five-, and six-coordinate environments, bonded to oxygen atoms with Li-O bond lengths in the range of 1.91(2)-2.00(2) Å, 2.00(2)-2.08(2) Å, and 2.04(2)-2.52(2) Å, respectively. Bond valence calculations<sup>82</sup> for  $\text{Li}^+$ ,  $\text{Mo}^{6+}$ ,  $\text{Se}^{4+}$ ,

and  $O^{2-}$  ions resulted in values of 0.93-1.09, 5.96-6.07, 3.89-4.08, and 1.69-2.16, respectively.

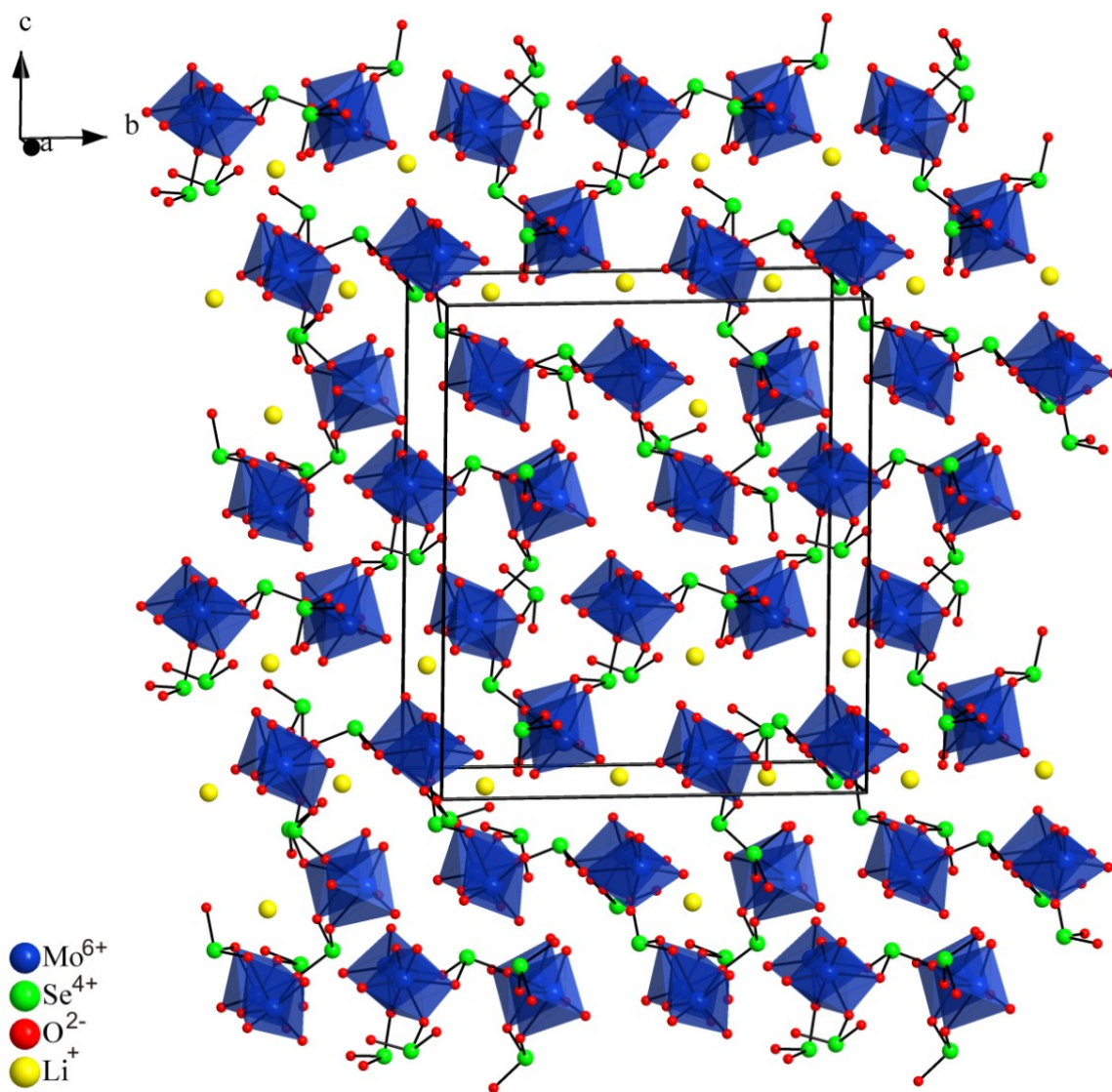


**Figure 4.1** The polyhedral representation of  $Li_6(Mo_2O_5)_3(SeO_3)_6$  in the bc-plane. Spheres in the diagram are  $Li^+$  cations (yellow),  $Mo^{6+}$  cations (blue),  $Se^{4+}$  cations (green), and  $O^{2-}$  anions (red).

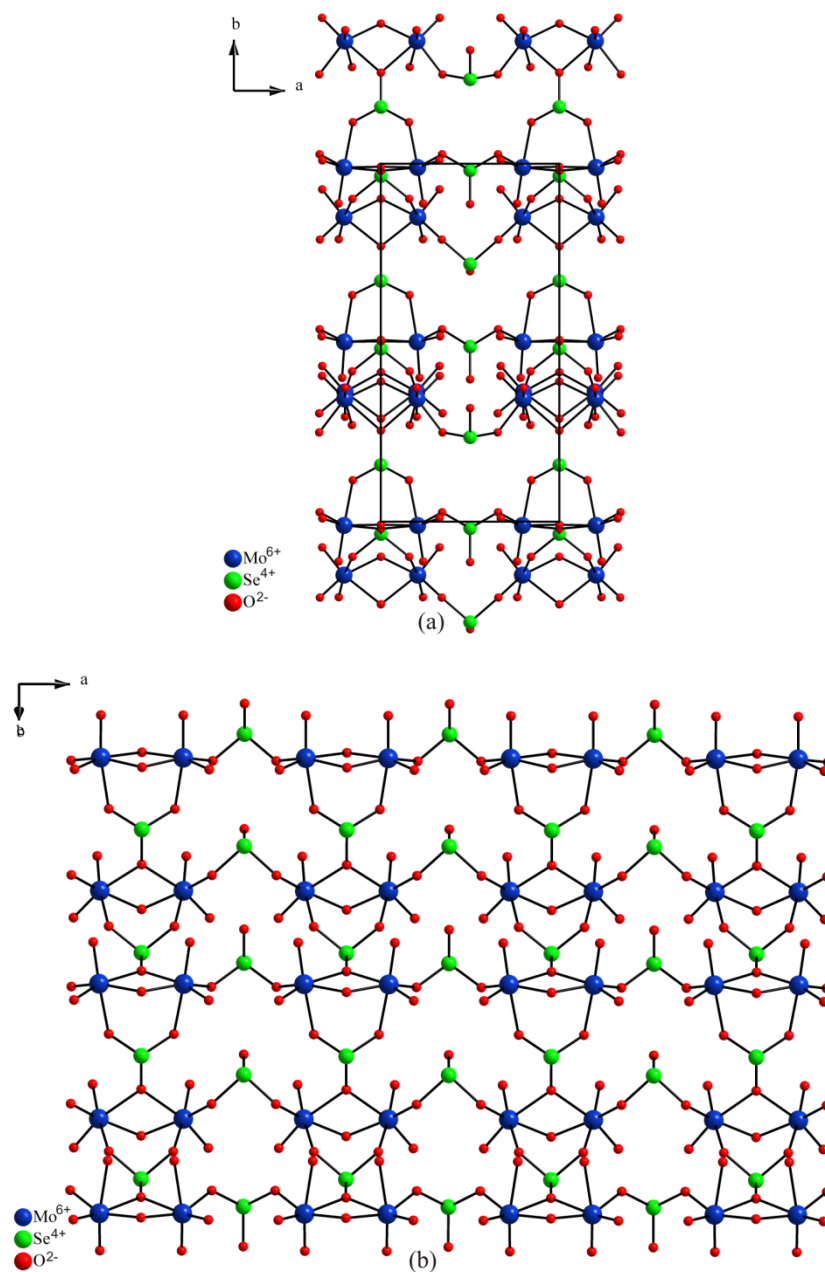


**Figure 4.2** Ball-and-stick representations of  $[6(\text{MoO}_{2/1}\text{O}_{3/2}\text{O}_{1/3})^{-5/3} 3(\text{SeO}_{2/2}\text{O}_{1/3})^{+4/3} 3(\text{SeO}_{1/1}\text{O}_{2/2})^0]^{6-}$  zig-zag layers in the ab-plane (top) and connectivity between Mo<sub>2</sub>O<sub>10</sub> dimers and SeO<sub>3</sub> polyhedra in the layer section (bottom). Spheres in the diagram are Mo<sup>6+</sup> cations (blue), Se<sup>4+</sup> cations (green), and O<sup>2-</sup> anions (red). The Li<sup>+</sup> cations have been removed for clarity.

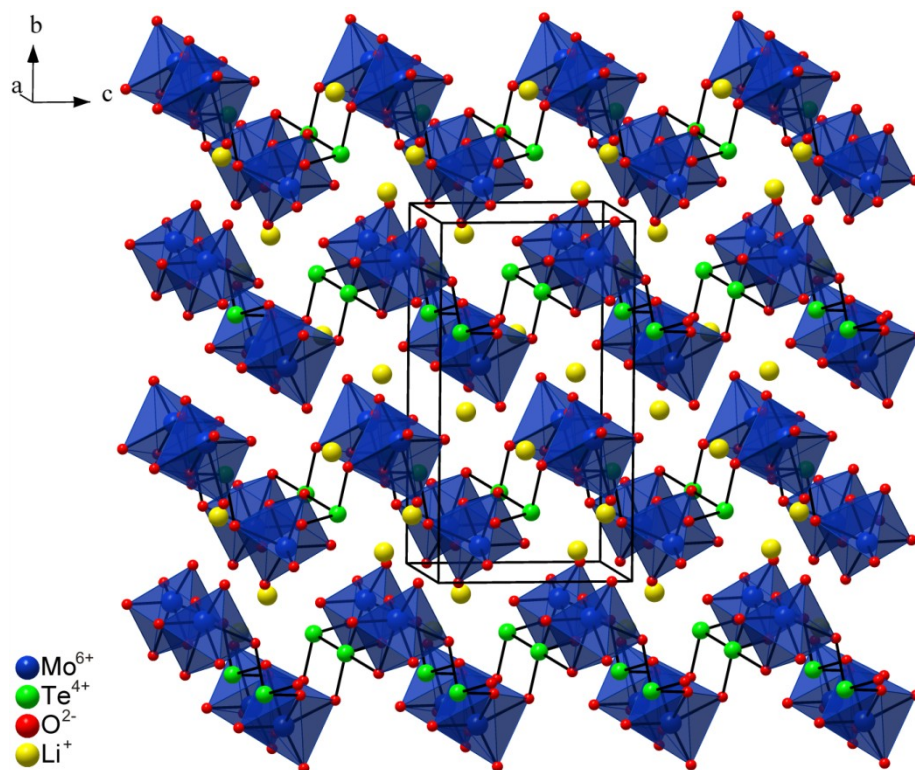


**Figure 4.3** The polyhedral representation of  $\text{Li}_2(\text{MoO}_3)(\text{TeO}_3)$  in the  $bc$ -plane. Spheres in the diagram are  $\text{Li}^+$  cations (yellow),  $\text{Mo}^{6+}$  cations (blue),  $\text{Te}^{4+}$  cations (green), and  $\text{O}^{2-}$  anions (red).

The isostructural materials,  $\text{Li}_2(\text{MoO}_3)(\text{TeO}_3)$  and  $\text{Li}_2(\text{WO}_3)(\text{TeO}_3)$ , crystallize in the CS monoclinic space group  $\text{P}2_1/n$ . Polyhedral representations of  $\text{Li}_2(\text{MoO}_3)(\text{TeO}_3)$  in the  $bc$ -plane are shown in Figure 4.3. Both materials also exhibit zigzag layers that consist of  $\text{MO}_6$  octahedra and  $\text{TeO}_3$  polyhedra (see Figure 4.4a). Each  $\text{MO}_6$  ( $\text{M} = \text{Mo}^{6+}$  or  $\text{W}^{6+}$ ) octahedron is connected to three  $\text{TeO}_3$  polyhedra, and each  $\text{TeO}_3$  polyhedron is also connected to three  $\text{MO}_6$  octahedra to form a layer in  $ac$ -plane (see Figure 4.4b). The layers stack along the  $b$ -axis direction, and are separated by the  $\text{Li}^+$  cations (see Figures 4.3). In connectivity terms, the structures may be written as  $[(\text{MO}_{3/1}\text{O}_{3/2})^{-3}(\text{TeO}_{3/2})^{+}]^{2-}$  with charge balance maintained by two  $\text{Li}^+$  cations.  $\text{Mo}^{6+}$  ( $\text{W}^{6+}$ )

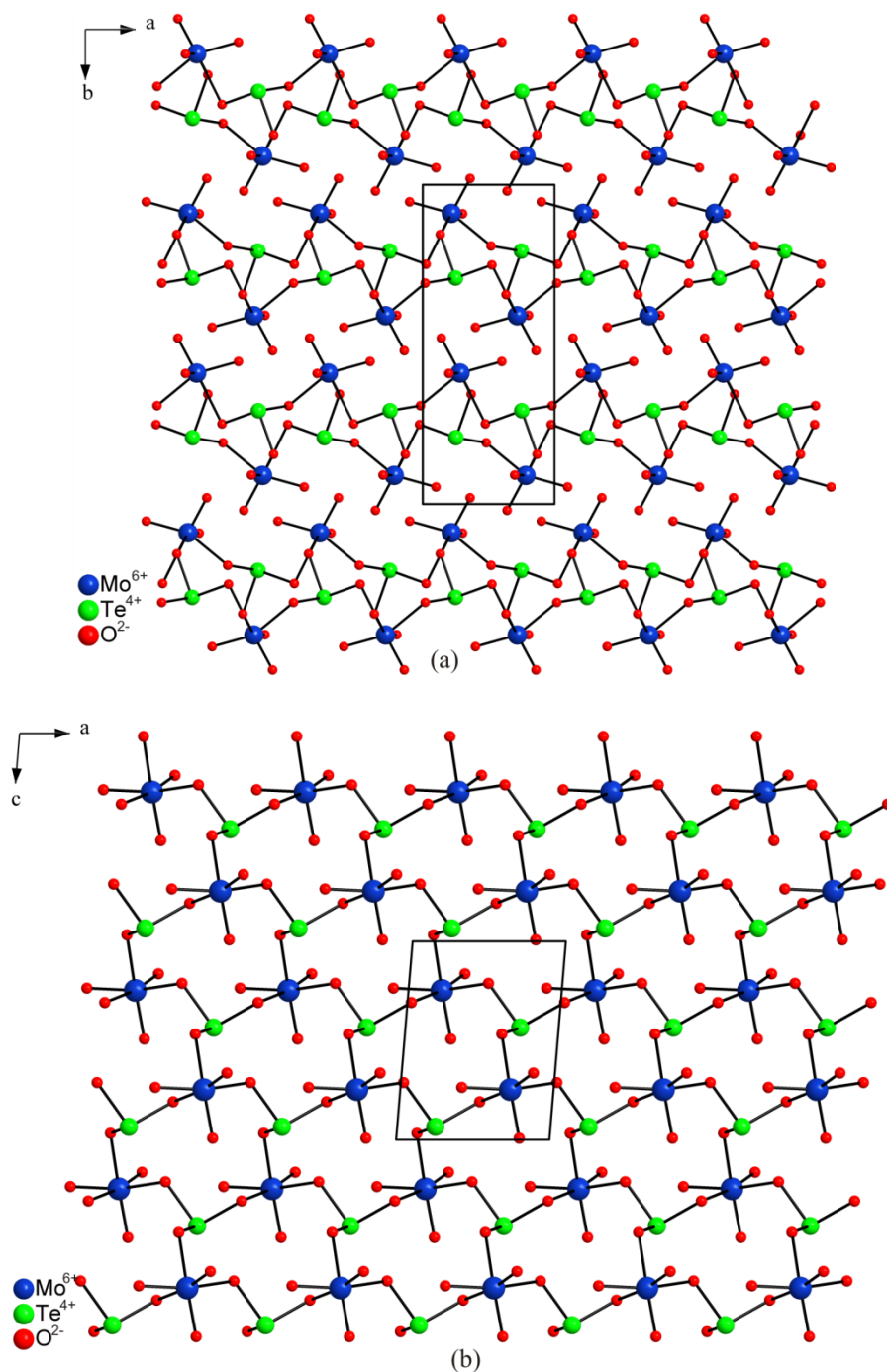


**Figure 4.4** Ball-and-stick representations of  $[(\text{MO}_3\text{O}_{3/2})_3 (\text{TeO}_{3/2})_1]^{2-}$  zig-zag layers in the  $ab$ -plane (top) and connectivity between  $\text{MoO}_6$  and  $\text{TeO}_3$  polyhedra in the layer (bottom). Spheres in the diagram are  $\text{Mo}^{6+}$  cations (blue),  $\text{Te}^{4+}$  cations (green), and  $\text{O}^{2-}$  anions (red). The  $\text{Li}^+$  cations have been removed for clarity.

cations are octahedrally coordinated to six O atoms with three ‘short’, 1.733(3) - 1.768(3) Å (1.755(4) - 1.796(4) Å) and three ‘long’, 2.124(3) - 2.369(3) Å, (2.091(4) - 2.314(4) Å) M-O bonds. The ‘short’ M-O bonds are terminal, and as expected the  $M^{6+}$  cation displaces towards these terminal oxygen atoms, i.e., a face,  $C_3$ -type distortion. The  $Te^{4+}$  cations are in trigonal pyramidal environments, coordinated to three oxygen atoms with Te-O bond distances that range between 1.869(3) - 1.920(3) Å (1.878(3) - 1.929(3) Å) for  $Li_2(MoO_3)(TeO_3)$  ( $Li_2(WO_3)(TeO_3)$ ). The  $Li^+$  cations are observed in four- and five-coordinate environments, bonded to oxygen atoms with Li-O bond lengths in the range of 1.929(10) - 2.106(10) Å and 1.964(11) - 2.273(11) Å, respectively. Bond valence calculations<sup>82</sup> for  $Li^+$ ,  $Mo^{6+}$  ( $W^{6+}$ ),  $Te^{4+}$ , and  $O^{2-}$  ions resulted in values of 0.84-1.01, 6.00(6.00), 3.64-3.74, and 1.78-2.12, respectively.

### **Octahedral Distortion, ELF, Dipole Moments, BSI and GII Calculations**

As mentioned earlier,  $Li_6(Mo_2O_5)_3(SeO_3)_6$  and  $Li_2(MO_3)(TeO_3)$  ( $M = Mo^{6+}$  or  $W^{6+}$ ) contain SOJT distorted cations, i.e. octahedrally coordinated  $d^0$  transition metal cations,  $Mo^{6+}$  and  $W^{6+}$ , and lone-pair cations,  $Se^{4+}$  and  $Te^{4+}$ . We are able to quantify the magnitude of the displacement of the  $M^{6+}$  cations by using the SHAPE program.<sup>83</sup> In the reported materials, the displacement magnitude is approximately 0.11 – 0.13 Å<sup>2</sup> (see Table 4.7). These values are consistent with those reported for  $Mo^{6+}$  and  $W^{6+}$  cations.<sup>84</sup>

With the lone-pair cations, ELF calculations were performed. As seen in Figure 4.5, violet lobe-like ELF isosurfaces ( $\eta = 0.9$ ) above the  $SeO_3$  and  $TeO_3$  polyhedra are consistent with a stereoactive lone-pair. In order to quantitatively examine the polarization magnitudes and directions of the  $MO_6$  and  $AO_3$  polyhedra, the dipole

moments were calculated using a method described earlier,<sup>21</sup> and extended subsequently for lone-pair cations.<sup>85</sup> The calculated dipole moments for the MoO<sub>6</sub>, WO<sub>6</sub>, SeO<sub>3</sub>, and TeO<sub>3</sub> polyhedra are 4.4-6.9D, 2.8D, 7.9-9.5D, and 13.1-13.5D, respectively. These values are consistent with those reported earlier.<sup>48,86</sup> The smaller dipole moment for the WO<sub>6</sub> octahedron is reasonable since in the method used, the magnitude of the dipole moment is inversely proportional to the atomic number. The approximate direction of the dipole moments of the MoO<sub>6</sub>, WO<sub>6</sub>, SeO<sub>3</sub>, and TeO<sub>3</sub> polyhedra are shown in Figure 4.5. With Li<sub>2</sub>(MO<sub>3</sub>)(TeO<sub>3</sub>) (M = Mo<sup>6+</sup> or W<sup>6+</sup>), the MO<sub>6</sub> and TeO<sub>3</sub> polyhedra in two adjacent [(MO<sub>3/1</sub>O<sub>3/2</sub>)<sup>-3</sup> (TeO<sub>3/2</sub>)<sup>+</sup>]<sup>2-</sup> layers are oriented in an anti-parallel manner that results in complete cancelation of the individual dipole moments. Whereas for Li<sub>6</sub>(Mo<sub>2</sub>O<sub>5</sub>)<sub>3</sub>(SeO<sub>3</sub>)<sub>6</sub>, the dipole moments of the MoO<sub>6</sub> and SeO<sub>3</sub> polyhedra are partly aligned along the c-axis - consistent with the polar axis direction of the crystal class, *mm2*.<sup>87</sup> However, as Li<sub>6</sub>(Mo<sub>2</sub>O<sub>5</sub>)<sub>3</sub>(SeO<sub>3</sub>)<sub>6</sub> has a zigzag layer topology (see Figure 4.1), the dipole moments of the MoO<sub>6</sub> and SeO<sub>3</sub> polyhedra do not fully ‘constructively add’, and only a small dipole moment of 3.7 D per unit cell is observed.

In order to better understand the influence of the polar MO<sub>6</sub> and AO<sub>3</sub> polyhedra on the structures of the reported materials, bond strain and global instability indices, BSI and GII respectively, were calculated.<sup>82,88,89</sup> The BSI and GII indices are indicative of electronic- and lattice-induced strains respectively. Values greater than 0.05 vu (valence units) indicate that the structures are strained. For the reported materials, the BSI and GII values are greater than 0.05 vu. This is not surprising given the occurrence of asymmetric polyhedra. As seen in Table 4, the BSI values are very similar, i.e., 0.11 – 0.12 vu. The BSI is attributable to electronic, or SOJT, distortions, and as the reported materials have



similar SOJT distorted cations it is reasonable to expect the BSI values to be similar. The GII indices increase from  $\text{Li}_6(\text{Mo}_2\text{O}_5)_3(\text{SeO}_3)_6$  (0.09 vu) to  $\text{Li}_2(\text{MoO}_3)(\text{TeO}_3)$  (0.14 vu) and  $\text{Li}_2(\text{WO}_3)(\text{TeO}_3)$  (0.17 vu). With  $\text{BSI} > \text{GII}$ , as is the situation with  $\text{Li}_6(\text{Mo}_2\text{O}_5)_3(\text{SeO}_3)_6$ , the structural strains are electronically induced, i.e., the bond distances of the SOJT distorted cations are mainly determined by electronic distortions. With  $\text{BSI} < \text{GII}$ , as is the case for  $\text{Li}_2(\text{MoO}_3)(\text{TeO}_3)$  and  $\text{Li}_2(\text{WO}_3)(\text{TeO}_3)$ , the structural strains are lattice-induced, i.e., the bond distances of the SOJT distorted cations – specifically  $\text{Te}^{4+}$  – are impacted greatly by the surrounding polyhedra. The average Te-O bond distances in  $\text{Li}_2(\text{MoO}_3)(\text{TeO}_3)$  and  $\text{Li}_2(\text{WO}_3)(\text{TeO}_3)$  are 1.896 Å and 1.907 Å respectively, longer than what is usually observed.<sup>33,63</sup> As such, the bond valence sums for the  $\text{Te}^{4+}$  cations in these materials are reduced and the GII increases.

**Table 4.6** Bond valence sum (vu), bond strain index, BSI (vu), global instability index, GII(vu), and net dipole moments,  $\mu$  (Debye) of  $\text{Li}_6(\text{Mo}_2\text{O}_5)_3(\text{SeO}_3)_6$  and  $\text{Li}_2(\text{MO}_3)(\text{TeO}_3)$  ( $\text{M} = \text{Mo}^{6+}$  or  $\text{W}^{6+}$ ).

Compound	Bond Valence Sum			BSI	GII	$\mu$
	$\text{Li}^+$	$\text{M}^{6+}$	$\text{A}^{4+}$			
$\text{Li}_6(\text{Mo}_2\text{O}_5)_3(\text{SeO}_3)_6$	0.93-1.09	5.96-6.07	3.89-4.08	0.12	0.09	10.4
$\text{Li}_2(\text{MoO}_3)(\text{TeO}_3)$	0.86-1.01	6.00	3.74	0.11	0.14	0.0
$\text{Li}_2(\text{WO}_3)(\text{TeO}_3)$	0.84-1.00	6.00	3.64	0.11	0.17	0.0



**Table 4.7** Distortion magnitudes of MO<sub>6</sub> octahedra and dipole moments of MO<sub>6</sub> (M = Mo<sup>6+</sup> or W<sup>6+</sup>) and AO<sub>3</sub> (A = Se<sup>4+</sup> or Te<sup>4+</sup>) polyhedra in Li<sub>6</sub>(Mo<sub>2</sub>O<sub>5</sub>)<sub>3</sub>(SeO<sub>3</sub>)<sub>6</sub> and Li<sub>2</sub>(MO<sub>3</sub>)(TeO<sub>3</sub>).

Compounds		Polyhedral dipole moment (Debye)				MO <sub>6</sub> distortion magnitude (Å <sup>2</sup> )	
Li <sub>6</sub> (Mo <sub>2</sub> O <sub>5</sub> ) <sub>3</sub> (SeO <sub>3</sub> ) <sub>6</sub>	Mo(1)O <sub>6</sub>	5.7	Se(4)O <sub>3</sub>	7.9	Li(1)O <sub>4</sub>	2.3	0.12
	Mo(2)O <sub>6</sub>	5.1	Se(5)O <sub>3</sub>	8.6	Li(2)O <sub>5</sub>	1.5	0.12
	Mo(3)O <sub>6</sub>	5.1	Se(6)O <sub>3</sub>	8.2	Li(3)O <sub>4</sub>	2.1	0.11
	Mo(4)O <sub>6</sub>	5.2	Se(7)O <sub>3</sub>	9.1	Li(4)O <sub>5</sub>	0.4	0.11
	Mo(5)O <sub>6</sub>	5.5	Se(8)O <sub>3</sub>	9.5	Li(5)O <sub>6</sub>	1.7	0.12
	Mo(6)O <sub>6</sub>	4.4	Se(9)O <sub>3</sub>	8.7	Li(6)O <sub>6</sub>	1.3	0.11
	Se(1)O <sub>3</sub>	8.1	Se(10)O <sub>3</sub>	8.5	Li(7)O <sub>6</sub>	1.4	
	Se(2)O <sub>3</sub>	8.6	Se(11)O <sub>3</sub>	8.4	Li(8)O <sub>5</sub>	6.6	
	Se(3)O <sub>3</sub>	8.5	Se(12)O <sub>3</sub>	8.4			
Li <sub>2</sub> (MoO <sub>3</sub> )(TeO <sub>3</sub> )	MoO <sub>6</sub>	6.9	TeO <sub>3</sub>	8.1	Li(1)O <sub>4</sub>	3.6	0.13
					Li(2)O <sub>5</sub>	4.1	
Li <sub>2</sub> (WO <sub>3</sub> )(TeO <sub>3</sub> )	WO <sub>6</sub>	2.8	TeO <sub>3</sub>	7.6	Li(1)O <sub>4</sub>	3.1	0.11
					Li(1)O <sub>5</sub>	4.1	

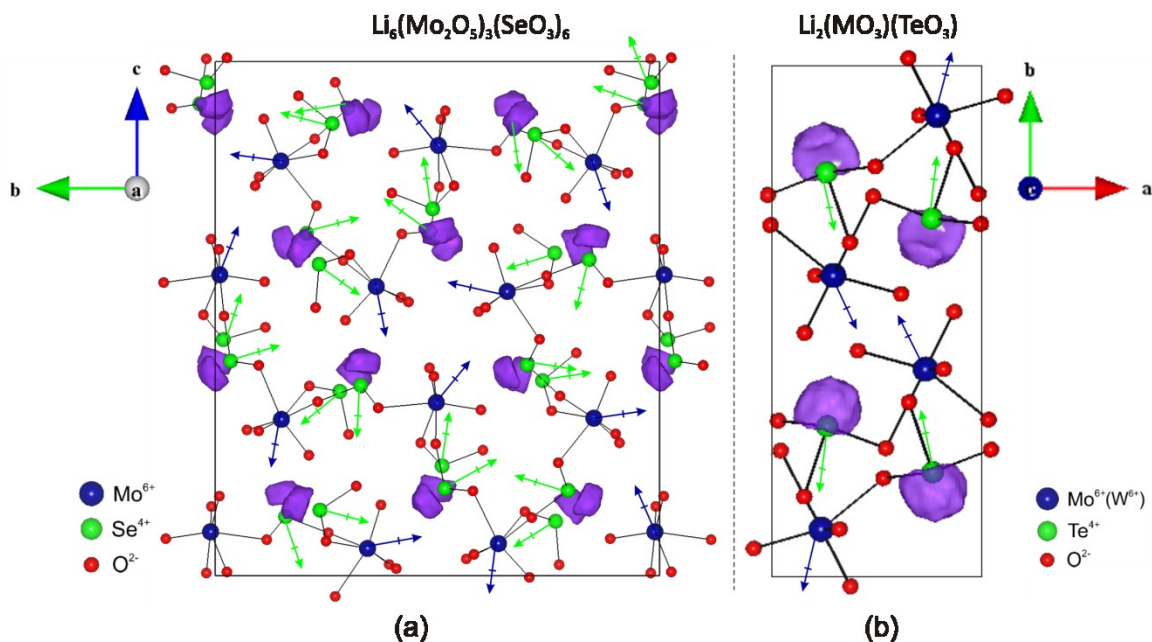


**Figure 4.5** Ball-and-stick representations of (a)  $\text{Li}_6(\text{Mo}_2\text{O}_5)_3(\text{SeO}_3)_6$  in bc-plane and (b)  $\text{Li}_2(\text{MO}_3)(\text{TeO}_3)$  ( $\text{M} = \text{Mo}^{6+}$  or  $\text{W}^{6+}$ ) in ab-plane. The arrows indicate the approximate directions of the dipole moments of the  $\text{MoO}_6$  (blue) and  $\text{AO}_3$  ( $\text{A} = \text{Se}^{4+}$  or  $\text{Te}^{4+}$ ) (green) polyhedra in the unit cell. Electron localization function (ELF) plots with  $\eta = 0.9$  is also shown. The lobe-like isosurfaces near top of  $\text{AO}_3$  polyhedra are consistent with a stereo-active lone-pair on the A cations. The  $\text{Li}^+$  cations have been removed for clarity.

### Infrared Spectroscopy

The infrared (IR) spectra for  $\text{Li}_6(\text{Mo}_2\text{O}_5)_3(\text{SeO}_3)_6$  and  $\text{Li}_2(\text{MO}_3)(\text{TeO}_3)$  ( $\text{M} = \text{Mo}^{6+}$  or  $\text{W}^{6+}$ ) showed no absorption bands in the IR region of  $4000\text{--}1000\text{ cm}^{-1}$ . Both spectra revealed absorption bands of  $\text{Mo(W)}\text{--O}$ ,  $\text{Se(Te)}\text{--O}$  vibrations in the  $400\text{--}1000\text{ cm}^{-1}$  range. The  $\text{Mo(W)}\text{--O}$  stretching vibrations were observed around  $811\text{--}940\text{ cm}^{-1}$ , whereas  $\text{Se(Te)}\text{--O}$  stretching vibrations were seen around  $673\text{--}750\text{ cm}^{-1}$ . The absorption band

occurring below  $650\text{ cm}^{-1}$  can be assigned to Mo(W)–O–Se(Te) bending vibrations.

These assignments are in good agreement with the literature (see Figure 4.6).<sup>90-92</sup>

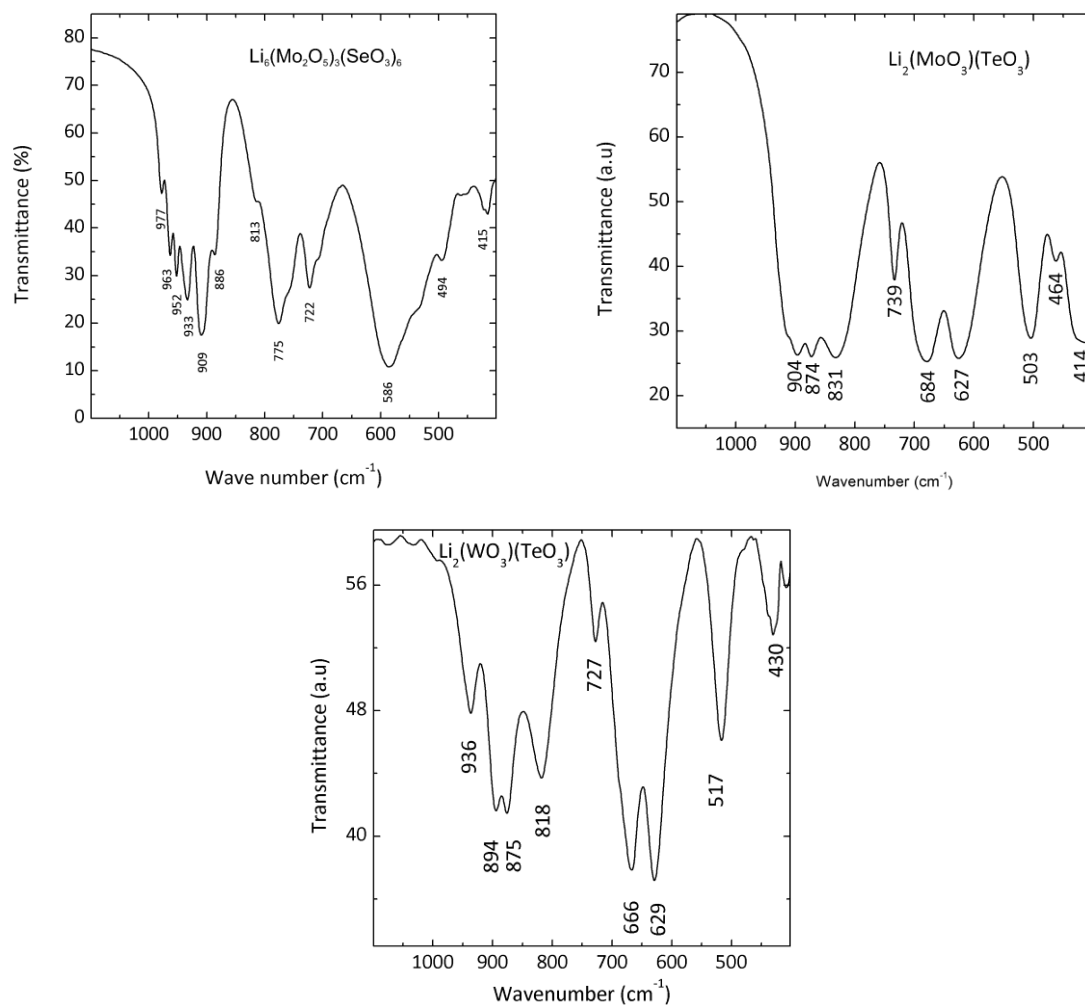


**Figure 4.6** IR data and assignments for  $\text{Li}_6(\text{Mo}_2\text{O}_5)_3(\text{SeO}_3)_6$  and  $\text{Li}_2(\text{MO}_3)(\text{TeO}_3)$  ( $\text{M} = \text{Mo}^{6+}$  or  $\text{W}^{6+}$ ).

**Table 4.8** IR peak assignments for  $\text{Li}_6(\text{Mo}_2\text{O}_5)_3(\text{SeO}_3)_6$  and  $\text{Li}_2(\text{MO}_3)(\text{TeO}_3)$  ( $\text{M} = \text{Mo}^{6+}$  or  $\text{W}^{6+}$ ).

Compound	Infrared absorption bands ( $\text{cm}^{-1}$ )		
	M-O ( $\text{M} = \text{Mo}^{6+}$ or $\text{W}^{6+}$ )	A-O ( $\text{A} = \text{Se}^{4+}$ or $\text{Te}^{4+}$ )	M-O-A
$\text{Li}_6(\text{Mo}_2\text{O}_5)_3(\text{SeO}_3)_6$	977, 952		
	933, 909, 886	775, 722	586, 494, 415
$\text{Li}_2(\text{WO}_3)(\text{TeO}_3)$	936, 896, 874, 815	728, 667, 628	516, 475, 421
$\text{Li}_2(\text{MoO}_3)(\text{TeO}_3)$	904, 874, 831	739, 684, 627	503, 464, 414

### UV–vis Diffuse Reflectance Spectroscopy

Reflectance spectra of  $\text{Li}_6(\text{Mo}_2\text{O}_5)_3(\text{SeO}_3)_6$  and  $\text{Li}_2(\text{MO}_3)(\text{TeO}_3)$  ( $\text{M} = \text{Mo}^{6+}$  or  $\text{W}^{6+}$ ) were converted to absorbance using the Kubelka–Munk function:<sup>70,71</sup>

$$F(R) = \frac{K}{S} = \frac{(1 - R)^2}{2R} \quad (4.1)$$

where  $R$ ,  $K$ , and  $S$  represent the reflectance, the absorption, and the scattering, respectively. In a  $F(R)$  versus  $E$  (eV) plot, extrapolating the linear part of the rising curve to zero provides onset absorption of 3.3 eV, 3.5 eV, and 4.0 eV for  $\text{Li}_6(\text{Mo}_2\text{O}_5)_3(\text{SeO}_3)_6$ ,  $\text{Li}_2(\text{MoO}_3)(\text{TeO}_3)$ , and  $\text{Li}_2(\text{WO}_3)(\text{TeO}_3)$ , respectively (see Figure 4.7). These values are consistent with the transparency of the materials in the visible wavelength.

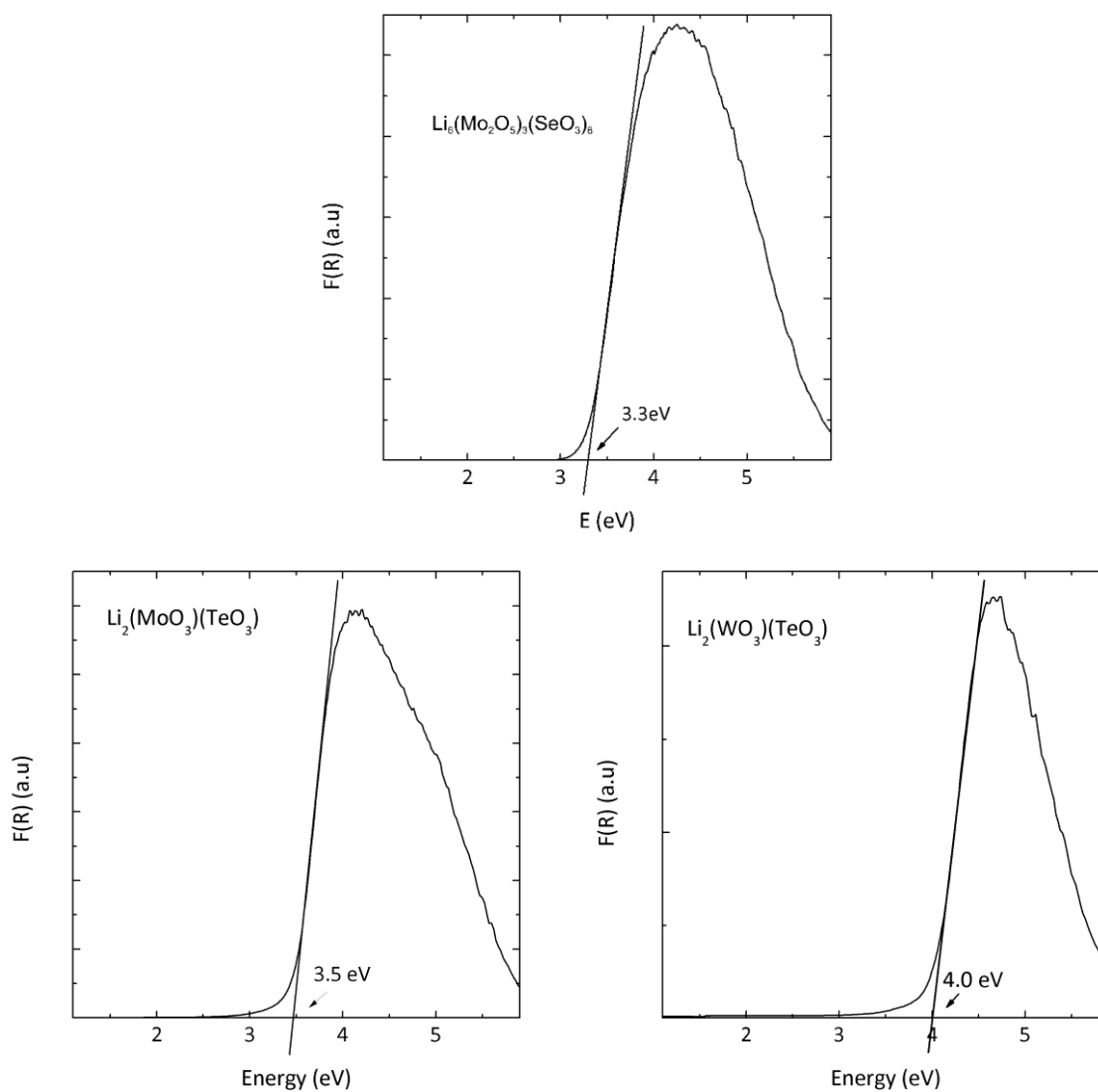


**Figure 4.7** UV–vis diffuse reflectance spectroscopy data for  $\text{Li}_6(\text{Mo}_2\text{O}_5)_3(\text{SeO}_3)_6$  and  $\text{Li}_2(\text{MO}_3)(\text{TeO}_3)$  ( $\text{M} = \text{Mo}^{6+}$  or  $\text{W}^{6+}$ ).

## Thermal Analysis

The thermal stability of  $\text{Li}_6(\text{Mo}_2\text{O}_5)_3(\text{SeO}_3)_6$ ,  $\text{Li}_2(\text{MoO}_3)(\text{TeO}_3)$  and  $\text{Li}_2(\text{WO}_3)(\text{TeO}_3)$  were investigated through thermogravimetric and differential thermal analyses (TGA and DTA). The TGA and DTA data of  $\text{Li}_6(\text{Mo}_2\text{O}_5)_3(\text{SeO}_3)_6$  indicated that the material releases  $\text{SeO}_2$  at  $\sim 460^\circ\text{C}$  and decomposes to  $\text{Li}_4\text{Mo}_5\text{O}_{17}$ . The experimental weight loss (41.4%) indicate that  $\text{Li}_6(\text{Mo}_2\text{O}_5)_3(\text{SeO}_3)_6$  releases six  $\text{SeO}_2$  equivalents during its thermal decomposition (calculated weight loss of 41.0%). The endothermic peak at  $\sim 520^\circ\text{C}$  on the heating curve and the exothermic peak at  $\sim 450^\circ\text{C}$  on the cooling curve of  $\text{Li}_6(\text{Mo}_2\text{O}_5)_3(\text{SeO}_3)_6$  are attributable to the melting and cooling processes of a congruent melting oxide,  $\text{Li}_4\text{Mo}_5\text{O}_{17}$ .<sup>93</sup> For  $\text{Li}_2(\text{MoO}_3)(\text{TeO}_3)$ , the heating curve showed a large endothermic peak at  $\sim 470^\circ\text{C}$  indicating  $\text{Li}_2(\text{MoO}_3)(\text{TeO}_3)$  had melted. For  $\text{Li}_2(\text{WO}_3)(\text{TeO}_3)$ , the heating curve revealed a small endothermic peak at  $\sim 485^\circ\text{C}$  and a large endothermic peak  $\sim 560^\circ\text{C}$  indicating that  $\text{Li}_2(\text{WO}_3)(\text{TeO}_3)$  had melted. No peak was observed on the cooling curves of both oxides and no weight loss was found on their TGA curves up to  $700^\circ\text{C}$ . The PXRD patterns of the residuals showed  $\text{Li}_2(\text{WO}_3)(\text{TeO}_3)$  decomposed to  $\text{Li}_2\text{WO}_4$ , whereas  $\text{Li}_2(\text{MoO}_3)(\text{TeO}_3)$  decomposed to  $\text{Li}_2\text{MoO}_4$ . The DTA and TGA data are shown in the Figure 4.8.

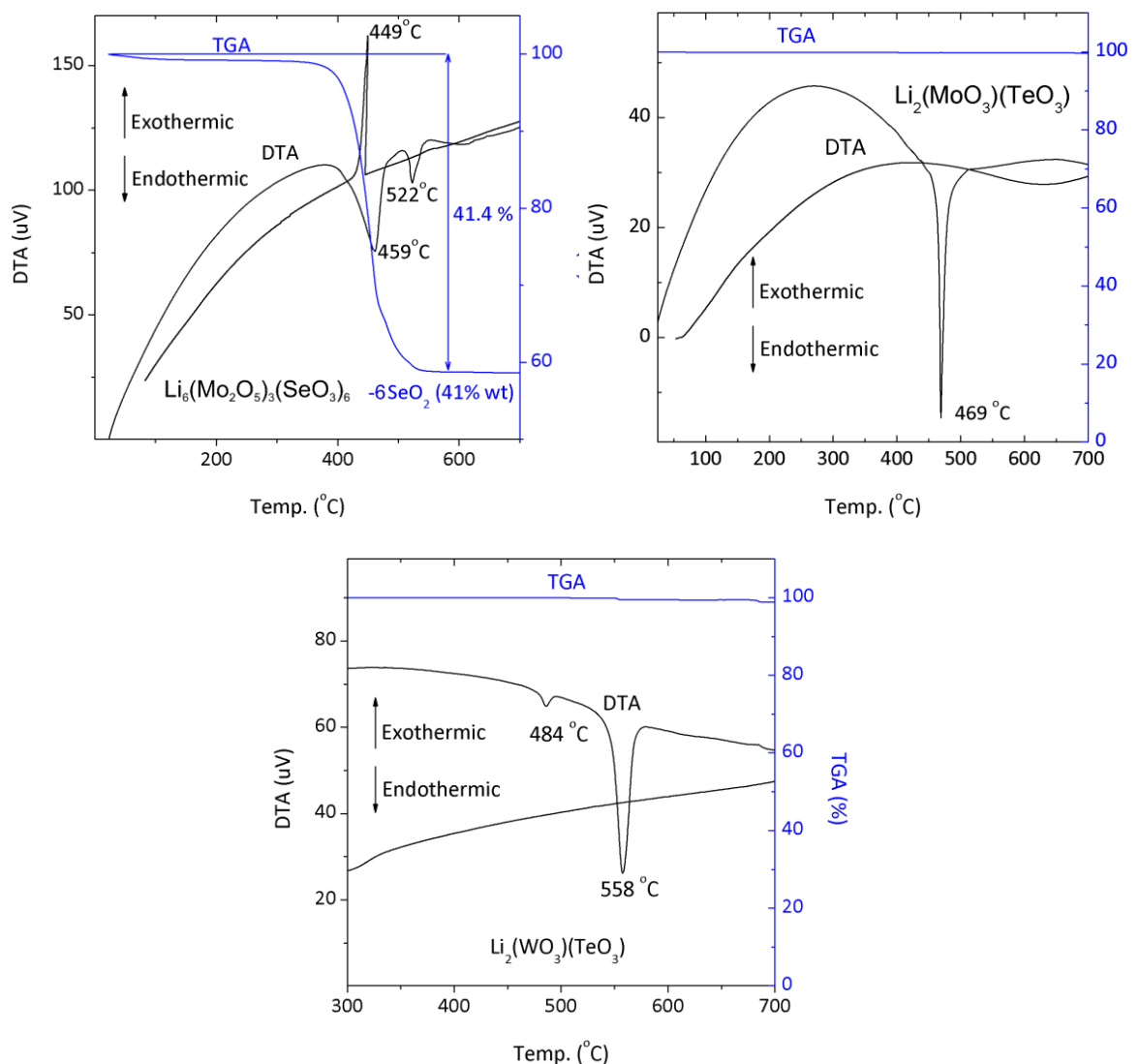


**Figure 4.8** Thermogravimetric and differential thermal analysis data for  $\text{Li}_6(\text{Mo}_2\text{O}_5)_3(\text{SeO}_3)_6$  and  $\text{Li}_2(\text{MO}_3)(\text{TeO}_3)$  ( $\text{M} = \text{Mo}^{6+}$  or  $\text{W}^{6+}$ ).

### Second-harmonic Generation

Powder SHG measurements on  $\text{Li}_6(\text{Mo}_2\text{O}_5)_3(\text{SeO}_3)_6$  indicated the material has an SHG efficiency of approximately  $170 \times \alpha\text{-SiO}_2$  in the particle size range of 45–63  $\mu\text{m}$ . The SHG efficiency as a function of particle size was measured, in the particle size range of 25–120  $\mu\text{m}$ . The measurements indicated that  $\text{Li}_6(\text{Mo}_2\text{O}_5)_3(\text{SeO}_3)_6$  is type 1 non-phase

matching.  $\text{Li}_6(\text{Mo}_2\text{O}_5)_3(\text{SeO}_3)_6$  falls into the class C of SHG materials as defined by Kurtz and Perry.<sup>72</sup> The average NLO susceptibility,<sup>73</sup>  $\langle d_{\text{eff}} \rangle_{\text{exp}}$ , can be estimated to be approximately 9.8 pm/V, compared to recently reported SHG efficiency of  $\text{Ba}(\text{Mo}_2\text{O}_5)(\text{SeO}_3)_2$  (10.3 pm/V).<sup>9</sup> The moderate SHG is attributable to the net polarization – the partial addition of the  $\text{MoO}_6$  and  $\text{SeO}_3$  dipole moments. As mentioned earlier, the alignment of their dipole moments along c-axis direction gives rise to the net dipole moment of 3.7 D per unit cell. That net dipole moment contributes not only to the SHG efficiency of  $\text{Li}_6(\text{Mo}_2\text{O}_5)_3(\text{SeO}_3)_6$  but also to its pyroelectric behavior. The powder SHG data are shown in the Figure 4.9.

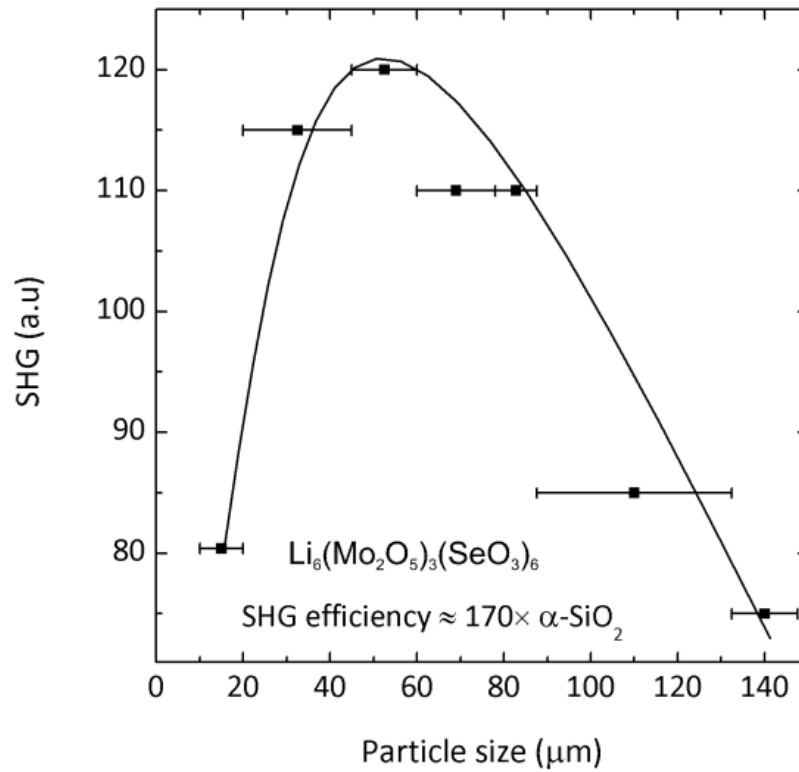


**Figure 4.9** Particle-size vs. SHG intensity data for  $\text{Li}_6(\text{Mo}_2\text{O}_5)_3(\text{SeO}_3)_6$ . The curve is drawn to guide the eye and is not a fit to the data.



## Piezoelectric Measurements

Converse piezoelectric measurements were performed on a  $\text{Li}_6(\text{Mo}_2\text{O}_5)_3(\text{SeO}_3)_6$  pellet at room temperature. A voltage of 750 V at 200 Hz was applied to  $\text{Li}_6(\text{Mo}_2\text{O}_5)_3(\text{SeO}_3)_6$ . The  $d_{33}$  piezoelectric charge constant,<sup>73</sup> which is defined as the ratio between the strain produced and the electrical voltage applied, for  $\text{Li}_6(\text{Mo}_2\text{O}_5)_3(\text{SeO}_3)_6$  was estimated to be 28 pm/V. This charge constant is comparable to that of  $\text{Zn}_2(\text{MoO}_4)(\text{SeO}_3)$  ( $d_{33} = 14$  pm/V).<sup>94</sup> The piezoelectric data are shown in Figure 4.10.

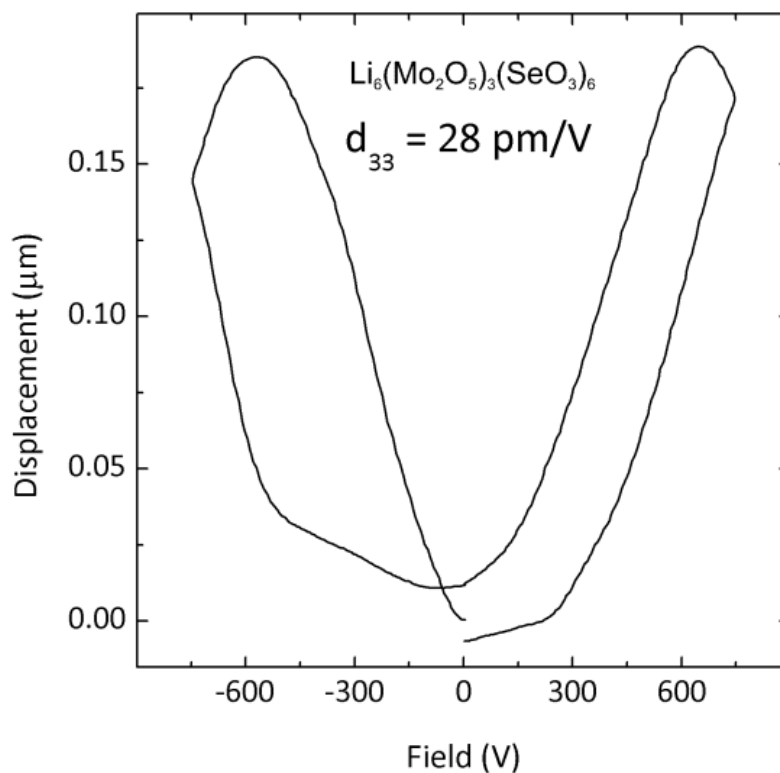


**Figure 4.10** The displacement vs. electric field plot for  $\text{Li}_6(\text{Mo}_2\text{O}_5)_3(\text{SeO}_3)_6$ .

## Polarization Measurements

$\text{Li}_6(\text{Mo}_2\text{O}_5)_3(\text{SeO}_3)_6$  is not only NCS, but also polar – a macroscopic dipole moment is observed. The macroscopic polarity suggests the possibility for ferroelectric behavior.

Ferroelectric hysteresis measurements were performed on pressed pellets, and ‘polarization loops’ were observed. In addition, these loops did appear to exhibit frequency dependence (see Figure 4.11). However, these loops are not attributable to ferroelectric hysteresis, but likely attributable to dielectric loss. Thus the reported materials are not ferroelectric – the macroscopic polarization cannot be reversed in the presence of an external electric field. It has been demonstrated that these types of loops have been erroneously attributed to ferroelectric behavior.<sup>95</sup> With the reported materials, it is important to understand why the materials, although polar, are not ferroelectric. As stated earlier, for ferroelectric behavior to occur the macroscopic polarization must be switchable, or reversible in the presence of an external electric field. This implies that the local moments must also be reversed. In  $\text{Li}_6(\text{Mo}_2\text{O}_5)_3(\text{SeO}_3)_6$  only the  $\text{SeO}_3$  and  $\text{MoO}_6$  polyhedra exhibit a local dipole moment. Thus it is these dipole moments that must be reversed for ferroelectric behavior to occur. We have already shown that the energy barrier to inverse a  $\text{SeO}_3$  trigonal-pyramid is  $\sim 5.3$  eV,<sup>45</sup> which is substantially larger than the value observed in ferroelectric  $\text{BaTiO}_3$  ( $1.8 \times 10^{-2}$  eV) and  $\text{PbTiO}_3$  ( $2.0 \times 10^{-1}$  eV).<sup>96</sup> Thus it is energetically unfavorable for polarization reversal to occur. Therefore,  $\text{Li}_6(\text{Mo}_2\text{O}_5)_3(\text{SeO}_3)_6$  is pyroelectric and not ferroelectric.

Pyroelectric measurements were performed by measuring the polarization ( $P$ ) as a function of temperature. The value of the pyroelectric coefficient, which is defined as  $dP/dT$ ,<sup>73</sup> for  $\text{Li}_6(\text{Mo}_2\text{O}_5)_3(\text{SeO}_3)_6$  at 50 °C is  $-0.43 \mu\text{C}/\text{m}^2\text{K}$ . The polarization data were shown in Figure 4.11.

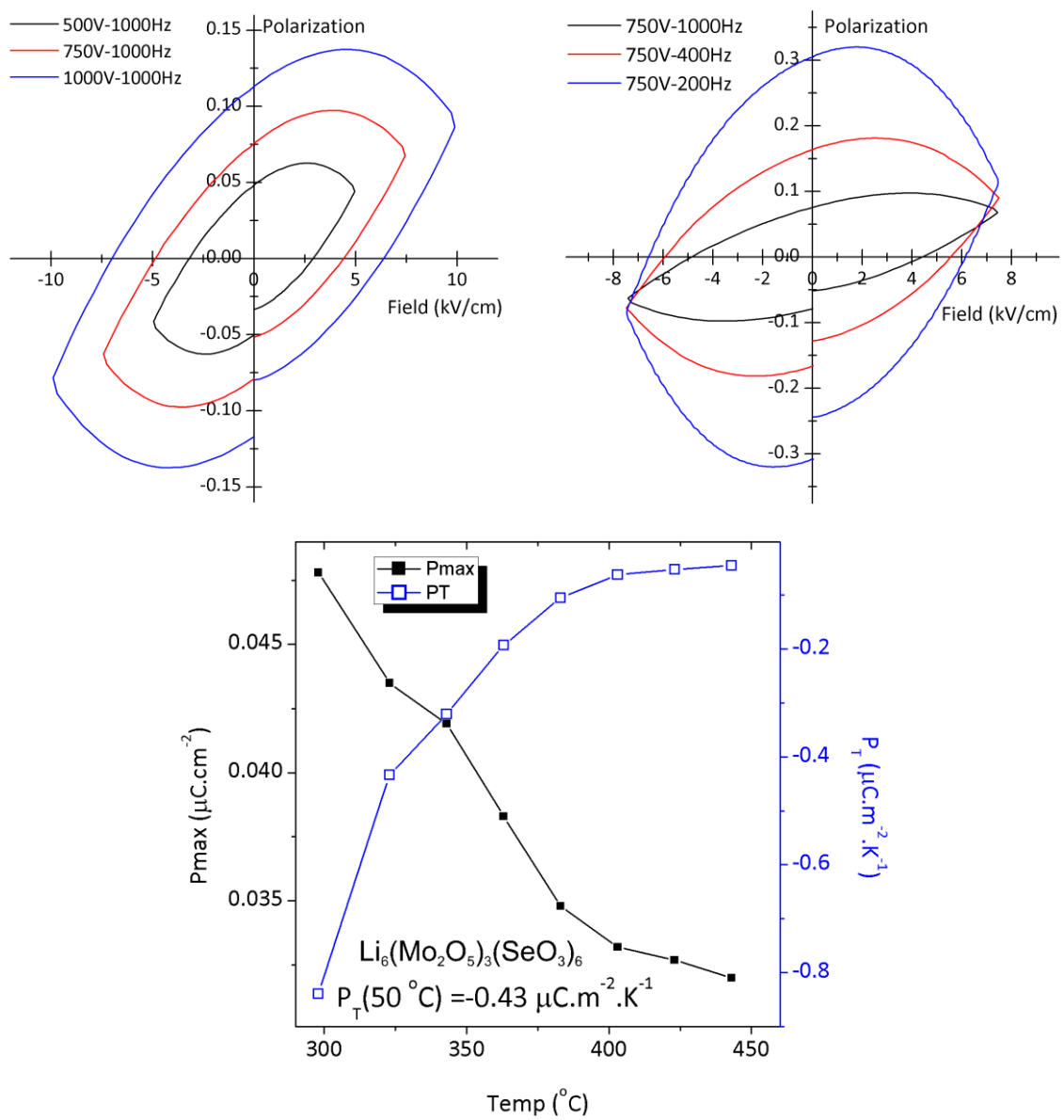


**Figure 4.11** Field-dependent (left) and frequency-dependent (right) polarization-electric field loops and a pyroelectric coefficient vs. temperature plot (bottom) for  $\text{Li}_6(\text{Mo}_2\text{O}_5)_3(\text{SeO}_3)_6$ .

**Table 4.9** SHG efficiency ( $\times \alpha\text{-SiO}_2$ ), piezoelectric response,  $d_{33}$  (pm/V), pyroelectric coefficient,  $P_T$  ( $\mu\text{C}/\text{m}^2\text{K}$ ), and maximum polarization,  $P_m$  ( $\mu\text{C}/\text{m}^2$ ) for  $\text{Li}_6(\text{Mo}_2\text{O}_5)_3(\text{SeO}_3)_6$

Compound	Functional properties			
	SHG	$d_{33}$	$P_T$	$P_m$
$\text{Li}_6(\text{Mo}_2\text{O}_5)_3(\text{SeO}_3)_6$	170	28	-0.43	0.05

#### 4.5 Conclusion

New quaternary lithium –  $d^0$  cation – lone-pair oxides, NCS polar  $\text{Li}_6(\text{Mo}_2\text{O}_5)_3(\text{SeO}_3)_6$  ( $\text{Pmn}2_1$ ) and CS  $\text{Li}_2(\text{MO}_3)(\text{TeO}_3)$  ( $\text{P}2_1/\text{n}$ ) ( $\text{M} = \text{Mo}^{6+}$  or  $\text{W}^{6+}$ ), have been synthesized and characterized. The oxides exhibit a layered structure with distorted  $\text{MO}_6$  ( $\text{M} = \text{Mo}^{6+}$  or  $\text{W}^{6+}$ ) and asymmetric  $\text{AO}_3$  ( $\text{A} = \text{Se}^{4+}$  or  $\text{Te}^{4+}$ ) polyhedra.  $\text{Li}_6(\text{Mo}_2\text{O}_5)_3(\text{SeO}_3)_6$  exhibits a SHG efficiency of  $170 \times \alpha\text{-SiO}_2$  and is type 1 nonphase-matchable. Although  $\text{Li}_6(\text{Mo}_2\text{O}_5)_3(\text{SeO}_3)_6$  is polar, the macroscopic polarization is not reversible, and the material is not ferroelectric.

#### 4.6 References

1. Jona, F.; Shirane, G. *Ferroelectric Crystals*; Pergamon Press, 1961.
2. Jaffe, B.; Cook, W. R. *Piezoelectric Ceramics*; Academic Press, 1971.
3. Munn, R. W.; Ironside, C. N. *Principles and Applications of Nonlinear Optical Materials*; Blackie Academic & Professional: Glasgow 1993.
4. Lang, S. B.; Das-Gupta, D. K. *Pyroelectricity: Fundamentals and Applications*; Academic Press, 2001; Vol. 4.
5. Marvel, M. R.; Lesage, J.; Baek, J.; Halasyamani, P. S.; Stern, C. L.; Poeppelmeier, K. R. *J. Am. Chem. Soc.* **2007**, *129*, 13963.
6. Chang, H.-Y.; Kim, S.-H.; Ok, K. M.; Halasyamani, P. S. *J. Am. Chem. Soc.* **2009**, *131*, 6865.
7. Porter, Y.; Halasyamani, P. S. *J. Solid State Chem.* **2003**, *174*, 441.
8. Yeon, J.; Kim, S.-H.; Hayward, M. A.; Halasyamani, P. S. *Inorg. Chem.* **2011**, *50*, 8663.
9. Oh, S.-J.; Lee, D. W.; Ok, K. M. *Inorg. Chem.* **2012**, *51*, 5393.
10. Donakowski, M. D.; Gautier, R.; Yeon, J.; Moore, D. T.; Nino, J. C.; Halasyamani, P. S.; Poeppelmeier, K. R. *J. Am. Chem. Soc.* **2012**, *134*, 7679.
11. Fry, A. M.; Seibel, H. A.; Lokuhewa, I. N.; Woodward, P. M. *J. Am. Chem. Soc.* **2011**, *134*, 2621.

12. Chen, C. T. *Acta Phys. Sin.* **1976**, 25, 146.
13. Chen, C. T. *Acta Phys. Sin.* **1977**, 26, 124.
14. Chen, C. T. *Acta Phys. Sin.* **1977**, 26, 468.
15. Chen, C. T. *Acta Phys. Sin.* **1979**, 22, 756.
16. Zou, G.; Ye, N.; Huang, L.; Lin, X. *J. Am. Chem. Soc.* **2011**, 133, 20001.
17. Heier, K. R.; Norquist, A. J.; Halasyamani, P. S.; Duarte, A.; Stern, C. L.; Poeppelmeier, K. R. *Inorg. Chem.* **1999**, 38, 762.
18. Welk, M. E.; Norquist, A. J.; Stern, C. L.; Poeppelmeier, K. R. *Inorg. Chem.* **2000**, 39, 3946.
19. Welk, M. E.; Norquist, A. J.; Stern, C. L.; Poeppelmeier, K. R. *Inorg. Chem.* **2001**, 40, 5479.
20. Welk, M. E.; Norquist, A. J.; Arnold, F. P.; Stern, C. L.; Poeppelmeier, K. R. *Inorg. Chem.* **2002**, 41, 5119.
21. Maggard, P. A.; Nault, T. S.; Stern, C. L.; Poeppelmeier, K. R. *J. Solid State Chem.* **2003**, 175, 27.
22. Izumi, H. K.; Kirsch, J. E.; Stern, C. L.; Poeppelmeier, K. R. *Inorg. Chem.* **2005**, 44, 884.
23. Marvel, M. R.; Pinlac, R. A. F.; Lesage, J.; Stern, C. L.; Poeppelmeier, K. R. *Z. Anorg. Allg. Chem.* **2009**, 635, 869.

24. Opik, U.; Pryce, M. H. L. *Proc. R. Soc. London, Ser. A* **1957**, 238, 425.
25. Bader, R. F. W. *Mol. Phys.* **1960**, 3, 137.
26. Bader, R. F. W. *Can. J. Chem.* **1962**, 40, 1164.
27. Pearson, R. G. *J. Am. Chem. Soc.* **1969**, 91, 4947.
28. Goodenough, J. B. *Annu. Rev. Mater. Sci.* **1998**, 28, 1.
29. Pearson, R. G. *J. Mol. Struct.:THEOCHEM* **1983**, 103, 25.
30. Kunz, M.; Brown, I. D. *J. Solid State Chem.* **1995**, 115, 395.
31. Halasyamani, P. S.; Poeppelmeier, K. R. *Chem. Mater.* **1998**, 10, 2753.
32. Goodey, J.; Broussard, J.; Halasyamani, P. S. *Chem. Mater.* **2002**, 14, 3174.
33. Goodey, J.; Ok, K. M.; Broussard, J.; Hofmann, C.; Escobedo, F. V.; Halasyamani, P. S. *J. Solid State Chem.* **2003**, 175, 3.
34. Ra, H.-S.; Ok, K. M.; Halasyamani, P. S. *J. Am. Chem. Soc.* **2003**, 125, 7764.
35. Ok, K. M.; Halasyamani, P. S. *Angew. Chem., Int. Ed.* **2004**, 43, 5489.
36. Chi, E. O.; Ok, K. M.; Porter, Y.; Halasyamani, P. S. *Chem. Mater.* **2006**, 18, 2070.
37. Kong, F.; Huang, S.-P.; Sun, Z.-M.; Mao, J.-G.; Cheng, W.-D. *J. Am. Chem. Soc.* **2006**, 128, 7750.
38. Jiang, H.-L.; Xie, Z.; Mao, J.-G. *Inorg. Chem.* **2007**, 46, 6495.

39. Kim, J.-H.; Baek, J.; Halasyamani, P. S. *Chem. Mater.* **2007**, *19*, 5637.
40. Sivakumar, T.; Chang, H. Y.; Baek, J.; Halasyamani, P. S. *Chem. Mater.* **2007**, *19*, 4710.
41. Chang, H. Y.; Sivakumar, T.; Ok, K. M.; Halasyamani, P. S. *Inorg. Chem.* **2008**, *47*, 8511.
42. Jiang, H.-L.; Huang, S.-P.; Fan, Y.; Mao, J.-G.; Cheng, W.-D. *Chem. Eur. J.* **2008**, *14*, 1972.
43. Chang, H. Y.; Kim, S.-H.; Ok, K. M.; Halasyamani, P. S. *Chem. Mater.* **2009**, *21*, 1654.
44. Hu, T.; Qin, L.; Kong, F.; Zhou, Y.; Mao, J.-G. *Inorg. Chem.* **2009**, *48*, 2193.
45. Kim, S.-H.; Yeon, J.; Halasyamani, P. S. *Chem. Mater.* **2009**, *21*, 5335.
46. Sun, C.-F.; Hu, C.-L.; Xu, X.; Ling, J.-B.; Hu, T.; Kong, F.; Long, X.-F.; Mao, J.-G. *J. Am. Chem. Soc.* **2009**, *131*, 9486.
47. Zhang, S.-Y.; Jiang, H.-L.; Sun, C.-F.; Mao, J.-G. *Inorg. Chem.* **2009**, *48*, 11809.
48. Chang, H. Y.; Kim, S. W.; Halasyamani, P. S. *Chem. Mater.* **2010**, *22*, 3241.
49. Li, P.-X.; Hu, C.-L.; Xu, X.; Wang, R.-Y.; Sun, C.-F.; Mao, J.-G. *Inorg. Chem.* **2010**, *49*, 4599.
50. Li, P.-X.; Kong, F.; Hu, C.-L.; Zhao, N.; Mao, J.-G. *Inorg. Chem.* **2010**, *49*, 5943.



51. Sun, C.-F.; Hu, C.-L.; Xu, X.; Mao, J.-G. *Inorg. Chem.* **2010**, *49*, 9581.
52. Yang, B.-P.; Hu, C.-L.; Xu, X.; Sun, C.-F.; Zhang, J.-H.; Mao, J.-G. *Chem. Mater.* **2010**, *22*, 1545.
53. Yeon, J.; Kim, S.-H.; Halasyamani, P. S. *Inorg. Chem.* **2010**, *49*, 6986.
54. Zhang, S.-Y.; Hu, C.-L.; Sun, C.-F.; Mao, J.-G. *Inorg. Chem.* **2010**, *49*, 11627.
55. Sun, C.-F.; Hu, C.-L.; Xu, X.; Yang, B.-P.; Mao, J.-G. *J. Am. Chem. Soc.* **2011**, *133*, 5561.
56. Darriet, J. *Bull. Soc. Fr. Mineral. Cristallogr.* **1973**, *96*, 97.
57. Johnston, M. G.; Harrison, W. T. A. *Acta Crystallogr., Sect. C: Cryst. Struct. Commun.* **2007**, *C63*, i57.
58. Chen, X.; Zhang, L.; Chang, X.; Xue, H.; Zang, H.; Xiao, W.; Song, X.; Yan, H. *J. Alloys Compd.* **2007**, *428*, 54.
59. Klevtsova, R. F.; Solodovnikov, S. F.; Glinskaya, L. A.; Alekseev, V. I.; Khalbaeva, K. M.; Khaikina, E. G. *J. Struct. Chem. (Transl. of Zh. Strukt. Khim.)* **1997**, *38*, 89.
60. Harrison, W. T. A.; Dussack, L. L.; Jacobson, A. J. *Inorg. Chem.* **1994**, *33*, 6043.
61. Harrison, W. T. A.; Dussack, L. L.; Vogt, T.; Jacobson, A. J. *J. Solid State Chem.* **1995**, *120*, 112.
62. Dussack, L. L.; Harrison, W. T. A.; Jacobson, A. J. *Mater. Res. Bull.* **1996**, *31*, 249.

63. Balraj, V.; Vidyasagar, K. *Inorg. Chem.* **1998**, 37, 4764.
64. *SAINT, Program for Area Detector Absorption Correction, version 4.05*; Siemens Analytical X-ray Systems, Inc.: Madison, WI, 1995.
65. North, A. C. T.; Phillips, D. C.; Mathews, F. S. *Acta Cryst.* **1968**, 24, 351.
66. Sheldrick, G. M. *SHELXL-97 - A Program for Crystal Structure Refinement.*; University of Goettingen: Goettingen, 1997.
67. Sheldrick, G. M. *SHELXS-97 - A Program for Automatic Solution of Crystal Structures.*; University of Goettingen: Goettingen, Germany, 1997.
68. Farrugia, L. J. *J. Appl. Crystallogr.* **1999**, 32, 837.
69. Flack, H. *Acta Cryst.* **1983**, 39, 876.
70. Kubelka, P. M., F Z. *Tech. Phys.* **1931**, 12, 593.
71. Tauc, J. *Mater. Res. Bull.* **1970**, 5, 721.
72. Kurtz, S. K.; Perry, T. T. *J. Appl. Phys.* **1968**, 39, 3798.
73. Ok, K. M.; Chi, E. O.; Halasyamani, P. S. *Chem. Soc. Rev.* **2006**, 35, 710.
74. Becke, A. D.; Edgecombe, K. E. *J. Chem. Phys.* **1990**, 92, 5397.
75. Silvi, B.; Savin, A. *Nature* **1994**, 371, 683.
76. Giannozzi, P. *J. Phys: Condens. Matter.* **2009**, 21, 395502.
77. Perdew, J. P.; Burke, K.; Ernzerhof, M. *Phys. Rev. Lett.* **1996**, 77, 3865.

78. Fuchs, M.; Scheffler, M. *Comput. Phys. Commun.* **1999**, *119*, 67.
79. Walkingshaw, A. D.; Spaldin, N. A.; Artacho, E. *Phys. Rev. B: Condens. Matter* **2004**, *70*, 165110.
80. Monkhorst, H. J.; Pack, J. D. *Phys. Rev. B* **1976**, *13*, 5188.
81. Momma, K.; Izumi, F. *J. Appl. Crystallogr.* **2008**, *41*, 653.
82. Brown, I. D. *The Chemical Bond in Inorganic Chemistry: The Bond Valence Model*; 1st ed.; Oxford University Press: Oxford, 2002.
83. Llunell, M.; Casanova, D.; Cirera, J.; Bofill, J. M.; Alemany, P.; Alvarez, S.; Pinsky, M.; Avnir, D.; *Shape Program*, v2.0, University of Barcelona: Barcelona, Spain: 2003.
84. Ok, K. M.; Halasyamani, P. S.; Casanova, D.; Llunell, M.; Alemany, P.; Alvarez, S. *Chem. Mater.* **2006**, *18*, 3176.
85. Ok, K. M.; Halasyamani, P. S. *J. Solid State Chem.* **2006**, *179*, 1345.
86. Chang, H. Y.; Ok, K. M.; Kim, J. H.; Halasyamani, P. S.; Stoltzfus, M.; Woodward, P. *Inorg. Chem.* **2007**, *46*, 7005.
87. *International Tables for Crystallography, Volume A, Space Group Symmetry*; Hahn, T., Ed.; Kluwer Academic: Dordrecht, Holland, 2006; Vol. A.
88. Preiser, C.; Losel, J.; Brown, I. D.; Kunz, M.; Skowron, A. *Acta Cryst.* **1999**, *55*, 698.

89. Salinas-Sanchez, A.; Garcia-Muñoz, J. L.; Rodriguez-Carvajal, J.; Saez-Puche, R.; Martinez, J. L. *J. Solid State Chem.* **1992**, *100*, 201.
90. Frechero, M. A.; Quinzani, O. V.; Pettigrosso, R. S.; Villar, M.; Montani, R. A. *J. Non-Cryst. Solids* **2007**, *353*, 2919.
91. Harrison, W. T. A.; Dussack, L. L.; Jacobson, A. J. *J. Solid State Chem.* **1996**, *125*, 234.
92. Kurilenko, L. N.; Serebryakova, N. V.; Saunin, E. I.; Gromov, V. V.; Sokolova, N. *P. Russ. Chem. Bull.* **1988**, *37*, 839.
93. Brower, W. S.; Parker, H. S.; Roth, R. S.; Waring, J. L. *J. Cryst. Growth* **1972**, *16*, 115.
94. Nguyen, S. D.; Kim, S.-H.; Halasyamani, P. S. *Inorg. Chem.* **2011**, *50*, 5215.
95. Scott, J. F. *J. Phys.: Condens. Matter* **2008**, *20*, 021001.
96. Cohen, R. E. *Nature* **1992**, *358*, 136.

## CHAPTER 5. Synthesis, Structure, and Characterization of Two New Polar Sodium Tungsten Selenites: $\text{Na}_2(\text{WO}_3)_3(\text{SeO}_3) \cdot 2\text{H}_2\text{O}$ and $\text{Na}_6(\text{W}_6\text{O}_{19})(\text{SeO}_3)_2$

### 5.1 Abstract

Two new quaternary sodium tungsten selenites,  $\text{Na}_2(\text{WO}_3)_3(\text{SeO}_3) \cdot 2\text{H}_2\text{O}$  ( $P3_1c$ ) and  $\text{Na}_6(\text{W}_6\text{O}_{19})(\text{SeO}_3)_2$  (C2), have been synthesized and characterized. The former exhibits the hexagonal tungsten oxide (HTO) layered structure, whereas the latter has the one-dimensional ‘ribbon’ structure. The layers and ‘ribbons’ consist of distorted  $\text{WO}_6$  and asymmetric  $\text{SeO}_3$  polyhedra. The layers in  $\text{Na}_2(\text{WO}_3)_3(\text{SeO}_3) \cdot 2\text{H}_2\text{O}$  and the ‘ribbons’ in  $\text{Na}_6(\text{W}_6\text{O}_{19})(\text{SeO}_3)_2$  are separated by  $\text{Na}^+$  cations. Powder SHG measurements on  $\text{Na}_2(\text{WO}_3)_3(\text{SeO}_3) \cdot 2\text{H}_2\text{O}$  and  $\text{Na}_6(\text{W}_6\text{O}_{19})(\text{SeO}_3)_2$  using 1064 nm radiation reveal SHG efficiencies of approximately  $450 \times$  and  $20 \times \alpha\text{-SiO}_2$ , respectively. Particle size vs. SHG efficiency measurements indicates the materials are type 1 nonphase-matchable. Converse piezoelectric measurements result in a  $d_{33}$  values of approximately 23 and 12 pm/V, whereas pyroelectric measurements reveal coefficients of -0.41 and -1.10  $\mu\text{C}/\text{m}^2\text{K}$  at 60 °C for  $\text{Na}_2(\text{WO}_3)_3(\text{SeO}_3) \cdot 2\text{H}_2\text{O}$  and  $\text{Na}_6(\text{W}_6\text{O}_{19})(\text{SeO}_3)_2$ , respectively. Frequency-dependent polarization measurements confirm that the materials are non-ferroelectric, i.e., the macroscopic polarization is not reversible, or ‘switchable’. Infrared, UV–vis, thermogravimetric, differential thermal analysis measurements, and electron localization function (ELF) calculations were also done for the materials. Crystal data:  $\text{Na}_2(\text{WO}_3)_3(\text{SeO}_3) \cdot 2\text{H}_2\text{O}$ , trigonal, space group  $P3_1c$  (No. 159),  $a = 7.2595(6)$  Å,  $b =$

7.2595(6) Å,  $c = 12.4867(13)$  Å,  $V = 569.89(9)$  Å<sup>3</sup>,  $Z = 2$ ; Na<sub>6</sub>(W<sub>6</sub>O<sub>19</sub>)(SeO<sub>3</sub>)<sub>2</sub>, monoclinic, space group  $C2$  (No. 5),  $a = 42.169(8)$  Å,  $b = 7.2690(15)$  Å,  $c = 6.7494(13)$  Å,  $\beta = 98.48(3)^\circ$ ,  $V = 2046.2(7)$  Å<sup>3</sup>,  $Z = 4$ .

## 5.2 Introduction

Polar materials, those crystallize in one of ten polar crystal classes (1, 2, 3, 4, 6, m, 3m, 2mm, 4mm, 6mm), exhibit technologically functional properties like second-harmonic generation (SHG), piezoelectricity, pyroelectricity, and possibly ferroelectricity.<sup>1-8</sup> The synthetic exploration and crystal engineering of new polar materials continue to be an active and challenging task for material scientists and solid-state chemists. The crystal engineering of polar materials studies designing and packing of new polar structural units. Molecules with organic  $\pi$ -conjugated systems, typically nitropyridine oxide (POM), alkali metal acid phthalate, (MAP), or nitro aniline (NA) families, are widely used as polar structural units in preparing new nonlinear optical (NLO) organic crystals.<sup>9,10</sup> Chen's anionic group theory proposed using acentric inorganic  $\pi$ -conjugated systems, particularly planar borate rings, to enhance nonlinear optical responses in noncentrosymmetric (NCS) borate-based materials.<sup>11-15</sup> Recently, Zou et al. have successfully reported new series of polar alkaline-alkaline earth fluoride carbonates with strong SHG efficiencies based on  $\pi$ -conjugated CO<sub>3</sub><sup>2-</sup> anions.<sup>16</sup> Poeppelmeier et al. have successfully used oxyfluoride groups to create new polar materials,<sup>17-25</sup> whereas cations that are susceptible to second-order Jahn-Teller (SOJT) distortions<sup>26-32</sup> have been successfully employed in preparing many new polar materials in our group, as well as others.<sup>33-72</sup>

While polar structural units can be successfully and specifically designed for preparing new polar materials, the understanding of how polar structures are created from structural building units is insufficient. The packing and alignments of polar structural units strongly depend on inter-molecular interactions, i.e., cation-anion interactions, hydrogen bonding. Hydrogen bonding has been widely used in NLO organic crystal engineering to obtain a designed crystal packing<sup>73-79</sup> but less obviously employed in preparing polar inorganic materials. A systematic review of hydrogen bonding in inorganic materials and its influence on NLO properties of polar materials has been recently published.<sup>80</sup> Recently, using hydrogen bonding to direct the alignment of polar lambda structural building units, Donakowski et al. have been able to prepare a new polar material,  $\text{CuVOF}_4(\text{H}_2\text{O})_7$ , from centrosymmetric (CS)  $\text{MVOF}_4(\text{H}_2\text{O})_7$  ( $\text{M} = \text{Co}^{2+}$ ,  $\text{Ni}^{2+}$ , or  $\text{Zn}^{2+}$ ).<sup>25</sup> Influence of cation sizes on altering packing and alignments of polar structural units has been observed and reported for several systems such as  $\text{MNaNbOF}_5$  ( $\text{M} = \text{K}^+$ ,  $\text{Cs}^+$ ),<sup>23</sup>  $\text{A}_2\text{Ti}(\text{IO}_3)_6$  ( $\text{A} = \text{Li}^+$ ,  $\text{Na}^+$ ,  $\text{K}^+$ ,  $\text{Rb}^+$ ,  $\text{Cs}^+$ , and  $\text{Tl}^+$ ),<sup>51</sup>  $\text{ACuTe}_2\text{O}_7$ ,<sup>56</sup> and  $\text{A}(\text{Mo}_2\text{O}_5)(\text{SeO}_3)_2$  ( $\text{A} = \text{Sr}^{2+}$ ,  $\text{Ba}^{2+}$ ,  $\text{Pb}^{2+}$ ).<sup>81</sup> Recently, using hard,  $\text{Na}^+$ , and soft,  $\text{Ag}^+$ , cations, Fry et al. have been able to direct the orientation of polar oxyfluoride groups, thereby altering the undoped polar  $\text{Na}_3\text{WO}_3\text{F}_3$  ( $R3$ ) to the doped CS  $\text{Na}_{1.5}\text{Ag}_{1.5}\text{MoO}_3\text{F}_3$  and  $\text{Na}_{1.5}\text{Ag}_{1.5}\text{WO}_3\text{F}_3$  ( $R\bar{3}$ ).<sup>82</sup> Despite these successes, the systematic engineering and design of new polar crystal structures remain an ongoing challenge.

With respect to sodium compounds containing SOJT cations, many sodium –  $d^0$  – tellurites,  $\text{NaTeVO}_5$  ( $P2_1/c$ ),<sup>83,84</sup>  $\text{Na}_2\text{MTe}_4\text{O}_{12}$  ( $\text{M} = \text{Mo}^{6+}$  and  $\text{W}^{6+}$ ) ( $C2/c$ ),<sup>85</sup>  $\text{Na}_2\text{Mo}_3\text{Te}_3\text{O}_{16}$  ( $I2$ ),<sup>44</sup> and  $\text{Na}_2\text{TeW}_2\text{O}_9$  ( $Ia$ ),<sup>37</sup> were reported, whereas for sodium –  $d^0$  – selenites only  $\text{Na}_2\text{SeMoO}_6$  ( $P2_13$ )<sup>39</sup> was found. In this chapter, we report on the synthesis

and characterization of two new polar sodium tungsten selenites:  $\text{Na}_2(\text{WO}_3)_3(\text{SeO}_3) \cdot 2\text{H}_2\text{O}$  ( $P3_1C$ ) and  $\text{Na}_6(\text{W}_6\text{O}_{19})(\text{SeO}_3)_2$  ( $C2$ ). The former has a Class 2 hexagonal tungsten oxide (HTO) layered structure, i.e., the  $\text{SeO}_3$  group ‘cap’ on one side of the HTO layer,<sup>55</sup> and the latter has an one-dimensional ‘ribbon’ structure. In addition to the crystal structures, UV–vis and IR spectroscopy, thermal analyses, SHG, piezoelectricity, and polarization measurements for all materials are also reported.

### 5.3 Experimental details

#### 5.3.1 Synthesis

$\text{Na}_2\text{CO}_3$  (Alfa Aesar, 99%),  $\text{SeO}_2$  (Alfa Aesar, 99.4%),  $\text{Na}_2\text{WO}_4 \cdot 2\text{H}_2\text{O}$  (Alfa Aesar, 99%), and  $\text{WO}_3$  (Alfa Aesar, 99.8%) were used as received. Crystals and polycrystalline powder of  $\text{Na}_2(\text{WO}_3)_3(\text{SeO}_3) \cdot 2\text{H}_2\text{O}$  were prepared using hydrothermal techniques. A 23 mL Teflon-lined autoclave containing 0.159 ( $1.50 \times 10^{-3}$  mol)  $\text{Na}_2\text{CO}_3$ , 0.174 g ( $7.50 \times 10^{-4}$ )  $\text{WO}_3$ , 0.330 g ( $3.00 \times 10^{-3}$ )  $\text{SeO}_2$ , 0.117 g  $\text{NaCl}$  ( $2.00 \times 10^{-3}$ ) and 2 mL of distilled  $\text{H}_2\text{O}$  was closed, heated to 230 °C, held for two weeks, and cooled slowly to room temperature at a rate of 6 °C h<sup>-1</sup>. The product was filtrated and washed three times with distilled water to obtain 0.137 g of tiny yellow hexagonal plate-shaped crystals (in 60% yield with respect to  $\text{WO}_3$ ). The crystals were structurally determined as  $\text{Na}_2(\text{WO}_3)_3(\text{SeO}_3) \cdot 2\text{H}_2\text{O}$ . The experimental and calculated powder X-ray diffraction (PXRD) data for  $\text{Na}_2(\text{WO}_3)_3(\text{SeO}_3) \cdot 2\text{H}_2\text{O}$  are identical.

Crystals of  $\text{Na}_6(\text{W}_6\text{O}_{19})(\text{SeO}_3)_2$  were prepared by solid state techniques. A mixture of 0.106 ( $1.00 \times 10^{-3}$  mol) of  $\text{Na}_2\text{CO}_3$ , 0.232 g ( $1.00 \times 10^{-3}$  mol) of  $\text{WO}_3$ , and 0.110 g ( $1.00 \times 10^{-3}$  mol) of  $\text{SeO}_2$  was ground and pressed into a pellet. The pellet was transferred to a



Pyrex tube and the tube was heated at 300 °C for one day. The thermal analysis of the pellet after heating at 300 °C shows that all CO<sub>2</sub> was removed (see Figure 6.1). The tube was then air-evacuated and flame-sealed to an ampule. The ampule was then heated to 450 °C for two days and cooled slowly to room temperature at a rate 6 °C h<sup>-1</sup>. The pellet was then washed with distilled water and revealed colorless rod-shaped crystals. The crystals were later structurally determined as Na<sub>6</sub>(W<sub>6</sub>O<sub>19</sub>)(SeO<sub>3</sub>)<sub>2</sub>.

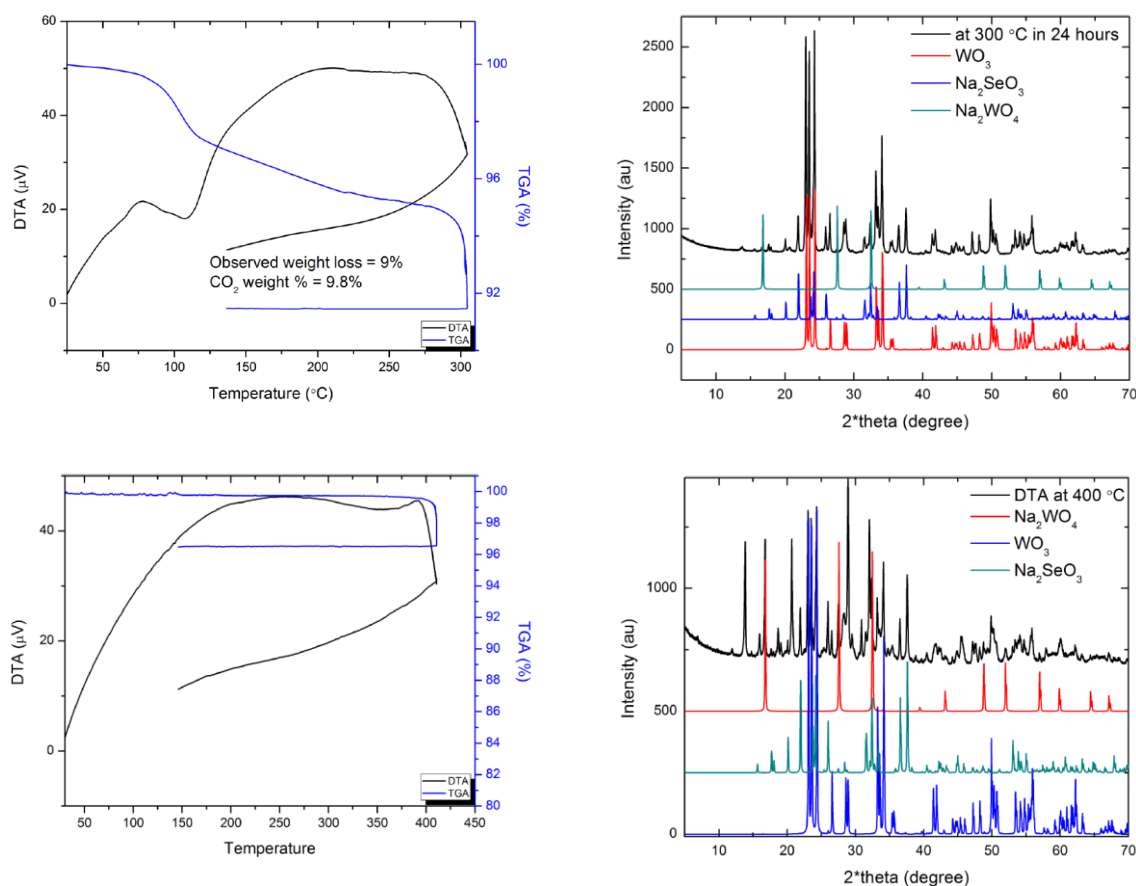


**Figure 5.1** Thermogravimetric and differential thermal analysis (TGA and DTA) data and powder X-ray diffraction for Na<sub>6</sub>(W<sub>6</sub>O<sub>19</sub>)(SeO<sub>3</sub>)<sub>2</sub> synthesis. The first TGA curve indicates near 90% of CO<sub>2</sub> was removed from the pellet at 300 °C during the thermal study (1 hour). XRD check of the residue showed that it mainly consisted of Na<sub>2</sub>SeO<sub>3</sub>,

WO<sub>3</sub>, and a small amount of Na<sub>2</sub>WO<sub>4</sub>. After heating the pellet at 300 °C in air for 24 hrs, the second TGA curve shows that all CO<sub>2</sub> was gone. At 400 °C, a weight loss corresponding to SeO<sub>2</sub> loss started to appear. XRD check of the residues showed that Na<sub>2</sub>SeO<sub>3</sub> and WO<sub>3</sub> phases were reduced while the fraction of Na<sub>2</sub>WO<sub>4</sub> increased.

Polycrystalline Na<sub>6</sub>(W<sub>6</sub>O<sub>19</sub>)(SeO<sub>3</sub>)<sub>2</sub> was prepared by combining 0.990 g ( $3.00 \times 10^{-3}$  mol) of Na<sub>2</sub>WO<sub>4</sub>·2H<sub>2</sub>O, 0.700 g ( $3.00 \times 10^{-3}$  mol) of WO<sub>3</sub>, and 0.220 g ( $2.00 \times 10^{-3}$  mol) of SeO<sub>2</sub>. The mixture was finely ground and pressed into a pellet. The pellet was transferred to a Pyrex tube and the tube was air-evacuated at 110 °C for one day and then flame-sealed to an ampule. The ampule was then heated to 450 °C for two days, and finally 550 °C for two days with three intermittent regrindings resulting in single phase Na<sub>6</sub>(W<sub>6</sub>O<sub>19</sub>)(SeO<sub>3</sub>)<sub>2</sub>. The experimental and calculated powder X-ray diffraction (PXRD) data for Na<sub>6</sub>(W<sub>6</sub>O<sub>19</sub>)(SeO<sub>3</sub>)<sub>2</sub> are identical.

### 5.3.2 Characterization

#### Single Crystal X-ray Diffraction

For Na<sub>2</sub>(WO<sub>3</sub>)<sub>3</sub>(SeO<sub>3</sub>)·2H<sub>2</sub>O, a yellow plate-shaped crystal (0.01 x 0.01 x 0.002 mm<sup>3</sup>); for Na<sub>6</sub>(W<sub>6</sub>O<sub>19</sub>)(SeO<sub>3</sub>)<sub>2</sub>, a colorless rod-shaped crystal (0.04 x 0.01 x 0.01 mm<sup>3</sup>) were used for single-crystal X-ray data collections. Data were collected using a Siemens SMART APEX diffractometer equipped with a 1K CCD area detector using graphite-monochromated Mo K $\alpha$  radiation. A hemisphere of data was collected using a narrow-frame method with scan widths of 0.30° in  $\omega$  and an exposure time of 60 second per frame. The first 50 frames were re-measured at the end of the data collection to monitor instrument and crystal stability. The data were integrated using the Siemens SAINT

program,<sup>86</sup> with the intensities corrected for Lorentz, polarization, air absorption, and absorption attributable to the variation in the path length through the detector face plate. Psi-scans were used for the absorption correction on the hemisphere of data.<sup>87</sup> The data were solved and refined using SHELXS-97 and SHELXL-97, respectively.<sup>88,89</sup> All of the atoms were refined with anisotropic thermal parameters, and the refinement converged for  $I > 2\sigma(I)$ . All calculations were performed using the WinGX-98 crystallographic software package.<sup>90</sup> During the refinement of  $\text{Na}_2(\text{WO}_3)_3(\text{SeO}_3)\cdot 2\text{H}_2\text{O}$ , the twin law -1 0 0 0 -1 0 0 0 1 suggested by ROTAX was successfully applied. Pseudo-merohedral twinning was consistent with the refined BASF value of 0.26. The twin law indicates the twinning lattices are related by a 180° rotation about the [001] direct lattice direction - the C3 rotation axis in the trigonal system that emulates higher hexagonal symmetry. In fact, when ADDSYM was run on the final model of  $\text{Na}_2(\text{WO}_3)_3(\text{SeO}_3)\cdot 2\text{H}_2\text{O}$  higher hexagonal symmetry was suggested. Attempts to refine  $\text{Na}_2(\text{WO}_3)_3(\text{SeO}_3)\cdot 2\text{H}_2\text{O}$  in hexagonal space groups failed. Partial occupancy was observed for the Na atom on the 6c site. The occupancy was set to 0.6667. Hydrogen atom positions were not determined for  $\text{Na}_2(\text{WO}_3)_3(\text{SeO}_3)\cdot 2\text{H}_2\text{O}$ , however, the  $\text{H}_2\text{O}$  molecules in it were experimentally confirmed by the infrared spectrum and thermogravimetric analysis. Merohedral twinning (type 1 – inversion twinning) was observed for  $\text{Na}_6(\text{W}_6\text{O}_{19})(\text{SeO}_3)_2$ , thus a twin law -1 0 0 0 -1 0 0 0 -1 was applied. This inversion twinning in combination with a two-fold rotation along the b-axis results in a pseudo-mirror plane. This mirror plane was detected by ADDSYM, however, the ADDSYM EXACT calculation confirmed C2 to be the correct space group. The Flack parameters<sup>79</sup> were refined to 0.01(5) and 0.00(10) for  $\text{Na}_2(\text{WO}_3)_3(\text{SeO}_3)\cdot 2\text{H}_2\text{O}$  and  $\text{Na}_6(\text{W}_6\text{O}_{19})(\text{SeO}_3)_2$ , respectively. Crystallographic data,

atomic coordination, and selected bond distances for  $\text{Na}_2(\text{WO}_3)_3(\text{SeO}_3)\cdot 2\text{H}_2\text{O}$  and  $\text{Na}_6(\text{W}_6\text{O}_{19})(\text{SeO}_3)_2$  are given in Tables 5.1-5.4.

**Table 5.1** Crystallographic data for  $\text{Na}_2(\text{WO}_3)_3(\text{SeO}_3)\cdot 2\text{H}_2\text{O}$  and  $\text{Na}_6(\text{W}_6\text{O}_{19})(\text{SeO}_3)_2$ .

formula	$\text{Na}_2(\text{WO}_3)_3(\text{SeO}_3)\cdot 2\text{H}_2\text{O}$	$\text{Na}_6(\text{W}_6\text{O}_{19})(\text{SeO}_3)_2$
fw (g/mol)	904.49	1798.96
T(K)	298.0(2)	298.0(2)
$\lambda$ (Å)	0.71073	0.71073
Crystal system	Trigonal	Monoclinic
Space group	$P3_1c$ (No.159)	$C2$ (No.5)
$a$ (Å)	7.2595(6)	42.169(8)
$b$ (Å)	7.2595(6)	7.2690(15)
$c$ (Å)	12.4867(13)	6.7494(13)
$\alpha$	90	90
$\beta$	90	98.48 (3)
$\gamma$	120	90
$V$ (Å <sup>3</sup> )	569.89 (9)	2046.2(7)
$Z$	2	4
$\rho_{\text{calcd}}$ (g/cm <sup>3</sup> )	5.248	5.840
$\mu$ (mm <sup>-1</sup> )	33.549	37.401
$R$ (int)	0.0671	0.0412
Reflections collected/unique	3673/944	6671/4321
Parameter refined	66	354
GOF ( $F^2$ )	1.030	1.064
$R(F)^a/R_w(F_o^2)^b$	0.0391/0.0870	0.0331/0.0895
Flack param.	0.01(5)	0.00(10)

$$^a R(F) = \Sigma ||F_o| - |F_c|| / \Sigma |F_o|. \quad ^b R_w(F_o^2) = [\Sigma w(F_o^2 - F_c^2)^2 / \Sigma w(F_o^2)^2]^{1/2}$$

**Table 5.2** Atomic coordinates and equivalent isotropic displacement parameters ( $\text{\AA}^2$ ) for  $\text{Na}_2(\text{WO}_3)_3(\text{SeO}_3)\cdot 2\text{H}_2\text{O}$ .

Atoms	x	y	z	U(eq)
W(1)	0.8078(1)	0.1464(1)	-0.0030(1)	0.010(1)
Se(1)	0.0000	0.0000	-0.2288(2)	0.010(1)
Na(1)	0.4960(20)	0.0060(20)	0.2600(20)	0.073(6)
O(1)	0.7930(20)	0.1910(20)	0.1313(10)	0.013(2)
O(2)	0.7518(17)	-0.1308(19)	0.0072(12)	0.011(2)
O(3)	0.5380(20)	0.0890(20)	-0.0469(10)	0.018(3)
O(4)	0.2470(20)	0.1270(20)	-0.1719(9)	0.014(3)
O(5)	0.6667	0.3333	0.3310(30)	0.047(11)
O(6)	0.3333	-0.3333	0.1600(50)	0.069(16)

U(eq) is defined as one third of the trace of the orthogonalized  $U_{ij}$  tensor

**Table 5.3** Atomic coordinates and equivalent isotropic displacement parameters ( $\text{\AA}^2$ ) for  $\text{Na}_6(\text{W}_6\text{O}_{19})(\text{SeO}_3)_2$

Atoms	x	y	z	U(eq)
W(1)	0.1081(1)	0.3578(1)	0.0311(1)	0.007(1)
W(2)	0.0453(1)	0.3707(1)	0.3042(1)	0.008(1)
W(3)	0.1077(1)	0.8731(1)	0.0277(1)	0.007(1)
W(4)	0.0454(1)	0.8705(1)	0.3044(1)	0.008(1)
W(5)	0.1814(1)	0.6183(1)	0.2271(1)	0.008(1)
W(6)	0.2516(1)	0.8446(1)	0.5311(1)	0.009(1)
Se(1)	0.1139(1)	0.6203(3)	0.5018(2)	0.008(1)
Se(2)	0.1893(1)	0.2638(2)	0.7688(2)	0.011(1)
Na(1)	0.1161(1)	0.1185(12)	-0.4944(9)	0.016(1)
Na(2)	-0.0378(1)	1.1222(13)	0.2313(10)	0.022(1)
Na(3)	0.0360(2)	0.6181(14)	0.8199(10)	0.028(1)
Na(4)	0.1787(1)	0.1111(16)	0.2622(10)	0.018(1)
Na(5)	0.2524(2)	0.5619(10)	-0.0501(10)	0.021(2)
Na(6)	0.1815(2)	-0.1610(11)	0.7586(10)	0.024(2)
O(1)	0.1118(3)	0.3056(13)	-0.2103(14)	0.014(2)
O(2)	0.0646(2)	0.3236(14)	0.0336(14)	0.011(2)
O(3)	0.1016(2)	0.6198(15)	-0.0141(13)	0.009(2)
O(4)	0.1196(2)	0.1163(15)	0.1442(12)	0.009(2)
O(5)	0.1521(2)	0.4346(12)	0.1398(14)	0.010(2)
O(6)	0.1010(2)	0.4326(12)	0.3488(14)	0.010(2)
O(7)	0.0601(2)	0.1205(15)	0.3516(13)	0.012(2)
O(8)	0.2394(2)	0.8699(15)	0.7647(13)	0.014(2)
O(9)	0.0436(2)	0.6199(16)	0.2031(14)	0.012(2)

**Table 5.3** Atomic coordinates and equivalent isotropic displacement parameters ( $\text{\AA}^2$ ) for  $\text{Na}_6(\text{W}_6\text{O}_{19})(\text{SeO}_3)_2$  (continued)

Atoms	x	y	z	U(eq)
O(10)	0.0055(2)	0.3225(16)	0.2220(15)	0.018(2)
O(11)	0.1005(2)	0.8057(12)	0.3468(15)	0.011(2)
O(12)	0.2018(2)	0.6201(17)	0.0230(14)	0.012(2)
O(13)	0.0054(3)	0.9210(15)	0.2234(16)	0.018(2)
O(14)	0.1536(2)	0.6278(16)	0.4974(13)	0.011(2)
O(15)	0.0649(2)	0.9154(13)	0.0273(13)	0.010(2)
O(16)	0.1137(3)	0.9291(14)	-0.2123(15)	0.016(2)
O(17)	0.0473(3)	0.8162(14)	0.5555(15)	0.017(2)
O(18)	0.1734(2)	0.1241(17)	0.5863(14)	0.016(2)
O(19)	0.0469(3)	0.4257(15)	0.5583(15)	0.017(2)
O(20)	0.2938(2)	0.9235(14)	0.6222(14)	0.013(2)
O(21)	0.2588(2)	0.5850(13)	0.5753(15)	0.013(2)
O(22)	0.1521(2)	0.8057(12)	0.1382(14)	0.010(2)
O(23)	0.1951(2)	0.1205(18)	0.9620(14)	0.016(2)
O(24)	0.2091(2)	0.7808(14)	0.3922(15)	0.012(2)
O(25)	0.2300(2)	0.2882(14)	0.7385(15)	0.015(2)

U(eq) is defined as one third of the trace of the orthogonalized  $U_{ij}$  tensor

**Table 5.4** Selected bond distances (Å) for Na<sub>2</sub>(WO<sub>3</sub>)<sub>3</sub>(SeO<sub>3</sub>)·2H<sub>2</sub>O and Na<sub>6</sub>(W<sub>6</sub>O<sub>19</sub>)(SeO<sub>3</sub>)<sub>2</sub>.

Na <sub>2</sub> (WO <sub>3</sub> ) <sub>3</sub> (SeO <sub>3</sub> )·2H <sub>2</sub> O <sup>a</sup>					
Bonds	Distances	Bonds	Distances	Bonds	Distances
W(1)–O(1)	1.728(12)	W(1)–O(3)	1.863(13)	Se(1)–O(4)	3×1.703(12)
W(1)–O(2)	1.835(12)	W(1)–O(3)#2	2.051(13)		
W(1)–O(2)#1	1.998(12)	W(1)–O(4)	2.187(11)		
Na <sub>6</sub> (W <sub>6</sub> O <sub>19</sub> )(SeO <sub>3</sub> ) <sub>2</sub> <sup>b</sup>					
Bonds	Distances	Bonds	Distances	Bonds	Distances
W(1)–O(1)	1.702(9)	W(3)–O(4)	1.969(10)	W(6)–O(8)	1.739(9)
W(1)–O(2)	1.851(9)	W(3)–O(22)	1.972(10)	W(6)–O(20)	1.885(10)
W(1)–O(3)	1.942(11)	W(3)–O(11)	2.273(10)	W(6)–O(21)#11	1.915(9)
W(1)–O(4)	1.947(11)	W(4)–O(17)	1.731(10)	W(6)–O(21)	1.928(9)
W(1)–O(5)	1.971(10)	W(4)–O(13)	1.735(11)	W(6)–O(24)	1.951(9)
W(1)–O(6)	2.274(10)	W(4)–O(7)	1.932(11)	W(6)–O(25)	2.122(11)
W(2)–O(10)	1.722(10)	W(4)–O(9)	1.943(11)	Se(1)–O(14)	1.680(8)
W(2)–O(19)	1.753(10)	W(4)–O(15)	2.176(9)	Se(1)–O(11)	1.748(9)
W(2)–O(9)	1.933(11)	W(4)–O(11)	2.347(10)	Se(1)–O(6)	1.750(9)
W(2)–O(7)	1.935(11)	W(5)–O(12)	1.730(9)	Se(2)–O(23)	1.658(10)
W(2)–O(2)	2.135(10)	W(5)–O(5)	1.857(10)	Se(2)–O(18)	1.660(11)
W(2)–O(6)	2.366(10)	W(5)–O(22)	1.877(9)	Se(2)–O(25)	1.765(10)
W(3)–O(16)	1.724(10)	W(5)–O(24)	1.902(9)		
W(3)–O(15)	1.830(9)	W(5)–O(20)	1.954(10)		
W(3)–O(3)	1.874(11)	W(5)–O(14)	2.309(9)		

Symmetry transformations used to generate equivalent atoms: <sup>a</sup>#1 -x+y+2,-x+1,z #2 -y+1,x-y,z; <sup>b</sup>#11 -x+1/2,y+1/2,-z+1



## **Powder X-ray Diffraction**

The powder X-ray diffraction data for all materials were collected in a continuous mode using a PANalytical X'Pert PRO diffractometer at room temperature (Cu  $K\alpha$  radiation, flat plate geometry) equipped with X'Celerator detector. Data were collected in the  $2\theta$  range of 5–70° with a step size of 0.016° and a step time of 10 second.

## **Infrared Spectroscopy**

Infrared (IR) spectra were recorded on a Matteson FTIR 5000 spectrometer in the spectral range of 400–4000  $\text{cm}^{-1}$  at room temperature.  $\text{Na}_2(\text{WO}_3)_3(\text{SeO}_3) \cdot 2\text{H}_2\text{O}$  and  $\text{Na}_6(\text{W}_6\text{O}_{19})(\text{SeO}_3)_2$  powders were heated to 150 °C for one week before being mixed and ground with dry KBr powder. These powder mixtures were then transferred to a stainless steel IR holder and pressed to semi-transparent pellets which were used for IR measurements.

## **UV–vis Diffuse Reflectance Spectroscopy**

UV–vis diffuse reflectance spectra were collected with a Varian Cary 500 scan UV–vis–NIR spectrophotometer over the spectral range of 200–2000 nm at room temperature. Polytetrafluoroethylene (PTFE) was used as a standard material for the baseline correction. The sample was thoroughly mixed with PTFE and this mixture was used for UV–vis measurements. Reflectance spectra were converted to absorbance using the Kubelka–Munk equation.<sup>93,94</sup>

## Thermal Analysis

Thermogravimetric and differential thermal analyses were simultaneously carried out on an EXSTAR6000 TG/DTA 6300 Thermogravimetric/Differential Thermal Analysis system (SII NanoTechnology Inc.). The sample (~20 mg) was placed in a platinum crucible that was heated (cooled) at a rate of 10 °C/min in the range of 25–700 °C under flowing nitrogen gas. An empty platinum crucible was used as the reference during the measurements.

## Second-harmonic Generation

Powder SHG measurements on  $\text{Li}_6(\text{Mo}_2\text{O}_5)_3(\text{SeO}_3)_6$  were performed at room temperature on a modified Kurtz-NLO system,<sup>95</sup> using a pulsed Nd:YAG laser with a wavelength of 1064 nm. The methodology and instrumentation details have been published.<sup>96</sup> The SHG efficiency has been shown to be particle size dependent.<sup>95</sup> Thus, the polycrystalline samples were ground and sieved into distinct particle size ranges (20–45, 45–63, 63–75, 75–90, and 90–120  $\mu\text{m}$ ). In order to evaluate relative SHG efficiencies of the measured samples with known SHG materials crystalline  $\alpha\text{-SiO}_2$  was also ground and sieved into the same particle size ranges. No index matching fluid was used in the experiments.

## Piezoelectric Measurements

Converse piezoelectric measurements were performed at room temperature using a Radiant Technologies RT66A piezoelectric test system with a TREK (model 609E-6) high voltage amplifier, Precision Materials Analyzer, Precision High Voltage Interface,

and MTI 2000 Fotonic Sensor.  $\text{Na}_2(\text{WO}_3)_3(\text{SeO}_3) \cdot 2\text{H}_2\text{O}$  and  $\text{Na}_6(\text{W}_6\text{O}_{19})(\text{SeO}_3)_2$  samples were pressed into a pellet with approximately 8 mm diameter and approximately 1 mm thick. The pellets were sintered in air at 200 °C for  $\text{Na}_2(\text{WO}_3)_3(\text{SeO}_3) \cdot 2\text{H}_2\text{O}$  or 300 °C for  $\text{Na}_6(\text{W}_6\text{O}_{19})(\text{SeO}_3)_2$  in one week. Silver paste was applied to both sides of the sintered pellets as electrodes, and the pellets were cured in air at 200 °C for  $\text{Na}_2(\text{WO}_3)_3(\text{SeO}_3) \cdot 2\text{H}_2\text{O}$  or 300 °C for  $\text{Na}_6(\text{W}_6\text{O}_{19})(\text{SeO}_3)_2$  during 72 hours. These pellets were also used in polarization measurements.

### **Polarization Measurements**

The polarization measurements were done on a Radiant Technologies Model RT66A ferroelectric test system with a TREK high-voltage amplifier in the temperature range of 25–160 °C in a Delta Model 9023 environmental test chamber. The unclamped pyroelectric coefficient, defined as  $dP/dT$ ,<sup>96</sup> was determined by measuring the polarization as a function of temperature. The methodology and instrumentation details have been published.<sup>96</sup> To measure the potential ferroelectric behavior, frequency-dependent polarization measurements were done at room temperature under static electric field of 5 kV/cm between 100–1000 Hz. For the pyroelectric measurements, the polarization was measured statically from room temperature to 140 °C with an electric field of 5 kV/cm at 1000 Hz for  $\text{Na}_2(\text{WO}_3)_3(\text{SeO}_3) \cdot 2\text{H}_2\text{O}$  and from room temperature to 160 °C with an electric field of 20 kV/cm at 100 Hz for  $\text{Na}_6(\text{W}_6\text{O}_{19})(\text{SeO}_3)_2$ . The temperature was allowed to stabilize before the polarization was measured.

## Electron Localization Function (ELF) Calculations

Electron localization function (ELF)<sup>97,98</sup> calculations were performed using the plane-wave pseudopotential method (PWPP) as implemented in Quantum ESPRESSO (4.1.2 version) package.<sup>99</sup> Norm-conserving MT pseudopotentials for all the elements were used with the GGA for exchange-correlation corrections.<sup>100</sup> The pseudopotentials generated from the Fritz Haber Institute (FHI) code<sup>101</sup> were converted for the calculations. The tungsten pseudopotential was generated using previously reported parameters<sup>102</sup> by LD1 program.<sup>99</sup> A plane wave energy cutoff was set to 37 Rydberg (Ry). The Brillouin zone was sampled using a  $4 \times 4 \times 3$  Monkhorst–Pack (MP) k-mesh.<sup>103</sup> A total energy convergence threshold was set to  $10^{-6}$  Ry indicated self-consistency. The experimental crystal structures were employed for all calculations. The program VESTA was used for all the structural diagrams.<sup>104</sup>

## 5.4 Results and discussion

### Structures

$\text{Na}_2(\text{WO}_3)_3(\text{SeO}_3) \cdot 2\text{H}_2\text{O}$  crystallizes in NCS polar trigonal space group  $P3_1c$ . Ball-and-stick and polyhedra representations of the material in (110) plane are shown in Figures 5.2a and 5.2b. The material exhibits a hexagonal tungsten oxide (HTO) layered structure with distorted  $\text{WO}_6$  and asymmetric  $\text{SeO}_3$  polyhedra (see Figure 5.3). Specifically each  $\text{WO}_6$  octahedron share four equatorial oxygen atoms to other four  $\text{WO}_6$  octahedra, thus forming a planar HTO layer with triangular and six-point star-ring holes. Regarding the connectivity of the  $\text{AO}_3$  groups ( $\text{A} = \text{Se}^{4+}$  or  $\text{Te}^{4+}$ ), the HTO layers can be further

classified into two classes. Class 1 HTO layers consist of  $\text{AO}_3$  groups ( $\text{A} = \text{Se}^{4+}$  or  $\text{Te}^{4+}$ ) alternatively ‘capping’ triangular holes of both sides of the HTO layers, whereas in Class 2 HTO layers  $\text{AO}_3$  groups ( $\text{A} = \text{Se}^{4+}$  or  $\text{Te}^{4+}$ ) ‘cap’ on the triangular holes of one side of the HTO layer.<sup>55</sup> In  $\text{Na}_2(\text{WO}_3)_3(\text{SeO}_3) \cdot 2\text{H}_2\text{O}$  the  $\text{SeO}_3$  polyhedra ‘cap’ on the triangular holes of one side of the HTO layer, thus forming a Class 2 HTO layered structure. The layers stack on top of each other along the c-axis direction and are separated by  $\text{Na}^+$  cations and the  $\text{H}_2\text{O}$  molecules. In connectivity terms, the structure may be written as  $[\text{3}(\text{WO}_{1/1}\text{O}_{5/2})^{-1} (\text{SeO}_{3/2})^{+1} 2(\text{H}_2\text{O})]^{2-}$  with charge balance maintained by two  $\text{Na}^+$  cations. The  $\text{W}^{6+}$  cations are octahedrally coordinated to six oxygen atoms with one ‘short’ (1.728(12) Å), four ‘normal’ (1.835(12) – 2.015(13) Å), and one ‘long’ (2.187(11) Å) W–O bonds. The ‘short’ W–O bonds are terminal, and as expected the  $\text{W}^{6+}$  cations displace towards terminal oxygen atoms, i.e., a corner,  $\text{C}_4$ -type distortion, whereas the ‘long’ W–O bonds are connected to  $\text{SeO}_3$  groups. The  $\text{Se}^{4+}$  cations are in trigonal pyramidal environments, coordinated to three oxygen atoms with the same Se–O bond distance (1.703(12) Å). Of six oxygen atoms in the asymmetric unit cell, O(5) and O(6) are isolated and have no bond to  $\text{W}^{6+}$  and  $\text{Se}^{4+}$  cations. Therefore, O(5) and O(6) are oxygen atoms of two  $\text{H}_2\text{O}$  molecules in  $\text{Na}_2(\text{WO}_3)_3(\text{SeO}_3) \cdot 2\text{H}_2\text{O}$ . The  $\text{Na}^+$  cations are observed in seven-coordinated environments, bonded to two oxygen atoms of the  $\text{H}_2\text{O}$  molecules with ‘short’ Na–O bond distances (2.25(2)–2.47(4) Å) and to five oxygen atoms of the  $\text{WO}_6$  and  $\text{SeO}_3$  polyhedra with ‘long’ Na–O bond distances (2.44(2)–2.61(2) Å). The experimental bond valence sums (vu)<sup>105</sup> for  $\text{Na}^+$ ,  $\text{W}^{6+}$ ,  $\text{Se}^{4+}$  cations and  $\text{O}^{2-}$  anions, except for O(5) and O(6), are 1.16, 6.17, 3.96, 2.01–2.07, respectively.

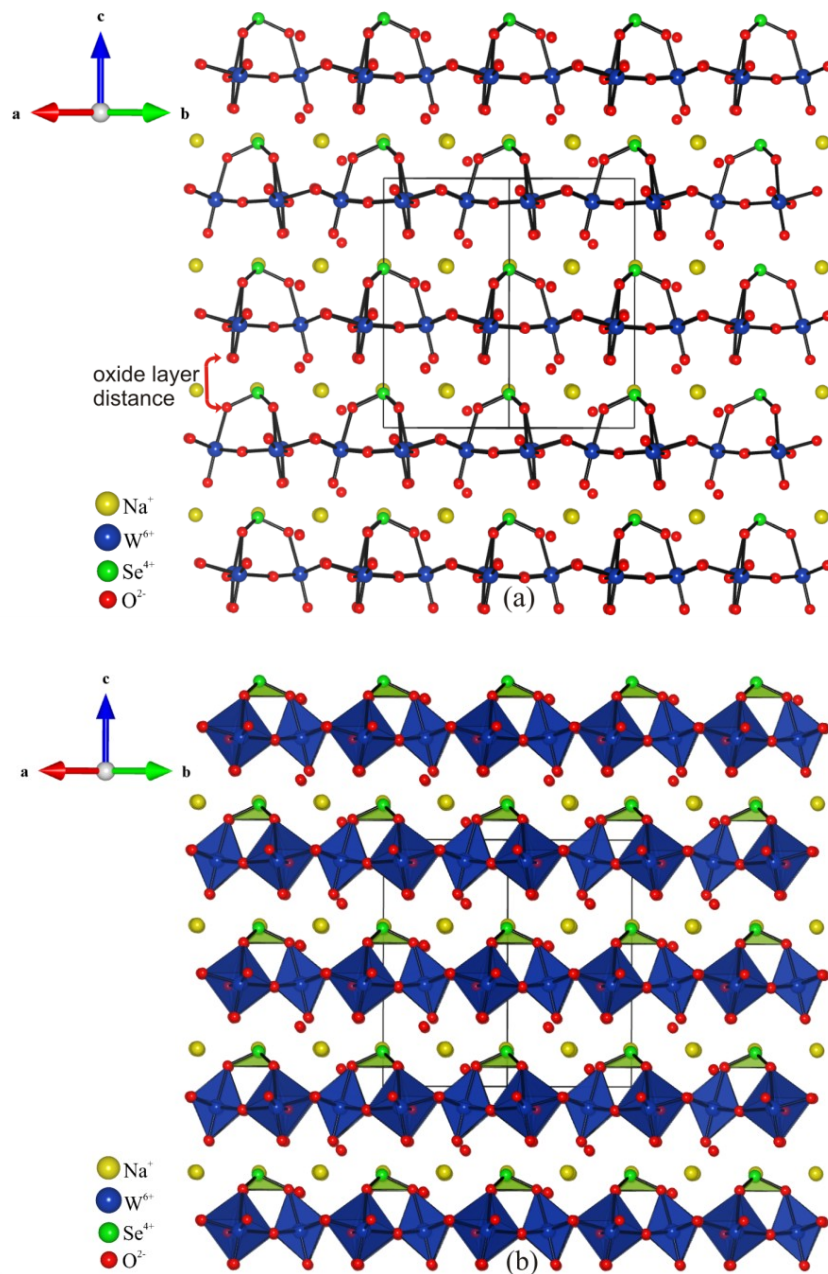


**Figure 5.2** Ball-and-stick (top) and polyhedral (bottom) representations of  $\text{Na}_2(\text{WO}_3)_3(\text{SeO}_3) \cdot 2\text{H}_2\text{O}$  in the (110) plane. Spheres in the diagram are  $\text{Na}^+$  cations (yellow),  $\text{W}^{6+}$  cations (blue),  $\text{Se}^{4+}$  cations (green), and  $\text{O}^{2-}$  anions (red). Isolated red spheres are the  $\text{H}_2\text{O}$  molecules.

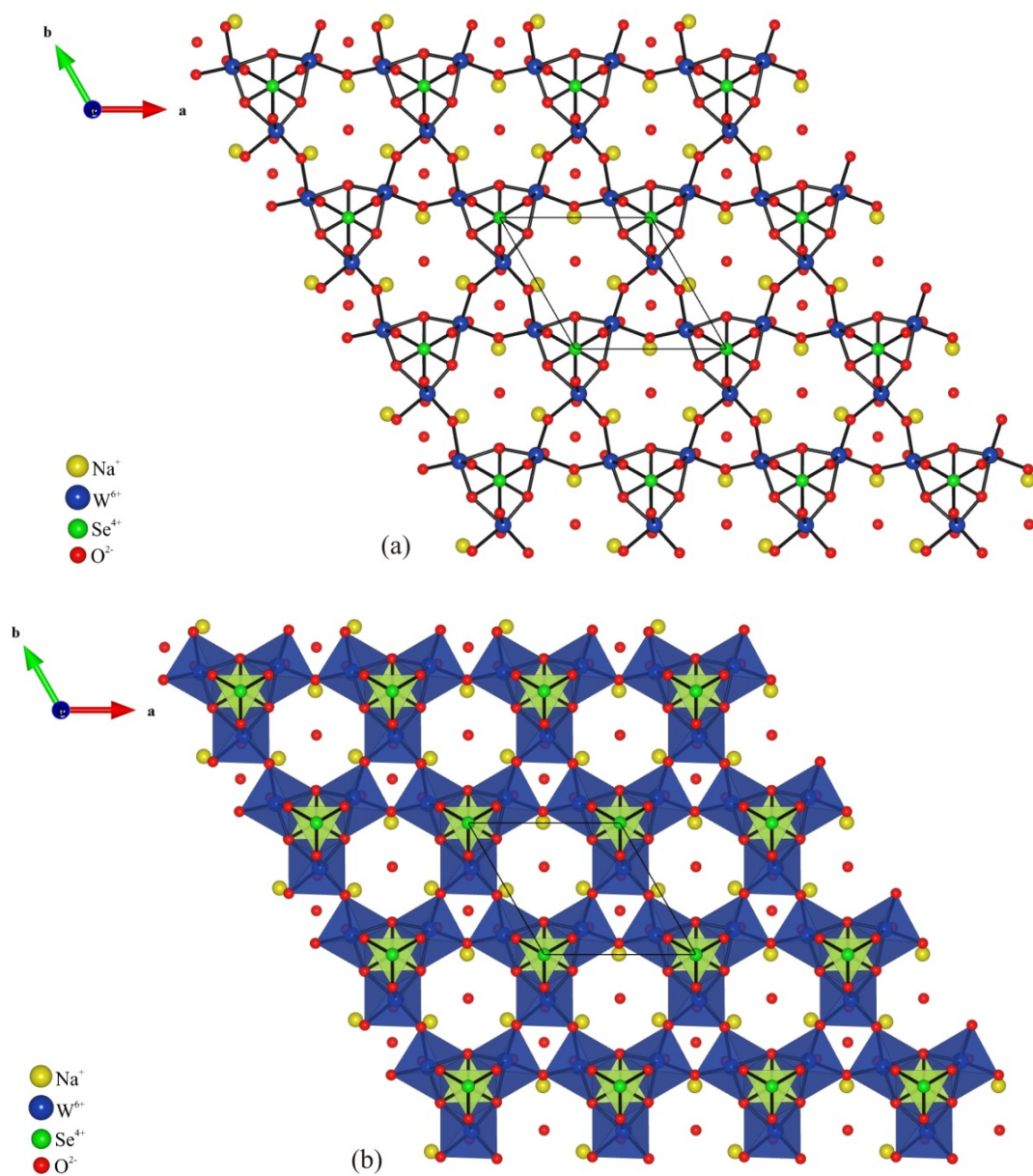


**Figure 5.3** Ball-and-stick (top) and polyhedral (bottom) representations of  $\text{Na}_2(\text{WO}_3)_3(\text{SeO}_3) \cdot 2\text{H}_2\text{O}$  in the  $ab$ -plane. Spheres in the diagram are  $\text{Na}^+$  cations (yellow),  $\text{W}^{6+}$  cations (blue),  $\text{Se}^{4+}$  cations (green), and  $\text{O}^{2-}$  anions (red). Isolated red spheres are the  $\text{H}_2\text{O}$  molecules.

$\text{Na}_6(\text{W}_6\text{O}_{19})(\text{SeO}_3)_2$  crystallizes in NCS polar monoclinic space group  $C2$ . Ball-and-stick and polyhedra representations of the material in the ac-plane are shown in Figures 5.4a and 5.4b. The material exhibits an infinitive one-dimensional ‘ribbon’ structure with distorted  $\text{WO}_6$  and asymmetric  $\text{SeO}_3$  polyhedra (see Figure 5.5). Specifically,  $\text{W}(1)\text{O}_6$  and  $\text{W}(2)\text{O}_6$  octahedra (similarly  $\text{W}(3)\text{O}_6$  and  $\text{W}(4)\text{O}_6$  octahedra) share an edge to form  $\text{W}_2\text{O}_{10}$  dimers. The  $\text{W}_2\text{O}_{10}$  dimers use apical oxygen atoms to connect and form a ‘double chain’ along the b-axis direction. Along the b-axis direction, the  $\text{W}(6)\text{O}_6$  octahedra share apical oxygen atoms to form a ‘single chain’ in between two ‘double chains’. Two ‘double chains’ and a ‘single chain’ run in a parallel manner along the b-axis direction and are bridged by  $\text{W}(5)\text{O}_6$  octahedra. The  $\text{W}(5)\text{O}_6$  octahedra use four equatorial oxygen atoms to connect the ‘double chain’ to the ‘single chain’, resulting a ‘ribbon’ structure.  $\text{SeO}_3$  polyhedra attach to the ‘ribbon’ in two different ways.  $\text{Se}(1)\text{O}_3$  polyhedra ‘cap’ on triangular holes formed by the ‘double chain’ and  $\text{W}(5)\text{O}_6$  octahedra. On the other hand,  $\text{Se}(2)\text{O}_3$  polyhedra are single-bonded to the ‘single chain’ and all  $\text{Se}(2)\text{O}_3$  polyhedra are oriented in the +b-axis direction. The ‘ribbons’ are separated by  $\text{Na}^+$  cations. In connectivity terms, the structure may be written as  $[2(\text{WO}_{1/1}\text{O}_{5/2})^{-1} 2(\text{WO}_{1/1}\text{O}_{4/2}\text{O}_{1/3})^{-2/3} 2(\text{WO}_{2/1}\text{O}_{3/2}\text{O}_{1/3})^{-5/3} (\text{SeO}_{2/1}\text{O}_{1/2})^{-1} (\text{SeO}_{1/2}\text{O}_{2/3})^{+5/3}]^{6-}$  with charge balance maintained by six  $\text{Na}^+$  cations. The  $\text{W}^{6+}$  cations are octahedrally coordinated to six oxygen atoms. Of these  $\text{W}^{6+}$  cations,  $\text{W}(1)$ ,  $\text{W}(3)$ ,  $\text{W}(5)$ , and  $\text{W}(6)$  cations are subjected to a corner,  $C_4$ -type distortion with one ‘short’ (1.702(9)–1.739(9) Å), four ‘normal’ (1.830(9)–1.972(10) Å), and one ‘long’ (2.122(11)–2.309(9) Å) W–O bonds. Whereas,  $\text{W}(2)$  and  $\text{W}(4)$  cations are subjected to an edge,  $C_2$ -type distortion with two ‘short’ (1.722(10)–1.753(10) Å), two ‘normal’ (1.932(11)–1.943(11) Å), and two ‘long’ (2.135(10)–2.366(10) Å) W–O bonds.



All ‘short’ W–O bonds are terminal, and as expected the  $W^{6+}$  cations displace towards these terminal oxygen atoms, whereas the ‘long’ W–O bonds are connected to  $SeO_3$  groups. The  $Se^{4+}$  cations are in trigonal pyramidal environments, coordinated to three oxygen atoms with Se–O bond distances in the range of 1.658(10)–1.765(10) Å. The  $Na^+$  cations are in seven- and eight-coordinate environments, bonded to oxygen atoms with Na–O bond distances in the range of 2.233(11)–3.098(11) Å. The experimental bond valence sums (vu)<sup>105</sup> for  $Na^+$ ,  $W^{6+}$ , and  $Se^{4+}$  cations and  $O^{2-}$  anions are in the range of 0.92–1.26, 6.00–6.24, 3.79–4.15, and 1.88–2.28 vu, respectively.

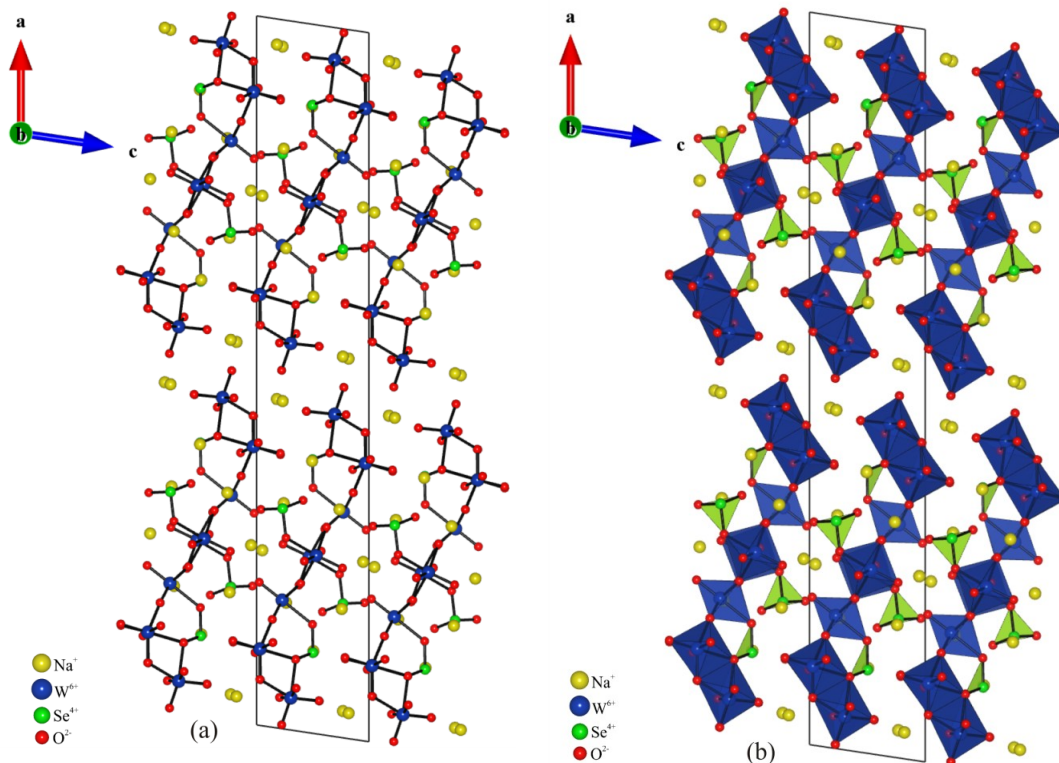


**Figure 5.4** Ball-and-stick (left) and polyhedral (right) representations of  $Na_6(W_6O_{19})(SeO_3)_2$  in the  $ac$ -plane. Spheres in the diagram are  $Na^+$  cations (yellow),  $W^{6+}$  cations (blue),  $Se^{4+}$  cations (green), and  $O^{2-}$  anions (red).

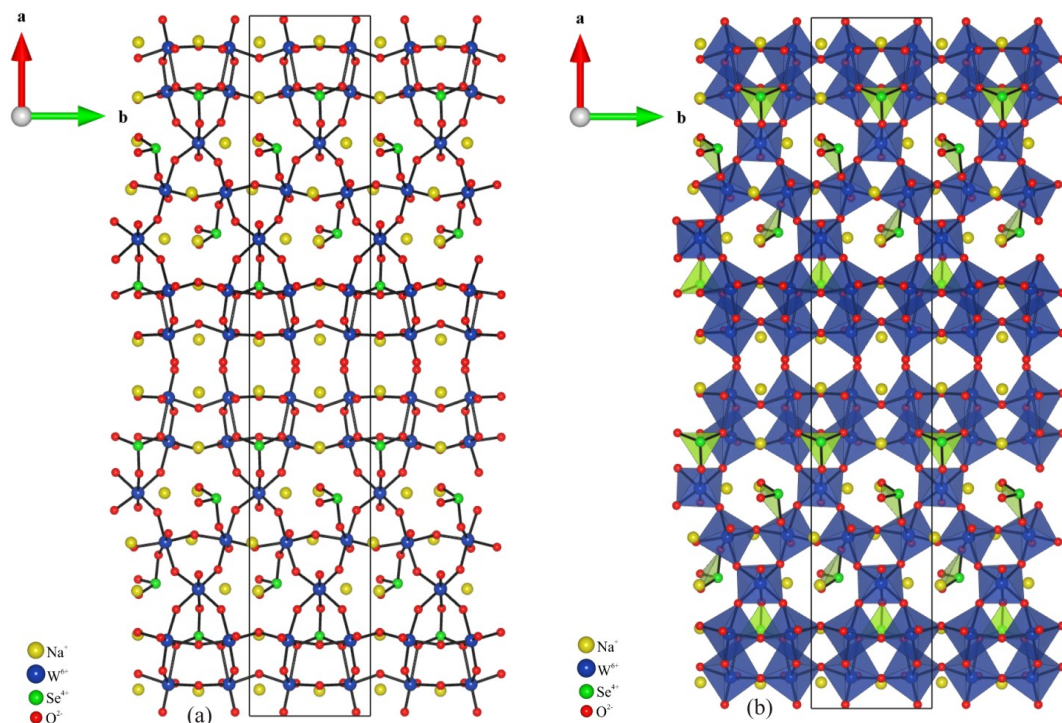


**Figure 5.5** Ball-and-stick (left) and polyhedral (right) representations of  $\text{Na}_6(\text{W}_6\text{O}_{19})(\text{SeO}_3)_2$  in the  $ab$ -plane. Spheres in the diagram are  $\text{Na}^+$  cations (yellow),  $\text{W}^{6+}$  cations (blue),  $\text{Se}^{4+}$  cations (green), and  $\text{O}^{2-}$  anions (red).

**Table 5.5** Bond valence sums, BSI and GII index values for  $\text{Na}_2(\text{WO}_3)_3(\text{SeO}_3) \cdot 2\text{H}_2\text{O}$  and  $\text{Na}_6(\text{W}_6\text{O}_{19})(\text{SeO}_3)_2$ .

Compound	Bond Valence Sums (vu)				
	$\text{Na}^+$	$\text{W}^{6+}$	$\text{Se}^{4+}$	BSI	GII
$\text{Na}_2(\text{WO}_3)_3(\text{SeO}_3) \cdot 2\text{H}_2\text{O}$	1.16	6.17	3.96	0.18	0.11
$\text{Na}_6(\text{W}_6\text{O}_{19})(\text{SeO}_3)_2$	0.92–1.25	6.00–6.18	3.79–4.15	0.16	0.13

The relevant questions are the role of the  $\text{H}_2\text{O}$  molecules in  $\text{Na}_2(\text{WO}_3)_3(\text{SeO}_3) \cdot 2\text{H}_2\text{O}$  crystal structure and the structural relationships between  $\text{Na}_2(\text{WO}_3)_3(\text{SeO}_3) \cdot 2\text{H}_2\text{O}$  and

$\text{Na}_6(\text{W}_6\text{O}_{19})(\text{SeO}_3)_2$  where two  $\text{H}_2\text{O}$  molecules are replaced by one  $\text{Na}^+$  cation. To answer this question, let us re-examine the crystal structures of compounds with  $\text{B}_2(\text{MO}_3)_3(\text{AO}_3)$  chemical formula ( $\text{B} = \text{Ag}^+, \text{K}^+, \text{NH}_4^+, \text{Rb}^+, \text{Cs}^+, \text{Tl}^+$ ;  $\text{M} = \text{Mo}^{6+}, \text{W}^{6+}$ ;  $\text{A} = \text{Se}^{4+}, \text{Te}^{4+}$ )<sup>55,106-110</sup> with respect to B cation sizes. Except  $\text{Ag}_2(\text{MoO}_3)_3(\text{SeO}_3)$  and  $\text{K}_2(\text{WO}_3)_3(\text{TeO}_3)$ , all other compounds exhibit the HTO layers capped one side by the  $\text{AO}_3$  polyhedra (Class 2 HTO layer). To examine the role of B cations, we plotted the HTO layer distances, that is, the oxide layer distances (see Figure 5.2a) and their cell parameters versus the B cation radius<sup>111-113</sup> for these Class 2 HTO layered materials.

**Table 5.6** Alkali cation radius, hexagonal tungsten oxide (HTO) layer distances, and space groups of the polar HTO layered materials

Alkali cation	Ionic radii (pm) <sup>111-113</sup>	HTO Compounds	Space group	HTO layer Distance (Å)	Cell parameter <b>c</b> (Å)
$\text{Na}^+$	102	$\text{Na}_2(\text{WO}_3)_3(\text{SeO}_3) \cdot 2\text{H}_2\text{O}$	$P3_1$	2.56	12.486(13)
$\text{K}^+$	151	$\text{K}_2(\text{WO}_3)_3(\text{TeO}_3)$	$P2_1/n$	1.32	11.669(2) <sup>*</sup>
$\text{Rb}^+$	161	$\text{Rb}_2(\text{MoO}_3)_3(\text{SeO}_3)$	$P6_3$	2.31	11.978(5)
		$\text{Rb}_2(\text{WO}_3)_3(\text{TeO}_3)$	$P3_1c$	2.27	12.0640(2)
$\text{Cs}^+$	171	$\text{Cs}_2(\text{MoO}_3)_3(\text{SeO}_3)$	$P6_3$	2.49	12.377(2)
		$\text{Cs}_2(\text{WO}_3)_3(\text{SeO}_3)$	$P6_3$	2.55	12.5426(3)
$\text{Tl}^+$	159	$\text{Tl}_2(\text{MoO}_3)_3(\text{SeO}_3)$	$P3_1c$	2.21	11.794(3)
		$(\text{NH}_4)_2(\text{MoO}_3)_3(\text{SeO}_3)$	$P6_3$	2.31	12.031(3)
$(\text{NH}_4)^+$	146	$(\text{NH}_4)_2(\text{MoO}_3)_3(\text{TeO}_3)$	$P6_3$	2.33	12.028(4)
		$(\text{NH}_4)_2(\text{WO}_3)_3(\text{SeO}_3)$	$P6_3$	2.34	12.1486(3)

<sup>\*</sup>cell parameter **b**

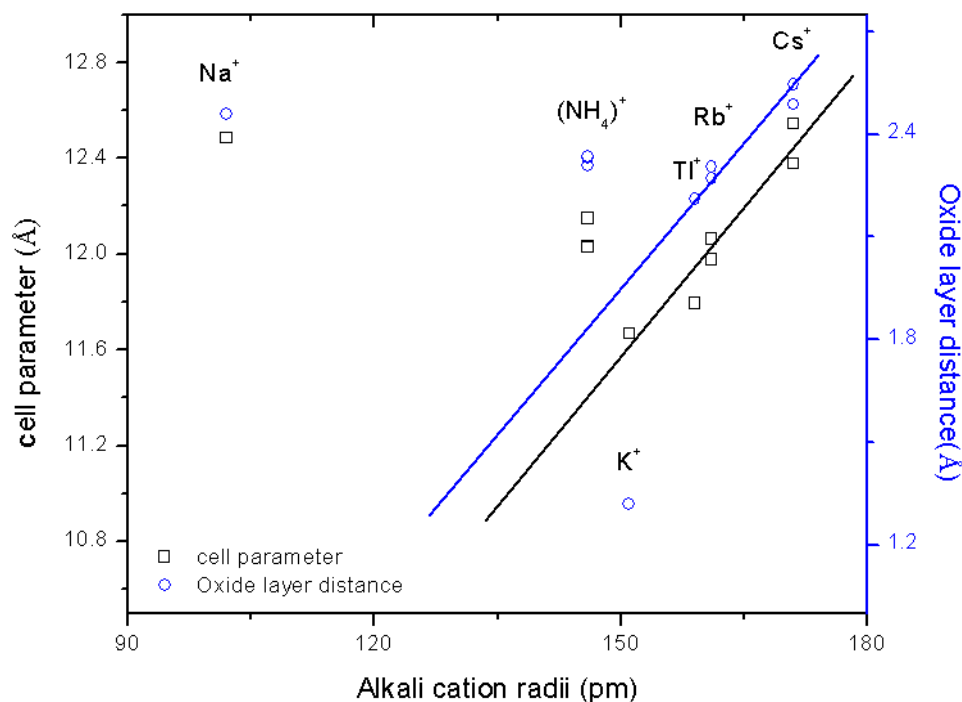


**Figure 5.6** Plots of hexagonal tungsten oxide (HTO) layer distances and cell parameters of the polar HTO layered materials versus alkali cation radius.

As seen in Figure 5.6, the blue circles are the oxide layer distances. For  $\text{Ti}^+$ ,  $\text{Rb}^+$ , and  $\text{Cs}^+$  compounds, the distances linearly increase with B cations (the blue line), consistent with the Vegard's law.<sup>114,115</sup> For  $\text{NH}_4^+$  the distance deviates from the blue line, with  $\text{NH}_4^+$  points above the blue line. These deviations indicate new structural aspects occurring for  $(\text{NH}_4)_2(\text{MO}_3)_3(\text{AO}_3)$  compounds. In fact, the  $\text{N}\cdots\text{O}$  distances varying from 2.8(1) – 3.4(1) Å in  $(\text{NH}_4)_2(\text{MO}_3)_3(\text{AO}_3)$  compounds indicate the weak hydrogen bonding between  $\text{NH}_4^+$  cations and oxide ligands of the HTO layers. Because  $\text{NH}_4^+$  and  $\text{K}^+$  cations have the similar cation sizes, we may expect  $\text{K}_2(\text{WO}_3)_3(\text{TeO}_3)$  will also adopt  $(\text{NH}_4)_2(\text{MO}_3)_3(\text{AO}_3)$  structure if considering only cation size effects. However,  $\text{K}_2(\text{WO}_3)_3(\text{TeO}_3)$  exhibits a centrosymmetric structure with HTO layers connected using

$\text{TeO}_3$  linkers. That was explained by the cation size effects as the  $\text{K}^+$  cations are too small to fit in the space between the Class 2 HTO layers, comparing to bigger B cations like  $\text{Tl}^+$ ,  $\text{Rb}^+$ , and  $\text{Cs}^+$ . Therefore, the weak hydrogen bonding has a critical role in supporting the Class 2 HTO layered structure for  $(\text{NH}_4)_2(\text{MoO}_3)_3(\text{AO}_3)$ . As mentioned earlier, the  $\text{Na}^+$  cations are coordinated by seven oxygen atoms in  $\text{Na}_2(\text{WO}_3)_3(\text{SeO}_3) \cdot 2\text{H}_2\text{O}$ , of which two are from the  $\text{H}_2\text{O}$  molecules with ‘short’ Na–O bond distances (2.25(2)–2.47(4) Å). The nearest oxygen-oxygen distances between the  $\text{H}_2\text{O}$  molecules and two adjacent HTO layers are in the range of 3.013(34)–3.380(40) Å. The O...O distances for hydrogen bonding in hydrated oxides are in the range of 2.59–3.48 Å.<sup>116</sup> That suggests the  $\text{H}_2\text{O}$  molecules are hydrogen bonding to the Class 2 HTO layers. To see the importance of the  $\text{H}_2\text{O}$  molecules in forming the  $\text{Na}_2(\text{WO}_3)_3(\text{SeO}_3) \cdot 2\text{H}_2\text{O}$  structure, let us examine the  $(\text{Ag})_2(\text{MoO}_3)_3(\text{SeO}_3)$  structure as  $\text{Ag}^+$  and  $\text{Na}^+$  cations are of similar ionic sizes. Without the  $\text{H}_2\text{O}$  molecules, we expect  $(\text{Ag})_2(\text{MoO}_3)_3(\text{SeO}_3)$  will exhibit a different crystal structure as  $\text{Ag}^+$  cation sizes are approximate to  $\text{Na}^+$  cations but much smaller than  $\text{K}^+$  cations. In fact,  $(\text{Ag})_2(\text{MoO}_3)_3(\text{SeO}_3)$  crystallizes to a centrosymmetric layered structure consisting of double-chain  $\text{MoO}_6$  ribbons connected by  $\text{SeO}_3$  polyhedra.<sup>109</sup> It is clear that the weak hydrogen bonding between  $\text{H}_2\text{O}$  molecules and oxide ligands of the Class 2 HTO layers in  $\text{Na}_2(\text{WO}_3)_3(\text{SeO}_3) \cdot 2\text{H}_2\text{O}$  is essential to its polar structure. As expected, on removing the  $\text{H}_2\text{O}$  molecules,  $\text{Na}_2(\text{WO}_3)_3(\text{SeO}_3) \cdot 2\text{H}_2\text{O}$  loses its Class 2 HTO layered structure. In fact,  $\text{Na}_6(\text{W}_6\text{O}_{19})(\text{SeO}_3)_2$  was formed with interesting structural aspects as described earlier. As the  $\text{H}_2\text{O}$  molecules were removed,  $\text{Na}^+$  cation size was too small to fit in the space between the Class 2 HTO layers. The other aspect is that the Se–O bond lengths (~1.7 Å) are substantially shorter than the Te–O bond lengths (~1.9 Å).

Therefore, the  $\text{SeO}_3$  group cannot ‘serve’ as an ‘inter-layer’ linker like  $\text{TeO}_3$  groups in connecting two adjacent HTO layers in  $\text{K}_2(\text{WO}_3)_3(\text{TeO}_3)$ . Thus, the hydrogen bonding of the  $\text{H}_2\text{O}$  molecules together with ionic bonding of  $\text{Na}^+$  cations stabilize the Class 2 HTO layered structure of  $\text{Na}_2(\text{WO}_3)_3(\text{SeO}_3) \cdot 2\text{H}_2\text{O}$ .

### Octahedral Distortion, ELF, Dipole Moments, BSI and GII Calculations

As mentioned earlier,  $\text{Na}_2(\text{WO}_3)_3(\text{SeO}_3) \cdot 2\text{H}_2\text{O}$  and  $\text{Na}_6(\text{W}_6\text{O}_{19})(\text{SeO}_3)_2$  contain SOJT distorted cations, i.e. octahedrally coordinated  $d^0$  transition metal cations,  $\text{W}^{6+}$ , and lone-pair cations,  $\text{Se}^{4+}$ . We are able to quantify the magnitude of the displacement of the  $\text{W}^{6+}$  cations using the SHAPE program.<sup>117</sup> In the reported materials, the displacement magnitude is approximately  $0.02 - 0.07 \text{ \AA}^2$  for octahedrally  $\text{C}_4$ -type distorted  $\text{W}^{6+}$  cations and  $0.11 \text{ \AA}^2$  for octahedrally  $\text{C}_2$ -type distorted  $\text{W}^{6+}$  cations (see Table 5.7). These observations are consistent with those reported for  $\text{W}^{6+}$  cations.<sup>118</sup>

**Table 5.7** Distortion magnitudes of  $\text{WO}_6$  octahedra and dipole moments of  $\text{WO}_6$  and  $\text{SeO}_3$  polyhedra in  $\text{Na}_2(\text{WO}_3)_3(\text{SeO}_3) \cdot 2\text{H}_2\text{O}$  and  $\text{Na}_6(\text{W}_6\text{O}_{19})(\text{SeO}_3)_2$ .

Compounds	Polyhedral dipole moment (D)				$\text{MO}_6$ distortion magnitude ( $\text{\AA}^2$ )
$\text{Na}_2(\text{WO}_3)_3(\text{SeO}_3) \cdot 2\text{H}_2\text{O}$	$\text{WO}_6$	1.9	$\text{SeO}_3$	7.4	0.05
$\text{Na}_6(\text{W}_6\text{O}_{19})(\text{SeO}_3)_2$	$\text{W}(1)\text{O}_6$	1.5	$\text{Se}(1)\text{O}_3$	7.2	0.07
	$\text{W}(2)\text{O}_6$	1.4	$\text{Se}(2)\text{O}_3$	9.3	0.11
	$\text{W}(3)\text{O}_6$	1.8			0.07
	$\text{W}(4)\text{O}_6$	1.8			0.11
	$\text{W}(5)\text{O}_6$	0.7			0.05
	$\text{W}(6)\text{O}_6$	1.3			0.02

With the lone-pair cations, electron localization function (ELF) calculations were performed. As seen in Figure 5.7, violet lobe-like ELF isosurfaces ( $\eta = 0.9$ ) above the  $\text{SeO}_3$  polyhedra are consistent with stereoactive lone-pairs. In order to quantitatively examine the polarization magnitudes of the  $\text{MO}_6$  and  $\text{AO}_3$  polyhedra, the dipole moments were calculated using a method described earlier,<sup>21</sup> and extended subsequently for lone-pair cations.<sup>43</sup> The calculated dipole moments for the  $\text{WO}_6$  and  $\text{SeO}_3$  polyhedra are 0.7–2.0 D and 7.2–9.5 D, respectively. These values are consistent with those reported earlier.<sup>47,55</sup> With  $\text{Na}_2(\text{WO}_3)_3(\text{SeO}_3) \cdot 2\text{H}_2\text{O}$ , all dipole moments of the  $\text{WO}_6$  and  $\text{SeO}_3$  polyhedra are aligned in a parallel manner, and a large dipole moments of 64.8 D per unit cell is obtained along the c-axis direction, consistent with the polar axis direction of the crystal class,  $3m$ .<sup>119</sup> For  $\text{Na}_6(\text{W}_6\text{O}_{19})(\text{SeO}_3)_2$ , the dipole moments of the  $\text{WO}_6$  and the  $\text{Se}(1)\text{O}_3$  polyhedra are aligned in an anti-parallel manner, whereas dipole moments of the  $\text{Se}(2)\text{O}_3$  polyhedra are all aligned in a parallel manner along b-axis direction, resulting in a dipole moment of 34.4 D per unit cell along that direction, consistent with the polar axis direction of the crystal class,  $2$ .<sup>119</sup>

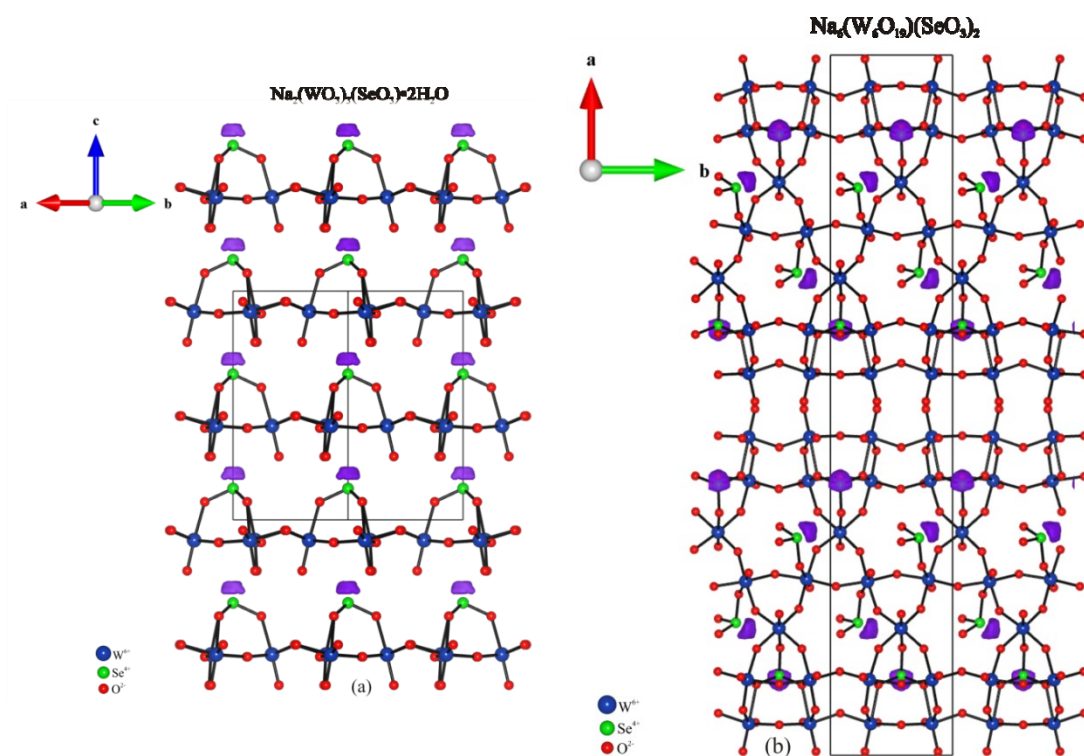


**Figure 5.7** Ball-and-stick representations of (a)  $\text{Na}_2(\text{WO}_3)_3(\text{SeO}_3) \cdot 2\text{H}_2\text{O}$  in (110) plane and (b)  $\text{Na}_6(\text{W}_6\text{O}_{19})(\text{SeO}_3)_2$  in ab-plane. Electron localization function (ELF) plots with  $\eta = 0.9$  is also shown. The lobe-like isosurfaces near the tops of  $\text{SeO}_3$  polyhedra are consistent with stereo-active lone-pairs on the  $\text{Se}^{4+}$  cations. The  $\text{H}_2\text{O}$  molecules in  $\text{Na}_2(\text{WO}_3)_3(\text{SeO}_3) \cdot 2\text{H}_2\text{O}$  and  $\text{Na}^+$  cations have been removed for clarity.

In order to better understand the influence of the polar  $\text{WO}_6$  and  $\text{SeO}_3$  polyhedra on the structures of the reported materials, bond strain and global instability indices, BSI and GII respectively, were calculated.<sup>105,120,121</sup> The BSI and GII indices are indicative of electronic- and lattice-induced strains respectively. Values greater than 0.05 vu (valence units) indicate the structures are strained. For the reported materials, the BSI and GII values are greater than 0.05 vu (see Table 5.5). This is not surprising given the occurrence of asymmetric polyhedra. As seen in Table 5.5, the BSI values are 0.18 and



0.16 vu for  $\text{Na}_2(\text{WO}_3)_3(\text{SeO}_3) \cdot 2\text{H}_2\text{O}$  and  $\text{Na}_6(\text{W}_6\text{O}_{19})(\text{SeO}_3)_2$ , respectively. The BSI values for  $\text{Na}_2(\text{WO}_3)_3(\text{SeO}_3) \cdot 2\text{H}_2\text{O}$  are relatively larger than other Class 2 HTO layered materials (0.11–0.15 vu).<sup>55</sup> The larger BSI values are attributable to hydrogen bonding between polyhedra of the SOJT cations and the  $\text{H}_2\text{O}$  molecules. As no hydrogen bonding presents in  $\text{Na}_6(\text{W}_6\text{O}_{19})(\text{SeO}_3)_2$  the BSI decreases but is still large as the SOJT distorted cations experienced two types of octahedral distortions, i.e,  $\text{C}_2$ - and  $\text{C}_4$ -type distortions with a variety of distortion magnitudes (0.02–0.11 Å<sup>2</sup>). The GII indices are 0.11 and 0.13 vu for  $\text{Na}_2(\text{WO}_3)_3(\text{SeO}_3) \cdot 2\text{H}_2\text{O}$  and  $\text{Na}_6(\text{W}_6\text{O}_{19})(\text{SeO}_3)_2$  respectively.  $\text{BSI} > \text{GII}$  for both materials suggests the structural strains are electronically-induced, i.e., bond distances of SOJT cations are mainly determined by electronic SOJT distortions.

### **Infrared Spectroscopy**

As described in the measurement procedure,  $\text{Na}_2(\text{WO}_3)_3(\text{SeO}_3) \cdot 2\text{H}_2\text{O}$  and  $\text{Na}_6(\text{W}_6\text{O}_{19})(\text{SeO}_3)_2$  powder were heated at 150 °C for one week to remove absorbed moisture before collecting their infrared (IR) spectra (see Figure 5.8). The IR spectrum of  $\text{Na}_2(\text{WO}_3)_3(\text{SeO}_3) \cdot 2\text{H}_2\text{O}$  showed a broad absorption peak at 3550 cm<sup>-1</sup> attributable to O–H stretching vibrations and a sharp strong absorption peak at 1619 cm<sup>-1</sup> attributable to H–O–H bending vibrations.<sup>122</sup> The existence of these peaks therefore clearly confirms the presence of the  $\text{H}_2\text{O}$  molecules in the crystal structure of  $\text{Na}_2(\text{WO}_3)_3(\text{SeO}_3) \cdot 2\text{H}_2\text{O}$ . In the IR spectrum of  $\text{Na}_6(\text{W}_6\text{O}_{19})(\text{SeO}_3)_2$ , there are no absorption peaks in the range of 1000–4000 cm<sup>-1</sup>. Below 1000 cm<sup>-1</sup>, both materials showed W–O stretching vibrations in the range of 814–977 cm<sup>-1</sup>, Se–O stretching vibrations in the range of 613–760 cm<sup>-1</sup>, and Se–

O–Se(W) bending vibrations below  $600\text{ cm}^{-1}$ . These assignments are in good agreement with the literature.<sup>123-125</sup>

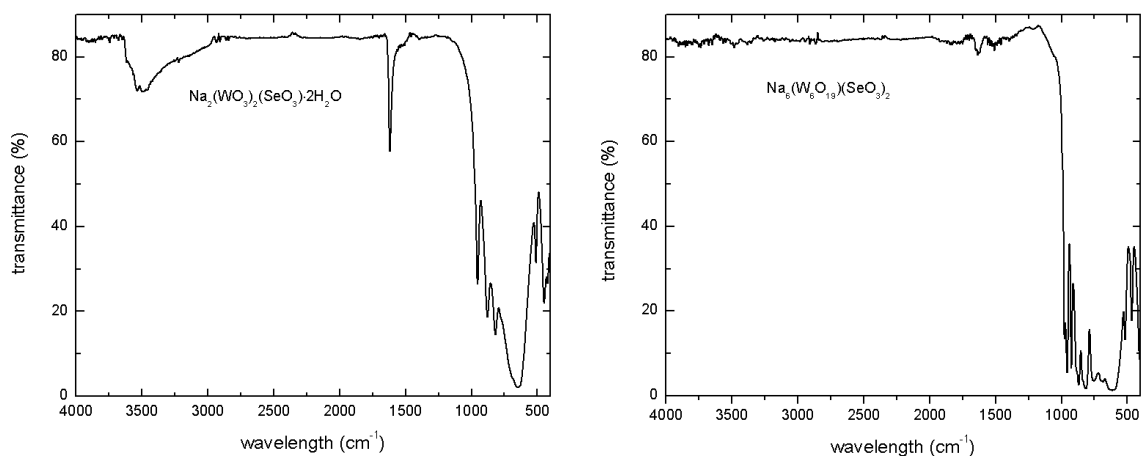


**Figure 5.8** IR data and assignments for  $\text{Na}_2(\text{WO}_3)_3(\text{SeO}_3)\cdot 2\text{H}_2\text{O}$  and  $\text{Na}_6(\text{W}_6\text{O}_{19})(\text{SeO}_3)_2$ .

**Table 5.8** IR peak assignments for  $\text{Na}_2(\text{WO}_3)_3(\text{SeO}_3)\cdot 2\text{H}_2\text{O}$  and  $\text{Na}_6(\text{W}_6\text{O}_{19})(\text{SeO}_3)_2$ .

Compound	Infrared absorption bands ( $\text{cm}^{-1}$ )			
	$\text{H}_2\text{O}$	W-O	Se-O	W-O-Se
$\text{Na}_2(\text{WO}_3)_3(\text{SeO}_3)\cdot 2\text{H}_2\text{O}$	3550, 1619	953, 878, 818	648	510, 448
$\text{Na}_6(\text{W}_6\text{O}_{19})(\text{SeO}_3)_2$	-	977, 956, 924, 868, 839, 814	760, 694, 613	516, 466, 408

### UV–vis Diffuse Reflectance Spectroscopy

Reflectance spectra of  $\text{Na}_2(\text{WO}_3)_3(\text{SeO}_3)\cdot 2\text{H}_2\text{O}$  and  $\text{Na}_6(\text{W}_6\text{O}_{19})(\text{SeO}_3)_2$  were converted to absorbance using the Kubelka–Munk function:<sup>93,94</sup>

$$F(R) = \frac{K}{S} = \frac{(1 - R)^2}{2R} \quad (5.1)$$

where R, K, and S represent the reflectance, the absorption, and the scattering, respectively. In a  $F(R)$  vs.  $E$  (eV) plot (see Figure 5.9), extrapolating the linear part of the rising curve to zero provides onset absorption of 3.2 eV and 2.9 eV for  $\text{Na}_2(\text{WO}_3)_3(\text{SeO}_3) \cdot 2\text{H}_2\text{O}$  and  $\text{Na}_6(\text{W}_6\text{O}_{19})(\text{SeO}_3)_2$ , respectively. These values are consistent with the transparency of the materials in the visible wavelength range.

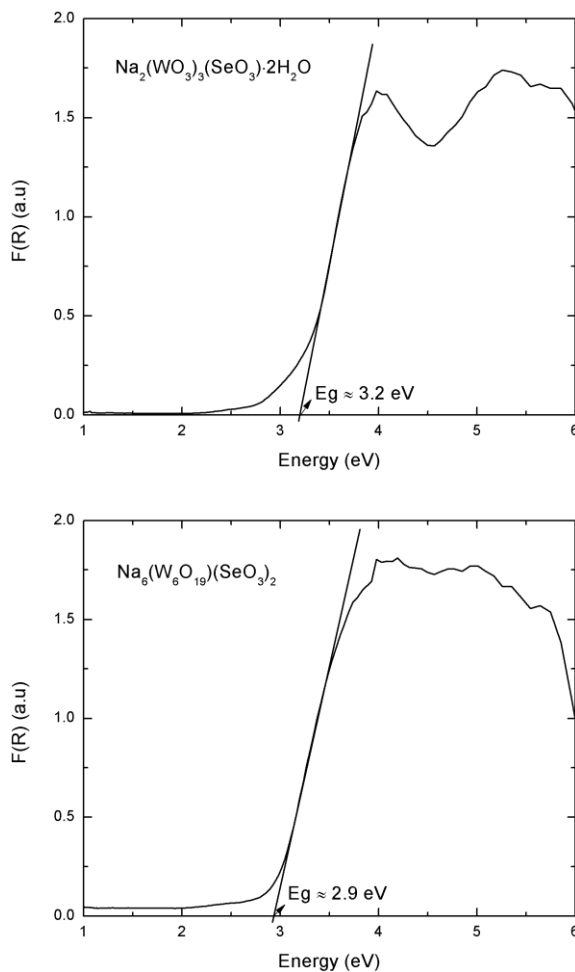
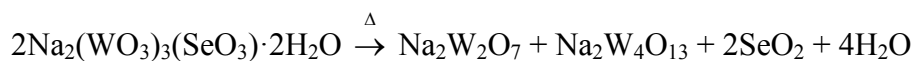


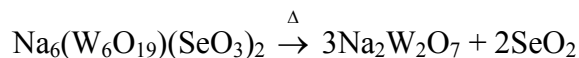
**Figure 5.9** UV–vis diffuse reflectance spectroscopy data  $\text{Na}_2(\text{WO}_3)_3(\text{SeO}_3) \cdot 2\text{H}_2\text{O}$  and  $\text{Na}_6(\text{W}_6\text{O}_{19})(\text{SeO}_3)_2$ .

## Thermal Analysis

The thermal stability of  $\text{Na}_2(\text{WO}_3)_3(\text{SeO}_3) \cdot 2\text{H}_2\text{O}$  and  $\text{Na}_6(\text{W}_6\text{O}_{19})(\text{SeO}_3)_2$  was investigated through thermogravimetric and differential thermal analyses, TGA and DTA, respectively (see Figure 5.10). The TGA and DTA data of  $\text{Na}_2(\text{WO}_3)_3(\text{SeO}_3) \cdot 2\text{H}_2\text{O}$  showed that the oxide experienced two weight loss steps in the temperature range of 25–700 °C. The first weight loss (3.8%) happened in the temperature range of 200 – 300 °C where the  $\text{H}_2\text{O}$  molecules were released from the material (calculated weight percentage of the  $\text{H}_2\text{O}$  is 4.0%). The second weight loss (11.9%) happened above 450 °C where the material released  $\text{SeO}_2$  (calculated weight percentage of  $\text{SeO}_2$  is 12.2%). The PXRD analysis showed  $\text{Na}_2(\text{WO}_3)_3(\text{SeO}_3) \cdot 2\text{H}_2\text{O}$  finally decomposed to a mixture of  $\text{Na}_2\text{W}_2\text{O}_7$  and  $\text{Na}_2\text{W}_4\text{O}_{13}$  as described by the following equation



The TGA and DTA data of  $\text{Na}_6(\text{W}_6\text{O}_{19})(\text{SeO}_3)_2$  showed that the oxide experienced two consecutive weight loss steps in the temperature range of 450–700 °C. The total experimental weight loss of 12.3% is in agreement with the fact that  $\text{Na}_6(\text{W}_6\text{O}_{19})(\text{SeO}_3)_2$  lost two  $\text{SeO}_2$  molecules at high temperature (calculated weight percentage of  $\text{SeO}_2$  is 12.3%). The observation of two consecutive weight losses during the thermal analysis of  $\text{Na}_6(\text{W}_6\text{O}_{19})(\text{SeO}_3)_2$  reflects two different  $\text{SeO}_3$  bonding groups: one capped on triangular holes and one single-bonded to the  $\text{W}(6)\text{O}_6$  ‘single chain’. The PXRD analysis showed  $\text{Na}_6(\text{W}_6\text{O}_{19})(\text{SeO}_3)_2$  finally decomposed to  $\text{Na}_2\text{W}_2\text{O}_7$  as described by the following equation



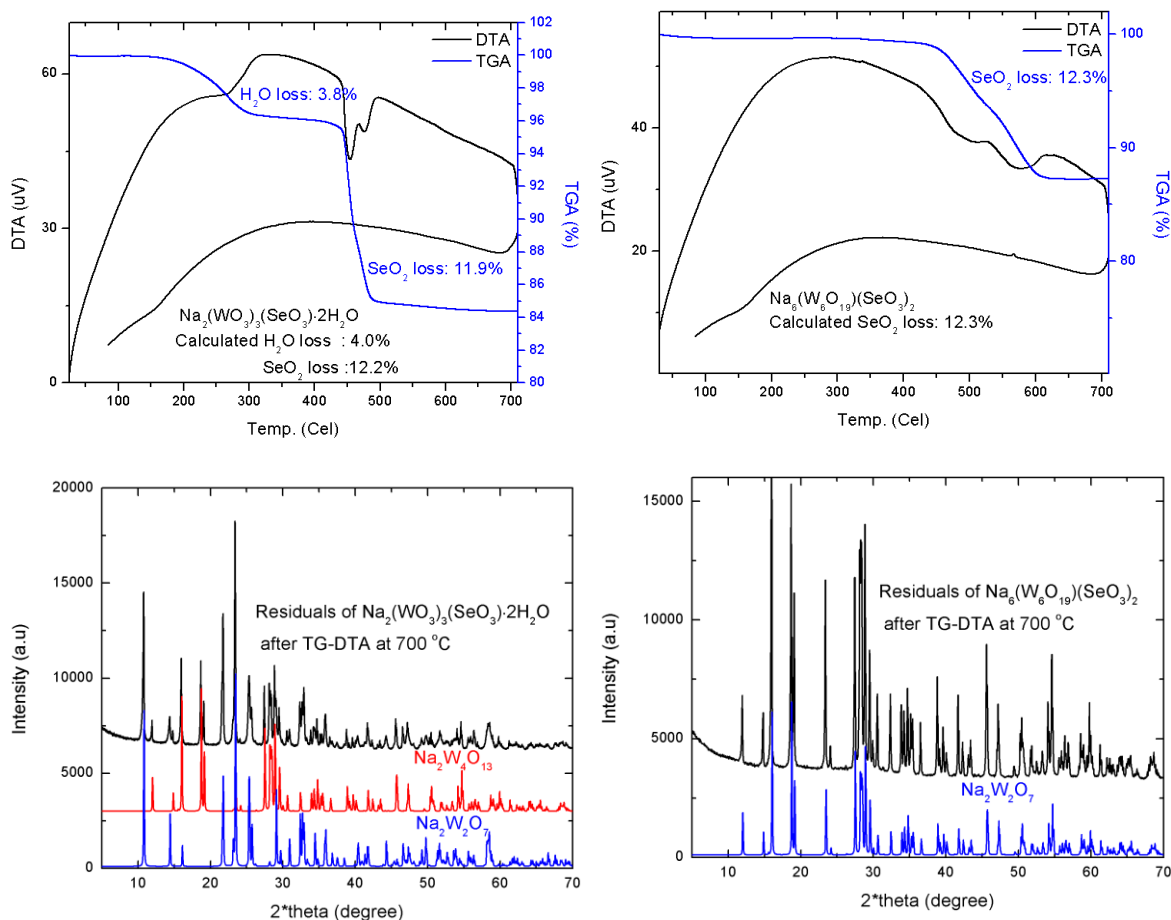


**Figure 5.10** Thermogravimetric and differential thermal analysis data, and powder X-ray diffraction patterns of  $\text{Na}_2(\text{WO}_3)_3(\text{SeO}_3) \cdot 2\text{H}_2\text{O}$  and  $\text{Na}_6(\text{W}_6\text{O}_{19})(\text{SeO}_3)_2$  residuals after thermal analyses.

### Second-harmonic Generation

Powder SHG measurements in the particle size range of 25–120  $\mu\text{m}$  indicated that  $\text{Na}_2(\text{WO}_3)_3(\text{SeO}_3) \cdot 2\text{H}_2\text{O}$  and  $\text{Na}_6(\text{W}_6\text{O}_{19})(\text{SeO}_3)_2$  were nonphase matching materials (see Figure 5.11). In the particle size range of 45–63  $\mu\text{m}$ ,  $\text{Na}_2(\text{WO}_3)_3(\text{SeO}_3) \cdot 2\text{H}_2\text{O}$  has a strong SHG efficiency of  $450 \times \alpha\text{-SiO}_2$ , which is similar to the magnitudes of SHG efficiencies of other Class 2 HTO layered materials,<sup>55</sup> whereas  $\text{Na}_6(\text{W}_6\text{O}_{19})(\text{SeO}_3)_2$

exhibit a weak SHG efficiency of  $20 \times \alpha\text{-SiO}_2$ . As defined by Kurtz and Perry,<sup>95</sup>  $\text{Na}_2(\text{WO}_3)_3(\text{SeO}_3) \cdot 2\text{H}_2\text{O}$  falls into the class C of SHG materials, and  $\text{Na}_6(\text{W}_6\text{O}_{19})(\text{SeO}_3)_2$  belongs to the class D of SHG materials. The average NLO susceptibilities,  $\langle d_{\text{eff}} \rangle_{\text{exp}}$ , for  $\text{Na}_2(\text{WO}_3)_3(\text{SeO}_3) \cdot 2\text{H}_2\text{O}$  and  $\text{Na}_6(\text{W}_6\text{O}_{19})(\text{SeO}_3)_2$  can be estimated to be  $\sim 11.7$  and  $2.5$  pm/V, respectively. The strong SHG efficiency of  $\text{Na}_2(\text{WO}_3)_3(\text{SeO}_3) \cdot 2\text{H}_2\text{O}$  can be understood as all stereoactive lone-pairs of  $\text{SeO}_3$  groups are aligned in a parallel manner towards c-axis direction. For  $\text{Na}_6(\text{W}_6\text{O}_{19})(\text{SeO}_3)_2$ , because of the internal two-fold rotation of the ‘ribbon’ about the  $\text{W}(6)\text{O}_6$  ‘single chain’, all dipole moments of  $\text{W}(x)\text{O}_6$  ( $x = 1-5$ ) and  $\text{Se}(1)\text{O}_3$  polyhedra cancel. Only the dipole moments of the  $\text{W}(6)\text{O}_6$  and  $\text{Se}(2)\text{O}_3$  polyhedra, with a net magnitude of 34.4 Debye along b-axis direction, remain. Thus, it is expected that the SHG efficiency of  $\text{Na}_6(\text{W}_6\text{O}_{19})(\text{SeO}_3)_2$  will be weaker than that of  $\text{Na}_2(\text{WO}_3)_3(\text{SeO}_3) \cdot 2\text{H}_2\text{O}$ . In fact,  $\text{Na}_6(\text{W}_6\text{O}_{19})(\text{SeO}_3)_2$  was experimentally observed as having a weaker SHG efficiency than  $\text{Na}_2(\text{WO}_3)_3(\text{SeO}_3) \cdot 2\text{H}_2\text{O}$ .

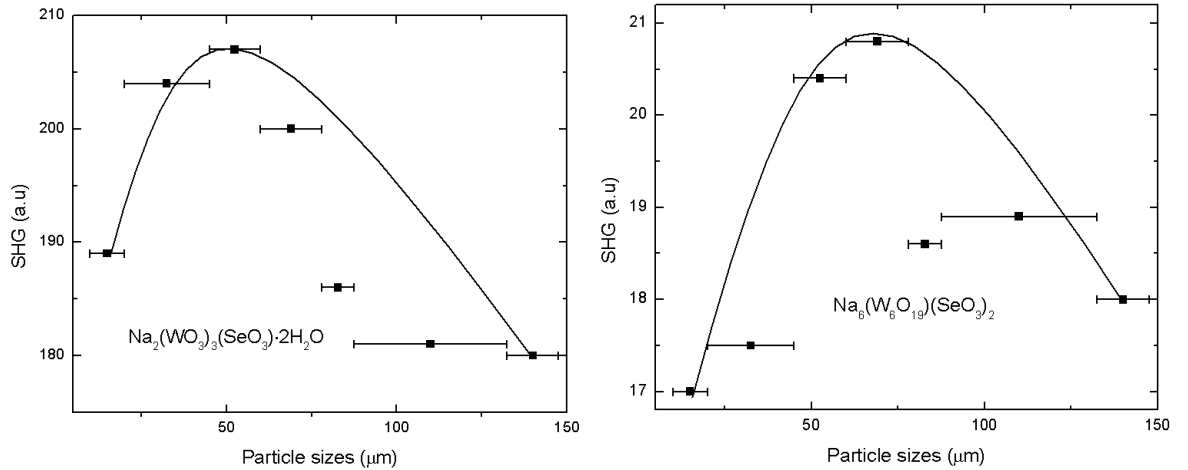


**Figure 5.11** Particle-size vs. SHG intensity data for  $\text{Na}_2(\text{WO}_3)_3(\text{SeO}_3) \cdot 2\text{H}_2\text{O}$  and  $\text{Na}_6(\text{W}_6\text{O}_{19})(\text{SeO}_3)_2$ . The curves are drawn to guide the eye and are not a fit to the data.

## Piezoelectric Measurements

Converse piezoelectric measurements were performed on  $\text{Na}_2(\text{WO}_3)_3(\text{SeO}_3) \cdot 2\text{H}_2\text{O}$  and  $\text{Na}_6(\text{W}_6\text{O}_{19})(\text{SeO}_3)_2$  pellets at room temperature. A voltage of 1000 V at 100 Hz was applied to the  $\text{Na}_2(\text{WO}_3)_3(\text{SeO}_3) \cdot 2\text{H}_2\text{O}$  pellet and a voltage of 2000 V at 100 Hz was applied to the  $\text{Na}_6(\text{W}_6\text{O}_{19})(\text{SeO}_3)_2$  pellet. The  $d_{33}$  piezoelectric charge constants,<sup>96</sup> which are defined as the ratio between the strain produced and the electrical voltage applied, for  $\text{Na}_2(\text{WO}_3)_3(\text{SeO}_3) \cdot 2\text{H}_2\text{O}$  and  $\text{Na}_6(\text{W}_6\text{O}_{19})(\text{SeO}_3)_2$  were estimated to be 23 and 12 pm/V, respectively (see Figure 5.12). These charge constants are comparable to Class 2 HTO layered materials,  $\text{A}_2(\text{MoO}_3)_3(\text{SeO}_3)$  ( $\text{A} = \text{Rb}^+$  and  $\text{Tl}^+$ ) ( $d_{33} = 9\text{--}11$  pm/V),<sup>55</sup> or  $\text{Na}_2\text{TeW}_2\text{O}_9$  ( $d_{33} = 13.9$  pm/V).<sup>126</sup>

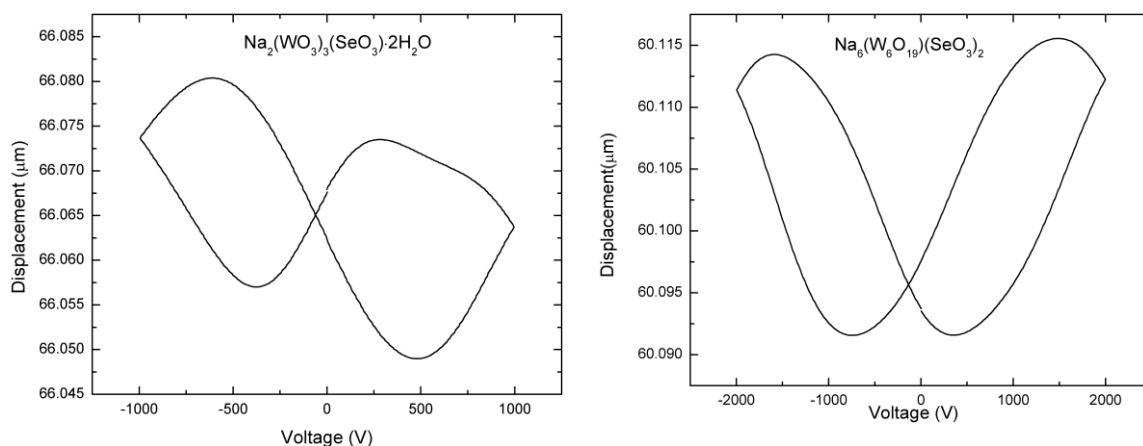


**Figure 5.12** The displacement vs. electric field plot for  $\text{Na}_2(\text{WO}_3)_3(\text{SeO}_3) \cdot 2\text{H}_2\text{O}$  and  $\text{Na}_6(\text{W}_6\text{O}_{19})(\text{SeO}_3)_2$ .

**Table 5.9** SHG efficiency ( $\times \alpha\text{-SiO}_2$ ), piezoelectric responses,  $d_{33}$  (pm/V), pyroelectric coefficients at 60 °C,  $P_T$  ( $\mu\text{C}/\text{m}^2\text{K}$ ), and maximum polarization,  $P_m$  ( $\mu\text{C}/\text{m}^2$ ) for  $\text{Na}_2(\text{WO}_3)_3(\text{SeO}_3)\cdot 2\text{H}_2\text{O}$  and  $\text{Na}_6(\text{W}_6\text{O}_{19})(\text{SeO}_3)_2$ .

Compound	Functional Properties			
	SHG	$d_{33}$	$P_T$	$P_m$
$\text{Na}_2(\text{WO}_3)_3(\text{SeO}_3)\cdot 2\text{H}_2\text{O}$	450	23	-0.41	0.025
$\text{Na}_6(\text{W}_6\text{O}_{19})(\text{SeO}_3)_2$	20	12	-1.10	0.085

### Polarization Measurements

$\text{Na}_2(\text{WO}_3)_3(\text{SeO}_3)\cdot 2\text{H}_2\text{O}$  (*P3<sub>1</sub>c*) and  $\text{Na}_6(\text{W}_6\text{O}_{19})(\text{SeO}_3)_2$  (*C2*) are polar materials – a macroscopic dipole moment is observed. The macroscopic polarity suggests the possibility for ferroelectric behavior. Ferroelectric hysteresis measurements were performed on the pressed pellets, and polarization loops were observed. In addition, these loops did appear to exhibit frequency dependence (see Figure 5.13). Thus these loops are not attributable to ferroelectric hysteresis, i.e., the reported materials are not ferroelectric – the macroscopic polarization cannot be reversed in the presence of an external electric field. It has been demonstrated that these types of loops have been erroneously attributed to ferroelectric behavior.<sup>127</sup> With the reported materials, it is important to understand why the materials, although polar, are not ferroelectric. As stated earlier, for ferroelectric behavior to occur the macroscopic polarization must be switchable in the presence of an external electric field. This implies that the local moments must also be reversed. In  $\text{Na}_2(\text{WO}_3)_3(\text{SeO}_3)\cdot 2\text{H}_2\text{O}$  and  $\text{Na}_6(\text{W}_6\text{O}_{19})(\text{SeO}_3)_2$  the dipole moments are associated with distorted  $\text{WO}_6$  and asymmetric  $\text{SeO}_3$  polyhedra. We have already shown that the energy



barrier to invert a  $\text{SeO}_3$  trigonal pyramid is  $\sim 5.3 \text{ eV}$ ,<sup>49</sup> which is substantially larger than what is observed in ferroelectric  $\text{BaTiO}_3$  ( $1.8 \times 10^{-2} \text{ eV}$ ) and  $\text{PbTiO}_3$  ( $2.0 \times 10^{-1} \text{ eV}$ ).<sup>128</sup> Thus it is energetically unfavorable for polarization reversal to occur. Therefore,  $\text{Na}_2(\text{WO}_3)_3(\text{SeO}_3) \cdot 2\text{H}_2\text{O}$  and  $\text{Na}_6(\text{W}_6\text{O}_{19})(\text{SeO}_3)_2$  are pyroelectric and not ferroelectric.

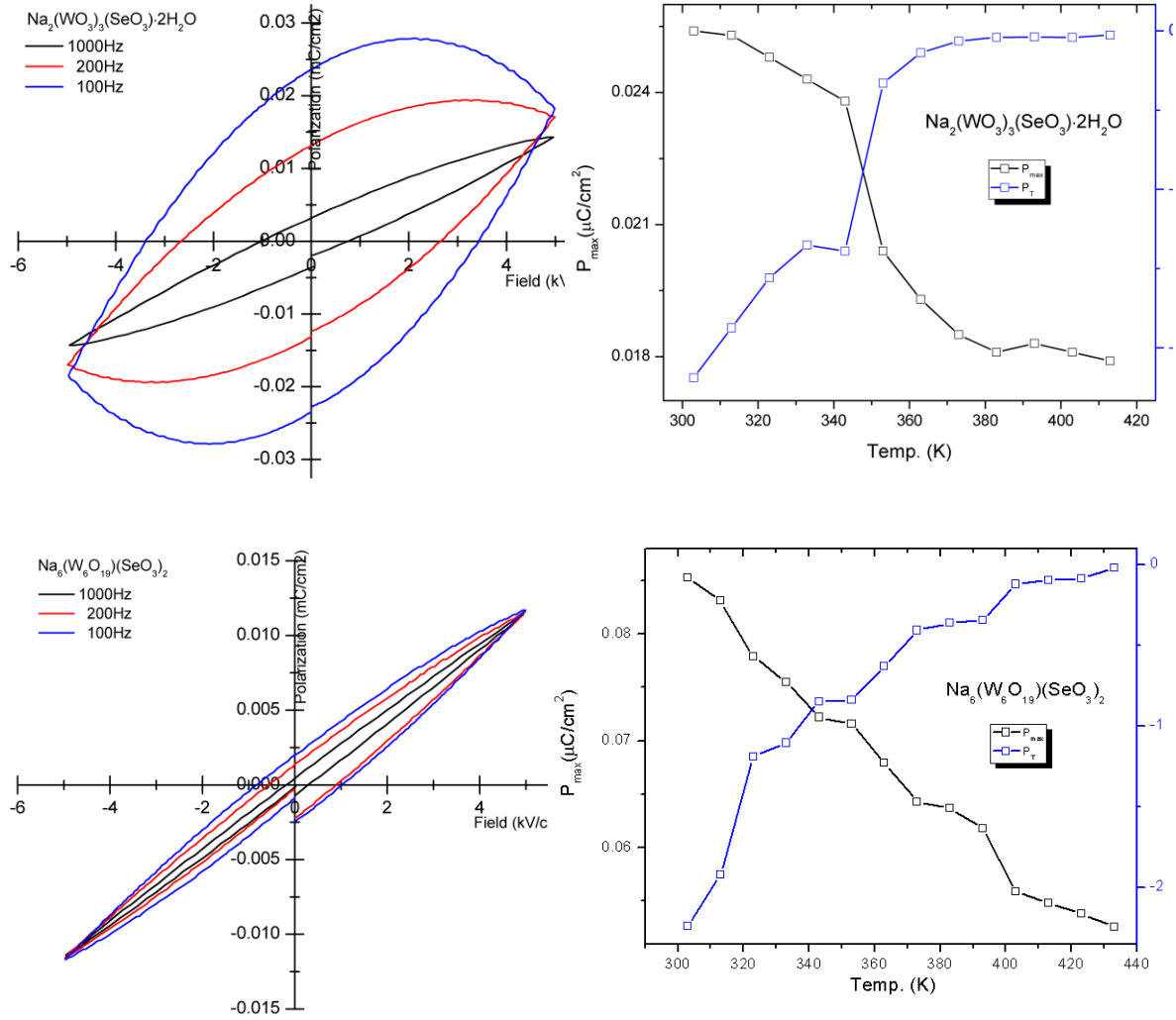


**Figure 5.13** Frequency-dependent (left) polarization-electric field loops and a pyroelectric coefficient vs. temperature plot (right) for  $\text{Na}_2(\text{WO}_3)_3(\text{SeO}_3) \cdot 2\text{H}_2\text{O}$  and  $\text{Na}_6(\text{W}_6\text{O}_{19})(\text{SeO}_3)_2$ .

Pyroelectric measurements were performed by measuring the spontaneous polarization ( $P_s$ ) as a function of temperature (see Figure 5.13). The values of the pyroelectric coefficient, which is defined as  $dP/dT$ ,<sup>96</sup> for  $\text{Na}_2(\text{WO}_3)_3(\text{SeO}_3) \cdot 2\text{H}_2\text{O}$  and  $\text{Na}_6(\text{W}_6\text{O}_{19})(\text{SeO}_3)_2$  at 60 °C are -0.41 and -1.10  $\mu\text{C}/\text{m}^2\text{K}$ , respectively. The magnitudes of these pyroelectric coefficients are similar to other Class 2 HTO layered materials,  $\text{A}_2(\text{MoO}_3)_3(\text{SeO}_3)$  ( $\text{A} = \text{Rb}^+$  and  $\text{Tl}^+$ ) (-1.1 to -2.1  $\mu\text{C}/\text{m}^2\text{K}$ ).<sup>55</sup>

## 5.5 Conclusion

Two new sodium tungsten selenites,  $\text{Na}_2(\text{WO}_3)_3(\text{SeO}_3) \cdot 2\text{H}_2\text{O}$  ( $P3_1c$ ) and  $\text{Na}_6(\text{W}_6\text{O}_{19})(\text{SeO}_3)_2$  (C2), have been synthesized and characterized.  $\text{Na}_2(\text{WO}_3)_3(\text{SeO}_3) \cdot 2\text{H}_2\text{O}$  exhibits a Class 2 HTO layered structure, i.e., the  $\text{SeO}_3$  groups ‘cap’ on one side of the HTO layers, and  $\text{Na}_6(\text{W}_6\text{O}_{19})(\text{SeO}_3)_2$  exhibits an one-dimensional complex ‘ribbon’ structure.  $\text{Na}_2(\text{WO}_3)_3(\text{SeO}_3) \cdot 2\text{H}_2\text{O}$  exhibits a strong SHG efficiency of  $450 \times \alpha\text{-SiO}_2$  and  $\text{Na}_6(\text{W}_6\text{O}_{19})(\text{SeO}_3)_2$  shows a weak SHG efficiency of  $20 \times \alpha\text{-SiO}_2$ . Finally, the polarization measurements indicate both oxides are pyroelectric and not ferroelectric materials.

## 5.6 References

1. Boyd, R. W. *Nonlinear Optics*; Third ed.; Academic Press, 2008.
2. Cady, W. G. *Piezoelectricity: An Introduction to the Theory and Applications of Electromechanical Phenomena in Crystals. Revised ed*; Dover, 1964.
3. Capper, P. *Bulk Crystal Growth of Electronic, Optical and Optoelectronic Materials*; John Wiley & Sons, Inc, 2005.
4. Jaffe, B.; Cook, W. R. *Piezoelectric Ceramics*; Academic Press, 1971.
5. Jona, F.; Shirane, G. *Ferroelectric Crystals*; Pergamon Press, 1961.
6. Lang, S. B. *Sourcebook of Pyroelectricity*; Gordon and Breach, 1974.
7. Lang, S. B.; Das-Gupta, D. K. *Pyroelectricity: Fundamentals and Applications*; Academic Press, 2001; Vol. 4.
8. Lines, M. E.; Glass, A. M. *Principles and Applications of Ferroelectrics and Related Materials*; Oxford University Press: Oxford, 1991.
9. Bosshard, C.; Hulliger, J.; Florsheimer, M. *Organic Nonlinear Optical Materials*; CRC Press, 2001.
10. Eaton, D. F. *Science* **1991**, 253, 281.
11. Chen, C. T. *Acta Phys. Sin.* **1976**, 25, 146.
12. Chen, C. T. *Acta Phys. Sin.* **1977**, 26, 124.

13. Chen, C. T. *Acta Phys. Sin.* **1977**, *26*, 468.
14. Chen, C. T. *Acta Phys. Sin.* **1979**, *22*, 756.
15. Chen, C.; Wu, Y.; Li, R. *Int. Rev. Phys. Chem.* **1989**, *8*, 65.
16. Zou, G.; Ye, N.; Huang, L.; Lin, X. *J. Am. Chem. Soc.* **2011**, *133*, 20001.
17. Heier, K. R.; Norquist, A. J.; Halasyamani, P. S.; Duarte, A.; Stern, C. L.; Poeppelmeier, K. R. *Inorg. Chem.* **1999**, *38*, 762.
18. Welk, M. E.; Norquist, A. J.; Stern, C. L.; Poeppelmeier, K. R. *Inorg. Chem.* **2000**, *39*, 3946.
19. Welk, M. E.; Norquist, A. J.; Stern, C. L.; Poeppelmeier, K. R. *Inorg. Chem.* **2001**, *40*, 5479.
20. Welk, M. E.; Norquist, A. J.; Arnold, F. P.; Stern, C. L.; Poeppelmeier, K. R. *Inorg. Chem.* **2002**, *41*, 5119.
21. Maggard, P. A.; Nault, T. S.; Stern, C. L.; Poeppelmeier, K. R. *J. Solid State Chem.* **2003**, *175*, 27.
22. Izumi, H. K.; Kirsch, J. E.; Stern, C. L.; Poeppelmeier, K. R. *Inorg. Chem.* **2005**, *44*, 884.
23. Marvel, M. R.; Lesage, J.; Baek, J.; Halasyamani, P. S.; Stern, C. L.; Poeppelmeier, K. R. *J. Am. Chem. Soc.* **2007**, *129*, 13963.

24. Marvel, M. R.; Pinlac, R. A. F.; Lesage, J.; Stern, C. L.; Poeppelmeier, K. R. Z. *Anorg. Allg. Chem.* **2009**, 635, 869.
25. Donakowski, M. D.; Gautier, R.; Yeon, J.; Moore, D. T.; Nino, J. C.; Halasyamani, P. S.; Poeppelmeier, K. R. *J. Am. Chem. Soc.* **2012**, 134, 7679.
26. Bader, R. F. W. *Mol. Phys.* **1960**, 3, 137.
27. Bader, R. F. W. *Can. J. Chem.* **1962**, 40, 1164.
28. Goodenough, J. B. *Annu. Rev. Mater. Sci.* **1998**, 28, 1.
29. Kunz, M.; Brown, I. D. *J. Solid State Chem.* **1995**, 115, 395.
30. Opik, U.; Pryce, M. H. L. *Proc. R. Soc. London, Ser. A* **1957**, 238, 425.
31. Pearson, R. G. *J. Am. Chem. Soc.* **1969**, 91, 4947.
32. Pearson, R. G. *J. Mol. Struct.:THEOCHEM* **1983**, 103, 25.
33. Ok, K. M.; Halasyamani, P. S. *Chem. Mater.* **2001**, 13, 4278.
34. Porter, Y.; Bhuvanesh, N. S. P.; Halasyamani, P. S. *Inorg. Chem.* **2001**, 40, 1172.
35. Porter, Y.; Ok, K. M.; Bhuvanesh, N. S. P.; Halasyamani, P. S. *Chem. Mater.* **2001**, 13, 1910.
36. Ok, K. M.; Bhuvanesh, N. S. P.; Halasyamani, P. S. *Inorg. Chem.* **2001**, 40, 1978.
37. Goodey, J.; Broussard, J.; Halasyamani, P. S. *Chem. Mater.* **2002**, 14, 3174.
38. Ra, H.-S.; Ok, K. M.; Halasyamani, P. S. *J. Am. Chem. Soc.* **2003**, 125, 7764.

39. Porter, Y.; Halasyamani, P. S. *J. Solid State Chem.* **2003**, *174*, 441.
40. Goodey, J.; Ok, K. M.; Broussard, J.; Hofmann, C.; Escobedo, F. V.; Halasyamani, P. S. *J. Solid State Chem.* **2003**, *175*, 3.
41. Ok, K. M.; Halasyamani, P. S. *Angew. Chem., Int. Ed.* **2004**, *43*, 5489.
42. Sivakumar, T.; Ok, K. M.; Halasyamani, P. S. *Inorg. Chem.* **2006**, *45*, 3602.
43. Ok, K. M.; Halasyamani, P. S. *J. Solid State Chem.* **2006**, *179*, 1345.
44. Chi, E. O.; Ok, K. M.; Porter, Y.; Halasyamani, P. S. *Chem. Mater.* **2006**, *18*, 2070.
45. Kim, J.-H.; Baek, J.; Halasyamani, P. S. *Chem. Mater.* **2007**, *19*, 5637.
46. Sivakumar, T.; Chang, H. Y.; Baek, J.; Halasyamani, P. S. *Chem. Mater.* **2007**, *19*, 4710.
47. Chang, H. Y.; Ok, K. M.; Kim, J. H.; Halasyamani, P. S.; Stoltzfus, M.; Woodward, P. *Inorg. Chem.* **2007**, *46*, 7005.
48. Chang, H. Y.; Sivakumar, T.; Ok, K. M.; Halasyamani, P. S. *Inorg. Chem.* **2008**, *47*, 8511.
49. Kim, S.-H.; Yeon, J.; Halasyamani, P. S. *Chem. Mater.* **2009**, *21*, 5335.
50. Yeon, J.; Kim, S.-H.; Halasyamani, P. S. *J. Solid State Chem.* **2009**, *182*, 3269.
51. Chang, H.-Y.; Kim, S.-H.; Ok, K. M.; Halasyamani, P. S. *J. Am. Chem. Soc.* **2009**, *131*, 6865.

52. Chang, H. Y.; Kim, S.-H.; Ok, K. M.; Halasyamani, P. S. *Chem. Mater.* **2009**, *21*, 1654.
53. Chang, H.-Y.; Kim, S.-H.; Halasyamani, P. S.; Ok, K. M. *J. Am. Chem. Soc.* **2009**, *131*, 2426.
54. Yeon, J.; Kim, S.-H.; Halasyamani, P. S. *Inorg. Chem.* **2010**, *49*, 6986.
55. Chang, H. Y.; Kim, S. W.; Halasyamani, P. S. *Chem. Mater.* **2010**, *22*, 3241.
56. Yeon, J.; Kim, S.-H.; Hayward, M. A.; Halasyamani, P. S. *Inorg. Chem.* **2011**, *50*, 8663.
57. Nguyen, S. D.; Kim, S.-H.; Halasyamani, P. S. *Inorg. Chem.* **2011**, *50*, 5215.
58. Nguyen, S. D.; Yeon, J.; Kim, S.-H.; Halasyamani, P. S. *J. Am. Chem. Soc.* **2011**, *133*, 12422.
59. Shen, Y.-L.; Jiang, H.-L.; Xu, J.; Mao, J.-G.; Cheah, K. W. *Inorg. Chem.* **2005**, *44*, 9314.
60. Kong, F.; Huang, S.-P.; Sun, Z.-M.; Mao, J.-G.; Cheng, W.-D. *J. Am. Chem. Soc.* **2006**, *128*, 7750.
61. Jiang, H.-L.; Xie, Z.; Mao, J.-G. *Inorg. Chem.* **2007**, *46*, 6495.
62. Jiang, H.-L.; Huang, S.-P.; Fan, Y.; Mao, J.-G.; Cheng, W.-D. *Chem. Eur. J.* **2008**, *14*, 1972.
63. Zhang, S.-Y.; Jiang, H.-L.; Sun, C.-F.; Mao, J.-G. *Inorg. Chem.* **2009**, *48*, 11809.

64. Hu, T.; Qin, L.; Kong, F.; Zhou, Y.; Mao, J.-G. *Inorg. Chem.* **2009**, *48*, 2193.
65. Sun, C.-F.; Hu, C.-L.; Xu, X.; Ling, J.-B.; Hu, T.; Kong, F.; Long, X.-F.; Mao, J.-G. *J. Am. Chem. Soc.* **2009**, *131*, 9486.
66. Zhang, S.-Y.; Hu, C.-L.; Sun, C.-F.; Mao, J.-G. *Inorg. Chem.* **2010**, *49*, 11627.
67. Li, P.-X.; Hu, C.-L.; Xu, X.; Wang, R.-Y.; Sun, C.-F.; Mao, J.-G. *Inorg. Chem.* **2010**, *49*, 4599.
68. Yang, B.-P.; Hu, C.-L.; Xu, X.; Sun, C.-F.; Zhang, J.-H.; Mao, J.-G. *Chem. Mater.* **2010**, *22*, 1545.
69. Li, P.-X.; Kong, F.; Hu, C.-L.; Zhao, N.; Mao, J.-G. *Inorg. Chem.* **2010**, *49*, 5943.
70. Sun, C.-F.; Hu, C.-L.; Xu, X.; Mao, J.-G. *Inorg. Chem.* **2010**, *49*, 9581.
71. Kong, F.; Xu, X.; Mao, J.-G. *Inorg. Chem.* **2010**, *49*, 11573.
72. Sun, C.-F.; Hu, C.-L.; Xu, X.; Yang, B.-P.; Mao, J.-G. *J. Am. Chem. Soc.* **2011**, *133*, 5561.
73. Brammer, L. *Chem. Soc. Rev.* **2004**, *33*, 476.
74. Chang, Y.-F.; Lu, Z.-Y.; An, L.-J.; Zhang, J.-P. *J. Phys. Chem. C* **2011**, *116*, 1195.
75. Debrus, S.; Ratajczak, H.; Venturini, J.; Pinçon, N.; Baran, J.; Barycki, J.; Glowiak, T.; Pietraszko, A. *Synthetic Met.* **2002**, *127*, 99.



76. Etter, M. C.; Frankenbach, G. M.; Adsmond, D. A. *Mol. Cryst. Liq. Cryst.* **1990**, *187*, 25.
77. Hernández, E.; Mas, M.; Molins, E.; Rovira, C.; Veciana, J. *Angew. Chem. Int. Ed. Engl.* **1993**, *32*, 882.
78. Moulton, B.; Zaworotko, M. J. *Chem. Rev.* **2001**, *101*, 1629.
79. Subramanian, S.; Zaworotko, M. J. *Coord. Chem. Rev.* **1994**, *137*, 357.
80. Zhang, F.; Li, K.; Xue, D.; Pan, S. *Rev. Adv. Sci. Eng.* **2012**, *1*, 75.
81. Oh, S.-J.; Lee, D. W.; Ok, K. M. *Inorg. Chem.* **2012**, *51*, 5393.
82. Fry, A. M.; Seibel, H. A.; Lokuhewa, I. N.; Woodward, P. M. *J. Am. Chem. Soc.* **2011**, *134*, 2621.
83. Darriet, J.; Guillaume, G.; Galy, J. *C. R. Acad. Sci., Ser. C* **1969**, *269*, 23.
84. Darriet, J.; Guillaume, G.; Wilhelmi, K. A.; Galy, J. *Acta Chem. Scand.* **1972**, *26*, 59.
85. Vidyavathy, B.; Vidyasagar, K. *Inorg. Chem.* **1999**, *38*, 5809.
86. *SAINT, Program for Area Detector Absorption Correction, version 4.05*; Siemens Analytical X-ray Systems, Inc.: Madison, WI, 1995.
87. North, A. C. T.; Phillips, D. C.; Mathews, F. S. *Acta Crystallogr.* **1968**, *24*, 351.

88. Sheldrick, G. M. *SHELXL-97 - A Program for Crystal Structure Refinement.*; University of Goettingen: Goettingen, 1997.
89. Sheldrick, G. M. *SHELXS-97 - A Program for Automatic Solution of Crystal Structures.*; University of Goettingen: Goettingen, Germany, 1997.
90. Farrugia, L. J. *J. Appl. Crystallogr.* **1999**, 32, 837.
91. Spek, A. L. *PLATON*; Utrecht University: Utrecht, The Netherlands, 2001.
92. Flack, H. *Acta Crystallogr.* **1983**, 39, 876.
93. Kubelka, P.; Munk, F. *Z. Tech. Phys.* **1931**, 12, 593.
94. Tauc, J. *Mater. Res. Bull.* **1970**, 5, 721.
95. Kurtz, S. K.; Perry, T. T. *J. Appl. Phys.* **1968**, 39, 3798.
96. Ok, K. M.; Chi, E. O.; Halasyamani, P. S. *Chem. Soc. Rev.* **2006**, 35, 710.
97. Becke, A. D.; Edgecombe, K. E. *J. Chem. Phys.* **1990**, 92, 5397.
98. Silvi, B.; Savin, A. *Nature* **1994**, 371, 683.
99. Giannozzi, P. *J. Phys.: Condens. Matter* **2009**, 21, 395502.
100. Perdew, J. P.; Burke, K.; Ernzerhof, M. *Phys. Rev. Lett.* **1996**, 77, 3865.
101. <http://www.fhi-berlin.mpg.de/th/fhi98md/fhi98PP/>: 2004.
102. Fuchs, M.; Scheffler, M. *Comput. Phys. Commun.* **1999**, 119, 67.

103. Monkhorst, H. J.; Pack, J. D. *Phys. Rev. B* **1976**, *13*, 5188.
104. Momma, K.; Izumi, F. *J. Appl. Crystallogr.* **2008**, *41*, 653.
105. Brown, I. D. *The Chemical Bond in Inorganic Chemistry: The Bond Valence Model*; 1st ed.; Oxford University Press: Oxford, 2002.
106. Dussack, L. L.; Harrison, W. T. A.; Jacobson, A. J. *Mater. Res. Bull.* **1996**, *31*, 249.
107. Harrison, W. T. A.; Dussack, L. L.; Jacobson, A. J. *Inorg. Chem.* **1994**, *33*, 6043.
108. Harrison, W. T. A.; Dussack, L. L.; Jacobson, A. J. *Acta Crystallogr., Sect. C: Cryst. Struct. Commun.* **1995**, *C51*, 2473.
109. Ling, J.; Albrecht-Schmitt, T. E. *J. Solid State Chem.* **2007**, *180*, 1601.
110. Vidyavathy, B.; Vidyasagar, K. *Inorg. Chem.* **1998**, *37*, 4764.
111. Shannon, R. *Acta Crystallogr.* **1976**, *32*, 751.
112. Shannon, R. D.; Prewitt, C. T. *Acta Crystallogr.* **1969**, *25*, 925.
113. Shannon, R. D.; Prewitt, C. T. *Acta Crystallogr.* **1970**, *26*, 1046.
114. Denton, A. R.; Ashcroft, N. W. *Phys. Rev. A* **1991**, *43*, 3161.
115. Vegard, L. *Z Phys A-Hadron Nucl* **1921**, *5*, 17.
116. Libowitzky, E. *Monats.* **1999**, *130*, 1047.

117. Llunell, M.; Casanova, D.; Cirera, J.; Bofill, J. M.; Alemany, P.; Alvarez, S.; Pinsky, M.; Avnir, D.; *Shape Program*. 1.1b ed.; University of Barcelona: Barcelona, Spain: 2003.
118. Ok, K. M.; Halasyamani, P. S.; Casanova, D.; Llunell, M.; Alemany, P.; Alvarez, S. *Chem. Mater.* **2006**, *18*, 3176.
119. *International Tables for Crystallography, Vol. A, Space Group Symmetry*; Hahn, T., Ed.; Kluwer Academic: Dordrecht, Holland, 2006; Vol. A.
120. Preiser, C.; Losel, J.; Brown, I. D.; Kunz, M.; Skowron, A. *Acta Crystallogr.* **1999**, *55*, 698.
121. Salinas-Sanchez, A.; Garcia-Muñoz, J. L.; Rodriguez-Carvajal, J.; Saez-Puche, R.; Martinez, J. L. *J. Solid State Chem.* **1992**, *100*, 201.
122. Falk, M. *Spectrochim. Acta, Part A* **1984**, *40A*, 43.
123. Frechero, M. A.; Quinzani, O. V.; Pettigrosso, R. S.; Villar, M.; Montani, R. A. *J. Non-Cryst. Solids* **2007**, *353*, 2919.
124. Harrison, W. T. A.; Dussack, L. L.; Jacobson, A. J. *J. Solid State Chem.* **1996**, *125*, 234.
125. Kurilenko, L. N.; Serebryakova, N. V.; Saunin, E. I.; Gromov, V. V.; Sokolova, N. *P. Russ. Chem. Bull.* **1988**, *37*, 839.
126. Zhang, W.; Li, F.; Kim, S.-H.; Halasyamani, P. S. *Cryst. Growth Des.* **2010**, *10*, 4091.

127. Scott, J. F. *J. Phys.: Condens. Matter* **2008**, *20*, 021001.
128. Cohen, R. E. *Nature* **1992**, *358*, 136.

## CHAPTER 6. Conclusions and Future Work

### 6.1 General conclusions

We have successfully synthesized several new polar materials using the synthetic approach of combining cations (octahedrally coordinated  $d^0$  cations and lone pair cations) that are susceptible to second-order Jahn-Teller distortion (SOJT).<sup>1-7</sup> It has been experimentally confirmed in this dissertation that this synthetic approach enhances efficiently the chance of finding new noncentrosymmetric and polar materials. The synthesized polar oxide materials were fully characterized. The single crystal X-ray diffraction was used to elucidate the new polar crystal structure which is necessary for (i) understanding the origin of structural distortion using the bond valence model and (ii) the structure-property relationship of the reported materials. UV-vis diffuse reflectance spectroscopy, infrared spectroscopy, thermogravimetric, and differential thermal analyses were used to provide physical characterization of the reported materials. Electronic structure and electron localization function calculations provide insight into how the electronic distortion and the formation of stereoactive lone-pairs occur for the SOJT cations in the reported materials. Based upon study of structure-property relationships for the reported polar oxide materials in this dissertation, we proved that the distorted structures of the SOJT cations are primary sources for the polarization occurring in the reported materials. However, it is the alignment of these polarizations that plays a critical role in determining the SHG efficiency and affecting the pyroelectric coefficients.

## 6.2 $\text{Zn}_2(\text{MoO}_4)(\text{AO}_3)$ ( $\text{A} = \text{Se}^{4+}$ or $\text{Te}^{4+}$ ) system

Two isostructural polar oxide materials,  $\text{Zn}_2(\text{MoO}_4)(\text{AO}_3)$  ( $\text{A} = \text{Se}^{4+}$  or  $\text{Te}^{4+}$ ), have been successfully synthesized and characterized. The materials exhibit a three dimensional bond network consisting of tetrahedra of  $\text{ZnO}_4$  and  $\text{MoO}_4$ , asymmetric trigonal pyramids of  $\text{AO}_3$ , and octahedra of  $\text{ZnO}_6$ . The typical feature of their crystal structure is all  $\text{AO}_3$  trigonal pyramids partly aligned toward the same direction, resulting in the polar structure and moderate SHG efficiency for the materials. Another aspect is  $\text{ZnO}_6$  octahedra. It is possible that  $\text{Zn}^{2+}$  cations in the octahedrally coordinated environments can be substituted by other divalent cations such as  $\text{Mg}^{2+}$ ,  $\text{Mn}^{2+}$ ,  $\text{Fe}^{2+}$ ,  $\text{Co}^{2+}$ , and  $\text{Ni}^{2+}$ . We have been experimentally successful in preparing the crystal and polycrystalline of Zn-substituted polar materials such as  $\text{MgZn}(\text{MoO}_4)(\text{TeO}_3)$ ,  $\text{MnZn}(\text{MoO}_4)(\text{TeO}_3)$ , and  $\text{CoZn}(\text{MoO}_4)(\text{TeO}_3)$ . These materials could be interesting because they contain magnetic cations in the polar structure.

## 6.3 Bi-I-O system

$\text{BiO}(\text{IO}_3)$  is a polar oxide containing two lone-pair cations,  $\text{Bi}^{3+}$  and  $\text{I}^{5+}$ , with a very large SHG efficiency ( $500 \times \alpha\text{-SiO}_2$ ). Ternary noncentrosymmetric oxide materials containing two lone-pair cations are rarely found. There are few of them, such as  $\text{TeSeO}_4$ ,<sup>8,9</sup>  $\text{Te}_3\text{SeO}_8$ .<sup>10</sup> Beside  $\text{BiO}(\text{IO}_3)$ , we also successfully synthesized noncentrosymmetric nonpolar  $\text{Bi}_2(\text{IO}_4)(\text{IO}_3)_3$  crystals.<sup>11</sup>  $\text{BiO}(\text{IO}_3)$  exhibit a Aurivillius layered structure. The typical feature in the  $\text{BiO}(\text{IO}_3)$  structure is all stereoactive lone-pairs of the  $\text{I}^{5+}$  cations pointing in the same direction, resulting in its very large SHG response.  $\text{BiO}(\text{IO}_3)$  has the optical absorption onset at 3.3 eV. Therefore,  $\text{BiO}(\text{IO}_3)$  is a

promising SHG material used to generate the radiation with a wavelength in the visible range.

#### **6.4 Li - M - A oxide system (M = Mo<sup>6+</sup> or W<sup>6+</sup>; A = Se<sup>4+</sup> or Te<sup>4+</sup>)**

In chapter 5, two new isostructural centrosymmetric oxide materials, Li<sub>2</sub>(MO<sub>4</sub>)(TeO<sub>3</sub>) (M = Mo<sup>6+</sup> or W<sup>6+</sup>) and a new polar oxide material, Li<sub>6</sub>(Mo<sub>2</sub>O<sub>5</sub>)<sub>3</sub>(SeO<sub>3</sub>)<sub>6</sub> were reported. The materials exhibit a zigzag layered structure consisting of MO<sub>6</sub> and AO<sub>3</sub> polyhedra. Li<sub>6</sub>(Mo<sub>2</sub>O<sub>5</sub>)<sub>3</sub>(SeO<sub>3</sub>)<sub>6</sub> exhibit a moderate SHG efficiency of 170 x α-SiO<sub>2</sub>.

We tried to synthesize more oxides in Li - M - A oxide system. Based on the bond valence model, we expected that the isostructural series Li<sub>6</sub>(Mo<sub>2</sub>O<sub>5</sub>)<sub>3</sub>(TeO<sub>3</sub>)<sub>6</sub>, Li<sub>6</sub>(W<sub>2</sub>O<sub>5</sub>)<sub>3</sub>(SeO<sub>3</sub>)<sub>6</sub>, and Li<sub>6</sub>(W<sub>2</sub>O<sub>5</sub>)<sub>3</sub>(TeO<sub>3</sub>)<sub>6</sub> could exist. So far, we have been able to prepare the polycrystalline phase of Li<sub>6</sub>(Mo<sub>2</sub>O<sub>5</sub>)<sub>3</sub>(TeO<sub>3</sub>)<sub>6</sub> which has the same powder X-ray diffraction to Li<sub>6</sub>(Mo<sub>2</sub>O<sub>5</sub>)<sub>3</sub>(SeO<sub>3</sub>)<sub>6</sub>. We are attempting to synthetically explore and grow single crystals for these compounds.

#### **6.5 Na-W-Se oxide system**

Two new polar oxide materials, Na<sub>2</sub>(WO<sub>3</sub>)<sub>3</sub>(SeO<sub>3</sub>)·2H<sub>2</sub>O and Na<sub>6</sub>(W<sub>6</sub>O<sub>19</sub>)(SeO<sub>3</sub>)<sub>2</sub>, have been synthesized and characterized. Na<sub>2</sub>(WO<sub>3</sub>)<sub>3</sub>(SeO<sub>3</sub>)·2H<sub>2</sub>O exhibit a hexagonal tungsten oxide (HTO) layers which are capped on one side by SeO<sub>3</sub> trigonal pyramids (Class 2 HTO layered structure).<sup>12</sup> Na<sub>6</sub>(W<sub>6</sub>O<sub>19</sub>)(SeO<sub>3</sub>)<sub>2</sub> exhibits a one-dimensional “ribbon” structure. Both structures consist of WO<sub>6</sub> and SeO<sub>3</sub> polyhedra. The H<sub>2</sub>O molecules play a critical role in stabilizing the Na<sub>2</sub>(WO<sub>3</sub>)<sub>3</sub>(SeO<sub>3</sub>)·2H<sub>2</sub>O crystal structure via hydrogen bonding as Na<sup>+</sup> cations are too small to keep electrostatic interaction



between two consecutive HTO layers. Without the H<sub>2</sub>O molecules, the Na<sub>2</sub>(WO<sub>3</sub>)<sub>3</sub>(SeO<sub>3</sub>)·2H<sub>2</sub>O structure would collapse. Instead, Na<sub>6</sub>(W<sub>6</sub>O<sub>19</sub>)(SeO<sub>3</sub>)<sub>2</sub> was formed with a new bond network topology. Na<sub>2</sub>(WO<sub>3</sub>)<sub>3</sub>(SeO<sub>3</sub>)·2H<sub>2</sub>O exhibits a large SHG efficiency attributed to the Class 2 HTO layered structure. Na<sub>6</sub>(W<sub>6</sub>O<sub>19</sub>)(SeO<sub>3</sub>)<sub>2</sub> exhibits a weak SHG efficiency because of the internal C<sub>2</sub> rotation axis that results in the cancelation of the polarization of five WO<sub>6</sub> and one SeO<sub>3</sub> polyhedra.

Because of the importance of the alkali cation size in supporting the Class 2 HTO layered structures, only big single charge cations like Tl<sup>+</sup>, Rb<sup>+</sup>, and Cs<sup>+</sup> or cations with capability of hydrogen bonding like (NH<sub>4</sub>)<sup>+</sup> are able to keep the HTO layers stable. Single charge cations such as Ag<sup>+</sup> or K<sup>+</sup> are too small in size to form and stabilize the Class 2 HTO layered structures. In fact, Ag<sub>2</sub>(MoO<sub>3</sub>)<sub>3</sub>(SeO<sub>3</sub>)<sup>13</sup> and K<sub>2</sub>(WO<sub>3</sub>)<sub>3</sub>(TeO<sub>3</sub>)<sup>14</sup> crystallized in the centrosymmetric structure. For these cations to obtain the Class 2 HTO layered structure, the participation of any ions or molecules with a capability of forming hydrogen bonding is required in the HTO layers. We predict that this will work for the K-W-Se oxide system. The preliminarily synthetic exploration of the K-W-Se oxide system in combination with X-ray diffraction study, and SHG measurement showed very promising results. We have been able to separate four different types of crystals. All crystals are SHG-active with SHG efficiencies ranging from the 150 to 400 x α-SiO<sub>2</sub>. One of these crystals has a powder X-ray diffraction pattern very close to Na<sub>2</sub>(WO<sub>3</sub>)<sub>3</sub>(SeO<sub>3</sub>)·2H<sub>2</sub>O, indicating incorporation of H<sub>2</sub>O molecules in the crystal as the hydrogen bonding connectors.

## 6.6 References.

1. Bader, R. F. W. *Mol. Phys.* **1960**, 3, 137.
2. Bader, R. F. W. *Can. J. Chem.* **1962**, 40, 1164.
3. Goodenough, J. B. *Annu. Rev. Mater. Sci.* **1998**, 28, 1.
4. Kunz, M.; Brown, I. D. *J. Solid State Chem.* **1995**, 115, 395.
5. Opik, U.; Pryce, M. H. L. *Proc. R. Soc. London, Ser. A* **1957**, 238, 425.
6. Pearson, R. G. *J. Am. Chem. Soc.* **1969**, 91, 4947.
7. Pearson, R. G. *J. Mol. Struct.:THEOCHEM* **1983**, 103, 25.
8. Porter, Y.; Bhuvanesh, N. S. P.; Halasyamani, P. S. *Inorg. Chem.* **2001**, 40, 1172.
9. Porter, Y.; Ok, K. M.; Bhuvanesh, N. S. P.; Halasyamani, P. S. *Chem. Mater.* **2001**, 13, 1910.
10. Pico, C.; Castro, A.; Veiga, M. L.; Gutiérrez-Puebla, E.; Monge, M. A.; Ruiz-Valero, C. *J. Solid State Chem.* **1986**, 63, 172.
11. Cao, Z.; Yue, Y.; Yao, J.; Lin, Z.; He, R.; Hu, Z. *Inorg. Chem.* **2011**, 50, 12818.
12. Chang, H. Y.; Kim, S. W.; Halasyamani, P. S. *Chem. Mater.* **2010**, 22, 3241.
13. Ling, J.; Albrecht-Schmitt, T. E. *J. Solid State Chem.* **2007**, 180, 1601.
14. Goodey, J.; Ok, K. M.; Broussard, J.; Hofmann, C.; Escobedo, F. V.; Halasyamani, P. S. *J. Solid State Chem.* **2003**, 175, 3.